The applications of InSAR time series analysis for monitoring long-term surface change in peatlands

Zhiwei Zhou

Thesis submitted to the University of Glasgow for the degree of Doctor of Philosophy

School of Geographical and Earth Sciences

University of Glasgow

September 2013

Supervised by Dr Zhenhong Li and

Professor Susan Waldron

Abstract

In the past three decades, peatlands all over the world such as upland bogs, tropical fens, have been undergoing significant and rapid degradations. These degradations cause carbon loss and CO_2 emissions, and also fuel climate change. In this research, I present three case studies on how space geodetic tools, especially Radar Interferometry (InSAR), can be used to monitor and to advance our understanding of the long-term surface changes in peatlands.

First, I investigate the eroding extent and severity of upland UK peatlands using InSAR. Both short wavelength C-band and long wavelength L-band data are explored in this study. I detect a long-term peat subsidence rate of about 0.3 cm/yr, and 2 cm of decrease in peat height between 2002 and 2010. I also examine the coherence performance of C- and L-band over upland bogs. I find L-band data provides better coherence than C-band in upland bogs. Second, I use InSAR time series generated by L-band images to map the spatial and temporal subsidence of drained tropical peatlands in Sumatra, Indonesia. And based on InSAR-derived subsidence rate data, I estimate carbon loss or CO_2 emission. Third, I assess the effectiveness of peatland restoration work in in Central Kalimantan, Indonesia using InSAR (L-band images). Restoration effects and impact factors are investigated by the spatial and temporal changes of peat height, which also provide useful information for guiding future restoration activities in this region.

Overall, this research suggests that InSAR time series is feasible to monitor long-term peat height change in peatlands, provides new insights into the dynamic surface changes in peatlands, and helps to study the carbon loss and CO_2 emissions from peatlands, and understand restoration effects.

Declaration of originality

I confirm that the work described in this thesis is my own work unless otherwise cited or acknowledged. The thesis is of my own composition and has not been submitted for any other degree at the University of Glasgow or any other institution.

Zhiwei Zhou

September 2013

Acknowledgements

This research is supported by a joint program from the China Scholarship Council (CSC) and the University of Glasgow.

First and foremost, I would like to express my greatest and sincerely thanks to my supervisors Dr Zhenhong Li and Prof. Susan Waldron, for their creative and patient guidance, constructive criticism and question, constant encouragement and trust throughout my past four years' PhD study, and also for their invaluable time during the writing up of this thesis. It is an exhilarating, inspiring and delightful journey together with Zhenhong and Susan to learn the InSAR technique and to apply it to new areas in peatlands. Both taught me to think critically about my research and were always patient about my slow progress and negative results, and helped me build confidence.

I would like to thank Dr Noel Gourmelen for providing ALOS data for the uplands case study. Also I would like to thank Dr Akiko Tanaka for providing ALOS data for the Indonesia cases studies. I would like to thank Dr Peng Liu, Andrew Singleton, Wanpeng Feng for solving my endless InSAR questions, friendship, encouragement, discussions and help. I would like to thank Prof. Trevor Hoey, Prof. Paul Bishop for their discussions and suggestions. Thanks to Gary for maintaining the server in a good condition. Thanks to Les for printing the conference posters. Thanks to Prof. Lianying Li for his encouragement during the writing up of this thesis.

Thanks to Helen Murray, Leena Vihermaa, Alona Armstrong, Ben Smith, Hemanth Pasumarthi, and Martin Coleman for their useful discussions and help.

I also would like to thank Jin Shen, Zhenjie Qiu, Rong Li, Yuening Zhang, Shaochen Wang and Hanlin Xiao, for their friendship, encouragement and help. They made my life wonderful, happy and meaningful in Glasgow.

Finally, I am grateful to my parents and elder brothers for their selfless and endless support.

Table of Contents

List of Figures

List of Tables

List of Acronyms

3D	Three Dimension
ALOS	Advanced Land Observing Satellite
ASAR	Advanced Synthetic Aperture Radar
APS	Atmospheric Phase Screen
DEM	Digital Elevation Model
ECMWF	European Centre for Medium-range Weather Forecasts
ENVISAT	Environmental Satellite
ENSO	El Niño Southern Oscillation
EOSIDS	Earth Observing System Data and Information System
ERS	European Remote Sensing
ESA	European Space Agency
DePSI	Delft Persistent Scatterer InSAR
GPS	Global Positioning System
DOC	Dissolved organic carbon
GHG	Green House Gas
GPS	Global Positioning System
GTTM	Topography-dependent turbulence model
InSAR	Interferometric Synthetic Aperture Radar
IPCC	Intergovernmental Panel on Climate Change
JAXA	Japan Aerospace Exploration Agency
JERS	Japanese Earth Resource Satellite
JPL	Jet Propulsion Laboratory
LiDAR	LIght Detection And Ranging
LULUCF	Land Use, Land Use Change and Forestry
LOS	Line Of Sight
MERIS	Medium Resolution Imaging Spectrometer
ML-PS	Maximum Likehihood Persistent Scatterer
MODIS	Moderate Resolution Imaging Spectroradiometer
MOFEC	Ministry of Forestry and Estate Crops
MRP	Mega Rice Project
NASA	National Aeronautics and Space Administration
NDVI	Normalized difference vegetation index
NEE	Net ecosystem exchange
N-SBAS	New SBAS
PALSAR	Phased Array type L-band Synthetic Aperture Radar
POC	Particulate organic carbon
PS	Persistent Scatterers
PSINSAR	Permanent Scatterer InSAR
RMS	Root Mean Square

SAR	Synthetic Aperture Radar
SBAS	Short BAseline Subset
SLC	Single Look Complex
SNR	Signal Noise Ratio
SRTM	Shuttle Radar Topography Mission
StaMPS	Stanford Method for Persistent Scatterers
STBAS	Small Temporal Baseline Subset
TLV	Temporarily Linear Velocity
USGS	United States Geological Survey
WGS	World Geodetic System

Chapter 1 Introduction

Abstract: Peatlands only cover 3% of the Earth's land, but they store up to 550 Gtonnes of carbon, equivalent to 1/3 of global soil carbon (Hooijer et al., 2006). They are of key value for biodiversity conservation and climate regulation, and provide important support for human welfare (Charman et al., 2008). However, if peatlands begin to degrade on a large scale, the stored carbon could be released in the form of C-gases and as dissolved and particulate material (Charman et al., 2008). Spaceborne repeat-pass Synthetic Aperture Radar Interferometry (InSAR) provides a means to detect surface movements with a few millimeter accuracy and tens of meters spatial resolution over a wide area (e.g. $100 \times 100\ km$) (Massonnet and Feigl, 1998; Rosen et al., 2000). And it has been commonly used to assess earthquake or volcano activities, land subsidence/landslides, or ice sheet/glacial movements. In my PhD I explore the potential and limitations of InSAR for monitoring peatland height change, and from this to estimate carbon loss or gain from peatlands based on InSAR observations.

1.1 Why peatland?

Peat is decaying organic matter that has accumulated under saturated conditions, and forming in areas of positive water balance. Therefore, peatlands are more likely to form in regions with high precipitation excess, such as upland areas of the temperate and boreal zones or tropical areas. Bogs and fens are the two main types of peatlands. Most existing peatlands have formed in the last 10,000 years since the last ice age, and now are important stores of carbon. Naturally peatlands may shift between being a carbon sink or source on a seasonal and inter-annual time scale (Charman et al., 2008), and can exert a net cooling effect on the global radiation balance. However, due to degradation processes such as upland erosion in UK (Evans and Lindsay, 2010b), radiatively forcing (greenhouse gas) emission from tropical peatlands (Couwenberg, 2011), the degradation associated with eroding and development is reducing, or even

reversing, their climate cooling effect (Grace, 2004; Limpens et al., 2008; Dise, 2009; Page et al., 2011b; O'Donnell et al., 2012).

In the UK, peat covers about 29,000 km^2, accounting for 13% of the land surface; 22,500 km^2 of the total peat is blanket bog (Milne and Brown, 1997; Holden et al., 2004). This is only a small proportion of the total northern heimisphere peat cover of 3.5 million km^2 (Gorham, 1991). However, the upland peatlands of the UK are being severely eroded, with large areas affected by gully erosion, because of the intense and extensive erosion (Evans and Warburton, 2007). Erosion causes local drainage of the peat and is a major source of particulate carbon loss in peatland streams (Holden, 2005; Evans et al., 2006; Evans and Warburton, 2007). Gully erosion also has secondary effects, it enhances drainage and lowers the water table potentially enhancing the decomposition of surface peats (Evans and Lindsay, 2010b). Generally, the carbon sequestration is in the order of 50 g C m^{-2} yr^{-1} in the peatland (Worrall et al., 2003), but the rate of particulate organic carbon (POC) flux is up to 79 g C m^{-2} yr^{-1} due to heavily eroding systems in South Pennines, England (Pawson et al., 2008). Evans and Lindsay (Evans and Lindsay, 2010b) also reported the Bleaklow plateau, UK, had shifted from a net carbon sink (-20.3 g C m^{-2} yr^{-1}) to a net carbon source (29.4 g Cm^{-2} yr^{-1}) due to gully erosion.

Tropical peatlands (Southeast Asia, Africa, etc) are also important for global ecosystem services (such as biodiversity and water), and terrestrial C storage. Globally, tropical peatlands cover ~ 441,025 km^2, equivalent to ~ 11% of the global peatland area; 56% of the tropical peatlands (247,778 km^2) is in Southeast Asia (Page et al., 2010). Due to the considerable thickness of peat soils, Southeast Asia contains 68.5 Pg of C, representing 77% of global tropical peatland carbon stores and ~ 11-14% of the global peat C pool. Indonesia accounts for the largest share (57.4 Pg or 65%), followed by Malaysia (9.1 Pg or 10%) (Page et al., 2010). On average, peatlands in Indonesian store about 2800 tons carbon per hectare and have an average thickness of 4.5 m (Jaenicke et al., 2008). Due to the increasing global demands for food and biofuels, degradation, drainage, fires, and conversion to plantation increased a lot during the past two decades. This not only threatened the existence of the Southeast-

Asia peat swap forest ecosystem, but has also created a constant source of GHG emission, and increased the global awareness of the significance of carbon emissions in this region (Hooijer et al., 2010; Miettinen and Liew, 2010; Yadvinder, 2010; Kimberly et al., 2012). It was estimated that about 880,000 ha (6%) of tropical peatlands in Southeast Asia had been converted to oil palm plantation in the early 2000s, which caused about 660,000 Mg of carbon loss annually (Koh et al., 2011); It was reported that CO_2 emissions from peatland drainage in Southeast Asia in 2006 was equivalent to 1.3% to 3.1 % of the current global CO_2 emission from fossil fuel (Hooijer et al., 2010).

Drainage of peatlands is thought to decrease absolute surface height (termed subsidence) because of peat shrinkage and biological oxidation of peat soils to carbon dioxide (Wösten et al., 1997; Hooijer et al., 2010), and is considered as a main source of carbon emissions in tropical peatlands (Jauhiainen et al., 2008; Hooijer et al., 2012). Therefore, it is also possible to estimate net carbon emission from drained peatland as a function of the change in peat surface height (Wösten et al., 1997; Couwenberg et al., 2010; Hooijer et al., 2010; Hooijer et al., 2012). Page et al (2011a) suggested that it was more reliable for estimating carbon losses from drained peat than closed chambers and eddy covariance (both described in Chapter 2) because it is capable of providing a time-integrated measure of the net carbon balance of the peat.

Since peat forms in areas of positive water balance, and drainage causes carbon loss, blocking the drainage channels by building dams is considered as one of the most practical and economical peatland restoration actions There is intensive experience and knowledge on peatland restoration in the boreal and temperate zones (e.g. Line *et al*, 2003), but very little has been known about the restoration of large areas of degraded tropical peatland (Wösten et al., 2006; Page et al., 2009b). Therefore, it is also important to assess the spatial and temporal effects of hydrological restoration in peatlands by dams.

1.2 Why InSAR?

Both the term of 'Synthetic Aperture Radar Interferometry' and that of 'Interferometric Synthetic Aperture Radar' (InSAR) represent an

interferometric technique associated with Synthetic Aperture Radar (SAR). Therefore, InSAR has inherited advantages from SAR, such as the operational capability in day and night, and in all weather conditions.

Initially, InSAR was applied to planetary (Venus) observations in the late 1960s (Rogers and Ingalls, 1969). The next application was to produce topographic maps (Graham, 1974; Zebker and Goldstein, 1986). In the late 1980s, Gabriel et al. (1989) first demonstrated the application of differential Interferometric SAR (DInSAR) technique fo r mapping the surface deformation on agricultural fields over a large swath (50 km) with centimeter accuracy in the Imperial Valley of California. With the launch of the ERS-1 satellite in 1991 (Attema, 1991), repeat-pass InSAR was successfully applied to detect the coseismic displacement field of the 1992 M_w 7.3 Landers earthquake (Massonnet et al., 1993). With a series of spaceborne SAR missions launched since the 1990s, such as ERS-2, JERS-1, Radarsat-1, Envisat, and ALOS-1, the development of repeat-pass InSAR techniques has been accelerated for measuring surface deformation. It has been widely used to map the Earth's surface dynamics, such as earthquakes (Massonnet et al., 1996; Yuri et al., 2001; Fialko, 2006; Stramondo et al., 2011), volcanoes (Massonnet et al., 1995; Lu et al., 1997; Pritchard and Simons, 2002; Papoutsis et al., 2013), faults/tectonic (Wright et al., 2004a; Elliott et al., 2010), land subsidence/landslides (Fielding et al., 1998; Buckley et al., 2003; Stramondo et al., 2008; Bovenga et al., 2012) and ice sheet/glacial motion (Goldstein et al., 1993; Madsen et al., 1999; Rignot, 2008; Jaber et al., 2012). In this thesis, I attempt to use repeat-pass InSAR (described further in chapter 3) for mapping peatland height change, and hereafter refer to it as InSAR for simplicity.

Traditional methods have been used to measure peat height change, such as perforated PVC tubes as poles anchored into the substrate underlying the peat, or Differential Global Positioning System (DGPS). But these methods are not applicable in terms of time, cost and scale, as it is difficult to assess most of peatlands due to vegetation or forest barriers. Comparing with these methods, InSAR has some obvious advantages: (1) comparable accuracy (a few mm), (2) high spatial resolution (meters to tens of meters), (3) wide coverage (say 100

km x 100 km or even wider), and (4) global coverage including inaccessible areas. Another advantage is access to a long-term archived dataset, e.g. ERS-1 SAR data, which can be traced back to 1991, and provides a possibility to investigate the evolution of peatland surfaces over the past two decades.

There are only a very limited number of reported InSAR studies on peatlands, most focusing on deforestation (Ribbes et al., 1997; Suga and Takeuchi, 2000; Deutscher et al., 2013) and ground biomass estimation (Santos et al., 2004; Morel et al., 2011; Basuki et al., 2013), rather than peat height change. In 2011, using 4 scenes of ERS tandem pairs (1 day interval) from October 1997 to January 2000 and the four-pass (four SAR images) InSAR method, a subsidence rate of 2 cm/year was observed in Central Kalimantan, Indonesia (Dahdal, 2011). However, the four-pass InSAR method only uses one pair SAR of images to detect the surface deformation, the other SAR image pair is used to generate topography information and then applied to remove the topographic phase contained in the first pair. So by the four-pass method, the surface movement rate could be over/under-estimated, and the surface movement history is not recovered. Therefore it is of great interest to investigate repeat-pass InSAR time series on mapping the spatial and temporal element of peat height change over different type of peatlands due to different reasons.

For repeat-pass InSAR, there are two main limitations: decorreation (Zebker and Villasenor, 1992) and atmospheric heterogeneities (Goldstein, 1995; Zebker et al., 1997). In recent years, several InSAR time series techniques have been developed to address these two limitations, including Small BAseline Subset (SBAS) InSAR. SBAS methods involve an appropriate combination of short orbital separation, to reduce the effect of decorrelaion (Berardino et al., 2002; Lanari et al., 2004; Hooper, 2008). In this thesis, the SBAS InSAR technique developed by *Li et al.* (2009a) is used to recover the evolution of peatland height changes.

Figure 1.1 illustrates the principle behind this PhD thesis. Peatland height changes are detected using InSAR time series, and then used to estimate carbon loss, which is one key parameter to understand climate change.

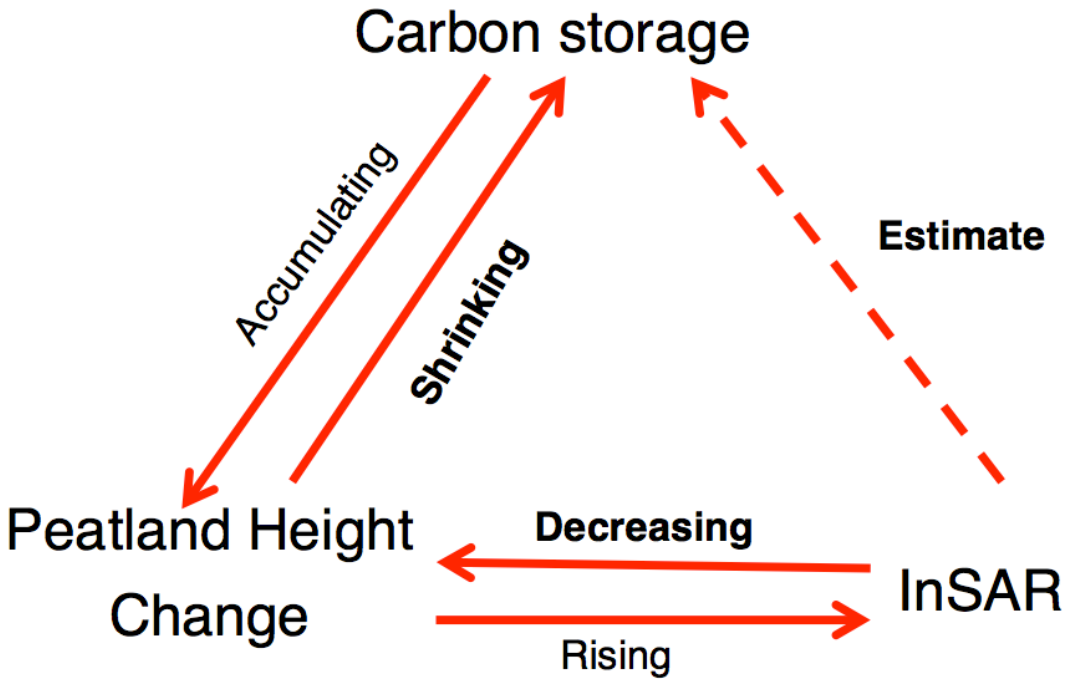

Figure 1.1 The application of InSAR to estimating carbon storage from peatland height change. With decreasing or rising of peatland height, the carbon storage is shrinking or accumulating. InSAR is sensitive to the height change of peatland. This provides key information to estimate carbon storage change. In this thesis, we use InSAR to estimate carbon loss from peatland.

1.3 Objectives

In this thesis, the repeat-pass InSAR time series technique is applied to mapping the spatiotemporal change of peatland height and estimating the carbon loss from peatland. The study areas include two globally important categories of peatland in the world: upland blanket bog (UK), and tropical fens (Indonesia), that are degrading with different mechanisms. Two different frequencies of SAR images (C-, L-band) are explored in this research.

The key questions addressed in this thesis are as follows:

1. Is it feasible to use InSAR to monitor peatland height change? What are the limitations in applying InSAR to peatlands? How accurate can InSAR results be in the case of peatlands? What is the optimal procedure to using InSAR for monitoring peatland deformation?

2. Is it applicable to estimate carbon loss from peatland height change derived from InSAR? What are the limitations for estimating carbon loss based on peatland subsidence data?

3. If peatlands are being restored, is InSAR a useful tool to monitor or guide the restoration activities?

1.4 overview of this thesis

Chapter 2 reviews how peatlands function; carbon losses in upland and tropical peatlands; and common approaches used currently to estimate carbon loss.

Chapter 3 introduces the principles of SAR and InSAR, including the main limitations. InSAR time series approaches are reviewed as well.

Chapter 4 investigates the eroding extent and severity of peatland over the Monadhliath Mountains, Scotland by InSAR. This study presents the coherence performance and InSAR time seriers analysis of Envisat C-band and ALOS L-band data over peatland in upland.

In Chapter 5, two adjacent tracks of ALOS L-band data are used to assess the subsidence and carbon loss of drainage peatland in Sumatra, Indonesia.

In Chapter 6, the restoration effects on peatland in Central Kalimantan, Indonesia, are examined using two adjacent tracks of ALOS data.

Finally, conclusions and recommendations for future work are given in Chapter 7.

Chapter 2 Peatlands and greenhouse gas emissions

Abstract: The purpose of this chapter is to introduce the peatland, its functions, and the relationship with climate change. As one of the most important natural wetland ecosystems in the world, peatlands only cover 3% (some 4 millions km^2) of the Earth's land area, but they store up to 550 Gtonnes of carbon, which is equivalent to 1/3 of global soil carbon (Hooijer et al., 2006). They are of key value for biodiversity conservation and climate regulation, and provide important support for human welfare (Charman et al., 2008). However, if peatlands begin to degrade on a large scale, this stored carbon could be released in the form of C-gases and as dissolved and particulate material (Charman et al., 2008). Degradation can occur through processes such as upland erosion (Evans and Lindsay, 2010b), and Green House gas emission in tropical peatlands (Couwenberg, 2011). Measurements and estimation on carbon loss from peatlands are reviewed in this chapter.

2.1 Peatland

A peatland is an area with a naturally accumulated layer of dead organic material (peat) of at least 30 cm depth at the surface (Charman et al., 2008). It is a special kind of wetland ecosystem, accounting for approximately 60% of the world's wetlands (Charman et al., 2008; Limpens et al., 2008; Joosten, 2009).

Peat is an accumulation of partially-decayed organic matter that has been grown where the peat now is and has not been transported after its formation; the accumulation may occur over tens of thousands of years. Peat can be found in wetland bogs, moons, muskegs, pocosins, mires, and peat swamp forests. A mire is a peatland where peat is being formed and accumulating (Charman et al., 2008).

Charman *et al.* (2008) provide an excellent overview of the process of peat formation, outlining the following to be important. Peat forms when plant

material, usually in a marshy area, is inhibited from decaying fully by acidic and anaerobic conditionss. This means peat accumulates in areas where the rate of plant production exceeds the rate of plant decomposition. It is composed mainly of marshland vegetation: trees, grasses, fungi, as well as other types of organic remains, such as insects and animal remains. Peat layer accumulation (or growth) and the degree of decomposition (or humification) depends principally on its composition and on the degree of water logging; while water-logging is a prerequisite for the creation and preservation of peat, the accumulation only takes place when the water level is just under, at, or just over the surface over the long-term. In addition, peat formed in very wet conditions accumulates considerably faster, and is less decomposed, than that in drier places. The formation of peat is a very slow process with a rate of about 0.5 - 1 mm per year and with locally strong variation, most peatlands that exist today formed in the last 10,000 years since the last ice age.

The major characteristics of natural peatlands are: 1) permanent water logging; the permanent water logging of the peat body keeps the peat from oxidation and makes the carbon storage possible; 2) the formation and globally long-term storage of peat (carbon); 3) the continuous upward growth of the surface. The water logging and the continuous upward growth of the surface further provide and determine the special and extreme site conditions for peat organisms. These above characteristics determine the specific goods, services, and functions associated with peatlands, such as water supply, and biodiversity.

Globally, peatlands are highly diverse, especially with respect to species and community composition, such as the plants that grow there, the colour and composition of the peat, the water content and the levels of nutrients the peat contains (Charman et al., 2008). Despite diversity in these areas peatlands generally share eco-hydrological functioning. There are two main groups of peatlands: bogs and fens, where bogs lie higher than their surroundings ("high mires") and are only fed by precipitation, and fens are in landscape depressions ("low mires"), and are fed by water that has been in contact with mineral soil or bedrock (Figure 2.1) (Charman et al., 2008). Bogs prevail in wet climates, whereas fens are ubiquitous. Bogs can be further characterized as either raised

or blanket bogs. Raised bogs are smaller, generally formed in lowland areas, while blanket bogs are expansive, generally formed in wet or upland areas (Figure 2.2).

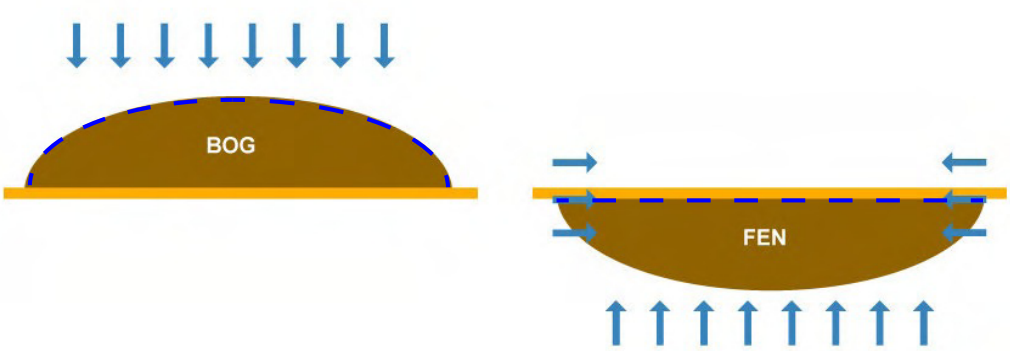

Figure 2.1 The classical difference between "bog" and "fen" peatlands. Dark brown = peat; Arrow= water flow, Blue dash line = water table. Taken from *Charman et al.* (2008).

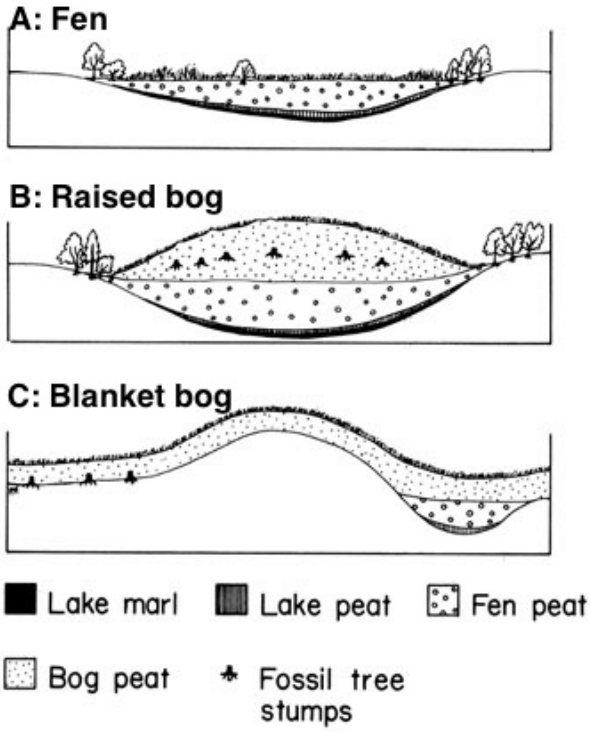

Figure 2.2 Peatland types: fen, raised bog and blanket bog, taken from (FIE, 2013)

Peatlands are found in 175 countries in the world, but are especially abundant in cold (i.e. boreal and sub-Arctic) and wet (i.e. oceanic and humid tropical) regions because peat formation is primarily a function of climate. Peatland distribution is therefore concentrated in specific climate regions. Climate determines the amount of water available in the landscape via the amount of net precipitation, while temperature affects both the production and decay of organic material. Generally, peatlands prevail on flat surfaces as water logging requires a flat surface. Large peatlands prevail on extensive flat land areas, such as western Siberia, the Hudson Bay Lowlands (Canada), the Southeast Asian coastal plains, and the Amazon Basin (Charman et al., 2008). The latest statistics of current status of peatland distribution can be seen in Figure 2.3 (Joosten, 2009; Kaat and Joosten, 2009). Peatland area and carbon stock of each country can be found in *Kaat and Joosten* (2009).

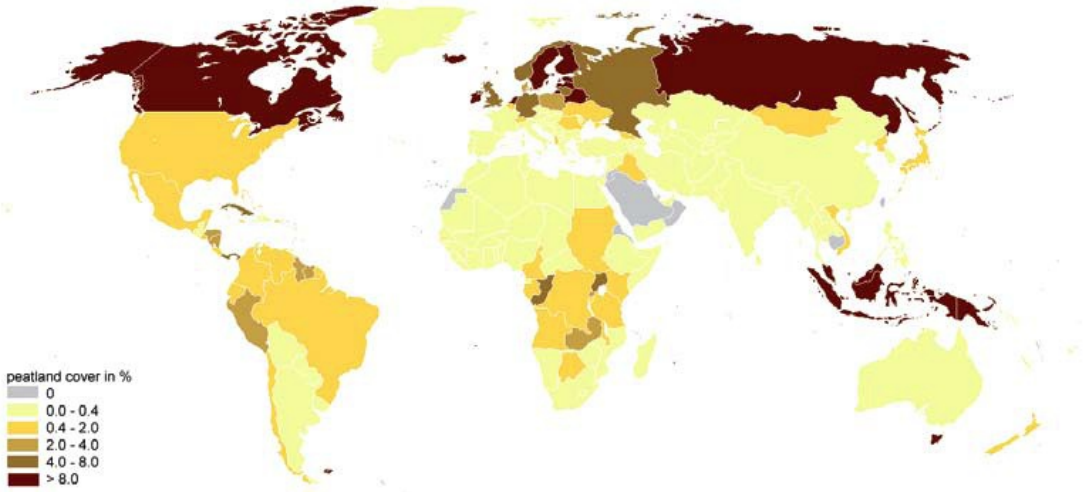

Figure 2.3 Peatland cover per country, adapted from Joosten (2009).

Peat accumulation rates depend on climatic, hydrological and hydrochemical conditions, so peat accumulation shows strong local and regional variation (Charman et al., 2008). Natural peatlands may shift between carbon sink and source on a seasonal and between-year time scale, but the accumulation of peat demonstrates that their long-term natural balance is positive (Charman et al., 2008), and then exert a net cooling effect on the global radiation balance.

However, peatlands begin to degrade on a large scale, this stored carbon could be released in the form of C-gases and as dissolved and particulate material (Charman et al., 2008). Direct damage by human activity is reducing, or even reversing, their climate cooling effect (Grace, 2004; Limpens et al., 2008; Dise, 2009; Page et al., 2011b; O'Donnell et al., 2012). Human interventions include drainage for agriculture, forestry activities (such as palm oil), windfarms, fires and peat extraction, and can result in increased aerobic decay, which is sufficiently large to change the peatland from a sink of carbon to a source. Carbon dioxide emissions from peatland drainage, fires and exploitation are estimated to currently be at least 3000 million tons a year, equivalent to more than 10 % of the global fossil fuel emissions (Charman et al., 2008). With ongoing global warming, the relationship between the peatland carbon emissions and global warming will be stronger and more complex (Grace, 2004; Dise, 2009; Page et al., 2011b), and will likely accelerate rates of atmospheric warming (O'Donnell et al., 2012).

2.2 Upland peat erosion

Areas of the upland peatlands of the UK are severely eroded, with large areas affected by gully erosion, and these have been labeled as 'the badlands of Britain' (Tallis, 1997a) because of the intense and extensive erosion (Evans and Warburton, 2007). This is particularly prevalent in the Pennines, England. The most widespread form of peatland erosion is the incision of deep gully systems into the peat surface, which causes local drainage of the peat and are a major source of particulate carbon loss in peatland streams (Holden, 2005; Evans et al., 2006; Evans and Warburton, 2007). Gully erosion also has secondary effects, it enhances drainage and lowers water table potentially enhancing decomposition of surface peats (Evans and Lindsay, 2010b). The possible causes of erosion include a range of anthropogenic factors such as overgrazing, moorland burning, sulphur dioxide pollution; but there are also natural causes, in particular climate change (Tallis, 1997b). Evans and Waburton (2010) suggested that climatic changes in peatland areas would enhance peatland erosion. According to the current Climate Change Scenarios for the UK, the average annual temperatures for the UK may increase by between 2°C and

3.5°C by the 2080s, and the UK may experience wetter winters and substantially drier summers in the future (Hulme et al., 2002). This implies that the a peat surface with weakened vegetation would be desiccated and cracked in drier summer seasons, and further eroded in winter seasons, thus accelerating physical disintegration of the peat mass through extensive gully erosion in the future, meanwhile the continuously increased temperatures may accelerate oxidation of the bare peat (Evans et al., 2006). Therefore, there is a risk that physical degradation of peatlands and peat oxidation could become a significant positive feedback to global warming (Evans et al., 2006).

2.2.1 Mapping the upland erosion

To assess the eroding extent and the carbon loss of the upland peatland, accurately mapping the gully eroding features is required. Gully erosion can be mapped manually by field surveys (Rothwell et al., 2008), aerial photographs (Grieve et al., 1995; Connolly and Holden, 2011), semi-automatically by optical satellite images (Keyworth et al., 2009), and automatically by aerial 'LIght Detection And Ranging' (LiDAR) images (Evans and Lindsay, 2010a).

In such an assessment we need to understand how confident we are in the measurements of change. Using aerial photographs acquired between 1988 and 1989 and a classfilcation method, *Grieve et al.* (1995) found that 12% of the upland area of Scotland was subject to some form of erosion, where the most significant erosion category was peat erosion, with 6% of the area being affected. However a field survey is impracticable in areas of extensive gully networks and impractical for larger areas, even with the aid of GPS; further, manual mapping from imagery can be very time consuming, labour intensive, and potentially subjective (Evans and Lindsay, 2010a). For example, in extracting a map of disturbed Irish peatlands using high resolution Geoeye-1 satellite imagery (0.5 m), the users' accuracy for each individual class ranged from 66% to 92%, and 85% for the overall accuracy assessment for the disturbance map (Connolly and Holden, 2011). Combining field work and optical satellite images, *Keyworth et al.* (2009) used an object-orientated classification approach to produce a classification map of peat erosion in the Monadhilaith Mountains, Scotland, and

the overall map accuracy was calculated as over 84%. More importantly, there is no quantitative information about erosion in the vertical direction.

Evans and Lindsay (2010a) suggest that airborne LiDAR is one of the most promising data sources for mapping peatland gully systems because of its fine resolution and high accuracy, but this method is limited by LiDAR data coverage. In a study of peatland gully erosion in Bleaklow Plateau in northern England, gully maps were generated automatically from two LiDAR DEMs with a pixel resolution of 2 m, and estimates of gully width and depth were reliable for gullies with a total width of larger than six or eight meters (Evans and Lindsay, 2010a).

2.2.2 Carbon loss from upland eroding

Peatland erosion has the potential to significantly impact carbon storage, including direct erosional losses of particulate organic carbon (POC) and indirect effects on peatland water tables, and consequently on dissolved (DOC) and gaseous carbons losses largely caused by the effects of gully erosion (Evans and Warburton, 2010).

Table 2.1 Measured POC flux from a variety of eroded upland peatland catchments in the UK. Where POC is not reported directly in the source publication, it has been calculated assuming 50% carbon content in the organic sediment fraction, adapted from (Evans and Warburton, 2010). Note: the POC range of Northeast Scotalnd is given in the original paper.

Location	Character	POC ($gC/m^2/yr$)	References
Northeast Scotland	Intact moorland	0.1-8.5	(Hope et al., 1997)
Plynlimon, Mid Wales	Eroding blanket peat	17.2	(Francis, 1990)
South Pennines, England	Eroding blanket peat	79	(Pawson et al., 2008)
Rough Sike (in Moor House), North Pennines, England	Eroded and revegetated	15.6	(Evans et al., 2006)
Moor House and Upper Teesdale National Nature Reserve (NNR), North Pennines, England	Eroded and revegetated	14.7	(Worrall et al., 2009)

The rates of POC flux from intact peatlands are relatively low, typically on the order of 0 ~ 8 g C m^{-2} yr^{-1} (Hope et al., 1997). With heavily eroding systems the rate of POC flux is up to 79 g C m^{-2} yr^{-1} (Pawson et al., 2008). Table 2.1 lists the POC flux from a variety of eroded upland peatlands in the UK.

As carbon sequestration is in the order of 50 g C m^{-2} yr^{-1} in peatland (Worrall et al., 2003), erosion of the peat at a rate greater than this (or through other losses such as lowered water table causing oxidation of the peat) has the potential to shift the net carbon sink to a net carbon source in eroded area. LiDAR data (with a ground resolution of 2 m) delineation of the extent of gully erosion in Bleaklow Plateau, UK, allows calculation that the Bleaklow plateau has shifted from a net carbon sink (-20.3 g C m^{-2} yr^{-1}) to a net carbon source of carbon (29.4 g Cm^{-2} yr^{-1}) due to gully erosion (Evans and Lindsay, 2010b).

2.3 Tropical peatlands, including Green House Gas emissions

Peatlands can also be a source of greenhouses gases to the atmosphere and the processes responsible for this will be outlined using tropical peatlands as an example. *Charman et al.* (2008) provides a good review on GHG fluxes from peatlands, summarised here as follows. GHG fluxes from peatlands have high temporal variability and the annual flux rate could change between years with different weather conditions. To estimate average GHG emissions, diurnal and seasonal fluctuations should be considered. In addition, because small changes in the ecology (temperature) and hydrology (water, water flow direction and rate, depth to the water table, etc.) of peatlands can lead to large changes in GHG fluxes through influence on peatland biogeochemistry, so peatlands could functions as sinks or sources of GHGs depending on the different time horizon under consideration of 20, 100 or 500 years.

Peatlands located in tropical zones (southeast-Asia, Africa, etc) are also important for global ecosystem services (such as biodiversity and water), and terrestrial C storage, in both their surface biomass and underlying thick peat soil. Natural lowland tropical peatlands are covered with trees (peat swamp

forests). On average, Indonesian peat swamp forests store about 2800 tons carbon per hectare and have an average thickness of 4.5 m (Jaenicke et al., 2008), while European peatlands, which mainly develop from non-woody material have an average thickness of only 1.75 m (Byrne et al., 2004). Globally, tropical peatlands cover ~ 441,025 km^2, which is ~ 11% of the global peatland area; 56% of total area (247,778 km^2) is in Southeast Asia (Page et al., 2010). Due to the considerable thickness of peat soils, Southeast Asia contains 68.5 Pg of C, representing 77% of global tropical peatland carbon stores and ~ 11-14% of the global peat C pool. Indonesia accounts for the largest share (57.4 Pg or 65%), followed by Malaysia (9.1 Pg or 10%) (Page et al., 2010).

The tropical peatland carbon and greenhouse gas (GHG) balance is determined largely by the net balance between carbon uptake in photosynthesis and carbon release through ecosystem respiration by vegetation (autotrophic respiration), and by the organisms involved in organic matter decomposition (heterotrophic respiration) (Figure 2.4) (Page et al., 2011a). Carbon dioxide, methane and nitrous oxide (CO_2, CH_4, and N_2O) are the three main peatland greenhouse gases. CO_2 emissions from a peatland includes autotrophic respiration, regulated by photosynthesis and temperature, and heterotrophic respiration controlled largely by soil temperature (Charman et al., 2008). The flux of CH_4 from a peatland is a function of the rates of CH_4 production and consumption in the profile and the transport mechanisms to the atmosphere, such as diffusion, ebullition, or plant-mediated (Charman et al., 2008). CH_4 production depends on the amount of high-quality organic material that reaches the anoxic zone. This means the plant primary productivity and depth to water table are the two most important factors controlling this process. Depth to water table is the key factor controlling the balance between CH_4 production and consumption and finally the ratio of CH_4 and CO_2 emitted from a peatland (Charman et al., 2008). The emission of nitrous oxide and other nitrogen oxide gases (NO and NO_2) from soils is a result of the cycling of N. Where N cycling is rapid, through nitrification and denitrification, and the microbial cycle is "leaky", signification emissions of these gases can occur (Charman et al., 2008).

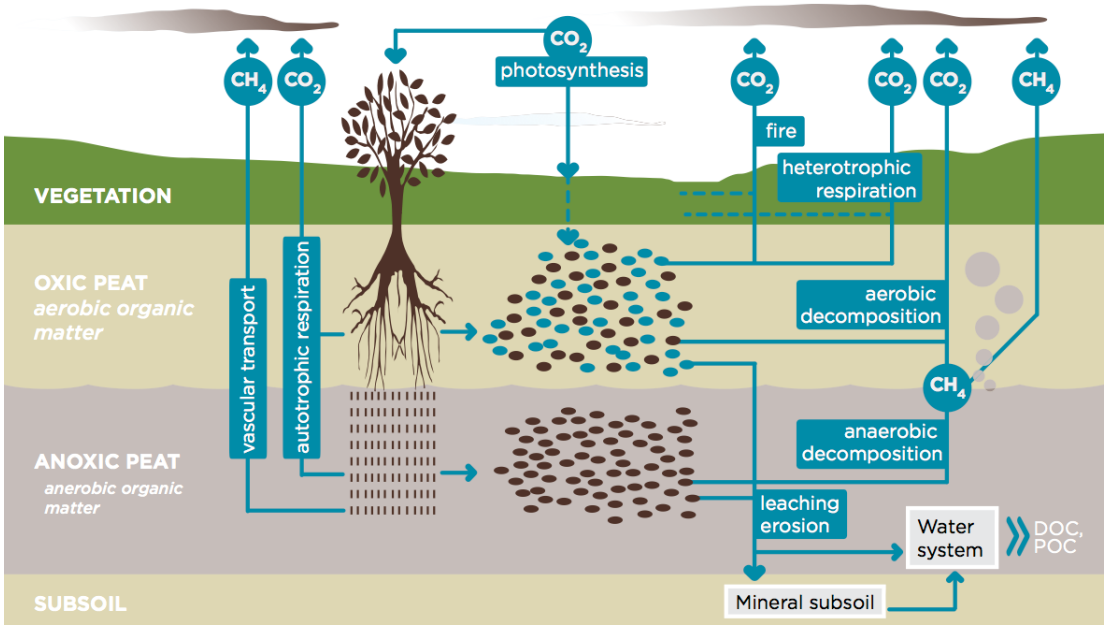

Figure 2.4 Schematic representation of carbon cycle process, flow paths and stores in tropical peat, taken from *Page et al.* (2011a).

Due to rising global demands for food and biofuels, increasing amounts of degradation, drainage, and fires and conversion to plantation during the past two decades have not only threatened the existence of the SE-Asia peat swamp forest ecosystem, but have also created a constant source of GHG emission, and increased global awareness of the significance of carbon emissions in this region (Hooijer et al., 2010; Miettinen and Liew, 2010; Yadvinder, 2010; Kimberly et al., 2012).

2.3.1 GHG flux from tropical peatlands

Anthropogenic disturbances (especially, deforestation, drainage and fires) have led to a significant increase in net emissions of GHG from peatlands, which are now a significant contribution to global anthropogenic emissions (Silvius et al., 2006; Charman et al., 2008; Couwenberg et al., 2010).

Human intervention and land-use may create multiple pressures on the GHG flux in peatlands, mainly connected with water level draw-down. There is a wide range of human activities that have a potential effect on GHG flux in peatlands, such as excavation, forestry, agriculture and other purposes. All

these activities need drainage since they are limited by highly-saturated conditions. Through drainage, the dry peat is in contact with the air and starts oxidizing, decomposing, and emitting carbon dioxide. This process happens very rapidly in the tropics, and is often accelerated by wildfires (Page et al., 2002; Hooijer et al., 2010). These fires can last for weeks, sometimes even months, burning thick layers of peat over large areas (Page et al., 2009a; Wooster et al., 2012; Zender et al., 2012).

The degradation and development of peatland is often associated with logging and the construction of drainage canals in order to make the land usable for agriculture or more often for oil palm and pulp wood plantations. It is estimated that about 880,000 ha (6%) of tropical peatland had been converted to oil palm plantation by the early 2000s, which caused about 660,000 Mg of carbon loss annually (Koh et al., 2011). Approximate 2.3 million ha of peat swamp forests were logged by 2010 (Koh et al., 2011); the peat swamp forest deforestation rate of peninsula Sotheast Asia (including the Indonesia part of New Guinea) averaged annually 2.2 % between 2000 and 2010, with a total loss of an area of 2756 Mha (Miettinen et al., 2011a). 5.1 Mha of the 15.5 Mha of peatlands in Malaysia and in the islands of Sumatra and Borneo have been deforested between 1990 and 2008, releasing to the atmosphere at least of 1.5 Gt of carbon (Miettinen and Liew, 2010). It is estimated that the total carbon emissions from degraded peatlands currently amounts to almost half of the worldwide emissions from Land Use, Land Use Change and Forestry (LULUCF) and to 5% of the total global anthropogenic carbon emissions (Figure 2.5) (Joosten, 2009; Kaat and Joosten, 2009).

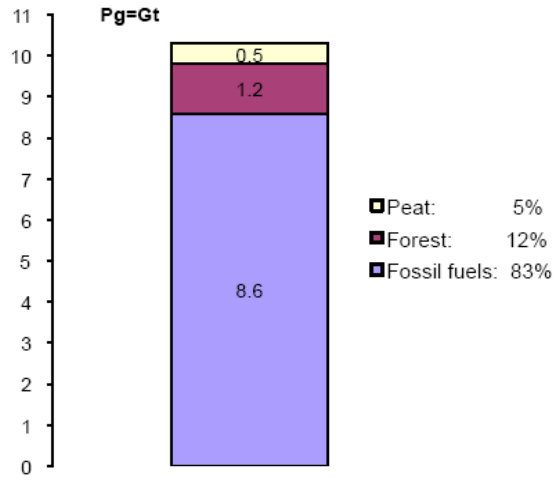

Figure 2.5 Carbon emissions in 2008, taken from Joosten (2009), Kaat and Joosten (2009)

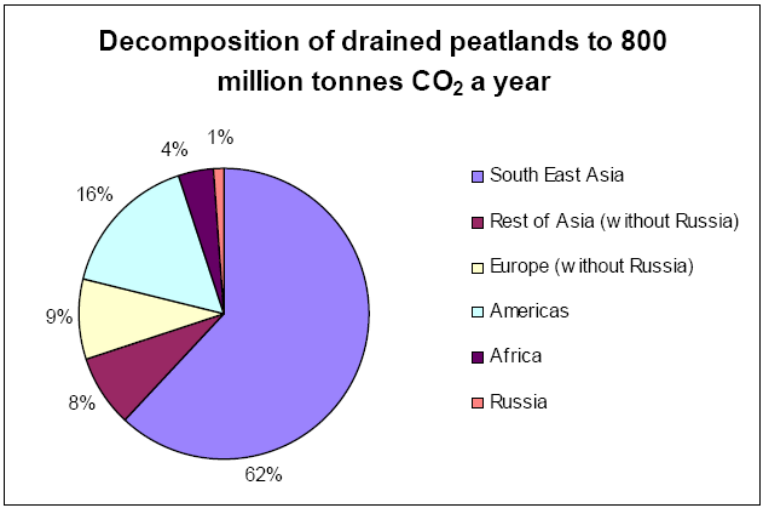

Figure 2.6 Decomposition of drained peatlands to CO_2 a year, taken from Silvius et al. (2006).

The process of decomposition after drainage alone (i.e. excluding fire) leads to a global emission from peatlands of 800 Mt CO_2/yr; 62% of the emission originates from South-east Asia as shown in the pie-chart (Figure 2.6) (Silvius et al., 2006). Currently millions of hectares of peatlands are drained and are decomposing.

Indonesia emits 6.5 times as much CO_2 from degraded peatlands as it does by burning fossil fuels every year. In a ranking of countries based on their total CO_2 emission amount, Indonesia comes 21st if peatland emissions are excluded. However, if peatland emissions are included, Indonesia is the third-largest CO_2 producer in the world (Silvius et al., 2006).

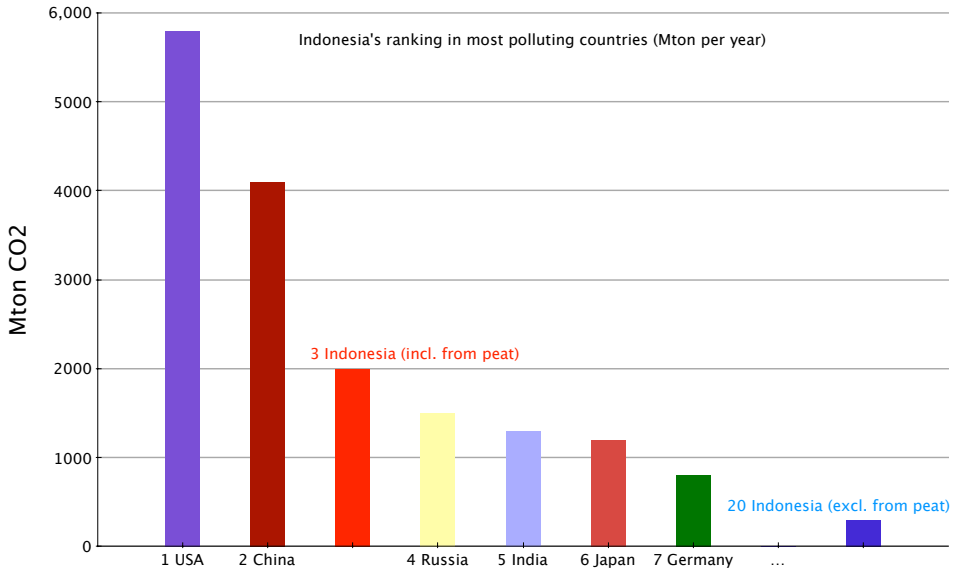

Figure 2.7 Indonesia's ranking in most polluting countries, re-produced from *Silvius et al.* (2006)

Meanwhile the degradation of peatland ecosystems has led to large-scale fires, which is another source of carbon emissions, especially during the EI Niño seasons (van der Werf et al., 2008; Ballhorn et al., 2009). For example, during the 1997-1998 EI Niño dry seasons, it was estimated that carbon emissions caused by peatland fires in Indonesia might be equal to 13-40 % of the mean annual global carbon emissions from fossil fuels (Ballhorn et al., 2009).

2.3.2 GHG flux in tropical peatlands caused by drainage

The other main source of carbon emissions is drainage (Jauhiainen et al., 2008; Hooijer et al., 2010; Hooijer et al., 2012). It is reported that CO_2 emissions from peatland drainage in Southeast Asia is equivalent to 1.3 % to 3.1 % of the current global CO_2 emissions from fossil fuels (Hooijer et al., 2010).

Drainage of peatlands is thought to decrease absolute surface height (termed subsidence) because of peat shrinkage and biological oxidation of peat soils to

carbon dioxide (Wösten et al., 1997; Hooijer et al., 2010). Generally, total subsidence due to drainage of peat soils is caused by consolidation, shrinkage and oxidation components (Figure 2.8). Consolidation is the compression of saturated peat below groundwater level because of the reduction of the buoyancy, resulting in an increase of strain on the peat below and peat bulk density. Shrinkage is the volume reduction of peat above groundwater table due to desiccation, resulting in an increase bulk density of peat (Hooijer et al., 2010).

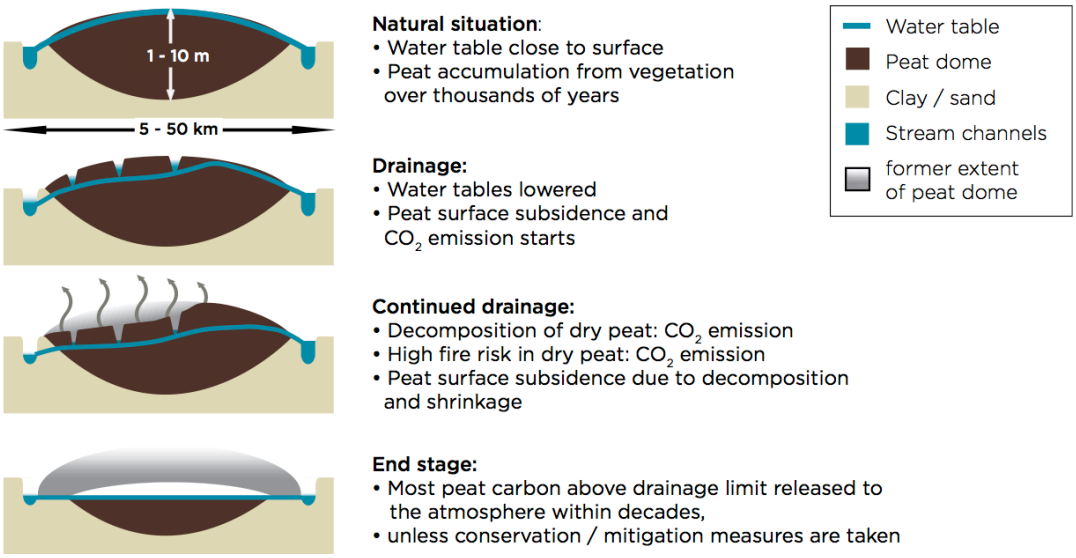

Figure 2.8 Schematic illustration of drainage effects on a peatland dome, taken from *Page et al.* (2011a).

Oxidation is the decomposition of peat in aerobic zone above groundwater table due to breakdown of organic matter, resulting in carbon loss by CO_2 emission to the atmosphere. This process does not cause increase of bulk density of the peat and could decrease it in fact.

The subsidence rate depends on a number of factors, such as peat type, density and thickness, decomposition rate, drainage depth, climate, land use and development history or period (Schothorst, 1982; Hooijer et al., 2010). To calculate the carbon loss based on subsidence data, it is necessary to separate

the volume of peat oxidation from consolidation and shrinkage (Wösten et al., 1997; Hooijer et al., 2012).

The most important GHG emission from drained peatland is $CO_{2,}$ as this contributes 98% or more of the total combined global warming potential (Charman et al., 2008). CH_4 fluxes in drained tropical peatlands are insignificant relative to losses of $CO_{2,}$ both in terms of the mass of carbon lost and overall climatic impact (Page et al., 2011a). Our knowledge is less well-developed of N_2O emissions, as the limited studies of peat N_2O fluxes in drained tropical peatland are unlikely to have adequately captured the true magnitude and dynamic of emission, particularly following fertilizer application (Page et al., 2011a). Therefore, where this thesis calculates C losses, as it is loss of drained peat (an oxidative environment) only the loss of this C as CO_2 has been calculated.

2.3.3 Relationship between loss of peat height and ground water level

There is a direct relationship between ground water level and subsidence rate. Using markers, long-term (21 years) peat subsidence records are collected in Sarawak and Western Johore, Malaysia, Wösten et al (1997) concluded a linear regression relationship between the subsidence and the groundwater depth as follows:

$$Subsidence\ rate\ (cm/yr) = x \times Groundwater\ depth \qquad \textbf{(2.1)}$$

where x is the coefficient, which is ranging from 0.1 to 0.04, groundwater depth in cm (blow the surface). After being first drained for 14 years (1974-1988), peat surface height decreased by up to 0.9 cm/yr for each 10 cm drop in the water table, and this relationship decreased with time, to 0.4 cm/yr for each 10 cm lowering of the groundwater in the later years (1988-1995) (Wösten et al., 1997).

Couwenberg et al (2010) proposed a linear relationship between the rate of subsidence and mean annual water level in tropical peatlands in south east-Asia:

$$Subsidence\ rate\ (cm/yr) = -0.09 \times Groundwater\ depth \quad (2.2)$$

where groundwater depth is in cm (negative), and is best applicable for ground water level less than 50 cm (R^2 =95%). This relationship implies that peat surface height decreases by 0.9 cm every year for each 10 cm of additional drainage depth, which is similar to (Wösten et al., 1997).

In 2012, *Hooijer et al* (2012) suggested another relationship between the groundwater level and loss of peat surface height from a peatland drained for 6 or more years (Acacia plantation, Indonesia) after the drainage:

$$Subsidence\ rate\ (cm/yr) = 1.5 - 4.98 \times Groundwater\ depth \quad (2.3)$$

Where the groundwater depth is in meters (negative) (R^2 =21%). For every 10 cm of additional drainage depth, subsidence increases by 2 cm/yr.

2.3.4 Measurements of CO_2 emissions from tropical peatland

There are several approaches to measuring the CO_2 emission from peatlands, including direct measurements, such as flux chambers (Jauhiainen et al., 2012) and eddy covariance (EC) (Laine et al., 2006) or estimates based on peat subsidence rates measured by GPS (Hooijer et al., 2012), and these estimated from measurement by remote sensing method like optical images (Miettinen et al., 2011a), LiDAR (Page et al., 2002), and InSAR (Dahdal, 2011). This section provides an overview of these measurement techniques, and their advantages and disadvantages in capturing spatial and temporal variation.

2.3.4.1 Direct measurements of CO_2 emission

The closed chamber technique is the most widely used in assessing surface to atmosphere GHG fluxes in tropical peatlands (Figure 2.9) (Ali et al., 2006; Hirano et al., 2007; Hirano et al., 2009; Couwenberg et al., 2010; Jauhiainen et al., 2012). Chamber methods provide data on surface-to-atmosphere gaseous flux exchange from small, well-defined areas at specific points in time. Flux rates are determined by a linear regression of the change in gas concentration

as a function of incubation time which are then scaled up to provides time-integrated GHG budgets for longer time periods and large areas (Page et al., 2011a). The basic measurement principle of the method involves creating a sealed volume over an area considered to be representative of surface conditions, and variations occur due to the chamber size and design, or because whether chambers are static or dynamic, clear or opaque (Denmead, 2008).

Figure 2.9 Closed chamber measurements being made in the field; large static chamber (left) and dynamic chamber and CO2 analyzer, taken from (Page et al., 2011a)

The advantages of the chamber technique are: 1) enabling the quantification of peat surface emission of all three biogenic GHGs in a range of tropical peatlands; 2) enabling real-time data quality assessment (Ali et al., 2006; Hirano et al., 2009). The disadvantages of the measurement are:

1) It is not possible to quantify CO_2 emission contributed by peat or litter decomposition (heterotrophic respiration) from emission from vegetation root respiration (autotrophic respiration), because this approach only provides a measure of total peat respiration (Page et al., 2011a);

2) Emission rates from the soil may be influenced by long chamber incubation times, which may alter temperature and pressure conditions, and result in

uncertainty when upscaling this small-scale measurements to larger spatial and temporal scales (Denmead, 2008);

3) Spatial and temporal up-scaling, typically involves using averages of replicate measurements, assumed to represent the full range of spatial variability present in the ecosystem, multiplied by area and time.

4) This method provides an insufficient number of replicate measurements over sufficient length of time (Page et al., 2011a).

Eddy covariance (EC) measurements are based on micrometeorological theory (Figure 2.10). EC uses fast response (20 Hz) sensors mounted on a tower several metres above the vegetation canopy to sample the vertical component of atmospheric turbulence (using a sonic anemometer) and the atmospheric component of interest (such as GHG, water vapor and temperature), using infrared gas analysis for CO_2 or quantum cascade laser for CH_4 and N_2O. The fluxes are calculated as the mean covariance between the vertical wind speed and the concentration of the relevant GHG (Baldocchi, 2003; Lee et al., 2004). This technique provides direct measurements of net ecosystem atmosphere GHG exchange across the vegetation-soil-atmosphere interface, and it is widely considered as the most appropriate method of quantifying ecosystem-atmosphere greenhouse gas budgets (Baldocchi, 2003), and so has widespread use across the globe as the primary tool e.g. the global FLUXNET community (FLUXNET, 2013).

Compared to closed chambers, EC has the advantage of recording continuous, multiyear, whole net ecosystem gaseous flux data from a relatively large (hectares to km^2) source area or "flux footprint" (Baldocchi, 2003). But there are disadvantages: 1) data gaps are inevitable when constructing long data records, and generally data gaps are filled with values produced from statistical and empirical models to produce daily and annual sums of gaseous exchange (Baldocchi, 2003); 2) EC does not provide information on small-scale process operating at lower spatial scales, which could lead to missing "hot spot" emissions (Laine et al., 2006; Becker et al., 2008; Teh et al., 2011); 3) as the footprint of EC measurements varies depending on wind direction and

atmospheric conditions, care is required in interpreting results where surface condition changes, and for inferring large scale flux measures variable derivers such as drainage depth (Page et al., 2011a).

Figure 2.10 An eddy covariance flux tower measuring surface-atmosphere exchanges of CO2 water and energy at a restored fen peatland in the United Kingdom (left). Eddy covariance instrumentation, consisting of a sonic anemometer, an infrared gas analyzer, and sensors for measuring photosynthetically active radiation, air temperature and relative humidity (right), taken from (Page et al., 2011a).

2.3.4.2 Indirect measurements of GHG emission

In addition to direct flux measurements, it is also possible to estimate net carbon emission from drained peatland as a function of the change in peat surface height which causes oxidative losses (Wösten et al., 1997; Couwenberg et al., 2010; Hooijer et al., 2010; Hooijer et al., 2012). The subsidence method measures the total carbon loss, and is insensitive to the differing forms of carbon (CO_2, CH_4, POC and DOC). In comparison of the direct measurements (closed chambers and EC), subsidence monitoring is generally considered to be more reliable for estimating carbon losses from drained peat because it is capable of providing a time-integrated measure of the net carbon balance of the peat (Page et al., 2011a). As a relatively long period of monitoring is required to apply the subsidence method, the sensitivity to detecting changes in carbon

dynamics over short time scales, such as diurnal or seasonal difference on carbon loss, is low.

As the subsidence is a function of both physical process of peat compaction and consolidation, and the biological process of peat decomposition (oxidation), *Couwenberg et al.* (2010) and *Hooijer et al.* (2012) suggest that before applying the subsidence rate to estimate the carbon loss, the relative contribution of peat decomposition to the overall subsidence must be determined using peat bulk density profiles and measurement of peat carbon concentration obtained both before and after drainage. Globally, the relative contribution of peat decomposition to overall subsidence varies significantly in response to temperature (Stephens et al., 1984), from 40% in temperate climates to 100% in tropical climates (Couwenberg et al., 2010; Murdiyarso et al., 2010; Hooijer et al., 2012). Further, the study of *Hooijer et al.* (2012) suggests that the percentage of subsidence attributed to decomposition increases in the years following drainage, with 75% after 5 years drainage, and 92% after 18 years drainage. This means the decomposition (subsidence rate) is high in the initial years after drainage, which results in highest carbon emission in the first few years after drainage. Therefore, drainage age of a peatland is considered in estimating its carbon loss and CO_2 emission in this thesis.

Typical subsidence data is measured using perforated PVC tubes as poles anchored into the substrate underlying the peat. However, due to the slow decomposition rate, a number of years are required to monitor the subsidence data, which increases the risk of occasional disturbance at individual poles. Additionally, most peatlands in SE-Asia are highly inaccessible as the peatland is covered by peat swamp forests, thus usually there is a trade-offs in balancing the monitoring duration, the number of monitoring points and monitoring quality (Page et al., 2011a).

Remote sensing can also be used as an alternative indirect measurement of GHG emission, because it is a powerful tool in large inaccessible areas for collecting land-surface data in a spatially continuous manner across a range of spatial scales. Generally, remote sensing is classified into passive and active sensors (Ulaby et al., 1981; Lillesand et al., 2004). Passive sensors detect

natural radiation that is reflected by sunlight and optical remote sensing is included in the passive model. Active sensors emit energy, detect and measure the radiation that is reflected from the target. Radar and Light Detection And Ranging (LiDAR) are examples of active remote sensing (Ulaby et al., 1981).

Remotely-sensed data is able to generate vegetation maps and retrieve vegetation biophysical properties, which could help carbon balance models in peatland (Harris and Bryant, 2009b). Due to the importance of hydrology in carbon balance, *Harris and Bryant* (2009a) discussed the possibilities and challenges of monitoring northern peatland hydrology by an airborne and spaceborne optical remote sensing approach, and the preliminary results generated from remote-sensing products suggested that remote-sensing could be used to provide high-resolution, quantitative information of hydrology that surpassed the capabilities of conventional hydrological measurement techniques, which are small-scale or point-based techniques.

Using Moderate Resolution Imaging Spectroradiometer (MODIS) images (250-m spatial resolution), *Koh et al* (2011) estimated that about 6% of tropical peatlands in the lowlands of Peninsular Malaysia had been deforested and converted to oil-palm plantations by the early 2000s. This resulted in a loss of ~ 140 million Mg of aboveground biomass carbon, ~ 4.6 million Mg of belowground carbon from peat oxidation, and loss of ~ 660,00 Mg sequestrated carbon (Koh et al., 2011). However, optical images are available only when acquired in daytime and in clouds-free conditions.

Using an airborne LiDAR scanner with a footprint of 0.25m, *Ballhorn* (2009) detected an average 0.33 ± 0.18m peat burn scar depth in Central Kalimantan, Borneo, Indonesia. Based on these results, the study area was estimated to have released 49.15 ± 26.81 Mton carbon during the 2006 EI Niño, which represented 10-33 % of all carbon emissions from transport within the European community in the year 2006 (Ballhorn et al., 2009). The accuracy of LiDAR is favorable, but it is not economically viable for long-term data collection over a regular repeat cycle, and the weather (clouds) is an obstacle for airborne LiDAR.

Deforestation and inundation was investigated using Japanese Earth Resource Satellite-1 (JESR) L-band SAR data in Central Kalimantan Indonesia, and an area of 347,948 ha of forests was detected to have been destroyed between 1994 and 1998 (Romshoo, 2004). Using 4 ERS1/2 tandem SAR images pairs (1 day interval) from October 1997 to January 2000, subsidence rates of 2 cm/year were estimated using a 4-pass InSAR method in Central Kalimantan, Indonesia (Dahdal, 2011). This was considered to represent carbon loss of between 53 and 83 Mton.

2.4 Estimation of carbon emissions

Based on the measurements and methods discussed in Section 2.3 Tropical peatlands, including Green House Gas emissions, several approaches (but not limited to these) can be used to estimate the carbon emissions. These approaches include: 1) the carbon gain-loss based on land use change (LUC) (IPCC, 2006; Murdiyarso et al., 2010; Koh et al., 2011); 2) estimation based on water table depth (Melling et al., 2005; Ali et al., 2006; Hooijer et al., 2006; Jauhiainen et al., 2008; Hooijer et al., 2010; Hirano et al., 2012; Jauhiainen et al., 2012); 3) measurement of peat subsidence (Wösten et al., 1997; Ballhorn et al., 2009; Couwenberg et al., 2010; Edwards et al., 2010; Dahdal, 2011; Hooijer et al., 2012). In the end of this section, a summary of CO_2 emissions related to these different estimation approaches is listed in Table 2.2.

2.4.1 Carbon loss based on land use change

The land use change (LUC) from peat swamp forest to oil palms or other industrial plantations in tropical peatlands affects the carbon stocks of the above/below-ground biomass and carbon stored in the peat (Wicke et al., 2008). *Murdiyarso et al* (2010) used the "gain-loss" methodology on GHG emission from LUC proposed by the Intergovernmental Panel on Climate Change (IPCC) (2006) to estimate the total carbon loss from converting peat swamp forest into oil palm in tropical peatlands; the results showed that the CO_2 emission from drained peat was 19.2 Mg $ha^{-1}yr^{-1}$. *Koh et al.* (2011) used the above emission rate in the their study to quantify the carbon emissions in Southeast Asia.

The study of *Murdiyarso et al* (2010) balanced the estimation of total peat surface CO_2 emission measured using closed chamber techniques with the above- and below ground input of oil palm biomass, and losses of carbon via root respiration, combustion and fluvial carbon loss. As the measurements involved in the above estimation are beyond this study scope, for more details, please refer to *IPCC* (2006), *Murdiyarso et al* (2010), and *Koh et al* (2011).

2.4.2 Estimation based on water table depth

Since drainage is one of the main driving factors accelerating carbon loss from the tropical peatlands, the relationship between CO_2 emissions and water depth have been discussed in many studies (Melling et al., 2005; Ali et al., 2006; Hooijer et al., 2006; Jauhiainen et al., 2008; Hooijer et al., 2010; Hirano et al., 2012; Jauhiainen et al., 2012). A linear relationship between water table depth and CO_2 emissions is considered in most case studies. *Hooijer et al* (2006) provided a good review of the peat CO_2 emissions from drained peat in SE-Asia and proposed a linear relationship between average drainage depth (within 1 m) and CO_2 emissions to calculate the CO_2 emissions from drained peat in this area. It was suggested that the linear relationship is most suitable for the assessment of CO_2 emissions at water table depths between 30 and 100 cm in SE-Asia (Hooijer et al., 2010). This range is the most common groundwater depths of drained peatlands in SE- Asia. Using seven measured estimates of CO_2 emission as a function of water depth (Murayama and Bakar, 1996; Jauhiainen et al., 2004; Melling et al., 2005; Ali et al., 2006), and one long term (21 years) monitoring study of peat subsidence in drained peatland (Wösten et al., 1997; Wösten and Ritzema, 2001), the following regression relationship between CO_2 emission and water table depth was proposed (Hooijer et al., 2010):

$$CO_2\ emission = 91 * Groundwater\ depth \quad \textbf{(2.4)}$$

where CO_2 emission is expressed in t/ha/yr, and groundwater depth is the average depth of the water table below the peat surface in metres. This equation implies that each 10 cm water table decrease each year in peatland will result in an additional CO_2 emission of 9.1 t CO_2 /ha/yr.

By assessing the mean annual net ecosystem CO_2 exchange (NEE) for four years from July 2004 to July 2008 in a swamp forest of Central Kalimantan, Indonesia, *Hirano et al* (2012) also suggested a linear relationship between the NEE and groundwater level on an annual basis, with an annual CO_2 emission increase of 0.29-0.87 t CO_2/ha for every 10 cm of groundwater level lowering.

As the above linear relationship (Equation 2.1) was fitted in agricultural areas in peatland, including oil palm plantations, *Hooijer et al* (2010) provided a formula to measure the CO_2 emissions from all land uses according to the above regression relationship:

$$CO_2\ emission = LU_{Area} * D_{Area} * D_{depth} * CO_{2\text{-}1m}(t / yr) \quad \textbf{(2.5)}$$

where: LU_{Area} is the peatland area with specific land use in ha; D_{Area} is the drained area within peatland area with specific land use in fraction; D_{depth} is the average groundwater depth in drained peatland area with specific land use in meters; $CO_{2\text{-}1m}$ is the CO_2 emission at an average groundwater depth of 1 m, equals to 91 t CO_2 ha/yr.

Although *Hooijer et at* (2006) derived a linear relationship between the groundwater level and CO_2 emissions, they suggested that this linear relationship needs to be further developed, because the actual relation is known to be non-linear. In some studies of tropical peatlands, a non-linear relationship between peat CO_2 emission and depth of the water table is applied (Jauhiainen et al., 2008; Hirano et al., 2009).

2.4.3 Estimation based on peat subsidence

Combining the information of peat loss (subsidence height and subsidence area, bulk density and oxidation fraction), CO_2 emission estimation from loss of peat loss can be expressed as follows (Wösten et al., 1997; Ballhorn et al., 2009):

$$CO_2\ emission = 3.67 \times \Delta h \times S \times \rho \times C \times V_{oxi} \quad \textbf{(2.6)}$$

where Δh is the loss of peat height in meters; S is the drained area in ha; ρ is the peat bulk density in g/cm^{-3}; V_{oxi} is the oxidation part over the whole

subsidence volume in fraction;C is the carbon content in fraction;, 3.67 is the conversion factor from C to CO_2.

However, there is a large variation in CO_2 emission estimation due to a large uncertainty in bulk density and oxidation fraction in tropical peatlands (Wösten et al., 1997; Hooijer et al., 2012). Assuming a bulk density of 0.1 g/cm^3, 60% carbon content of the peat and 60% loss due to oxidation, a decrease in peat surface height of 1 cm/yr results in a carbon loss of 3.6 ton/ha/yr or CO_2 emisssion of 13.3 t/ha/yr. The CO_2 emissions will be 6.6 and 19.8 t/ha/yr if the bulk density is set at 0.05 or 0.15 g/cm^3.

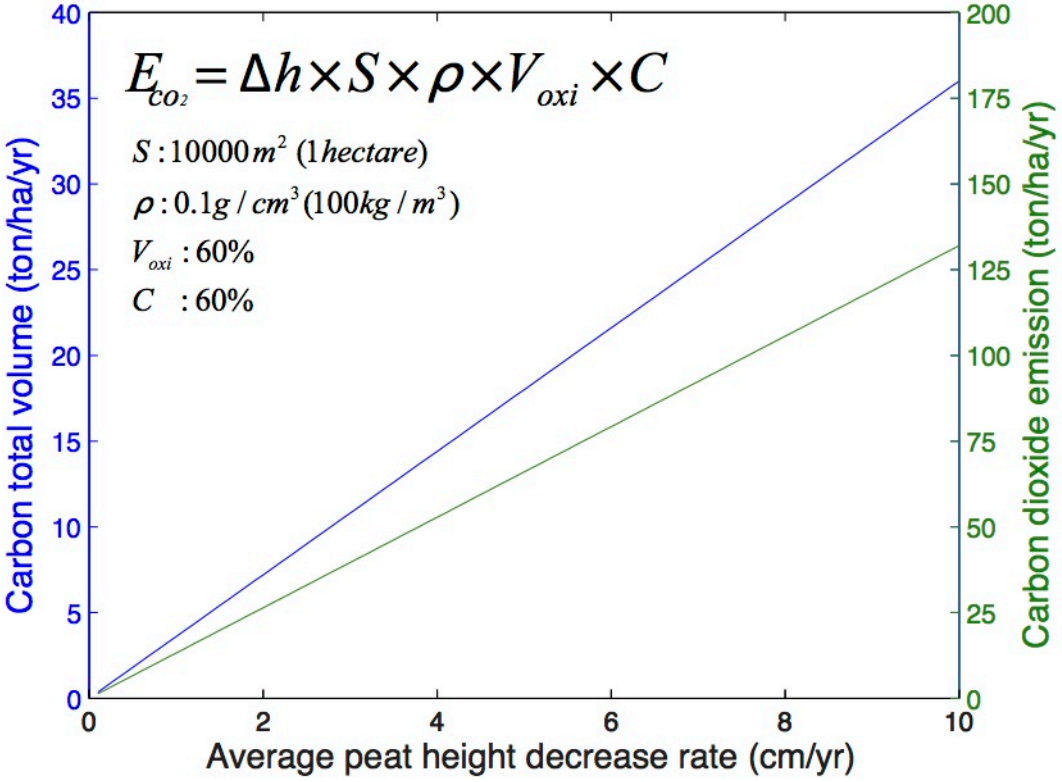

Figure 2.11 Carbon loss and CO_2 emission based on absolute peat height decrease rate.

Table 2.2 A summary of CO_2 emissions related to different estimation method.

Location	Character	Method	CO_2 emission t/ha/yr	Reference
Southasia tropical peatland	Drained peat	gain-loss	19.2	Murdiyarso et al., 2010
Southasia tropical peatland	Drained peat	gain-loss	19.2	Koh et al., 2011
Southasia tropical peatland	Drained peat (Oil palm plantation)	subsidence rate (4.5 cm/yr)	57	Edwards et al., 2010
Sarawak and Western Johore, Malaysia	Drained peat	subsidence rate (2 cm/yr)	26.5	Wösten et al., 1997
Southasia tropical peatland	Drained peat	subsidence rate (0.9 cm/yr)	9	Couwenberg et al., 2010
Riau, Sumatra, Indonesia	Drained peat (Acaica plantation)	subsidence rate (5 +/- 2.2 cm/yr for over 25 years)	90	Hooijer et al., 2012
Jambi, Sumatra, Indonesia	Drained peat (Oil palm plantation)	subsidence rate (5.4 +/- 1.1 cm/yr for over 25 years drainage)	109	Hooijer et al., 2012
Block C, Ex-MRP, Central Kalimantan, Indonesia	Drained peat	subsidence rate (0〜5.4 cm/yr, mean 2.4 cm/yr)	52.6	Dahdal, 2011
Block A, Ex-MRP, Central Kalimantan, Indonesia	Drained peat	subsidence rate (0〜3.5 cm/yr, mean 0.6 cm/yr)	18.09	Dahdal, 2011
Sarawak, Malaysia	Drained peat (Oil palm plantation)	Drainage depth (60 cm)	55	Melling et al., 2005
Sarawak, Malaysia	Drained peat (Sago)	Drainage depth (27 cm)	40	Melling et al., 2005
Jambi, Sumatra, Indonesia	Logged forest	Drainage depth (25 cm)	36	Ali et al., 2006
Jambi, Sumatra, Indonesia	Recently burned and cleared forest	Drainage depth (46 cm)	62	Ali et al., 2006
Jambi, Sumatra, Indonesia	Settled agriculture	Drainage depth (78 cm)	77	Ali et al., 2006
Central Kalimantan, Indonesia	Deforested, burned peatland	Drainage depth (21 cm)	26.08	Jauhiainen et al., 2008
Southasia tropical peatland	Drained peat	Drainage depth (10 cm)	9.1	Hooijer et al., 2010
Riau, Sumatra, Indonesia	Drained peat (Acacia plantation)	Drainage depth (80 cm)	94	Jauhiainen et al., 2012

2.5 Conclusions

In this section, the definition of a peatland and its importance in many ecosystem services are outlined, but most relevant to my research is that of C storage. The processes by which peatlands lose C (in the form of C-gases and as dissolved and particulate material) are outlined as well, and surveying methods (on-site and remoter) to assess this rate of peat loss are discussed. These include field surveys, use of aerial photographs, semi-automatically by optical satellite images and automatically by aerial LiDAR. Finally how researchers have investigated relationships between drainage or peatland and loss of peat (as assessed from change in surface height) and then how this is further developed to estimate how this stored C loss equates to CO_2 emitted to the atmosphere are summarized. Here is a fundatmental principal on how this understanding is adapted to my study cases (chapters 5 and 6). Firstly, peat height change is mapped by InSAR method, and then based on the results derived from InSAR, peat volume loss, C loss and CO_2 is estimated.

Chapter 3 Principles of SAR and Interferometric SAR (InSAR)

Abstract: Synthetic Aperture Radar (SAR) is a powerful remote sensing system, enabling observations of the Earth's surface day or night, in all weather conditions. Combining two SAR images with an interferometric technique is able to reveal subtle movements on the Earth's surface, which is known as Inteferometric SAR (InSAR). In this chapter, principles of Synthetic Aperture Radar (SAR) and Interferometric SAR are briefly introduced, and then InSAR processing and its error sources are discussed, specifically InSAR decorrelation and atmospheric effects. The final section focuses on advanced InSAR time series analysis.

3.1 Synthetic Aperture Radar

Synthetic Aperture Radar (SAR) is a microwave imaging system. It has cloud-penetrating capabilities as it uses microwaves, and because it is an active system, it has day and night operational capabilities. It is actively illuminating the ground with electromagnetic pulses with a microwave frequency (0.3–300 GHz, 1000-1 mm) emitting from a side looking radar antenna; a side-looking configuration is necessary in order to avoid the ambiguity of return from either side of the satellite track (Curlander and McDonough, 1991). Table 3.1 shows the typical microwave bands for satellite SAR systems (Attema, 1991; Hanssen, 2001; Buckreuss et al., 2003; Werninghaus, 2004; Rosenqvist et al., 2007; F.Covello et al., 2010):

Table 3.1 Typical SAR frequencies, Satellites and associated applications.

Band	Frequency (Wavelength)	SAR satellites	Availablity	Resolution (m)	Incidence angle (degrees)	Swath Width (km)	Repeat Cycle (days)	Applications
X	10 GHz (~ 3 cm)	TerraSAR-X	2007-	1~16	20~55	10~150	11	Earthquakes: (Stramondo et al., 2011) Ice sheet/Glacial motion: (Jaber et al., 2012) Landslides: (Bovenga et al., 2012) DEM generation: (Brautigam et al., 2012)
		TanDEM-X	2009-	1~16	20~55	>30	11	
		COSMO-SkyMed	2007-	1~100	25~50	10~200	16	
C	5.3 GHz (~ 6 cm)	ERS-1	1991-2000	20	21~26	100	3/35/176	Earthquakes: (Massonnet et al., 1993) (Fialko et al., 2005) Volcanoes: (Massonnet et al., 1995; Lu et al., 1997) Ice sheet/Glacial motion: (Goldstein et al., 1993; Madsen et al., 1999; Carolina et al., 2007) Fault/Tectonic: (Wright et al., 2004a; Elliott et al., 2010) DEM generation: (Farr et al., 2007)
		ERS-2	1995-2008	20	21~26	100	3/35	
		Envisat ASAR	2002-2010	20~150	20~50	> 100	35	
		RadarSat-1	1995-2013	8~100	20~49	45~500	24	
		RadarSat-2	2007-	3~100	20~50	20~500	24	
		Sentinel-1	to be launched in 2013	5~40	20~47	20~410	12	
L	1.2 GHz (~ 24 cm)	JERS-1	1992-1998	18	35	75	44	Earthquakes: (Shen et al., 2009; Simons et al., 2011) Ice sheet/Glacial motion: (Rignot, 2008; Meyer et al., 2011)
		ALOS-1/PALSAR	2006-2011	10~100	8~60	30~350	46	
		ALOS-2/PALSAR	to be launched in 2013	3~100	8~70	25~490	14	

The geometry of a side-looking SAR imaging system from a satellite is sketched in Figure 3.1. An antenna is mounted on a satellite that travels along the trajectory with a velocity of v, which is called the azimuth direction, and it is pointed to the Earth's surface, and perpendicular to the orbit with an inclined angle (look angle), the cross-track direction is also called the ground direction. It illuminates the shaded path (known as footprint) on the ground as the satellite moves in the direction of flight path. The direction along the Line of Sight (LOS) is usually called the slant-range direction.

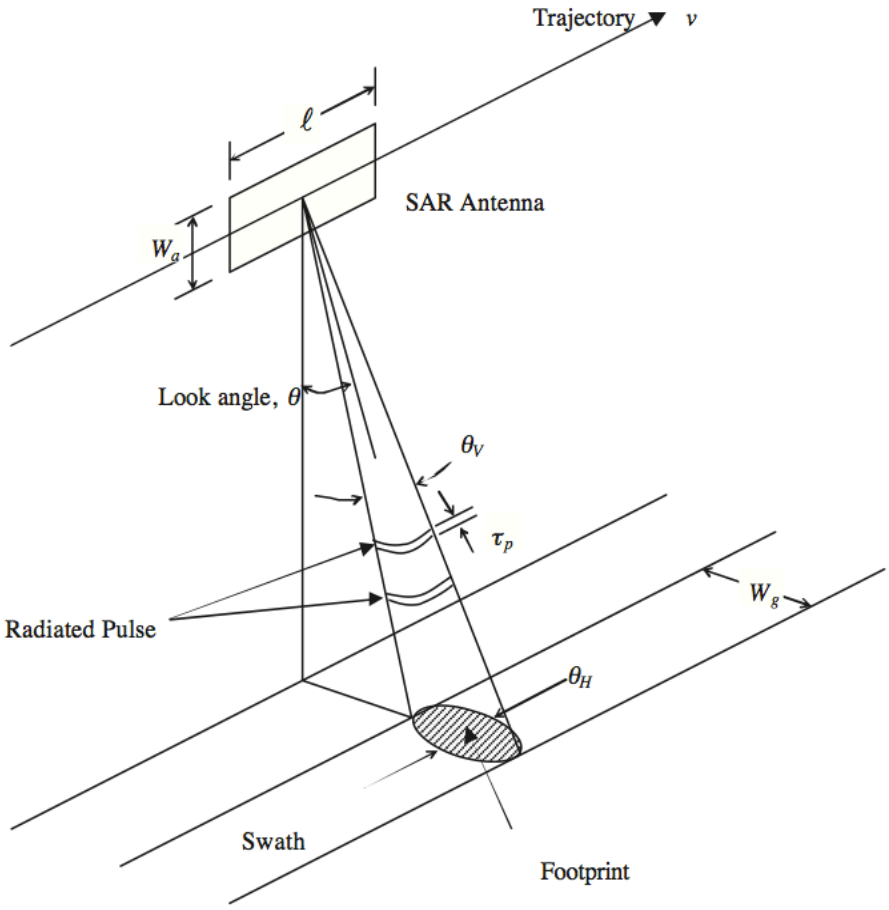

Figure 3.1 Imaging radar geometry, reproduced from (Curlander and McDonough, 1991). Generally, v - satellite velocity, l antenna length, W_a - antenna width, λ - wavelength, θ_v - beam width, τ_p - radar pulse duratio, θ_H - azimuth beam width, W_g - swath width.

In the case of ERS, the satellite speed is about 7100 m/s at an elevation of about 785 km, the look angle contributes an incidence angle with the ground of approximately 23° at the scene center (Hanssen, 2001), the antenna can illuminate an area about 5 km on the ground in the azimuth direction, and about 100 km in the range direction; in the mode of strip map, the footprint records a swath 100 km wide in the ground range direction on the Earth's surface, and captures a strip image of 445 km long every minute (Ferretti et al., 2007).

3.1.1 Range and azimuth resolution

There are many papers reviewing the fundamentals of SAR imaging mechanism, and here I present the general concept of the mechanism drawing on the detail available in the literature (Smith et al., 1996; Bamler and Hartl, 1998; Balzter, 2001). When the SAR sensor emits pulses of electromagnetic radiations, the energy hits an object (a scatterer), the electromagnetic energy is dispersed and a fraction of energy is reflected back to the sensor. The quantity of radiation received by the sensor is referred to as radar backscatter, and a resolution cell of a SAR image is the total spatial volume of radar echoes of all individual elements (scatterers) received by the sensor for that area of surface. The resolution cell size is determined by the resolution in range and azimuth. A pixel, however, is an infinitesimally small point in which the complex digitized signal value corresponding with a resolution cell is centered. Pixel size indicates the spatial distance between two pixel-nodes, or pixel spacing.

The geometric and dielectric properties of the surface or volumes imaged determine the magnitude of backscatter. Backscatter is sensitive to surface geometry, roughness, plant geometry, and water content of surface ingredients, such as soil moisture, snow wetness (Ribbes et al., 1997). The ground geometry affects the return energy and the typical scattering mechanisms are shown in Figure 3.2. Backscatters contribute brighter areas in a radar image, i.e. a larger portion of radar energy is reflected back to the radar. Brighter areas are observed with urban streets or buildings than vegetated areas, because the emitted radar pulses are able to bounce off the streets and then rebound again

off the buildings (also called a double-bounce), and directly back towards the radar (Figure 3.2c and d). The backscattered intensity in vegetated areas is still higher than that in bare soil, because of the multiple scattering in the vegetation layer (Figure 3.2b and e). Backscatter contributes darker areas in a radar image due to less radar energy received by the sensor e.g., a calm water body is dark in a SAR image because of the smooth water surface acting as a flat surface, which reflect the incoming radar energy away from a target (Figure 3.2a) (ESA, 2011b).

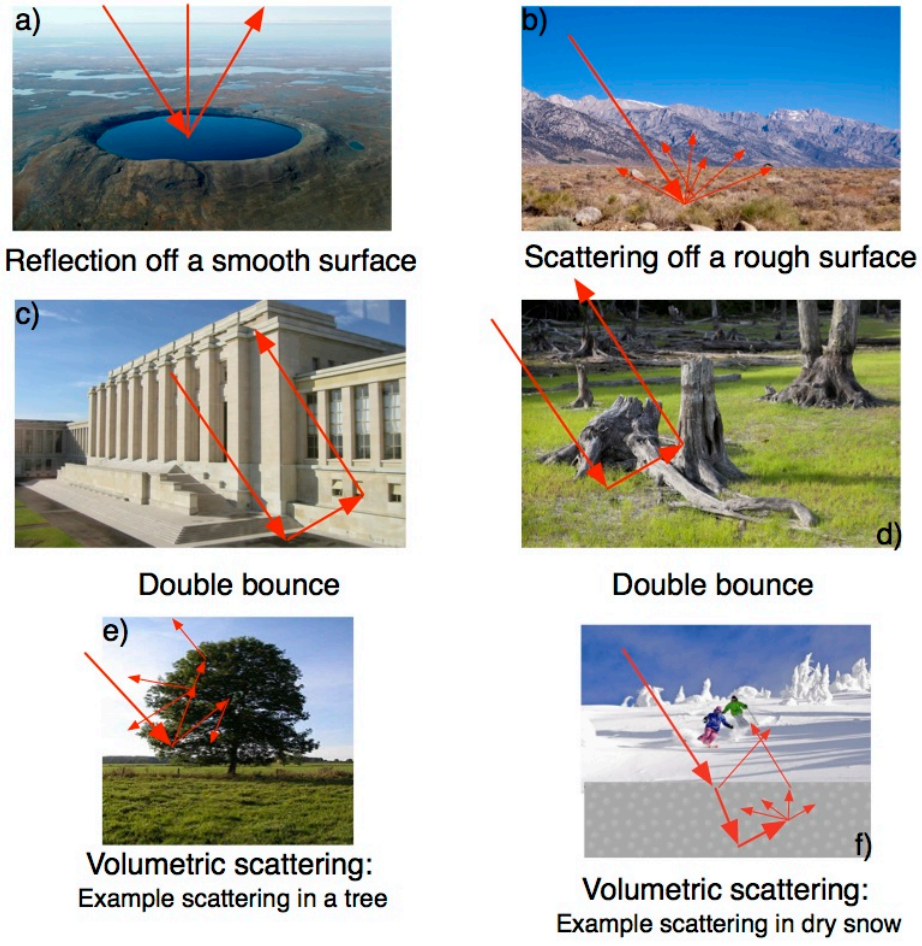

Figure 3.2 SAR scattering mechanisms, reproduced from (ESA, 2011b). (a) reflection scattering from a smooth surface; (b) scattering off a rough surface; (c) and (d): double bounce scattering; (e) and (f): volumetric scattering in a tree and in dry snow. Note: In the case of volumetric scattering in dry snow, the incident radiation is both reflected and refracted/transmitted through a layer of dry snow. The refracted radiation then reflects off underlying ice, scatters off a chunk of ice in the snow, and finally refracts back to the receiver.

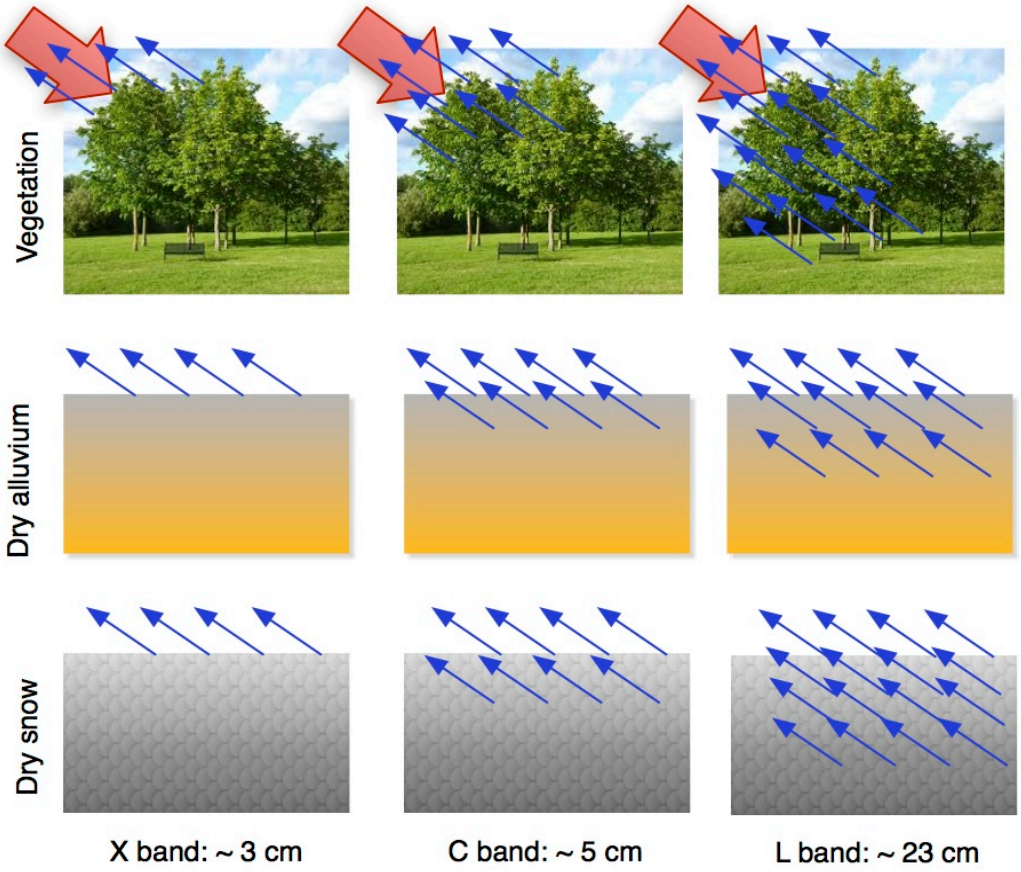

Figure 3.3 SAR penetration depths versus radar wavelengths, reproduced from (ESA, 2011a). The longer the wavelength, the deeper the penetration.

The degree of backscatter is also affected by SAR wavelength as this determines the penetration depth (Figure 3.3), which in turn affects the relative roughness of the surface imaged. Longer wavelengths penetrate deeper than shorter wavelengths. In general, short wavelengths of 2 to 6 cm, such as X and C bands, are suitable for sensing crop canopies and tree leaves, because they are not able to penetrate canopies, and radar signals return from the tree leaves or crop canopies. In contrast, long wavelengths of approximately 10 to 30 cm, such as S and L bands, are suitable for sensing tree trunks or limbs (Bamler and Hartl, 1998) as they can penetrate canopies and radar signals are reflected from the tree trunks and limbs.

By analyzing radar responses at P-, L- and C- band to biomass of mono-species conifer plantations at Les Landes, France, and Duke forest, North Carolina, *Dobson et al.* (1992) found there was an approximately linear response of backscatter to increasing biomass, and the saturation levels reach around 200 t/ha for P-band and 100 t/ha for L-band. Another study showed that the saturation was 100 t/ha for P band, and 40 t/ha for L-band and 20 t/ha for C-band in coniferous in North Carolina and France, and tropical broadleaf evergreen forests in Hawaii (Imhoff, 1993). For tropical forests of Amazon state In Brazil, a saturation of 60 t/ha for L-band was found (Luckman et al., 1998). Above the biomass level radar signals cannot penetrate forests well.

In addition, the penetration depth of soil is influenced by moisture, density and geometry structure of the plants (Figure 3.4) (Nolan and Fatland, 2003; ESA, 2011a). Nolan and Fatland (2003) developed a model for this relationship between penetration depths for X-, C-, and L-band and moisture (Figure 3.4). The model includes transmission loss and attenuation loss, while the transmission loss is presumed to be more realistic than attenuation loss alone. Therefore, for volumetric water content above 35%, the radar wave does not penetrate into the ground at X-, C- and L-band, and all these three bands penetrate greater than 1 cm when the soil moisture content is 11% or less.

Tropical forests are prone to flooding in wet seasons, and in areas with ground biomass less than 100 t/ha, once it is flooded, the radar wave penetrates canopies, but smooth open water surfaces results in no returned radar signal, and vegetated areas cause double bounced radar signals. This phenomena can be applied to detect the hydrological dynamics in tropical peat swamp (Tralli et al., 2005; Hoekman, 2009).

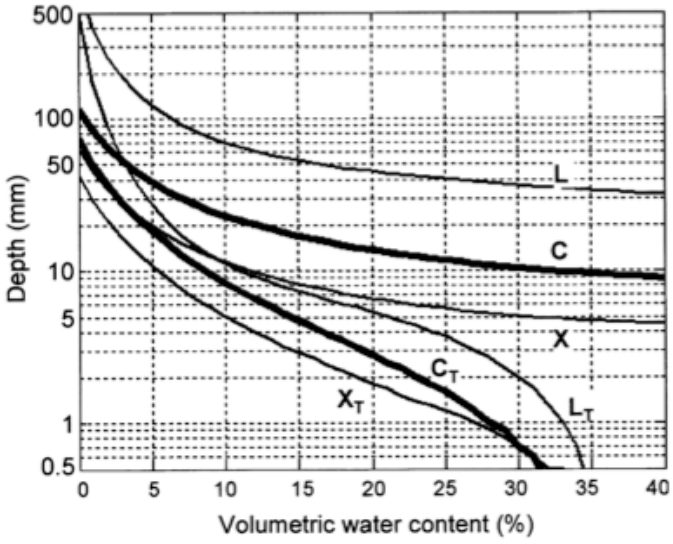

Figure 3.4 Penetration depth of SAR microwaves as a function of soil moisture for L-,C- and X-bands, taken from (Nolan and Fatland, 2003). Subscript T indicates penetration depths when transmission losses at 0.1-mm increments have been assumed; the other curves indicate attenuation losses only. Soil moisture is assumed uniform with depth.

Ground range resolution is defined as the minimum distance between two targets on the ground that can be distinguished, as shown in Figure 3.5. Points near the antennae are called near range, and points far away the antennae are called far range. The range resolution of a real aperture radar is given as:

$$\rho_g = \frac{c\tau_\rho}{2\sin\theta} \tag{3.1}$$

where τ_ρ is the pulse length and c is the speed of light. Obviously, the range resolution is a function of pulse width and look angle but independent of height. In the case of ERS, the pulse length τ_ρ is 37.12 μs, which contributed to a ground resolution of approximate 14 km (Attema, 1991). To achieve the desired 10s of meter scale resolution, a very short pulse length is required. For example, for a resolution of 5 m, an order of 10^{-8} pulse length is required. In order to obtain desired signal-to-noise ratio in the return signal, the power requirement for satellite SAR systems would appear to be excessively high. Therefore, a specific signal processing called range compression is used to produce the desired resolution, through using a frequency modulated (chirped) pulse with a

frequency bandwidth of B_r. Range compression is applied to the received raw SAR signals, and produces a shorter effective pulse length τ_e equal to $1/B_r$. Therefore the ground resolution is given by:

$$\Delta R_g = \frac{c\tau_e}{2\sin\theta} = \frac{c}{2B_r \sin\theta} \tag{3.2}$$

In the case of ERS satellites, a bandwidth of 15.5 MHz provides a ~ 20m ground range resolution (Elliott, 2009).

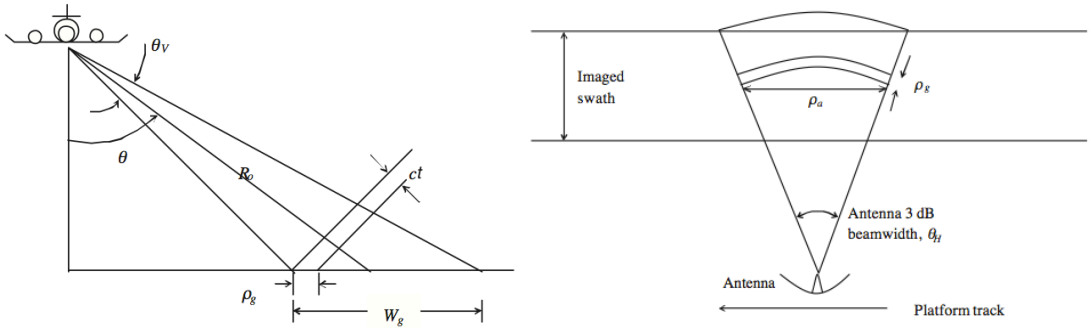

Figure 3.5 Ground range resolution (left) and azimuth resolution (right), taken from (Chan and Koo, 2008)

Azimuth resolution is the minimum distance on the ground in the direction parallel to the flight path of the aircraft or satellite at which two targets can be separately imaged. Two targets located at the same slant range can be resolved only if they are not within the same beam width, as shown in Figure 3.5, the antenna length determines this azimuth resolution from the intersection of the azimuth beam width, thus azimuth resolution ρ_α can be written as,

$$\rho_\alpha = R\theta_H = \frac{R\lambda}{l} \tag{3.3}$$

where R is the slant range. In the case of ERS, a typical value of $R = 850km$, a 10 m antenna provides about 4.8 km azimuth resolution. In order to produce an azimuth resolution of 20 m, a longer antenna (~ 2.4 km) need to be employed (Hanssen, 2001). By moving a real antenna with a limited length along a

reference path, which is illuminating the target on the ground with pulse repetition frequency (PRF) at the same time, a much longer synthetic aperture than the real aperture can be simulated, referred to as the Synthetic Aperture Radar (SAR). Many echoes received successively at the different antenna positions are coherently detected and stored and then post-processed together to resolved elements in an image of the target region, thus the azimuth resolution is defined as:

$$\rho_{\alpha} = l/2 \tag{3.4}$$

The azimuth resolution is equal to one half of the actual antenna length l, independent of range, wavelength and pointing, implying that a smaller antenna is able to obtain a better resolution. For ERS, the azimuth resolution is improved by three orders of magnitude from 4.8 km to 5 m by using a synthetic aperture radar (Hanssen, 2001).

3.1.2 Single Look Complex (SLC) image

A digital SAR image consists of a two-dimensional array (formed by columns and rows) of small picture elements (pixels), Figure 3.6. Each pixel is associated with a small area of the Earth's surface, which is called resolution cell. Each pixel gives a complex number that carries amplitude and phase information about the microwave field backscattered by all the scatterers (buildings, rives, rocks and etc.) within the corresponding resolution cell on the ground. Different SAR systems produce different locations and dimensions of the resolution cell in the azimuth and slant range coordinates, because the range pixel dimension depends on the sampling frequency and the azimuth pixel dimension is determined by v/PRF. Generally, the resolutions in both range and azimuth direction are different. To produce pixels with similar sizes in both directions, a procedure called multi-looking is often performed, which is to average a small number of pixels together. In the case of ERS, the range pixel is about 20 m when projected onto the flat ground, while the azimuth resolution is 4.6 m (Hanssen, 2001). Typically, 5 pixels in the azimuth direction are averaged together to produce a pixel with $20m \times 20m$ in both directions.

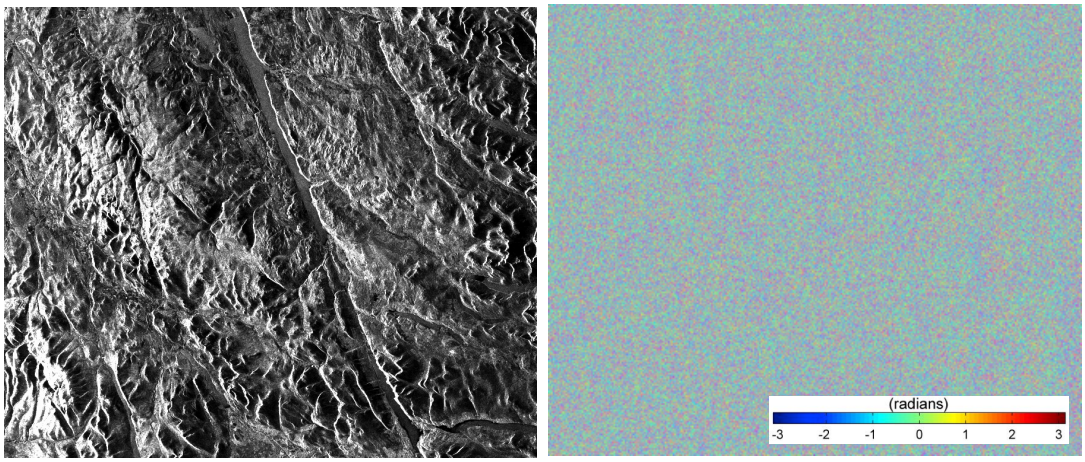

Figure 3.6 EnviSat SAR image over the Monadhliath Mountains, Scotland. Left: amplitude image; Right: phase image. It is multi-looked in 4 x 20 in range and azimuth direction, the pixel size is about 80 m x 80 m.

SAR amplitude image is a measurement of the radiation back scattered return to the radar by all the scatterers in the resolution cell on the ground. Radar amplitude depends more on surface roughness than on the chemical composition of the terrain. Typically, bare rocks and urban areas show strong amplitudes, whereas smooth flat surfaces (water body) show low amplitudes, since the radiation is mainly mirrored away from the radar.

The phase is a measurement of the distance between the scatterers and the SAR sensor. The phase of each pixel in a SAR image is related to all the scatterers within the resolution cell on the ground, refractivity of the atmosphere, and additional scatterering phase shifts caused by electromagnetic scatterering of the incident radiation off the targets in that cell. Typically, the phase is given as (Hanssen, 2001):

$$\phi = -2\pi \times \frac{2R}{\lambda} + \phi_{scat} \tag{3.5}$$

where ϕ_{scat} is additional scatterering phase contribution. The scatterering phase shift results in a random phase shift within any one pixel, thus the phase shifts are typically uncorrelated even in adjacent pixels. Equation (3.5) indicates that for SAR phase measurements every 2π phase change corresponds to a range change of $\lambda/2$. In addition, there is a modulo 2π ambiguity in the phase measurement as the total path length is unknown. The phase information is meaningful only it comes to the differencing of the phase measurements in

the process of interferometry. The full complex (amplitude and phase) data is used to perform a complex cross correlation during the coregristration processing of Interferometry SAR.

3.2 SAR interferometry

Interferometry SAR (InSAR) exploits the phase information contained in at least two SAR single look complex (SLC) images of the same area, acquired at different times (repeat-pass) with the same wavelength, but slightly different viewing geometries because satellite orbits do not repeat exactly. The following sections and the InSAR time series analysis used in the later chapters are related to repeat-pass InSAR.

3.2.1 Principle of InSAR

InSAR extracts the phase differences between two SAR images. The phase of two images can be compared after sub-pixel level registration (Massonnet and Feigl, 1998). The difference of phase between the two well-aligned SAR images produces a new kind of image, which is called an interferogram. The interferogram contains the deformation signals and other disturbance signals (Bamler and Hartl, 1998; Massonnet and Feigl, 1998). The deformation of the surface, by an earthquake for example, can be detected if the two SAR images are acquired over the same area during a certain time interval. In order to derive surface displacement, topographic contributions in the interferogram should be removed using a digital elevation model (DEM), as the radar observes the topography from two slightly different points of view (Massonnet and Feigl, 1998). A typical InSAR imaging geometry is illustrated in Figure 3.7.

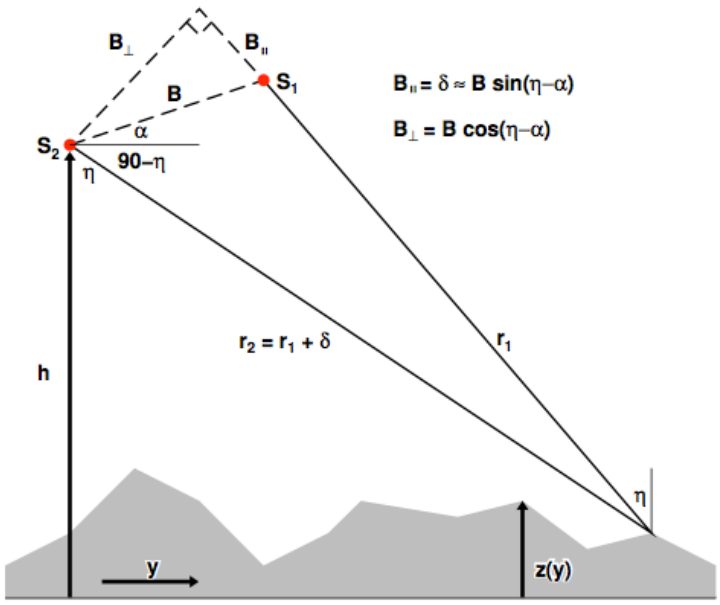

Figure 3.7 Imaging geometry of repeat-pass InSAR, taken from (Elliott, 2009). Two radar sensors $S_{1,2}$ illuminate the same target on the ground on both passes 1 and 2. They are separated by a baseline distance B; $B_{\parallel}$ denotes its parallel component and $B_{\perp}$ denotes its perpendicular component. The distance between the sensor and the target are r_1 and r_2, where r_2 is equal to r_1 plus the difference δ between the two observations. Radar look angle η satellite height h and ground range direction are indicated.

The interferomeric phase is a two-dimensional array arranged in a range y and azimuth x coordinate system and is equal to the path length differences between a resolution cell on the ground and the two SAR antennas (Hanssen, 2001):

$$\phi_{InSAR} = \frac{4\pi\delta}{\lambda} \tag{3.6}$$

where $\delta = r_2 - r_1$ denotes the path length differences as shown in Figure 3.7, geometrically. δ can be approximated as:

$$\delta = B\sin(\eta - \alpha) \tag{3.7}$$

Actually, several components contribute to the interferometric phase ϕ_{InSAR} in addition to deformation signals:

$$\phi_{InSAR} = \phi_{defo} + \phi_{topo} + \phi_{flat} + \phi_{orbit} + \phi_{APS} + \phi_{noise} \tag{3.8}$$

where ϕ_{defo} is the phase due to line-of-sight (LOS) range changes caused by coherent motion of scatteres between the two SAR acquisitions, ϕ_{topo} is the phase due to the height of resolution cell above a reference surface that is typically the reference ellipsoid, ϕ_{flat} is the phase due to the curvature of the Earth, ϕ_{orbit} is the phase due to inaccuracies in the knowledge of satellite orbits, ϕ_{APS} is the phase due to the signal delays caused by the heterogeneous refractivity distribution in the atmosphere, usually called atmospheric phase screen (APS), and ϕ_{noise} is the phase noise resulting from thermal noise internal to the radar system and loss of coherence between the individual SAR observations forming the interferogram.

To extract precise deformation from the interferometic phase, all the other components should be removed carefully. Topographic phase is a result of the variation of topography for a given perpendicular baseline, which can be used to generate DEMs (Zebker and Goldstein, 1986). Topographic phase is given by (Zebker et al., 1994a):

$$\phi_{topo} = \frac{-4\pi B_{\perp} z}{\lambda r_1 \sin\theta} \tag{3.9}$$

where r_1 is the slant range, θ is the viewing or look angle of the satellite, $B_{\perp}$ is the perpendicular baseline, z is the height of a particular resolution cell above the reference ellipsoid.

The topographic phase component is often removed using a Digital Elevation Model (DEM), such as the DEM produced by the Shuttle Radar Topography Mission (SRTM) (Farr et al., 2007). SRTM produced a near-global topography product for latitudes smaller than 60°, with the SRTM data sampled over a grid of 3 arc-second by 3 arc-second (approximately 90 m by 90 m) globally, with a relative height error of less than 10 m (Rodriguez et al., 2005; Farr et al., 2007). As shown in Equation (3.9), the sensitivity of interferometric phase with respect to height errors increases proportionally to the perpendicular from height errors. Interferograms generated by shorter baselines can reduce the impact of height error. In the case of Envisat with a 500 m spatial baseline, a

DEM with 10 m error can introduce about 1.5 cm error. This error can be removed in the post-processing, such as in time series analysis (Section 3.3.2).

The phase ϕ_{flat} can be calculated by the satellite orbits and the geodetic datum (e.g. World Geodetic System 1984 (WGS84)). SAR images are created with an assumption of a flat Earth, therefore, it is necessary to estimate the phase difference between the flat and actual Earth surfaces, and so phase ϕ_{flat} is given by (DEOS, 2008):

$$\phi_{flat} = \frac{-4\pi}{\lambda} B_{\perp} \Delta\eta \tag{3.10}$$

where $\Delta\eta$ is the difference of the viewing or look angles at two observation times.

Satellite orbits are disturbed by a number of phenomena and nonconservation forces, such as atmospheric drag and solar radiation pressure (Hanssen, 2001). For example, in the condition of orbital manouevres, the ERS satellites were operated to σ_{α} 1 km of the nominal ground track (Biggs et al., 2007). As a result, two radar images involved in interferogram generation are often acquired from different locations. This baseline separation is used to remove the topography phase during displacement mapping, while inaccurate knowledge of the spatial baseline will result in poor determination of the interferometric phase from the reference ellipsoid and topography, leaving residual fringes in the interferogram. The residual phase caused by the orbit error can be removed by fitting a linear or quadratic polynomial plane across the whole interferogram (Hanssen, 2001). For short strips of data (100~200 km along track), a linear plane is sufficiently accurate, but for longer strips of data, a quadratic polynomial plane is required, and the ratio between the coefficient of the quadratic term and the linear term is approximately 10^{-6}, which means the signal is only weakly curved (Hanssen, 2001). A typical linear, best-fitting plane is as follows:

$$z = ux + vy + w \tag{3.11}$$

where z is the orbit best-fitting plane, x,y is the pixel coordinate, u,v are the gradient parameters, and w is a phase offset.

Interferometric phase caused by the heterogeneous refractivity distribution in the atmosphere has been observed in radar interferograms (Goldstein, 1995; Massonnet and Feigl, 1995; Zebker et al., 1997), especially due to the spatiotemporal variations of tropospheric water vapour (Hanssen, 2001; Li et al., 2005). More details are discussed in section 3.2.5 Atmospheric phase screen.

After removing the phase contributions from the topography ϕ_{topo}, curvature of the Earth ϕ_{flat}, orbit ϕ_{orbit}, and APS ϕ_{APS}, the remaining signal is mainly the range change due to surface deformation, and this can be written as following by giving range change ΔR (Elliott, 2009):

$$\phi_{defo} = \frac{4\pi\Delta R}{\lambda} = -(\frac{4\pi}{\lambda})\hat{n} \bullet u \qquad \textbf{(3.12)}$$

where u represents the three-dimensional (3D) ground displacement projected into the line-of-sight (LOS) direction between the ground and the radar sensor, $\hat{n}$ is the unit vector. Equation (3.12) indicates that a ground displacement of half-wavelength in the LOS produces a single interference fringe. InSAR measures only relative range changes, rather than absolute range changes, interferograms are hence maps of relative deformation, not absolute values. As a result with long-wavelengths such as L-band, small gradient signals are not easy to detect, and become convolved with orbital ramp errors (Elliott, 2009). For example, it requires nearly 23 years to produce a fringe for a low gradient signal of 5 mm/yr for L-band at a wavelength of 23 cm.

Additionally, LOS change can be projected to North, East and Up, three components of ground deformation (Fialko et al., 2001):

$$\left[U_n \sin\varphi - U_e \cos\varphi\right]\sin\eta + U_u \cos\eta + \delta_{los} = \phi_{defo} \qquad \textbf{(3.13)}$$

where φ is the azimuth of the satellite, heading vector (positive clockwise from the North), δ_{los} is measurement error,$\mathrm{U_n}, \mathrm{U_e}, \mathrm{U_u}$ represent the North, East and Up components of ground deformation. Therefore there is an ambiguity

regarding the contributions of the three components. A practical way to mitigate the ambiguity is to combine both ascending and descending acquisitions, which produces different LOS directions (Fujiwara et al., 2000; Wright et al., 2004c), as well as azimuth offsets which provides a fraction of the pixel along-track displacement from amplitude matching of two SAR images (Fialko et al., 2001). One alternative way is to employ GPS 3D components to constrain the 3D deformation in joint inversions (Delouis et al., 2002; Simons et al., 2002). Another possibility is to assume there is only one component of motion, such as assuming only the vertical components of land subsidence is significant when detecting land subsidence Antelope Valley, Mojave Desert, California, US (Galloway et al., 1998) and a single horizontal component is assumed to study the long strike-slip faults in Tibetan plateau, China (Elliott, 2009; Liu et al., 2013).

In this thesis, peat subsidence is assumed to happen in the vertical direction only, and no horizontal component or movement is considered. In the case of Envisat, the incidence angle of SAR image acquired in an image mode ranges from 19.2° to 26.2° between near and far ranges. A velocity of 1 cm/yr in LOS corresponds to 1.06 cm/yr and 1.11 cm/yr in vertical ground deformation. For the case studies used here, an incidence angle of 23° is used, which means 1.09 cm/yr in vertical ground deformation. For ALOS SAR images acquired in Fine Beam Single (FBS) polarization mode, used in the case studies here, the incidence angle ranges approximately from 32° to 35° between near and far ranges. A velocity of 1 cm/yr in LOS corresponds to 1.17 cm/yr and 1.22 cm/yr in vertical ground deformation. In these case studies, an incidence angle of 34° is applied, which means 1.20 cm/yr in vertical ground deformation. In summary, the velocity between near and far range introduces ~3% uncertainty in real ground deformation if only the vertical component is considered. Therefore, a typical incidence angle of 23° for Envisat and 34° for ALOS is applied in the case studies here.

3.2.2 Differential InSAR processing and error sources

Massonnet and Feigl (1998) and *Hanssen* (2001) provided good reviews on InSAR processing. Here the general InSAR procedures of JPL/Caltech Repeat Orbit Interferometry PACkage (ROI_PAC, V3.1 Beta) (Rosen et al., 2004) are presented, because in this thesis all the interferograms are produced using ROI_PAC. It is a free package and more information and the manual can be found on the website of ROI_PAC Wiki (ROI_PAC, 2013). The general processing flow is shown in Figure 3.8.

Interferogram generation involves two SAR images (master and slave image), and requires a high resolution DEM (SRTM DEM (Farr et al., 2007)) and precise orbit information of both images. Firstly, two SAR images must be coregistered, and the slave image has to be resampled to the geometry of the master image, a pre-requirement for differencing the phase components. Usually the process involves a coarse coregistration and a fine coregistration. An initial offset is calculated from the orbit information and then the images are matched based on the amplitude information. The coarse coregistration is achieved by cross-correlation of a moving window between the master and slave images, and this procedure is performed in both azimuth and range directions. After the calculated transformation (translation, rotation, scaling) provides a good enough fit, the correlation procedure is repeated to produce a finer sub-pixel match, and achieve a final affine transformation. Then the slave image is re-sampled into the geometry of the master image.

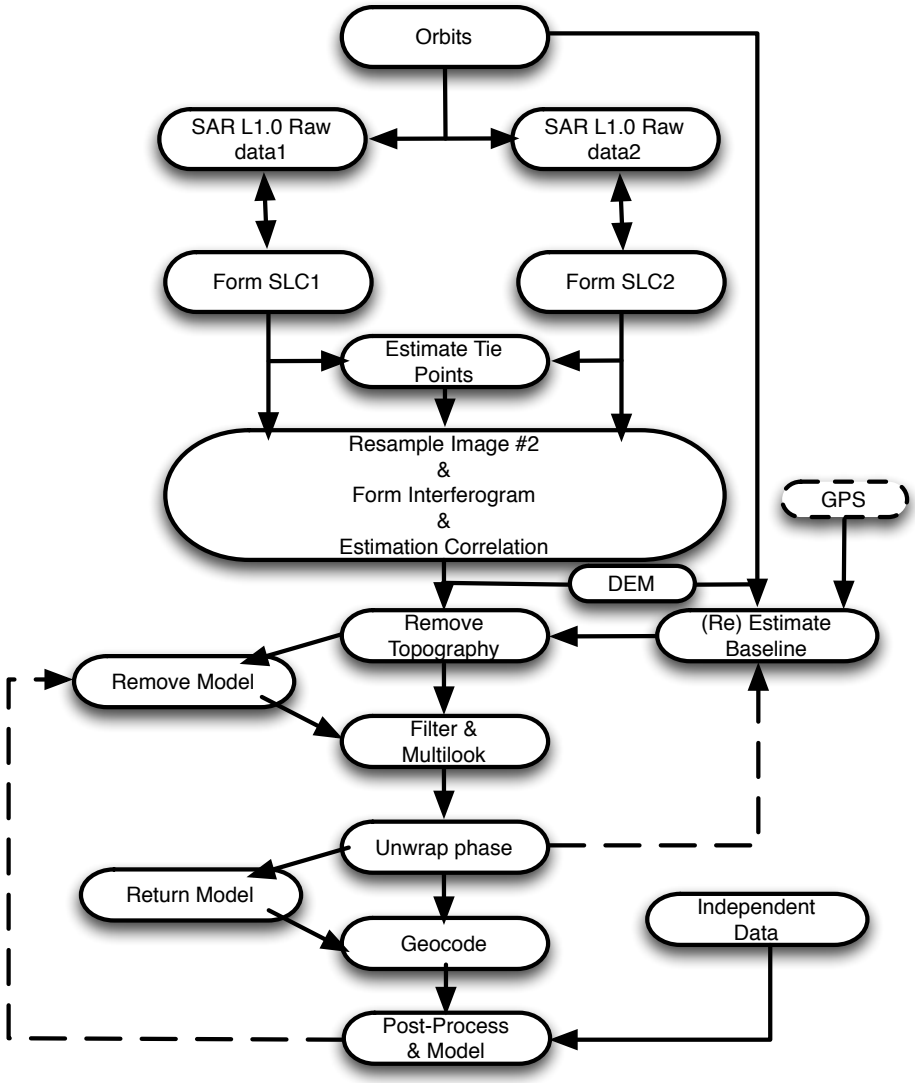

Figure 3.8 Flow chart of two-pass differential InSAR for ROI-PAC.

To generate an interferogram, the master SLC image (M) is multiplied by the complex conjugate of the slave (S^*), so the interferogram phase is the phase of the complex interferogram (MS^*); the asterisk denotes complex conjugation. Correlation is estimated following the step of interferogram formation, which will be described in Section 3.2.3 InSAR decorrelation . An external DEM is used to remove the topography contribution in the interferogram. Filtering and multi-looking of the complex interferograms provides an improvement of signal-to-noise. Since the interferogram phase is wrapped between $-\pi$ to $+\pi$, phase unwrapping is implemented to obtain continuous phase values. This is further

discussed in Section 3.2.4 Phase unwrapping. The geocoding procedure projects the unwrapped phase values from the radar coordinates system into the DEM-based coordinate system (such as WGS 84), and converts the unwrapped phase value to deformation distances. In most cases, the geocoding accuracy is in a sub-pixel level (Lauknes and Malnes, 2004).

Post-processing removes errors from the interferogram and extracts deformation signals. The main error sources of InSAR measurement can be classified as: 1) topographic error; 2) orbital ramp; 3) phase unwrapping; 4) APS. Besides the above error sources, the decorrelation of InSAR also is a limitation of InSAR. This will be further discussed in Section 3.2.3 InSAR decorrelation. Phase unwrapping will be considered in Section 3.2.4 Phase unwrapping, and APS and its correction will be further detailed in Sections 3.2.5 Atmospheric phase screen and 3.2.6 Atmospheric corrections.

In order to reduce decorrelation and topographic errors, mulitiple InSAR time series techniques have been developed, such as Persistent Scatterers Interferometry (PS InSAR) (Ferretti et al., 2001), and Small BAseline Subset (SBAS) (Berardino et al., 2002), which will be further considered in Section 3.3 Time series analysis methods.

3.2.3 InSAR decorrelation

The fundamental of InSAR measurements explore the phase difference generated by two SAR images that are acquired at two different times. Correlation or coherence is a measurement of degree of the similarity of the phase of two SAR images. Theoretically, correlation ranges between 0 and 1, where 0 means no correlation, and 1 corresponds to perfect correlation. High correlation ($>$0.2) is ideal for retrieving reliable phase information. While the correlation is lower than 0.1, phase information is hardly can be retrieved. The loss of correlation is known as decorrelation, which exists between two SAR images sampled at two different times.

There are several sources obstructing phase stability. Temporal and spatial decorrelations are the two main factors causing decorrelation (Zebker and

Villasenor, 1992; Smith et al., 1996; Hanssen, 2001). The changes in the strength and distribution of scattering with time are called temporal decorrelation, which is caused by the changes of wind, rain, snow, vegetation growth and death, and moisture of the ground, and the longer the temporal interval, the likelihood of less coherence. When the viewing angle of SAR sensor changes with each orbit, spatial decorrelation occurs. The distance between two orbits is called the spatial baseline. Spatial decorrelation is also a result of volume scattering and uncompensated topography: the longer the spatial baseline, and the likelihood of less coherence (Zebker and Villasenor, 1992; Smith et al., 1996). Other decorrelation sources include doppler centroid, thermal noise. For more details please refer (Zebker and Villasenor, 1992; Bamler and Just, 1993; Hanssen, 2001).

For repeat-pass InSAR, two radar signals S_1 and S_2 are acquired with the same antenna observing the same target at different time. Assuming the signal is composed by correlated part c, uncorrelated noise part n, which includes the thermal, baseline, temporal and other negligible noise (Smith et al., 1996), the two signals can be written as:

$$\begin{cases} S_1 = c + n_1 \\ S_2 = c + n_2 \end{cases} \tag{3.14}$$

The correlation between them can be measured by:

$$\gamma = \frac{\langle S_1 S_2^* \rangle}{\sqrt{\langle S_1 S_1^* \rangle \langle S_2 S_2^* \rangle}} \tag{3.15}$$

where $\langle\ \rangle$ denotes ensemble averaging, S^* represents the complex conjugate of S. The total decorrelation can be written as following (Zebker and Villasenor, 1992; Smith et al., 1996; Meng and Sandwell, 2010):

$$\gamma = \gamma_{temporal} \times \gamma_{spatial} \times \gamma_{thermal} \tag{3.16}$$

where γ denotes the total decorrelation, $\gamma_{temporal}$ denotes the temporal decorrelation part, $\gamma_{spatial}$ denotes the spatial decorrelation part, $\gamma_{thermal}$ denotes the thermal decorrelation part.

$\gamma_{thermal}$ is associated with the signal-to-noise ratio (SNR) of the radar signal:

$$\gamma_{thermal} = \frac{1}{1+SNR^{-1}} \tag{3.17}$$

Due to the high levels of SNR, this is only significant for areas with very low backscatters, which is negligible in most cases (Askne and Smith, 1997) and not considered in this study. So the spatial and temporal decorrelations are considered as the main sources of decorrelation in repeat-pass InSAR measurements.

3.2.3.1 Spatial decorrelation

The spatial decorrelation $\gamma_{spatial}$ depends on the spatial distribution of scatters, which is affected by the surface and volume scattering, and can be separated as:

$$\gamma_{spatial} = \gamma_{slantrange} \times \gamma_{volume} \tag{3.18}$$

γ_{volume} arises when the scatterers are not confined to a plane, but distributed in depth, such as in a vegetated area and so volume decorrelation occurs because of the radar signal interaction with vegetation canopy, stem and the ground soil. The spatial volume decorrelation is a function of perpendicular spatial baseline B, range resolution R_y, incidence angle η, local surface slope in range direction α, wavelength λ, the distance r between the satellite sensor and the target on the surface, and can be calculated using the following equation (Zebker and Villasenor, 1992):

$$\gamma_{spatial} = 1 - \frac{2|B|R_y \cos^2(\theta - \alpha)}{\lambda r} \tag{3.19}$$

It is clear that the volume decorrelation increases with the perpendicular baseline. When $\gamma_{spatial}$ equals to zero, the minimum value of B is called critical baseline B_c, and occurs when the change in look angle between the two acquisitions is sufficient to cause backscatter from each pixel to become completely uncorrelated. It is estimated that the critical baseline for ERS C-

band is 1115 m (Zebker et al., 1994b), and 6.5 and 13.1 km for ALOS L-band in FBD and FBS mode respectively (Sandwell et al., 2008).

3.2.3.2 Temporal decorrelation

The temporal decorrelation $\gamma_{temporal}$ arises from the surface scattering properties (size, shape, roughness, wetness) changing over the time between two acquisitions - the radar signal is sensitive to the geometric properties of the target and its dielectric properties. For example, the repeat cycle is 35-days for Envisat (Hanssen, 2001), therefore, the time interval for two acquisitions are 35, 70, 105 days an so on. It is expected that temporal decorrelation is low for stable and human-made structures such as buildings, and moderate for bare soil surface and agricultural crops, while significant for high vegetation such as forests.

In the case of vegetated areas, the geometric change of the surface is related to the movements of scatterers. It is estimated that a small motion (e.g. 2.8 cm) of scattering centers within resolution pixel cause complete decorrelation for C-band, and 11.8 cm for L-band (Zebker and Villasenor, 1992). Because of natural environmental change such as rainfall, melting of snow or ice, and temperature, the moisture content change of the surface results in the dielectric changes of the scatterers (Hagberg et al., 1995; Smith et al., 1996). In farmed areas, besides the decorrelation caused by the naturally changing vegetation structure, mechanical cultivation such as harvesting, ploughing, tillage, dicing, and mowing cause complete decorrelation as all or at least most scatterers are changed (Wegmuller and Werner, 1997).

3.2.4 Phase unwrapping

The interferogram phase is wrapped between $-\pi$ to $+\pi$. For most practical applications continuous phase values are required. The conversion from the modulo 2π phase to a continuous phase value is called phase unwrapping, where the phase gradient is integrated across pixels. Therefore closed loop path

integrals should theoretically sum to zero except where discontinuities in phase occur.

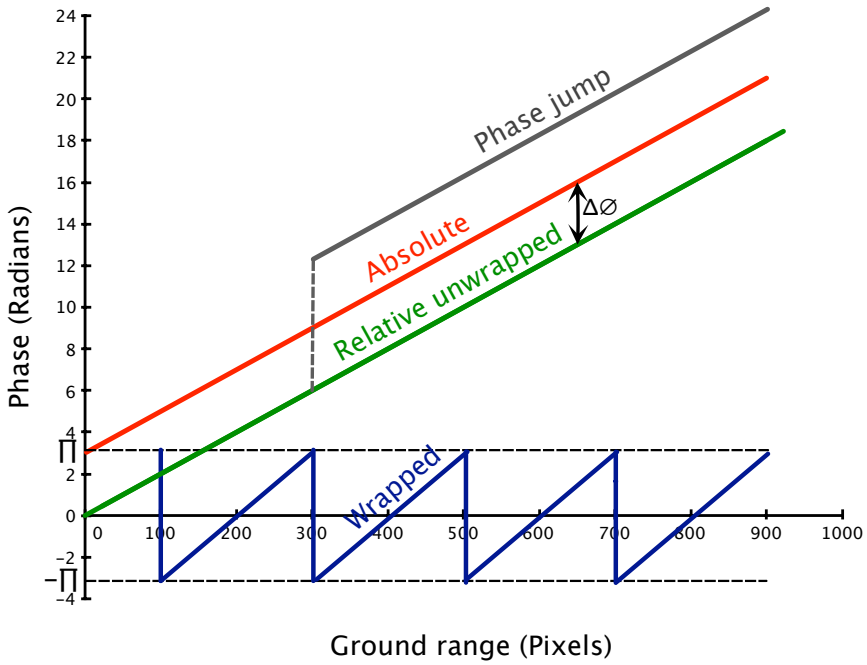

Figure 3.9 This cartoon shows the wrapped phase (blue), relative unwrapped phase (green), absolute phase (red) and phase jump (grey). A constant offset $\Delta\phi$ exists between the relative unwrapped and absolute phase, and can be resolved only by additional information, such as GPS measurements. The wrapped phase ranges from $-\pi$ to $+\pi$ (1 cycle). A phase unwrapping error causes a 2π phase jump, which must be corrected.

There is a large body of literature discussing unwrapping algorithms, for example the cited publications (Goldstein et al., 1988; Ghiglia and Pritt, 1998; Chen and Zebker, 2000; Herráez et al., 2002; Abdul-Rahman et al., 2007). In this thesis, a statistical-cost, network-flow phase-unwrapping (SNAPHU) algorithm is used to unwrap all the interferograms, as this algorithm is considered to be comparable and often better than that of other available algorithms (Chen and Zebker, 2002; Group, 2013). In addition, SNAPHU produces complete unwrapped solutions, and low coherence or no coherent pixels can be masked out. By default, the SNAPHUS algorithm chooses a high

coherent pixel as the reference point for phase unwrapping process automatically, which is applied in this thesis.

Unwrapping errors can still occur since there are incoherence and discontinuities in phase. Unwrapping errors appear as 2π phase jumps, which can be spotted visually and manually corrected. Phase unwrapping errors can be checked by a phase closure technique (Biggs et al., 2007):

$$\phi_{ab} + \phi_{bc} - \phi_{ac} = \sigma \tag{3.20}$$

where σ is the residual, ϕ_{ab} is the phase contributed by interferogram ab produced from SAR image a and b, the sequence of image acquisition time is from a, b to c and the phase here is in a conservative manner which contains deformation, orbit, and atmospheric errors. If there is any unwrapping error, the rule will be broken. Therefore phase unwrapping errors can be identified by summing a loop and checking the residuals. The phase unwrapping errors can be corrected by adding back or subtracting $2n*\pi$ manually.

3.2.5 Atmospheric phase screen

For a SAR antenna aboard on a satellite at an altitude of about 700 km, radar waves transmit through different layers of the atmosphere towards the ground, and are reflected back to the antenna. Propagation delays occur compared to when the radar waves propagate the same distance through a vacuum, because radar waves are refracted, which results in changes in the travel speed of radar waves, especially, when they propagate through the ionosphere (Tarayre and Massonnet, 1996; Hanssen, 2001; Wegmuller et al., 2006) and the troposphere (Goldstein, 1995; Massonnet and Feigl, 1995; Zebker et al., 1997). Since the atmospheric conditions are not identical in time and space, temporal and spatial propagation delay changes are expected at two SAR images acquired at different times. Even for a single SAR image, the propagation delays vary across the whole image. Therefore, the signal delay in time and space caused by the heterogeneous refractivity distribution in the atmosphere will result in variable APS across the interferogram.

3.2.5.1 Tropospheric errors

Refraction by the troposphere decreases the phase velocities of radar waves and thus causes propagation delays. A study by *Zebker et al.* (1997) shows that the time and space variations of tropospheric water vapour induce artifacts on InSAR interferograms. Other tropospheric variations, such as pressure and temperature also have effects on interferograms, but the effects are smaller in magnitude and more evenly distributed through out the interferogram than the wet troposphere term. Change in relative humidity results in 10 cm deformation errors (Zebker et al., 1997), and in the case of thunderstorms during SAR acquaints, the delay is up to 12 cm (Hanssen, 2001). Therefore mitigation of tropospheric effects is mainly focused on reducing the effects of water vapour variations in the troposphere.

3.2.5.2 Ionosphere errors

The charged ionosphere consistes of free electrons and ions. This affects the propagation of microwaves and is dispersive unlike neutral atmosphere. The activity of free electrons and ions is determined by the solar intensity. The phase refractive index can be given with a first-order form by (Klobuchar, 1996; Gray et al., 2000):

$$n \approx 1 - \frac{e^2}{8\pi^2 m_e \varepsilon_0} \frac{N_e}{f^2} \approx 1 - 40.3 \frac{N_e}{f^2} \qquad \textbf{(3.21)}$$

where N_e is the electron density (m^{-3}), e is electron charge ($1.6022 \times 10^{-19} C$), f is the microwave frequency (Hz), m_e is the electron mass ($9.1096 \times 10^{-31} kg$) and E_0 is the permittivity of a vacuum ($8.8542 \times 10^{-12} F/m$).

From Equation (3.21), it is clear that the ionosphere results in a phase advance rather than a phase delay. The longer wavelength L-band ($f_L \approx 1.27 GHz$) InSAR measurements are much more susceptible to ionospheric effects than those of C-band ($f_c \approx 5.3 GHz$) and are most visible as streaks in azimuth offsets of interferograms (Wegmuller et al., 2006; Meyer and Nicoll, 2008).

3.2.6 Atmospheric corrections

In the past two decades, a number of approaches have been developed and applied to correct atmospheric errors in interferograms, some using independent weather models and/or measurements, and some using interferograms themselves.

Numerical weather models are able to generate various atmospheric parameters for a given SAR acquisition, such as the temperature, pressure, and water vapour at varying temporal and spatial scale, which can be applied to estimate the APS. For example, correction on the interferograms over Mt. Fuji, Japan, by using European Centre for Medium Range Weather Forecasts (ECMWF, 2.5° spacing, 12 hourly) found that the accuracy for estimation surface deformation is improved from 4 cm to 2 cm (Shimada et al., 2001). Other examples please refer these publications: (Shimada, 2000; Foster et al., 2006; Puysségur et al., 2007; Doin et al., 2009). However, the numeric models are limited in spatial resolution, the finest resolution of weather models is at the km level, which is much coarser than that of InSAR. In addition, it also depends on the initial parameters, the choice of model physics (Webley et al., 2004; Foster et al., 2006). For example, *Foster et al.* (2013) used the numerical weather models developed by all available meteorological observations to mitigate atmospheric artifacts in interferograms over Mont St. Helens, Amboy, Washington, USA, and found that the approach was unable to model the refractive changes and provide no mean benefit for interferograms analysis. In addition, the performance of the numerical model was slightly improved by ingesting atmospheric delay estimated derived from the limited local GPS network.

The Global Positioning System (GPS) can not only be used to provide a high accuracy 3D position and deformation measurements, but also water vapour products. Using the GPS network in Los Angeles Southern California, *Li et al.* (2006a) developed a topography-dependent turbulence model (GTTM) to correct atmospheric effects of ERS Tandem interfergrams over this region. The water vapour effects on interferograms was reduced from ~ 10 mm down to ~ 5

mm by the use of GTTM. In addition, using an elevation-dependent water vapour (derived by GPS) interpolation model in southern California, *Xu et al.* (2011) demonstrated that the best RMS of the corrected interferogram was 5.5 mm. However, for a suitable APS measurements for InSAR correction, a sufficient coverage and dense CGPS network is required (Williams et al., 1998). Since there is not sufficient CGPS in our three study cases, APS corrections using CGPS are not implemented in this thesis.

Tropospheric water vapour delay can also be measured by water vapour radiometers (WVR), and space-based radiometers are the only effective way to produce water vapour globally with a high spatial resolution (Li, 2005). The Medium Resolution Imaging Spectrometer (MERIS) and Moderate Resolution Imaging Spectroradiometer (MODIS) are space-based instruments for water vapour measurements. MERIS and ASAR on-board the ESA ENVISAT satellite (ESA, 2013). Two MODIS are on board the Terra and Aqua satellites, launched on 18 December 1999 and 4 May 2002 respectively (NASA, 2013a). The Terra satellite flies in a near-polar sun-synchronous orbit, while ERS-2 is in a sun-synchronous polar orbit; both have a descending node across the equator at 10:30 local time, which provides a possibility of reducing water vapour effect on ERS-2 interferograms using Terra MODIS water vapour data (Li et al., 2003; Li, 2005; Li et al., 2009b). It is reported that, using MODIS and/or MERIS data to correct ASAR measurements, the root mean square (RMS) difference between GPS and InSAR range changes in LOS direction decreased from ~ 10 mm before correction to ~ 5 mm after correction (Li et al., 2006b). It should be noted that both MERIS and MODIS depend on water vapour absorption of near IR solar radiation reflected by the land, sea or clouds, which means this method is limited by daytime, cloud free conditions. The globally average percentage of cloud free conditions is about ~25% (Li et al., 2009b), but it is even lower (5-10%) in all three study sites of this thesis. Therefore, APS correction based on MERIS and MODIS is not applicable in this study.

There are other approaches for example phase stacking (Zebker et al., 1997; Williams et al., 1998; Wright et al., 2004b), Persistent Scatterers (PS) (Ferretti et al., 2000; Ferretti et al., 2001) and Small BAseline Subset (SBAS) (Berardino

et al., 2002; Lanari et al., 2004; Hooper, 2008). The first simply assumes atmospheric effects as random noise that can be neglected after stacking. On the contrary, the last two are able to estimate atmospheric effects and then deformation signals, which will be introduced in next section

3.3 Time series analysis methods

As described in above sections, the interferometric phase measurements are limited by decorrelation and APS. In recent years, by combining multiple SAR images, InSAR time series techniques can reduce various decorrelation phenomena and time series methods can be utilized for long-term observation. Two advanced multitemporal InSAR methods were developed for time series analysis: Persistent Scatterers Interferometry (PS InSAR), and Small BAseline Subset (SBAS). PS InSAR identifies pixels that provide good correlation and stable phases over long time intervals in a stack of interferograms (Ferretti et al., 2001; Hooper et al., 2004). By an appropriate combination of short orbital separation, SBAS methods are able to reduce the effect of spatial and temporal decorrelaion (Berardino et al., 2002; Lanari et al., 2004; Hooper, 2008). Despite inherent limitations, the advantages of PS and SBAS methods have proved to be effective in successfully estimating deformation in time series data in various applications (Kampes, 2006; Lanari et al., 2007).

3.3.1 Persistent scatterers InSAR

Permanent Scatterer InSAR (PSINSAR^{TM}) is proposed by *Ferretti et al.* (Ferretti et al., 2001). Also there are other algorithms such as Delft Persistent Scatterer InSAR (DePSI) (Sousa et al., 2010), Stanford Method for Persistent Scatterers (StaMPS) (Hooper et al., 2007), Maximum Likehihood Persistent Scatterer (ML-PS) (Zebker et al., 2007) and SqueeSAR (Ferretti et al., 2011). An overview of each algorithm is provided as follows.

PSINSAR^{TM} and DePSI have the same basic theory. The amplitude dispersion method is used to select PS points based on the normalized scatterer amplitude value over time, instead of a spatial analysis (Ferretti et al., 2001; Kampes,

2006). Each pixel is quantified by the ratio between the dispersion of the amplitude σ_α and the mean μ_α of the amplitudes through time:

$$D_\alpha = \sigma_\alpha / \mu_\alpha \quad \textbf{(3.22)}$$

Point scatterers with a low normalized amplitude dispersion have a low phase dispersion. Therefore, they are selected as PS candidates. Since the amplitude of urban environments is less affected with time, more abundant PS points are expected in urban areas (Perissin and Ferretti, 2007; Sousa et al., 2010).

StaMPS defines the PS points as scatterers with stable phase characteristics in space and time regardless of their amplitude (Hooper et al., 2004; Hooper et al., 2007). The advantage of this strategy is the capability to detect PS pixels with low amplitude, which is of the case in natural terrains and allows StaMPS for measuring deformation over non-urban terrains. Since amplitude dispersion is a good proxy for phase stability, StaMPS uses amplitude analysis to determine the PS candidates initially, and then the PS candidates are refined using phase analysis in an iterative process. ML-PS method is a more rigorous PS detection measurement. It applies a maximum likelihood test to each pixel to find scatterers that match the expected phase distribution (Zebker et al., 2007). The results showed the that ML-PS algorithm find more PS points than StaMPS in the rural terrains (Zebker et al., 2007).

Another algorithm to overcome the limits of PSINSAR^{TM} in non-urban areas is SqueeSAR. This approach processes PS and distributed scatterers (DS) jointly by taking into account their different statistical behavior (Ferretti et al., 2011). For a very challenging test site for any InSAR analysis over an Alpine area, the results of SqueeSAR validated this approach (Ferretti et al., 2011).

StaMPS time series approach was tested in upland using C-band. Our preliminary results suggest that this method cannot detect sufficient PS points. This also easily cause phase unwrapping error and introduce uncertainty in estimating atmospheric effect.

3.3.2 Small baseline subset InSAR

The SBAS algorithm was proposed by *Berardino et al.* (Berardino et al., 2002), and also there are other modified SBAS approaches such as Small Temporal Baseline Subset (STBAS) (Hong et al., 2010), New SBAS (N-SBAS) (Doin et al., 2011).

To understand this we should imagine a set of $N+1$ co-registered SLC images of the same area acquired at the ordered times $(t_0,.....,t_N)$. To mitigate the spatial baseline decorrelation, the first step of the SBAS approach is the generation of a number (M) of small baseline differential interferograms. To achieve this aim, the selections of SAR image pairs for the interferograms generation are designed by a small spatial and temporal baseline, as well as by a small frequency shift between the Doppler centroids (Hooper, 2008). However, the constraint of baseline can lead to a separation of interferograms into several independent subsets, so appropriate links between these subsets are required to produce the displacement time series.

The availability of absolute phase values (unwrapped phase) is required for the SBAS approach. After phase unwrapping, all pixel phase are reference to a given point, for example a high coherence pixel. We assume that the differential phase for a generic coherent pixel in interferogram j at pixel (x,r), generated by SAR images acquired at time t_B and t_A is (Berardino et al., 2002):

$$\begin{aligned}\delta\phi_j(x,r) &= \phi(t_B,x,r)-\phi(t_A,x,r)\\ &\approx \frac{4\pi}{\lambda}\left[d(t_B,x,r)-d(t_A,x,r)\right]+\frac{4\pi}{\lambda}\frac{B_{\perp j}}{r\sin\theta}\Delta z(x,r)\\ &+\frac{4\pi}{\lambda}\left[d_{atm}(t_B,x,r)-d_{atm}(t_A,x,r)\right]+n_j,\ \forall j=1,.....,M\end{aligned} \tag{3.23}$$

where λ is the transmitted signal central wavelength, $d(t_B,x,r)$ and $d(t_A,x,r)$ are the cumulative deformation in the line of sight (LOS) at times t_B and t_A respectively, with respect to the reference instant t_0 , i.e., implying $d(t_0,x,r)=0,\forall(x,r)$, $\Delta z(x,r)$ is the topographic error present in the DEM used for interferogram generation, and its impact on deformation maps, is also a

function of the perpendicular baseline component $B_{\perp j}$, the sensor-target distance λ, and the look angle θ. The terms $d_{atm}(t_B, x, r)$ and $d_{atm}(t_A, x, r)$ account for possible atmospheric variations between the acquisitions at times t_B and t_A respectively, and it is often referred to as atmospheric phase component. Finally, the n_j represent the phase caused by the baseline and the temporal decorrelation phenomena and by the thermal noise effects.

After removing the atmospheric effect phase, and ignoring the noise phase, Equation 3.23 contains the DEM error phase and the deformation phase. In order to guarantee continuities in cumulative deformation and a physically sound solution, we may manipulate the system of equation (3.23) in such a way to replace the present unknowns with the mean phase velocity between time adjacent acquisitions. Accordingly, the new unknowns become:

$$\phi_{disp} = \frac{4\pi}{\lambda}[d(t_B, x, r) - d(t_A, x, r)] = \frac{4\pi}{\lambda}\sum_{k=A}^{B-1} v_{k,k+1}(t_{k+1} - t_k)] \qquad \textbf{(3.24)}$$

where $v_{k,k+1}$ is the velocity between the kth and $(k+1)th$ time. For a given pixel, let V be a vector (of size $(N \times 1)$) of successive velocities for each internal between dates (i.e., $V^T = [v_{0,1}\ v_{1,2} \cdots v_{N-1,N}]$, and let T be a vector (of size matrix $M \times N$) of time intervals for each interferogram, Equation (3.24) can be generalized into a matrix equation for the entire set of network:

$$\begin{cases} \begin{bmatrix} T \\ M\times N \end{bmatrix} \begin{bmatrix} C \\ N\times 1 \end{bmatrix} \begin{bmatrix} V \\ N\times 1 \\ Z \\ 1\times 1 \end{bmatrix} = \begin{bmatrix} R \\ M\times 1 \end{bmatrix} \\ C^T = \left[\frac{B_{\perp 1}}{r\sin\theta}\ \frac{B_{\perp 2}}{r\sin\theta} \cdots \frac{B_{\perp N}}{r\sin\theta} \right] \\ R^T = [\frac{\lambda}{4\pi}\delta_1\ \ \frac{\lambda}{4\pi}\delta_2 \cdots \frac{\lambda}{4\pi}\delta_M] \end{cases} \qquad \textbf{(3.25)}$$

In Equation (3.25), if all the acquisitions are well connected (i.e., they belong to a single subnetwork), we should have $M \geq N$, and T matrix is a N-rank matrix. Therefore, Equation (3.25) is a well determined or an over determined system, its solution can be easily obtained in a least square sense. *Bernadino et al.* (2002) offered an solution for disconnected subnetworks that overlap in time.

The SBAS method used in this thesis was developed by *Li et al.* (2009a). It has modified the above process chain, and integrated the APS estimation module in the estimation of time series as follows:

$$\underset{M\times N}{\left[T\right]}\ \underset{N\times 1}{\left[A\right]}\ \underset{N\times 1}{\left[C\right]}\begin{bmatrix} \underset{N\times 1}{V} \\ \underset{1\times 1}{D} \\ \underset{1\times 1}{Z} \end{bmatrix} = \underset{M\times 1}{\left[R\right]} \tag{3.26}$$

where D is the APS to be estimated, and the elements of the $N\times 1$ vector A are given by:

$$\begin{cases} A_{t_M t_S} = 0, & (t_M \neq t_{APS} \text{ and } t_S \neq t_{APS}) \\ A_{t_M t_S} = -1, & (t_M = t_{APS} \text{ and } t_S \neq t_{APS}) \\ A_{t_M t_S} = +1, & (t_M \neq t_{APS} \text{ and } t_S = t_{APS}) \end{cases} \tag{3.27}$$

If a temporal deformation model is known V can be given by:

$$\underset{N\times 1}{V} = \underset{N\times p}{M} \times \underset{p\times 1}{P} \tag{3.28}$$

Where vector P contains p model parameters (typically less than four) and M is the model matrix describing the velocity vector V. If no temporal deformation model is known, a temporarily linear velocity (TLV) model can be used to estimate the APS at t_i:

$$\begin{cases} v_{1,2} = v_{2,3}, & (i = 1) \\ v_{i-1,i} = v_{i,i+1}, & (i \neq 1 \text{ and } i \neq N+1) \\ v_{N-1,N} = v_{N,N+1}, & (i = N+1) \end{cases} \tag{3.29}$$

From equation 3.29, it suggests that the TLV model only makes an assumption on two consecutive intervals and thus has a minimum impact on the whole TS. Following equation 3.26, 3.29 can be rewritten as:

$$\begin{bmatrix} \underset{1\times N}{F} & \underset{1\times 1}{0} & \underset{1\times 1}{0} \end{bmatrix}\begin{bmatrix} \underset{N\times 1}{V} \\ \underset{1\times 1}{D} \\ \underset{1\times 1}{Z} \end{bmatrix} = 0 \tag{3.30}$$

Therefore, equation 3.26 can be rewritten as:

$$\begin{bmatrix} \underset{M\times N}{T} & \underset{N\times 1}{A} & \underset{N\times 1}{C} \\ \underset{1\times N}{F} & \underset{1\times 1}{0} & \underset{1\times 1}{0} \end{bmatrix} \begin{bmatrix} \underset{N\times 1}{V} \\ \underset{1\times 1}{D} \\ \underset{1\times 1}{Z} \end{bmatrix} = \begin{bmatrix} \underset{M\times 1}{R} \\ \underset{1\times 1}{0} \end{bmatrix} \tag{3.31}$$

If all the images are well-connected, then $M \geq N$, 3.31 is a well-determined ($M+1=N+2$) or an over-determined ($M+1>N+2$) system, a least squares algorithm can resolve it.

As described above, SBAS technique implies a pixel-by-pixel temporal analysis. However, despite the applied small (spatial and temporal) baseline constraints on the selected SAR image pairs, the density of the coherent pixels is typically not homogeneous in all interferograms, and spatially dense results mostly in urban and rocky areas are expected because the decorrelation phenomena is not significant as in vegetated or non-urban areas. In the case of peatlands in this thesis, temporal or intermittent coherent pixels strategy is applied to increase the density and distribution of points (Zhang et al., 2011; Sowter et al., 2013). In practice, a high coherent pixel is identified by the continuous coherence between each acquisition date, and also determined by the coherent continuity in the stack of all interferograms.

3.4 Summary

In this chapter, the principles of SAR and InSAR are briefly introduced. Then the processing chain of InSAR is discussed followed by its various error sources including decorrelation, phase unwrapping errors, orbit ramp, and APS effects. To address decorrelation and APS effects, InSAR time series analysis approaches (PS and SBAS) are discussed.

In the study I mainly use the existing Glasgow InSAR Time Series (InSAR TS) package to investigate peatland height change for the following two reasons: (1) small baseline interferograms can minimize spatial and temporal decorrelation, especially over vegetated areas, also can reduce DEM errors effects, and (2) the TLV model in the InSAR TS package is capable of estimating atmospheric effects in time series analysis.

Chapter 4 Mapping the eroding extent and severity of peatland surface over the Monadhliath Mountains, Scotland

Abstract: In this chapter, Envisat ASAR C-band and ALOS PALSAR L-band data are used to generate time series of the change in surface height of selected peatland areas in the Monadhliath Mountains, Scotland. The dataset used spans the period from December 2002 (Envisat) to July 2010 (ALOS). I consider temporal and spatial decorrelation to decide which data sets are the most reliable to generate useful inteferograms. InSAR results show that all mean height change rates range from -0.5 to 0.5 cm/year, and relatively stable areas (less than +/- 0.1 cm/year) dominate the whole study site. A correlation analysis suggests that InSAR provides high correlation in the main areas of surface height change, but in the other areas, a low correlation coefficient is observed because the noise is of the same level as signals. In the largest area of surface height change, a total amount of about 2 cm of decrease in peat height is measured during the observed period. Combing these suggests that the InSAR time series produced by Envisat C-band and ALOS L-band SAR images can be used for mapping the long-term eroding extent and severity of the upland peatland surface.

4.1 Introduction

Blanket peat cover is extensive across the UK uplands, and equals to 15% of the global stock of this peatland type (Tallis et al., 1997), however much of the blanket peat is actively eroding by extensive gullies (Tallis, 1997a). There are several methods to map the gully system and quantify the carbon loss from upland peats (see Section 2.2 Upland peat erosion), but the measurements are limited in space and time. Therefore, the objective of Chapter 4 is to investigate whether InSAR time series can be used to map spatiotemporal changes in the surface level of upland peatlands. Should this approach be

successful it will enable the monitoring of erosion process in upland peatland landscapes that are largely inaccessible to field approaches, and fluctuations over a much wider scale manageable in field approaches.

Since InSAR measurements rely on phase coherence, comparison of the C band and L band coherence characters is implemented before the InSAR time series analysis. Understanding spatial and temporal decorrelation factors are considered. Decorrelation related to thermal noise is not considered in this Chapter, because of the high levels of SNR; thermal noise is only significant for areas of very low backscatter, which is negligible in most of cases (Askne and Smith, 1997).

4.2 Study area

The study area, called the Monadhliath Mountains, is situated at 4.57°W, 57.09°N (see Figure 4.1). The Monadhliath Mountains are located within the westernmost range of the Grampian Mountains in the Highlands of Northern of Scotland. The altitude of the mountains peaks range from 900 m to 945 m and the average annual rainfall is over 1691 mm (Keyworth et al., 2009). Vegetation in the Monadhliath includes woodland (conifer, broad leaf), heaths, bogs, mires and grassland, and this area is known to contain large areas of blanket bogs (Keyworth et al., 2009; Great Britain, 2012), see Figure 4.2, Figure 4.3 and Figure 4.5. The woodland area shown in Figure 4.3 is identified by the national forest inventory of Scotland (Great Britain, 2012), including conifer and broad leaf trees. With snow cover for ~ 106 days in one year, the climate of the Monadhliath is one of the wettest in Britain. Average annual lowland temperature is approximately 8°C and just above freezing for parts of the uplands (Keyworth et al., 2009). A 30-year record from 1971 to 2000 shows that the frost-free season often happens only in June, July and August, and the average number of days of ground frost is approximate 17 days in December, 19 days in January and 18 days in February (MET, 2005).

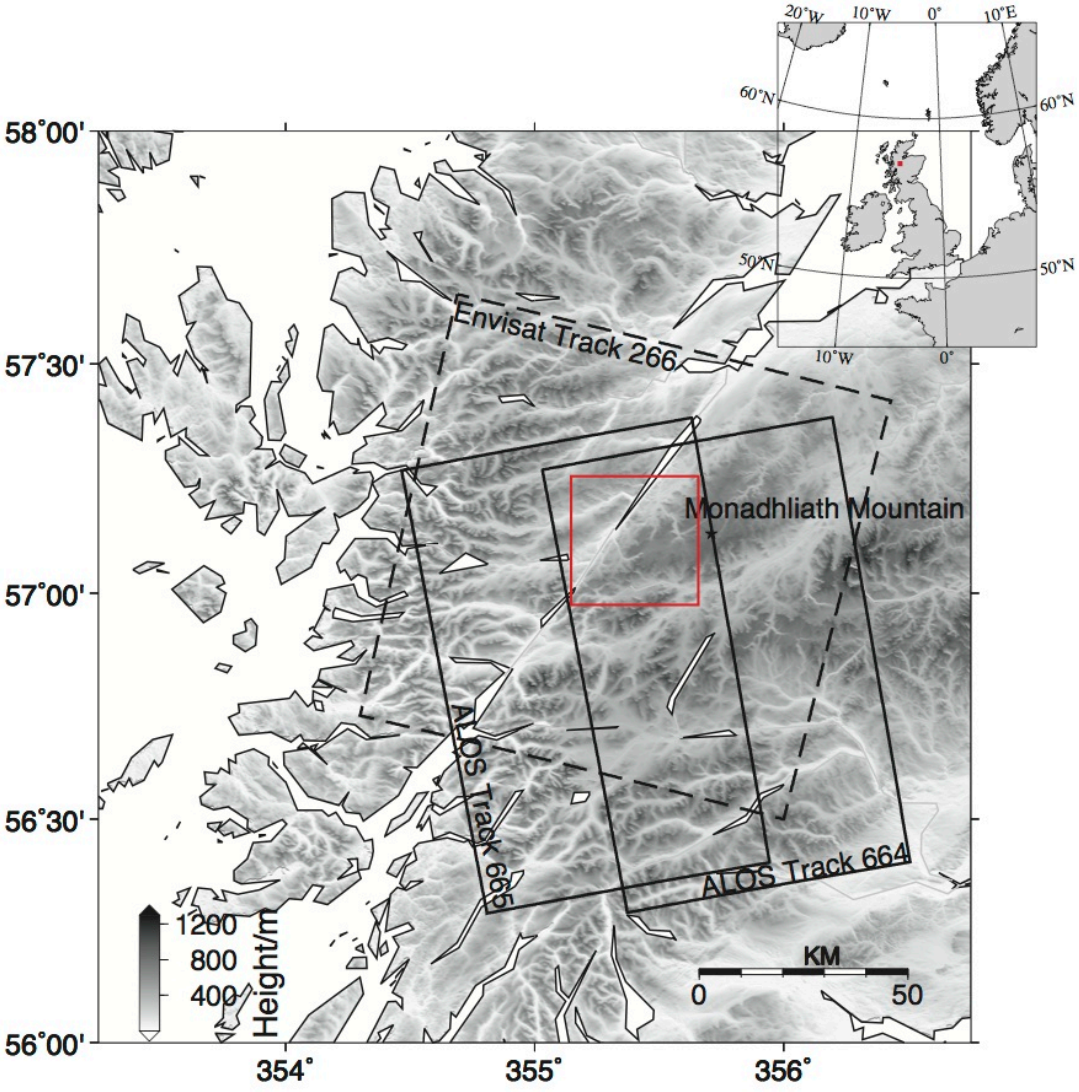

Figure 4.1 Shaded relief DEM of the study area (Small red rectangle block), Envisat track 266 and ALOS tracks 664, 665 cover this study area.

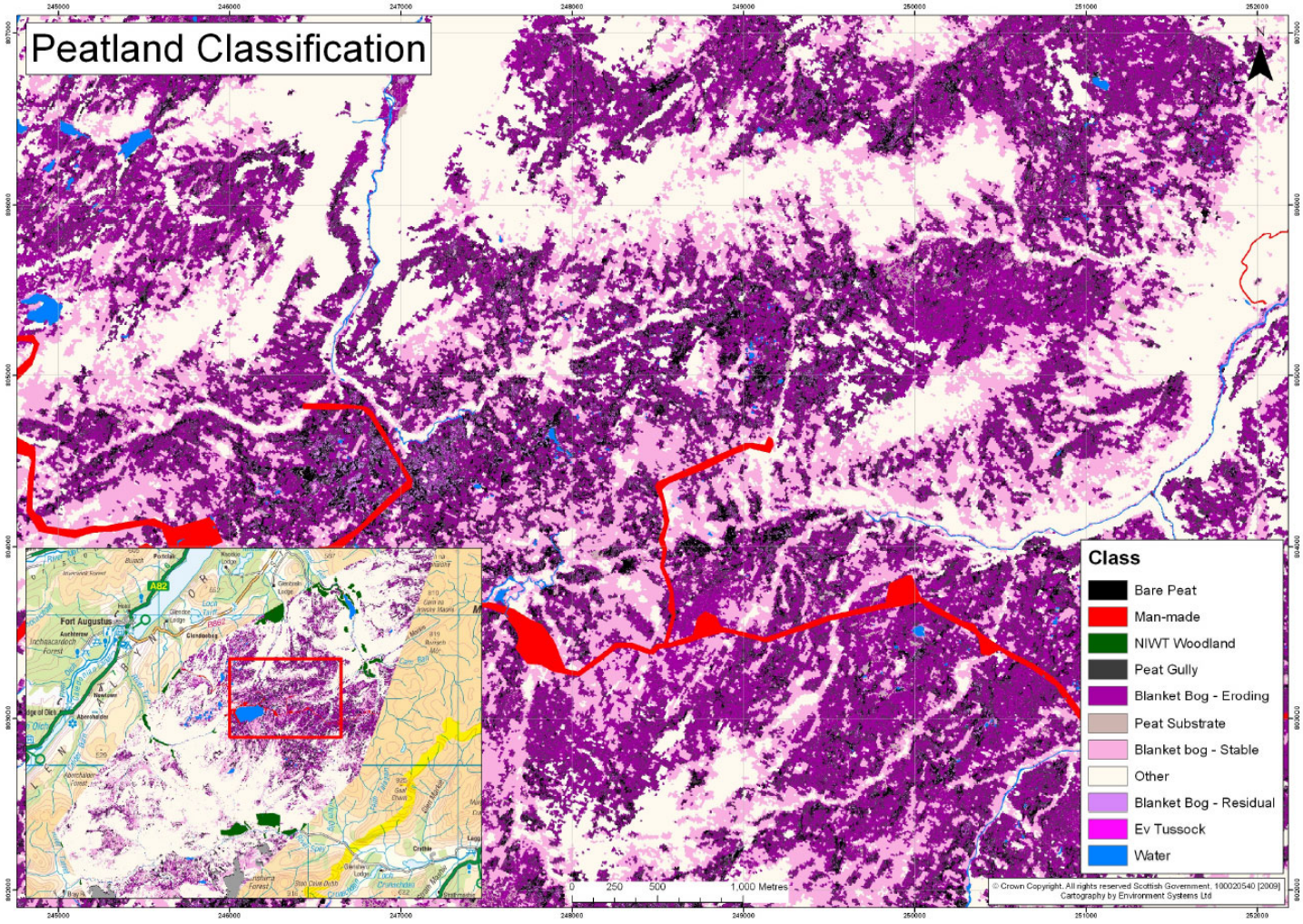

Figure 4.2 Peatland classification in 2007, adapted from *Keyworth et al.* (2009)

In this chapter, the normalized difference vegetation index (NDVI) data collected by NASA Moderate Resolution Imaging Spectroradiometer (MODIS) is used to consider temporal decorrelation effects due to seasonal vegetation (Hall et al., 2002; Lunetta et al., 2006). The NDVI indicates the photosynthetic activity of the vegetation; values range from -1 to 1, where negative values indicate non-vegetated features, positive value indicate green vegetation, and the higher the value the increasing amount of green vegetation (Pettorelli et al., 2005). For example, a positive value of 0.3 to 0.8 represents a densely vegetated surface. MODIS 16-day NDVI 250 m data is provided by the NASA's Earth Observing System Data and Information System (EOSIDS) (NASA, 2012).

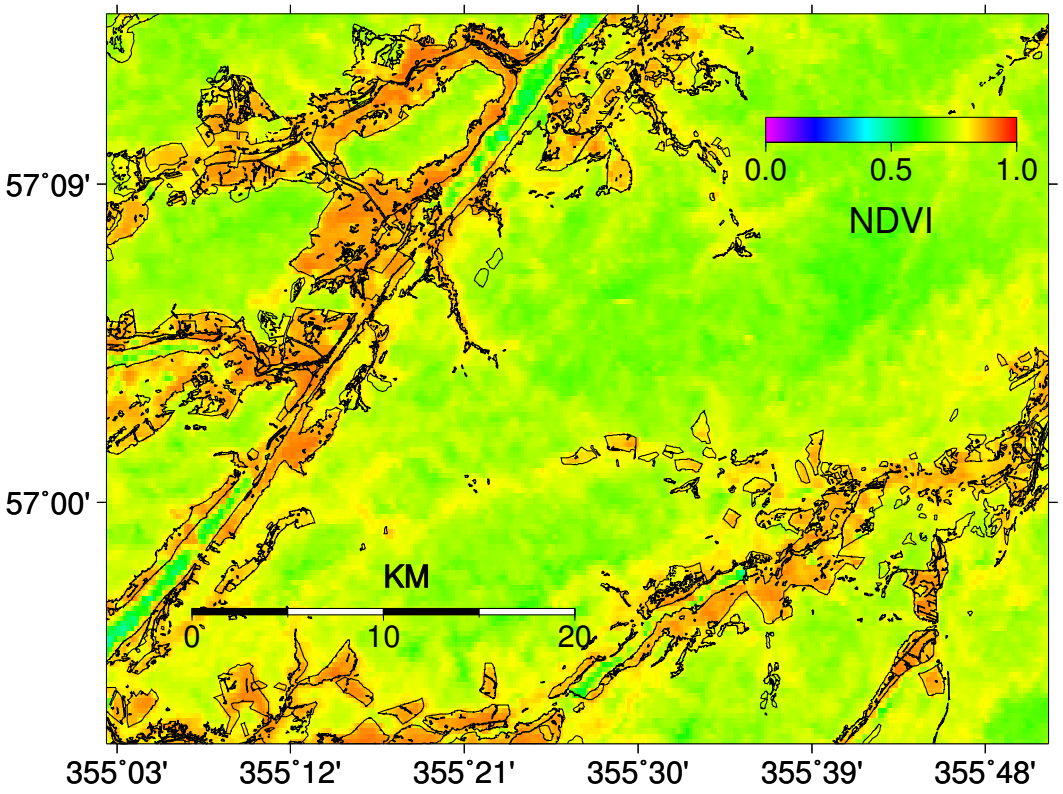

Figure 4.3 An NDVI map of the study area as acquired by MODIS satellite on 12th August 2004. The purple color represents no or little vegetation, whereas the green, yellow and red represent high density vegetation. The polygons (brown areas) show the woodland areas (conifer, broad leaf), adapted from *Great Britain* (2012).

As shown in Figure 4.3, most NDVI values are greater than 0.5, which confirms

that the study area contains dense vegetation in the summer. Comparing the woodland area shown in peatland classification map in Figure 4.2 (best shown in the inset diagram) and the national forest inventory of Scotland shown in Figure 4.3 (Great Britain, 2012), the high NDVI values (>0.8) in Figure 4.3 are caused by the woodland.

Through use of optical satellite images and field GPS surveying, peatland in the Monadhliath Mountains has been identified as at risk from erosion (Keyworth et al., 2009), see Figure 4.4. Erosion was identified in Carn, Glen and Melgarve site between 2006 and 2007 by GPS surveying (Keyworth et al., 2009), therefore it would be valuable to investigate the surface height change using InSAR in these sites and this region. The Landsat images in Figure 4.5 also show the erosion development from 2000 to 2009; the purple presents degraded peatlands. During this period, the degree of surface degrading is clear around the Carn, Glen and Melgarve areas. This is in agreement with the erosion risk level classification in Figure 4.4.

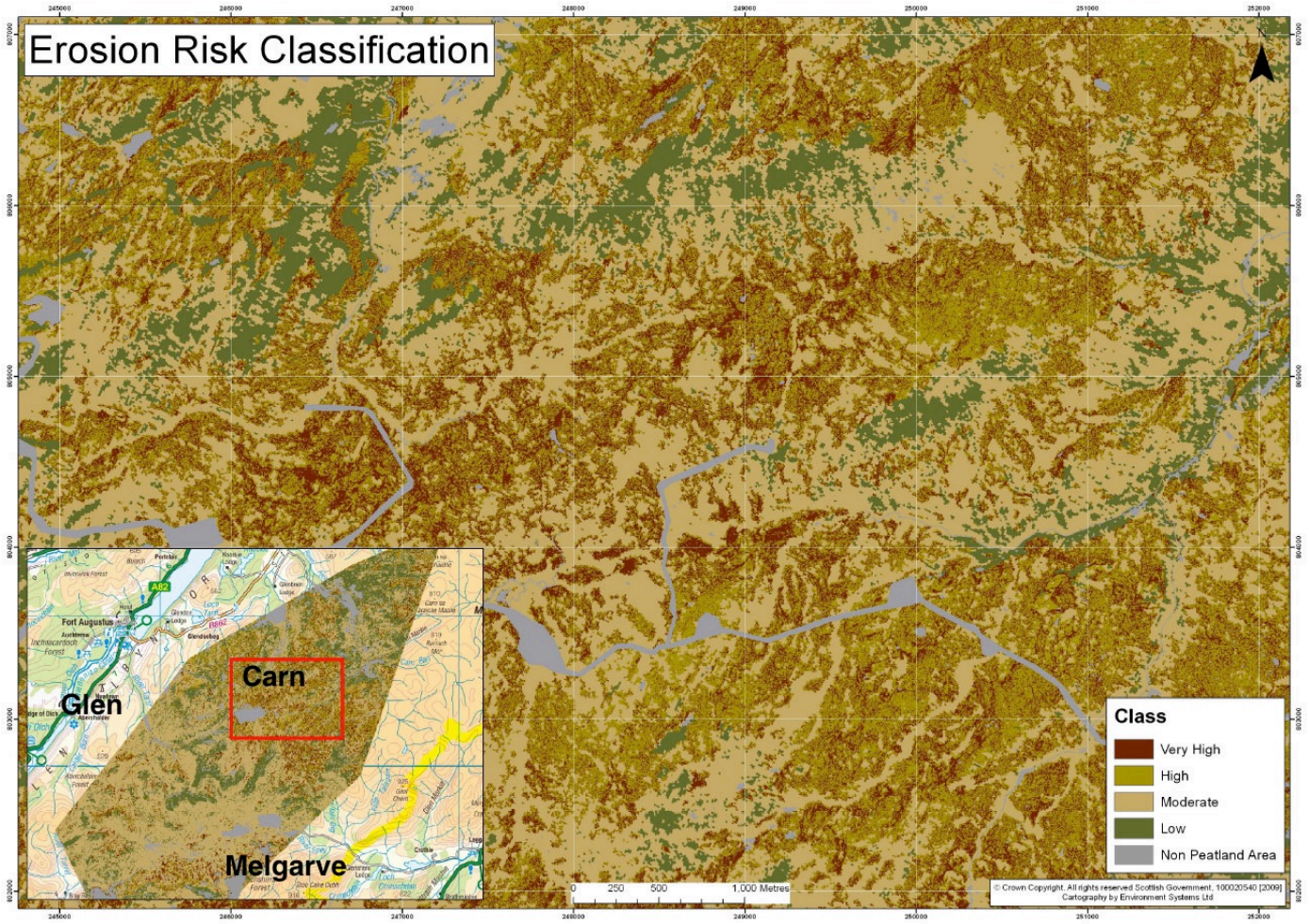

Figure 4.4 Erosion risk level classification in 2007, adapted from *Keyworth et al.* (2009). This study focuses on Carn, Glen and Melgarve.

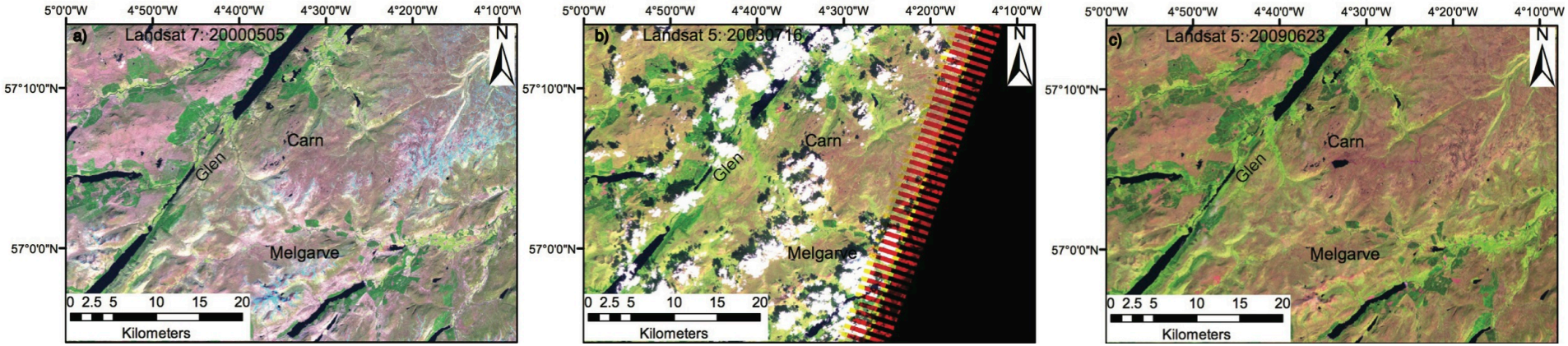

Figure 4.5 Degrading development in the study area during the period between 2000 and 2009. The images were collected by Landsat satellites (USGS, 2013). The RGB Landsat images are stacked with Bands 5, 4 and 3; the woodland area is shown in green (Great Britain, 2012), blanket bogs are shown in brown. (a) Landsat 7 image acquired on 20000505; (b) Landsat 5 image acquired on 20030718; (c) Landsat 5 images acquired on 20090623. The purple presents degraded peatlands. From 2000 to 2009, the degree of surface degradation is clear around Carn, Glen and Melgarve area in the map.

4.3 Envisat/ALOS data processing

4.3.1 Coherence processing

Nineteen images from Envisat track 266 were used for coherence analysis (Appendix 1). These SAR images acquired were from 28th December 2002 to 17 November 2007, in different seasons. Pairs with spatial baseline images >500 m are excluded because longer baselines cause lower coherence (Hanssen, 2001). Sixty-one interferograms were generated (Figure 4.6); details are listed in Appendix 1. Fifteen images from ALOS track 664 acquired from 11 December 2006 to 21 June 2010 were used, from which seventy-three interferograms were produced (Figure 4.6); details are listed in Appendix 2. The acquisition dates and the spatial baselines are illustrated in Figure 4.6. All interferograms and correlation maps are generated by the JPL/Caltech ROI_PAC software (Version 3.1Beta) (Rosen et al., 2004). All correlation maps were geocoded with a pixel size of ~ 90 m x 90 m.

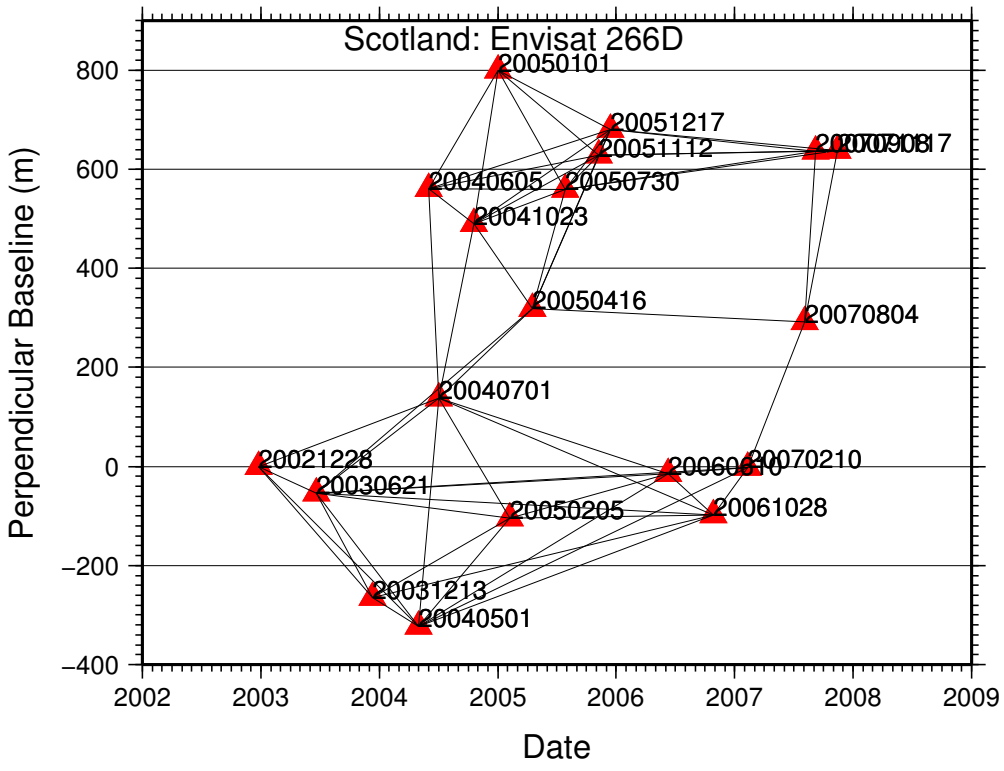

Figure 4.6a Temporal and spatial baseline of Envisat ASAR. Perpendicular baseline is related to first image. Each red rectangle presents an image, and black lines between two images indicate interferograms.

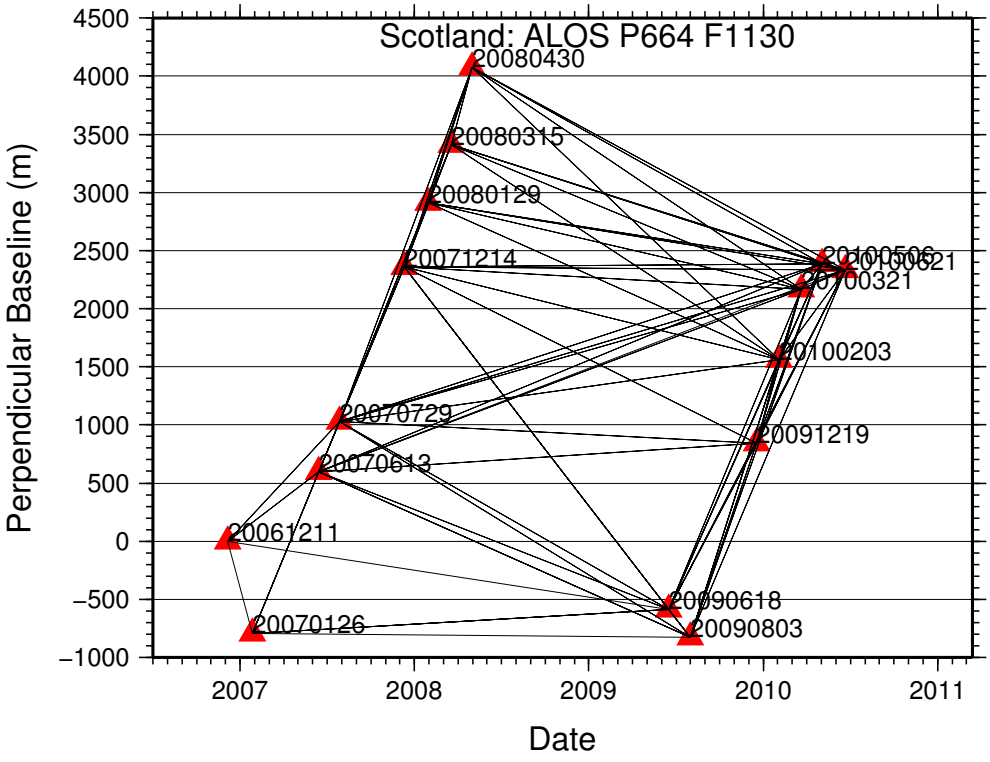

Figure 4.6b Temporal and spatial baseline of ALOS PALSAR images. Perpendicular baseline is related to first image. Each red rectangle presents an image, and black lines between two images indicate interferograms.

To compare the temporal decorrelation and limit the spatial decorrelation, three short spatial baseline interferograms were selected for both Envisat and ALOS. The spatial baseline for Envisat is limited to ~ 500 m, and for ALOS to ~ 800 m. The baseline and time interval details are listed in Table 4.1. The time intervals between three interferograms are 70 days, 175 days and 420 days for Envisat, and 184 days, 782 days and 920 days for ALOS. The time interval is longer for the ALOS because L-band can penetrate vegetated surfaces, and the impacts of temporal decorrelation are less (see Section 3.2.3 InSAR decorrelation). In order to compare the spatial baseline decorrelation, three short time interval interferograms were chosen to limit their temporal decorrelation. The baseline and time interval details are listed in Table 4.2. The time intervals for Envisat are shorter than 6 months, and the spatial baseline ranges from 0.8 m, 343.9 m to 460.3 m. For ALOS, the time intervals are shorter than 6 months as well, but the spatial baseline ranges from 553.4 m, 1718.1 m to 2388.8 m.

Table 4.1 Temporal decorrelation analysis with Envsiat track 266 and ALOS track 664. For reference, dates are given in Year-Month-Day (YYYYMMDD) format.

Envisat ASAR (Track 266)					
Master	Slave	Time interval (days)	Perpendicular baseline (m)	Average coherence	Coherence less than 0.2 (%)
20070908	20071117	70	0.8	0.32	27.26
20021228	20030621	175	-54.4	0.25	41.72
20040605	20050730	420	-1.4	0.19	66.05
ALOS PALSAR (Track 664)					
20061211	20070613	184	595.5	0.37	3.89
20071214	20100203	782	-797.37	0.29	17.22
20061211	20090618	920	-587.0	0.32	6.90

Table 4.2 Spatial decorrelation analysis with Envsiat track 266 and ALOS track 664. For reference, dates are given in Year-Month-Day (YYYYMMDD) format.

Envisat ASAR (Track 266)					
Master	Slave	Time interval (days)	Perpendicular baseline (m)	Average coherence	Coherence less than 0.2 (%)
20070908	20071117	70	0.9	0.32	27.26
20070804	20070908	35	343.9	0.31	32.72
20040501	20040710	70	460.3	0.21	56.72
ALOS PALSAR (Track 664)					
20071214	20080129	46	553.4	0.59	1.79
20071214	20080430	138	1718.1	0.52	1.93
20090803	20100203	184	2388.8	0.30	10.45

4.3.2 Coherence analysis

First temporal decorrelation is considered and then spatial baseline decorrelation.

4.3.2.1 Temporal decorrelation

The temporal decorrelation results and coherence histograms are shown in Figure 4.7 and Figure 4.8. Generally, a larger proportion (percentage) of higher coherence (>0.2) shown in histograms, the better of a coherence map. For C-band (Figure 4.7), forested areas always correspond to low coherence (< 0.2). This is because the short wavelength C-band radar is unable to penetrate trees, so return signals are mainly reflected from the top canopy of the trees and fewer signals return from their stems. For non-forest vegetation areas, the coherence is higher than that in forest area, and the longer time interval the lower the coherence. Poor coherence over the peatland area occurs with a long time interval due to changes in the surface because of vegetation growth and the changes in other environmental parameters (snow fall). The average coherence decreased from 0.32, 0.25, to 0.19 within 70 days, 175 days and 420 days intervals respectively (Figure 4.7a, b, c), and their corresponding percentages of low coherence (< 0.2) increased from 27.26%, 41.72%, to 66.05% (see Table 4.1).

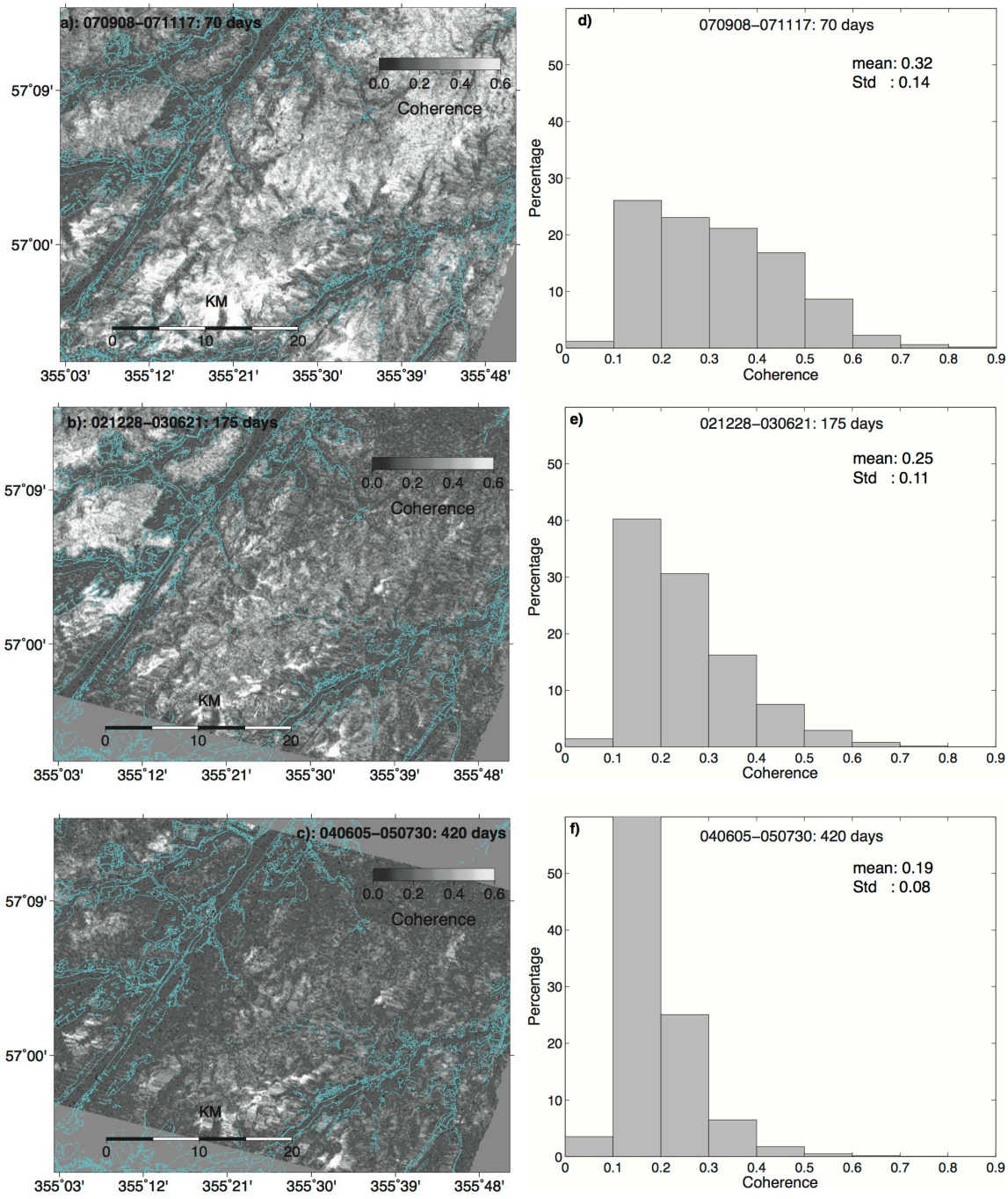

Figure 4.7 Coherence maps (a, b, c) generated from Envisat SAR images and their associated histograms (e, d, f). Coherence maps are produced by images listed in Table 4.1a. For C-band data, the longer time baseline, the less coherence in peatland area. Cyan-coloured areas denote woodland areas, and the woodland areas always show low coherence (< 0.2).

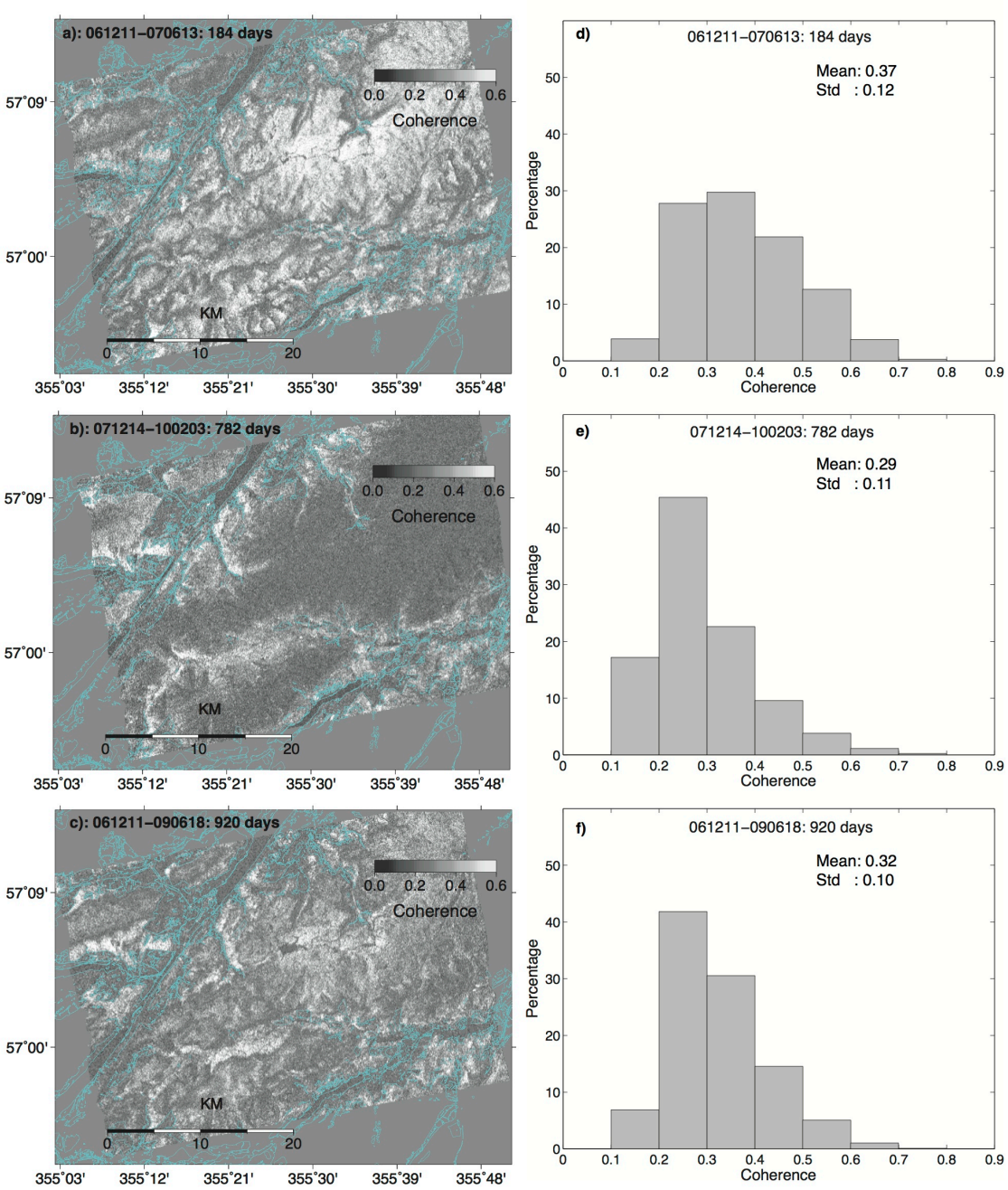

Figure 4.8 Coherence maps (a, b, c) generated from ALOS SAR images and their associated histograms (e, d, f). Coherence maps are produced by images listed in Table 4.1b. For L-band data, coherence decreases with temporal baselines, but temporal decorrelation is not significant in peatland areas. Cyan-coloured areas denote woodland areas.

For L-band (Figure 4.8), both forest area and non-forest vegetation areas show high coherence (>0.2), even when the time baseline is up to 920 days. The average coherence is high, and ranges from 0.29 - 0.37 within the 184 days, 782 days and 920 days time baseline separately (Figure 4.8a, b, c), which is

relatively higher than C-band. The corresponding percentages of low coherence (<0.2) are only 3.89%, 17.22%, 6.89%. These values are much lower than those from C-band. In Figure 4.8b, the low correlation proportion is relatively higher the other two (a, c). This is because both SAR images were acquired in the winter season, and both were covered by snow as evidenced by the MODIS daily/8-days snow coverage map (shown in Appendix 3) (Hall et al., 2002). Together the average correlation and lower number of pixel with low correlation (Table 4.1), suggest that no significant decorrelation relationship with the temporal baseline is observed for ALOS L-band, and the overall correlation is better than the C-band results for these peatland areas.

4.3.2.2 Spatial baseline decorrelation

The spatial baseline decorrelation for C-band data is presented in Figure 4.9. The average correlation decreased from 0.32 to 0.31, to 0.21 for interferograms with perpendicular baselines of 1 m, 344 m, and 460 m respectively (Figure 4.9a, b, c), and their corresponding percentages of low coherence (< 0.2) increased from 27.26%, 32.72%, to 56.72% (Table 4.2). Forested areas show low coherence, and for vegetated areas, the longer spatial baseline the less coherence. For L-band (Figure 4.10), the mean coherence decreased from 0.59, 0.52, to 0.30 for interferograms with perpendicular baselines of 553 m, 1718 m, and 2389 m respectively (Figure 4.10a, b, c), and their corresponding percentages of low coherence is very low (< 10%). All the average L-band coherence are very high (>0.30) and much greater than C-band. Both the forested and non-forested areas show high coherence; no obvious spatial decorrelation is observed in the peatland area.

Figure 4.10 shows ALOS coherence maps and their associated histograms in peatland area. Coherence map 090803-100203 (Figure 4.10c) shows much poorer coherence than others (Figure 4.10a and Figure 4.10b). This is because the interferogram is generated with two SAR images acquired in different seasons: one in the summer, the other in the winter. The surface condition (such as moisture and vegetation) changed significantly between this two seasons.

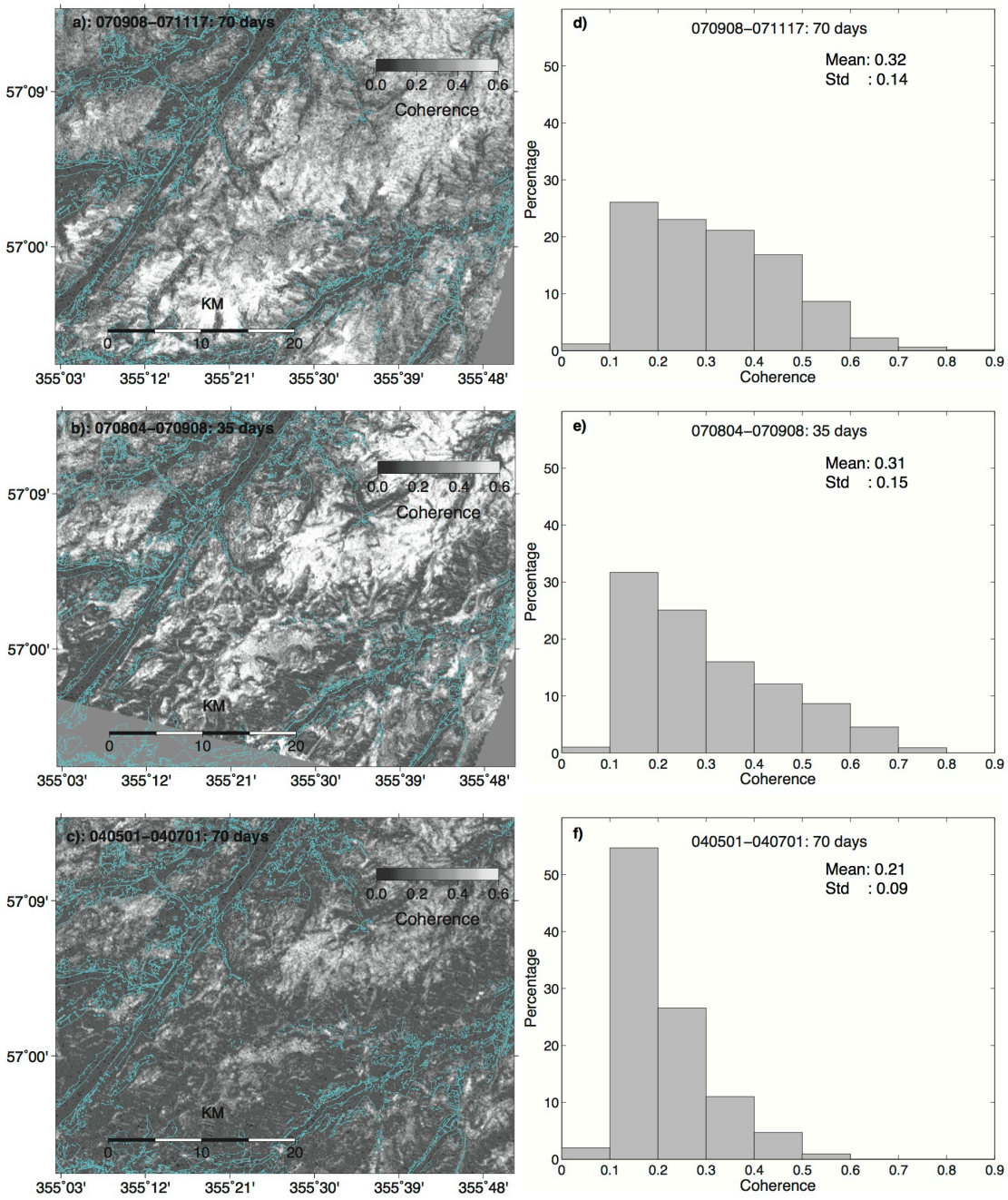

Figure 4.9 Coherence maps (a, b, c) generated from Envisat SAR images and their associated histograms (e, d, f). Coherence maps are produced by images listed in Table 4.1b. For C-band data, the longer spatial baseline, the less coherence. Cyan-coloured areas denote woodland areas.

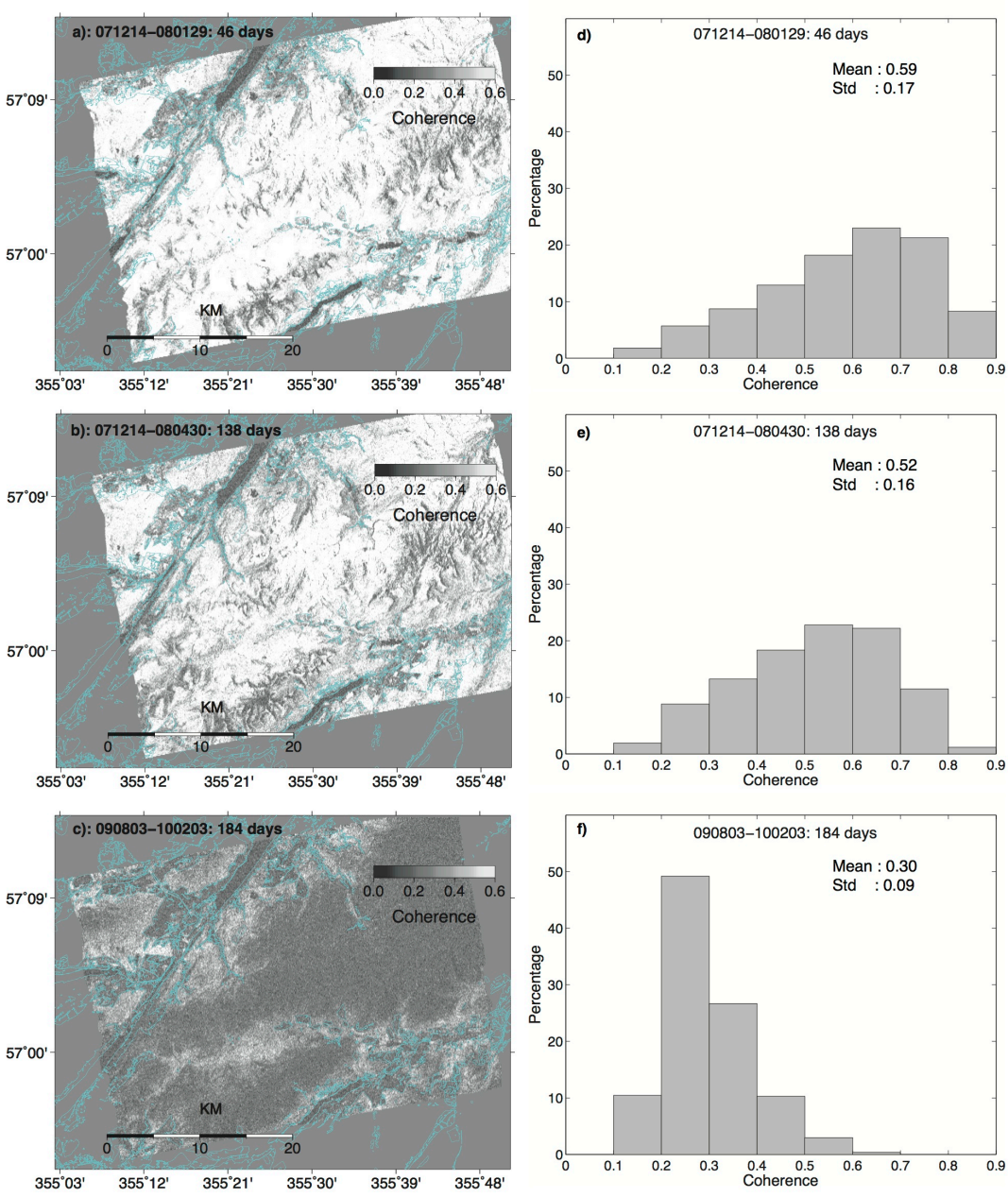

Figure 4.10 Coherence maps (a, b, c) generated from ALOS SAR images and their associated histograms (e, d, f). Coherence maps are produced by images listed in Table 4.1b. For L-band data, coherence decreases with temporal baselines, but temporal decorrelation is not significant in peatland areas. Cyan-coloured areas denote woodland areas.

Figure 4.11 shows the distributions of average coherence and percentages of coherence less than 0.2 of all the Envisat C-band interfrograms listed in Appendix 1. For Envisat C-band data, with a six month temporal baseline or shorter, the average coherence of each interferogram is greater than 0.2, even

when the spatial baseline is as long as 460 m. Furthermore, the total percentage of low coherence pixels is less than 40%, spatial basline decorrelation does not significantly increase with perpendicular baselines. Even for a 100 m spatial baseline or shorter, the average coherence of most C-band interferograms is lower than 0.2 and more than 50% of C-band interferograms are decorrelated when the time interval is larger than 5 months.

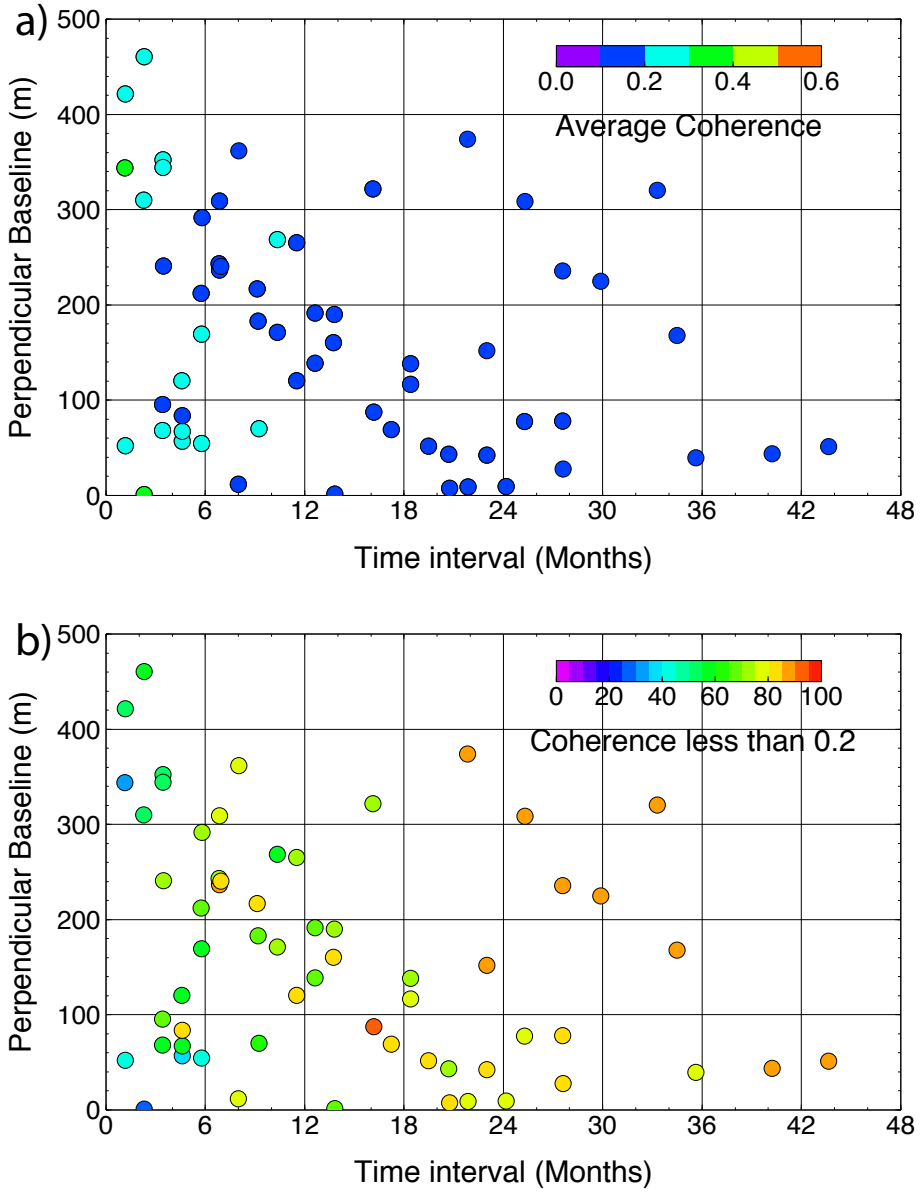

Figure 4.11 Envisat temporal and spatial baseline decorrelation, coherence is generated by images listed in Appendix 1. (a): Average coherence; (b): the percentage of coherence less than 0.2. Spatial decorrelation is not as significant as temporal decorrelation in blanket bog peatland.

Therefore, in comparison with spatial baseline decorrelation, the temporal decorrelation is the main source of loss of coherence for C-band in the blanket bogs area, most likely because C-band is more sensitive to environmental parameter changes (rain, wind, etc.) and the growth or die of vegetation (Smith et al., 1996; Meng and Sandwell, 2010). Shorter temporal baselines (within 6 months) and spatial baselines ($<$ 500 m) provide better coherence and larger correlated areas.

Figure 4.12 shows the distributions of average coherence and percentages of coherence less than 0.2 of all the ALOS L-band interferograms listed in Appendix 2. For L-band (Figure 4.12a), with a 36-month temporal baseline or shorter, the average coherence of each interferogram is greater or equal to 0.27. Even when the spatial baseline is 1790 m and the time interval is about 35 month, the average coherence is still up to 0.38 (Appendix 2). A shorter temporal baseline ($<$ 6 months) provides relatively higher ($\sim$ 0.6) average coherence, but no significant decorrelation with temporal baseline is observed when the time interval is between 24 and 36 months (Figure 4.12a). In Figure 4.12b, the maximum percentage of low coherent area is 22%. With increasing of time interval or spatial baseline, significant low coherence areas are not observed in this study. This is because L-band radar signals from the ground soil dominates the backscatters; compared to C-band, L-band is less sensitive to the change in the environment and the growth or die of vegetation. For L-band, the moisture change of the soil has an effect on coherence, but limited ALOS PALSAR images were acquired in the winter season in this study (Figure 4.8b and Figure 4.10c). These results confirmed the earlier observations of correlation over vegetated area: that L-band is less sensitive to the changes of both canopy and ground compared to C-band (Smith et al., 1996; Ribbes et al., 1997; Meng and Sandwell, 2010).

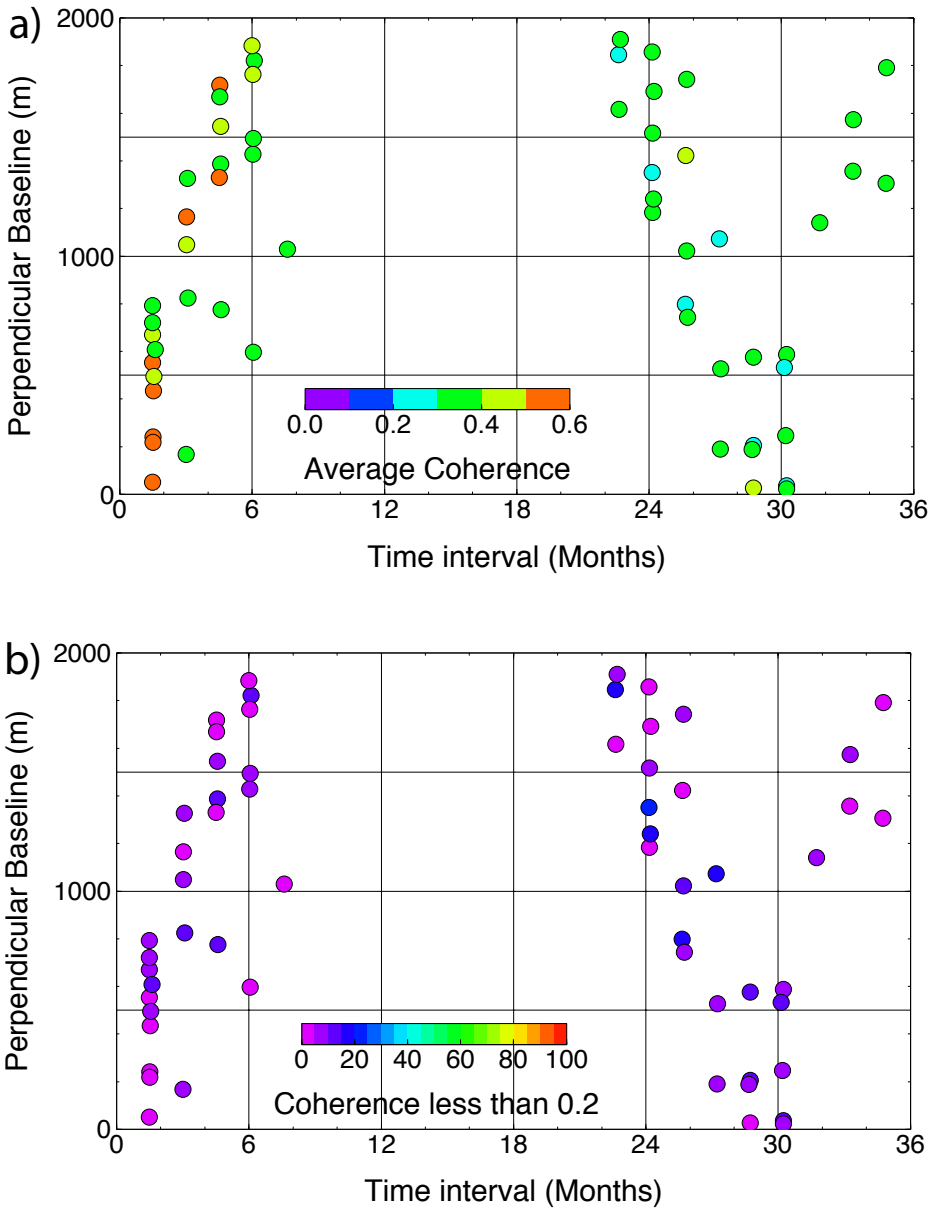

Figure 4.12 ALOS temporal and spatial baseline decorrelation, coherence is generated by images listed in Appendix 2. (a): Average coherence; (b): the percentage of coherence less than 0.2, spatial and temporal decorrelation is not significant in blanket bog peatland.

4.3.3 Time series processing

Used tracks above, one more extra ALOS track is used in this study. In areas without ground observations available, if the pattern of height change produced by two adjacent ALOS tracks with an overlapping area is consistent over the

same observation period, then this provides confidence that the approach yields reliable information. Temporal and spatial baselines of available images of each track are shown in Table 4.3 and Table 4.4.

Table 4.3 Images from track 266 used in this chapter. For reference, dates are given in Year-Month-Day (YYYYMMDD) format, and as number of days since the first images. Perpendicular baseline for track 266 is given relative to the reference date of 20070908. This reference date was chosen because of the limited atmospheric effects on this corresponding SAR image.

EnviSat Track 266				EnviSat Track 266			
Image Number	Date(YYYYMMDD)	Number of days	Baseline (m)	Image Number	Date(YYYYMMDD)	Number of days	Baseline (m)
1	20021228	0	-636.5	10	20050416	852	-316.9
2	20030621	182	-690.2	11	20050730	943	-77.1
3	20031213	365	-901.9	12	20051112	1066	-8.5
4	20040501	517	-958.7	13	20051217	1096	42.7
5	20040605	548	-76.4	14	20061028	1400	-732.9
6	20040710	578	-498.6	15	20070210	1523	-636.8
7	20041023	670	-146.8	16	20070804	1704	-344.3
8	20050101	762	162.3	17	20070908	1735	0
9	20050205	793	-741.4	18	20071117	1796	0.6

Table 4.4 Images from tracks 664 and 665 used in this chapter. For reference, dates are given in Year-Month-Day (YYYYMMDD) format, and as number of days since the first images. Perpendicular baseline for track 664 is given relative to the reference date of 20070613, and 20070630 for track 665. This reference date was chosen because of the limited atmospheric effects on this corresponding SAR image.

ALOS P664				ALOS P665			
Image Number	Date(YYYYMMDD)	Number of days	Baseline (m)	Image Number	Date(YYYYMMDD)	Number of days	Baseline (m)
1	20070613	0	0.0	1	20070212	0	-890.0
2	20070729	46	433.9	2	20070630	138	0.0
3	20071214	184	1763.6	3	20070815	184	303.4
4	20080129	230	2316.9	4	20070930	230	732.4
5	20080430	322	3482.2	5	20071231	322	1318.0
6	20090618	736	-1182.7	6	20080401	414	2810.1
7	20090803	782	-1423.1	7	20080517	460	3035.9
8	20091219	920	246.3	8	20090820	920	-1125.4
9	20100321	1012	1573.0	9	20091005	966	-519.4
10	20100506	1058	1790.6	10	20100407	1150	1352.3
				11	20100523	1196	1440.3
				12	20100708	1242	1506.2

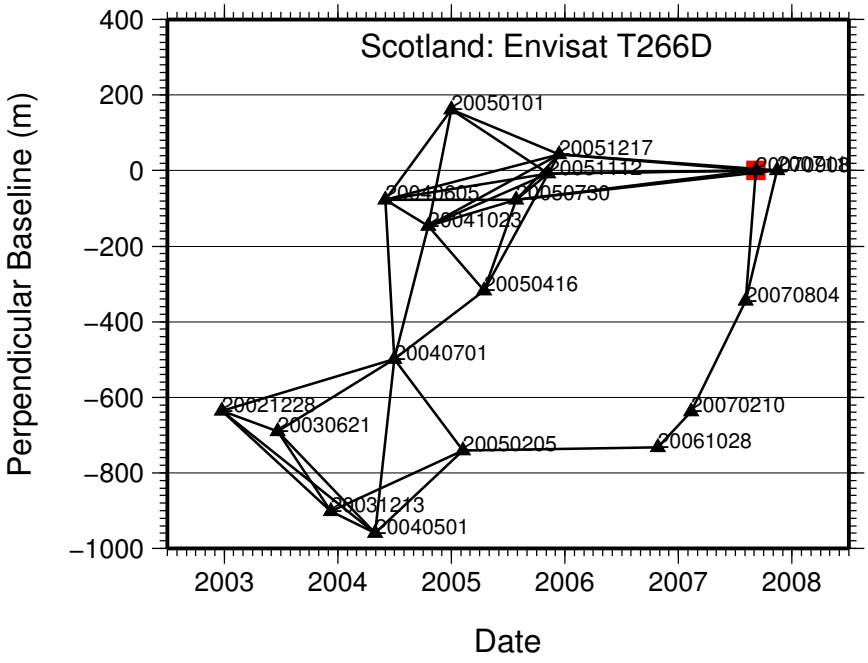

Figure 4.13 SBAS network for Envisat track 266. Black triangles denote SAR images, black square represents reference SAR image, and black solid lines between two black triangles represent interferograms. Low coherence interferograms are excluded

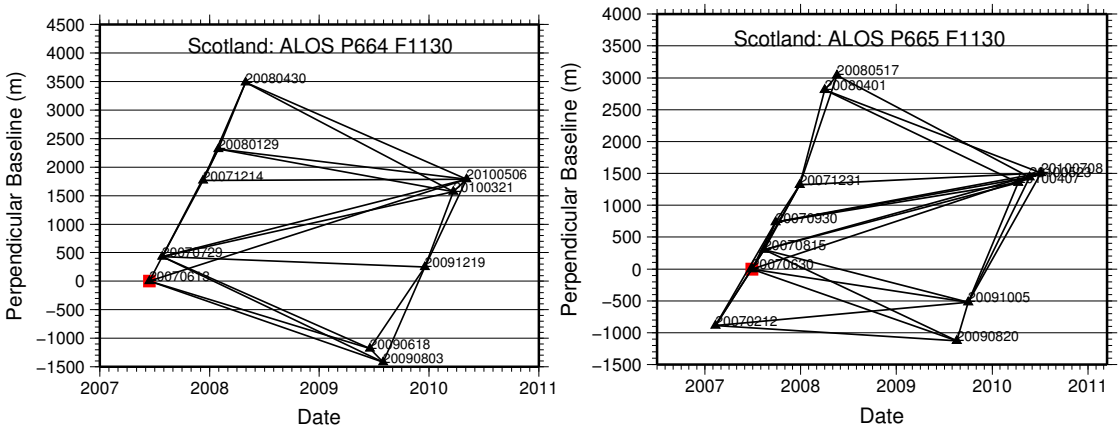

Figure 4.14 SBAS network for ALOS tracks 664 and 665. Black triangle denote SAR images, black square represents reference SAR image, and black solid lines between two black triangles represent interferograms.

For Envisat track 266, 18 images are included in this study and 44 interfergrams are used; low coherence interferograms are excluded. For L-band, to minimize the phase variation caused by snow, several images acquired in the winter season are excluded. For ALOS track 664, 10 PALSAR images are used to produce 25 interferograms, and for ALOS track 665, 33 interferograms are generated from 12 PALSAR images (Figure 4.14). The reference dates selected

are close to each other for three tracks: 8 September 2007, 27 September 2007, and 30 September 2007 for tracks 266, 664 and 665 respectively.

For validation, four sites are selected: Carn, Glen, Melgarve and B. Because the first three sites were eroding between 2006 and 2007 (Keyworth et al., 2009), therefore relatively significant surface change are expected within these three sites; Region B is chosen for the purpose of comparison. Four points a, b, c, d are randomly selected within the Glen, B, Carn and Melgarve four areas for the time series analysis, each one represents a 3 pixels x 3 pixels window (approximately 270 m by 270 m in ground).

4.3.4 Interferograms

For C-band interferograms (Figure 4.15), to limit the impacts of decorrelation, interferograms are generated from two SAR images with short temporal and spatial baselines only. For L-band, decorrelation is not significant in blanket bog peatland (Figure 4.16).

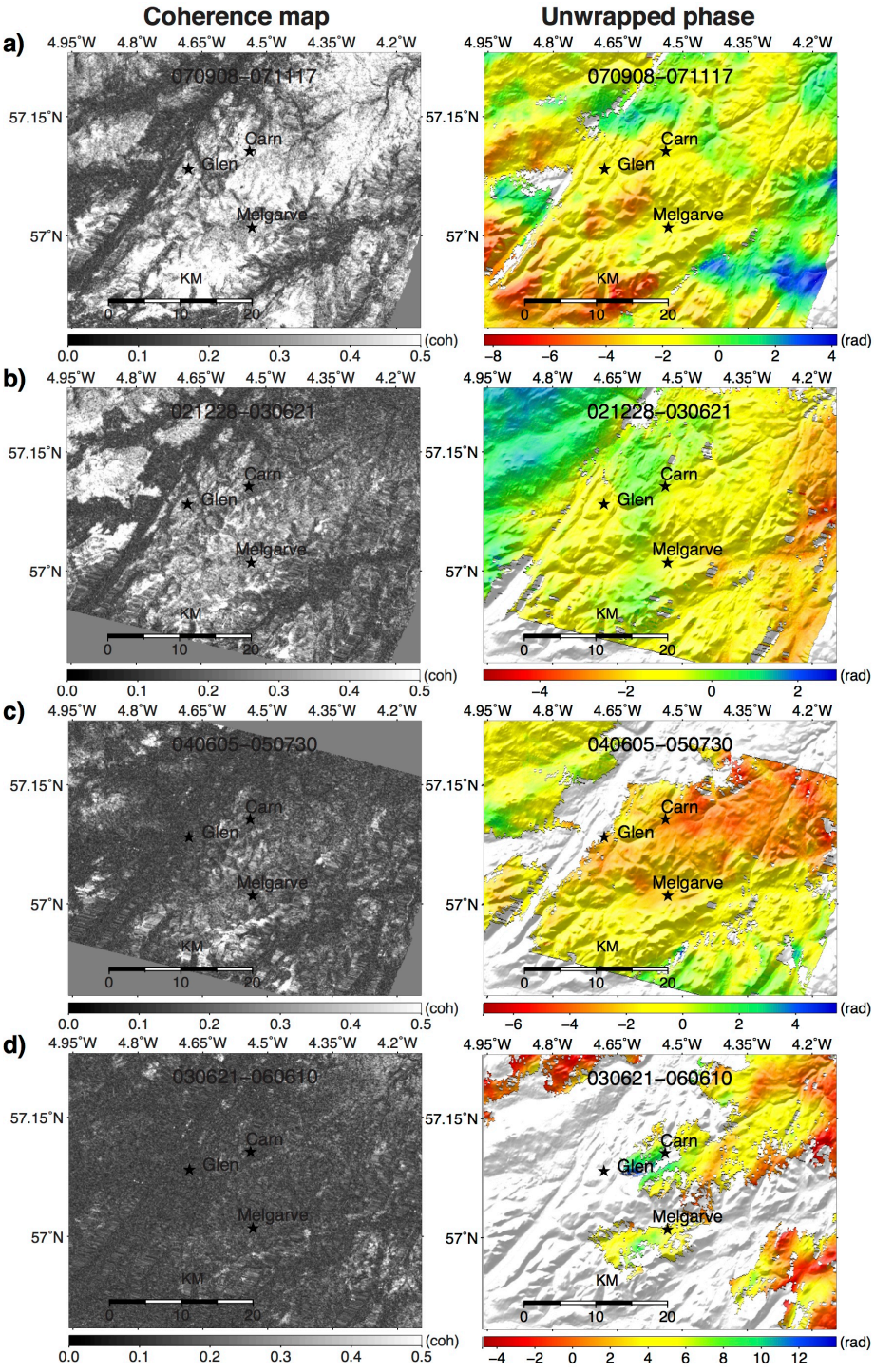

Figure 4.15 Interferograms from C-band data with different temporal baselines superimposed on an SRTM DEM shown as shaded relief. (a) Interferogram from 070908 and 071117; (b) Interferogram from 021228 and 030621; (c) Interferogram 040605 and 050730; (d) Interferogram from 030621 and 060610. Each radian represents an increase of 0.5 cm in the range from ground to satellite. With the increase of time interval between two SAR images, the random noises of interferogram increase as well, which results in relatively low coherence and less useful unwrapped phase, such as interferogram d; it is not included in the final time series analysis.

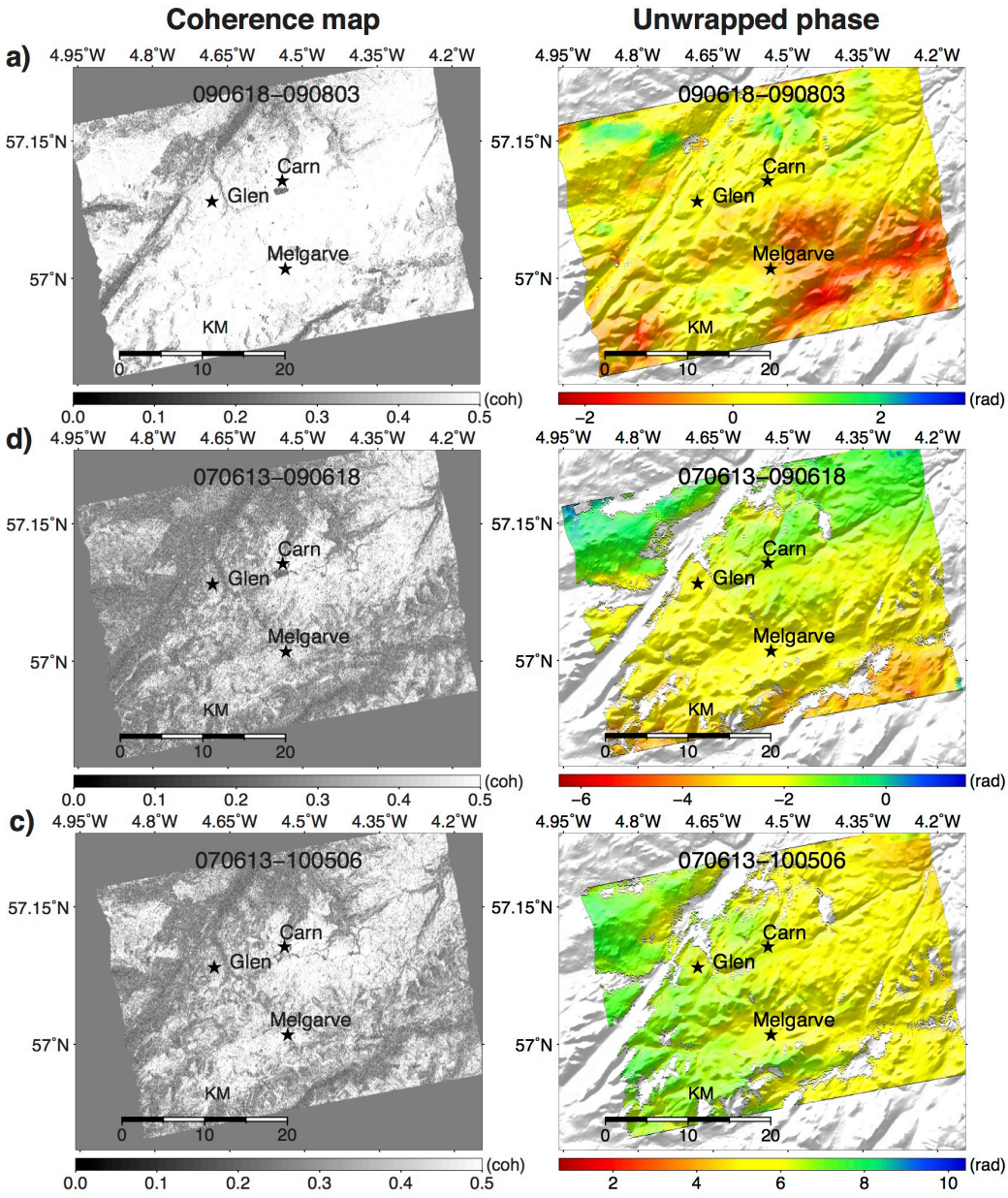

Figure 4.16 Interferograms from L-band data with different temporal baselines superimposed on an SRTM DEM shown as shaded relief. (a) Interferogram from 090618 and 090803; (b) Interferogram from 070613 and 090618; (c) Interferogram from 070613 and 100506. Each radian represents an increase of 1.8 cm in the range from ground to satellite. With the increase of time interval between two SAR images, the random noises of interferogram is not significant, useful phases dominate the unwrapped phase map.

4.3.5 Phase unwrapping error

In this study, phase unwrapping error is checked before time series analysis with the phase closure technique (see Section 3.2.4 Phase unwrapping) (Biggs et al., 2007). Figure 4.17 shows a closure loop example from C-band interferograms (Figure 4.17a, b, c), and 4π phase jumps (~ -6 rad in L area, ~ 6 rad in the R area) can be identified in the residual (d). To find the interferogram with unwrapping errors, each one should be investigated. By checking the phase of each interferogram visually, 4π phase jumps can be identified in interferogram a, since the phase value of L area jump to approximate -6 rad from 6 rad in R area. When 4π is added back to L (e), the closure residual (f) becomes zero, suggesting successful phase unwrapping. Another difficulty of phase closure method is finding the exact location of unwrapping error, because the loop is only valid for pixels that occur in all three interferograms. If pixels are not coherent in all interferograms, unwrapping errors cannot be identified, such as the area labeled as 'U' in Figure 4.17.

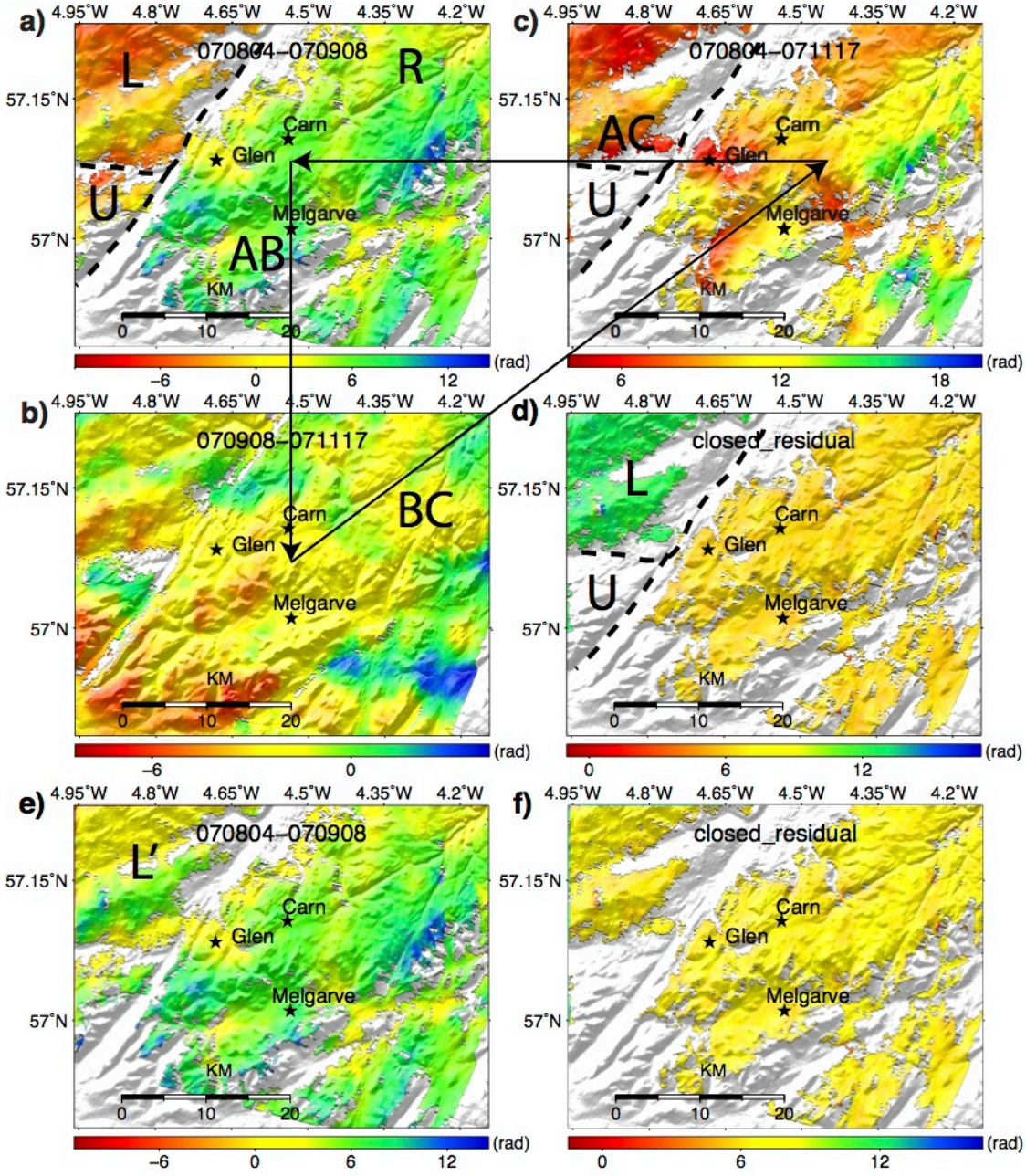

Figure 4.17 Phase closure and unwrapping error from C-band interferograms. Unwrapped phases are from interfrograms a (AB: 070804-070908), b (BC: 070908-071117) and c (AC: 070804-071117). Unwrapping errors can be identified by checking their closed residual (d). Phase jumps are shown in (d), which may contribute from one or more interferogram. In this case, the phase jump area labeled as L is from interferogram a, since the phase value of Area L jump to approximate -6 rad from 6 rad in Area R. After correction (e), there is no phase jump in the residual (f). Pixels in area labeled as U are not coherent in all the three interferograms, hence phase unwrapping errors in this area cannot be identified.

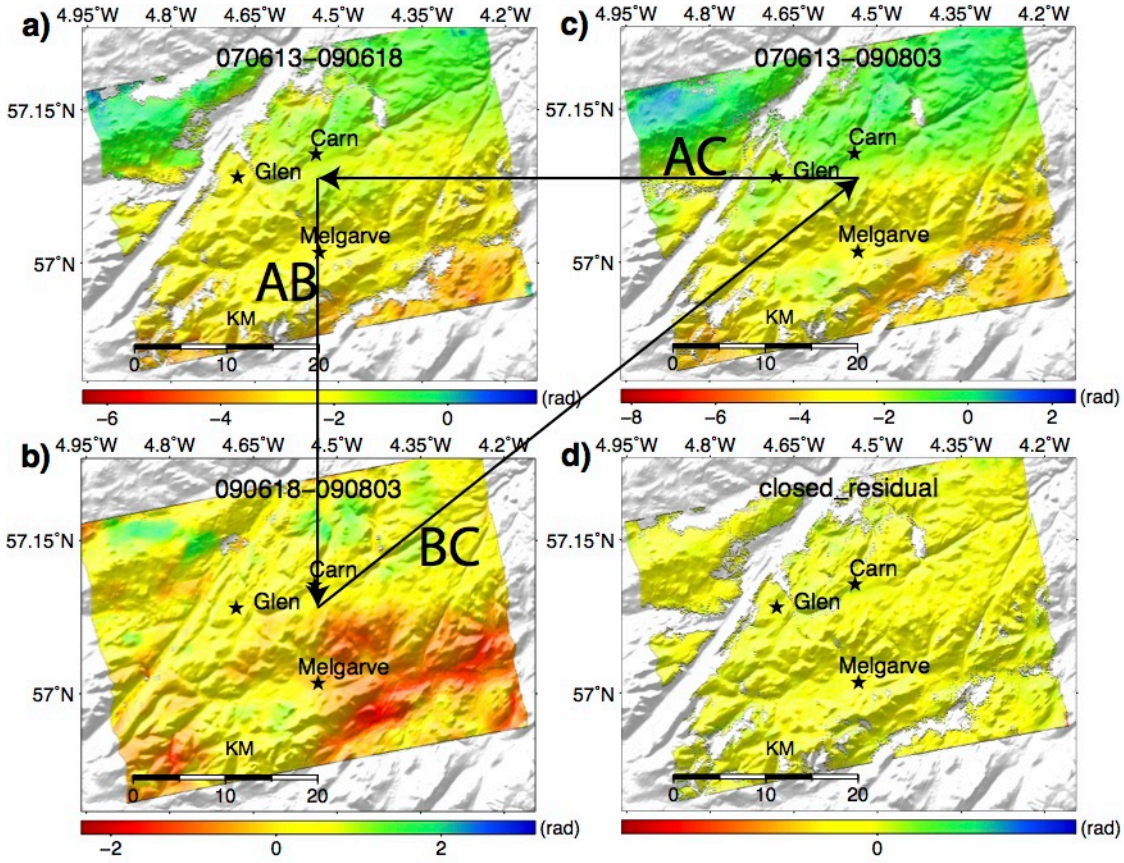

Figure 4.18 Phase closure and unwrapping error from L-band interferograms. Unwrapped phases are from interferograms a (AB: 070613-090618), b (BC: 090618-090803) and c (AC: 070613-090803). Unwrapping errors can be identified by checking the closed residual (d). In this case, there is no clear unwrapping error since no phase jump exists.

Figure 4.18, shows a closure loop example form L-band interferograms (a, b, c), and the residual (d). The three interferograms are successfully unwrapped because no phase jump is shown in the residual map.

4.3.6 Orbit ramp

In this study, the orbit error is estimated using a best fit plane and subtracted from the unwrapped interferogram.

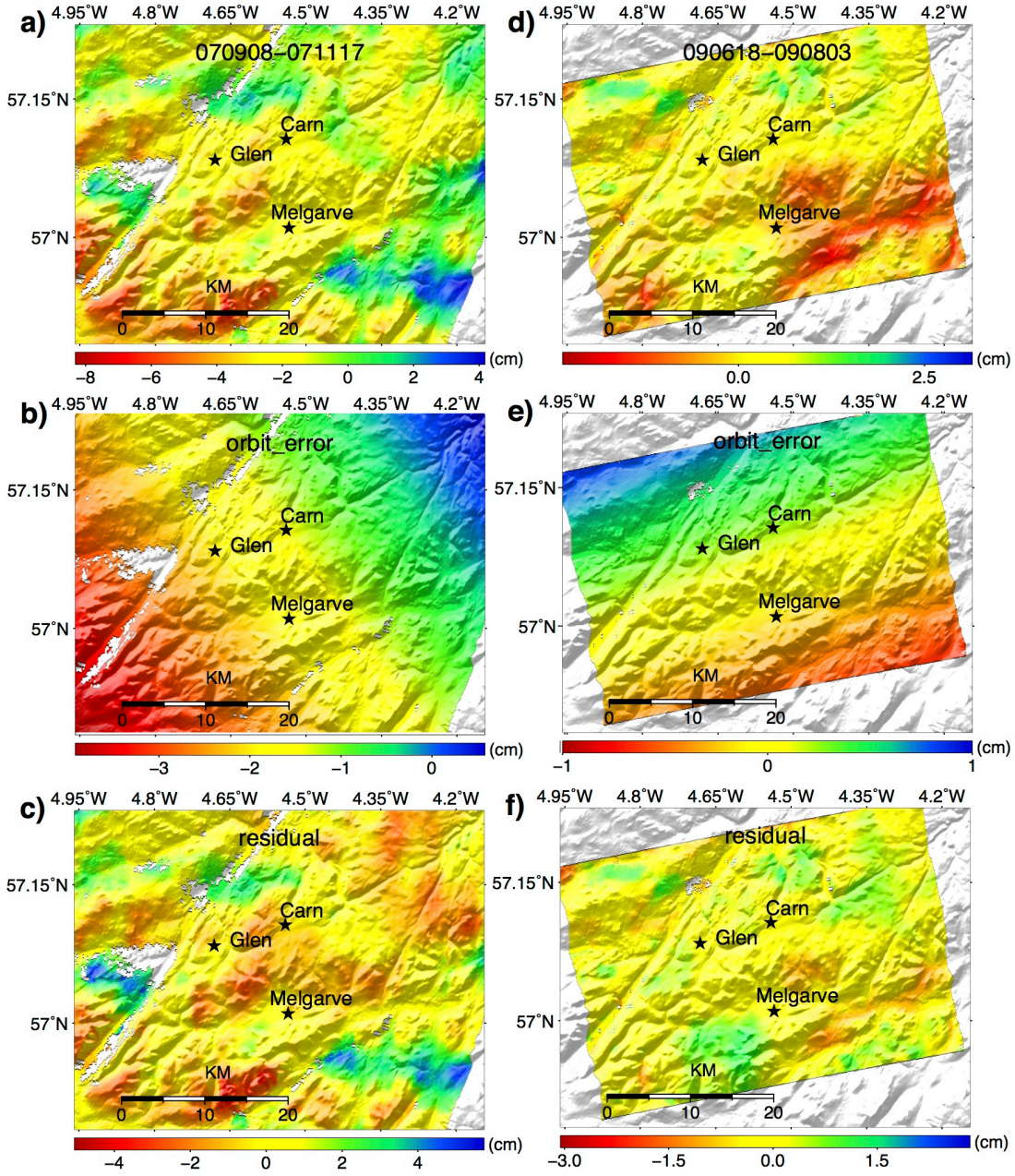

Figure 4.19 Orbit ramps from C–band interferograms (a, b, c), and L-band interfrograms (d,e,f). (a) Unwrapped C-band interferogram. (b) The best fit orbit ramp. (c) The corrected interferogram phase by subtracting (b) from (a). (d) Unwrapped L-band interferogram. (e) The best fit orbit ramp. (f) The corrected interferogram phase by subtracting (e) from (d).

4.3.7 Atmospheric phase screen (APS)

APS is estimated using the TLV model (Li et al., 2009a). Figure 4.20 shows an example of estimated APS: because the time interval between two SAR images

is 46 days, no obvious ground surface change is expected and therefore the phase contribution to the interferogram is mainly from APS.

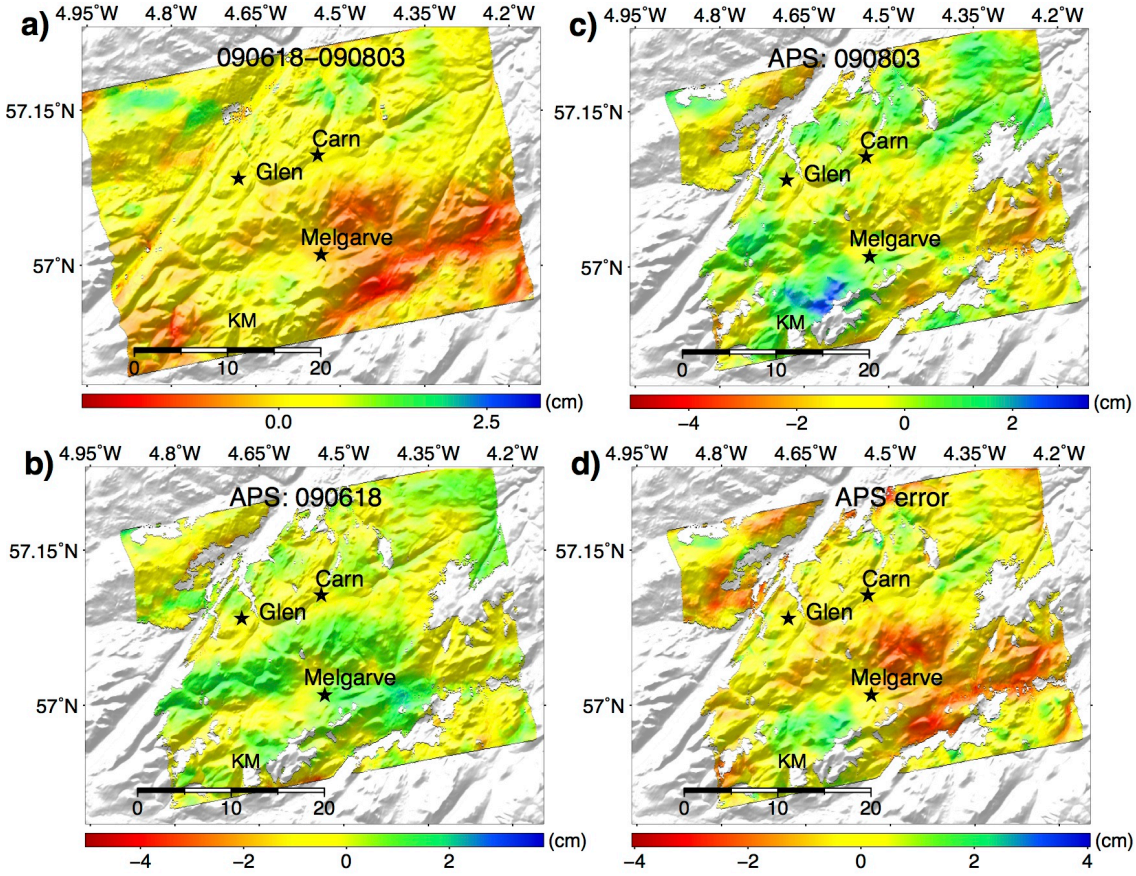

Figure 4.20 Individual APS and APS error. (a) interferogram after remove the orbit error. (b) estimated APS for image 090618. (c) estimated APS for image 090803. (d) estimated APS effects on Interferogram 090618-090803, which is expected to be similar to (a). Note: APS is estimated by stacking all interferograms, since not all pixels are coherent through all of the interferograms, so the number of valid pixels in b, c, d is smaller than a.

4.4 Results

The mean LOS peat height change rate maps from three tracks and associated histograms are shown in Figure 4.21. All maps have common pixels, and share the same pixel grid (~ 90 m); positive values in the maps represent an increase in peat height whilst negative values present a decrease in peat height.

For all the three tracks, mean height change rates range from - 0.5 cm/year to 0.5 cm/year (Figure 4.21a, b, c). For Envisat track 266 (Figure 4.21a), approximately 75% of this study area is between -0.1 cm/year to 0.1 cm/year in the 5-year observation period, such as the Carn, Melgarve and B areas. In about 20% of the study area, mean height change rates are greater than -0.1 cm/year, and Glen area shows the largest rate of decrease in surface height ~ 0.3 cm/year. The uplift signals are about 0.2 cm/yr and less than 5% of the area, was similar to the magnitude of peat height change. For ALOS track 664 (Figure 4.21b), about 40% of the study area has a change rate from -0.1 cm/year to 0.1 cm/year, and the areas Melgarve and B also show a relatively small rate of change from -0.1 cm/year to 0.1 cm/year. Approximately 45% of the area shows change a rate less than -0.1 cm/year. The largest surface height change area is in Glen, which is up to -0.5 cm/year, while 15% of the rest of study area shows uplift rate ranging from 0.2 to 0.5 cm/year. These uplift signals are highly correlated with 'topographical' features on the ground, such as uplift signals in areas labeled as U1 and U2, and the reason for this is probably because of the residual topography-dependent APS effects.

For track 665 (Figure 4.21c), (i) nearly 55% of the study area changes between -0.1 cm/year to 0.1 cm/year, for example Areas B and Melgarve; (ii) around 35% area contributes surface height change rate larger than 0.1 cm/year, for example the area Glen shows the greatest surface height change signals, and the rate is up to -0.5 cm/year; (iii) about 10% of the rest area shows increases in surface height about 0.2 cm/year, such area labeled as U3, and this area is also correlated with topography and the magnitude is in a similar level to the surface height change rate. It is believed that the differences of mean velocity maps Figure 4.21a, b and c are mainly result from the residual APS noise, which introduced uncertainties in estimating the low peat height change rate.

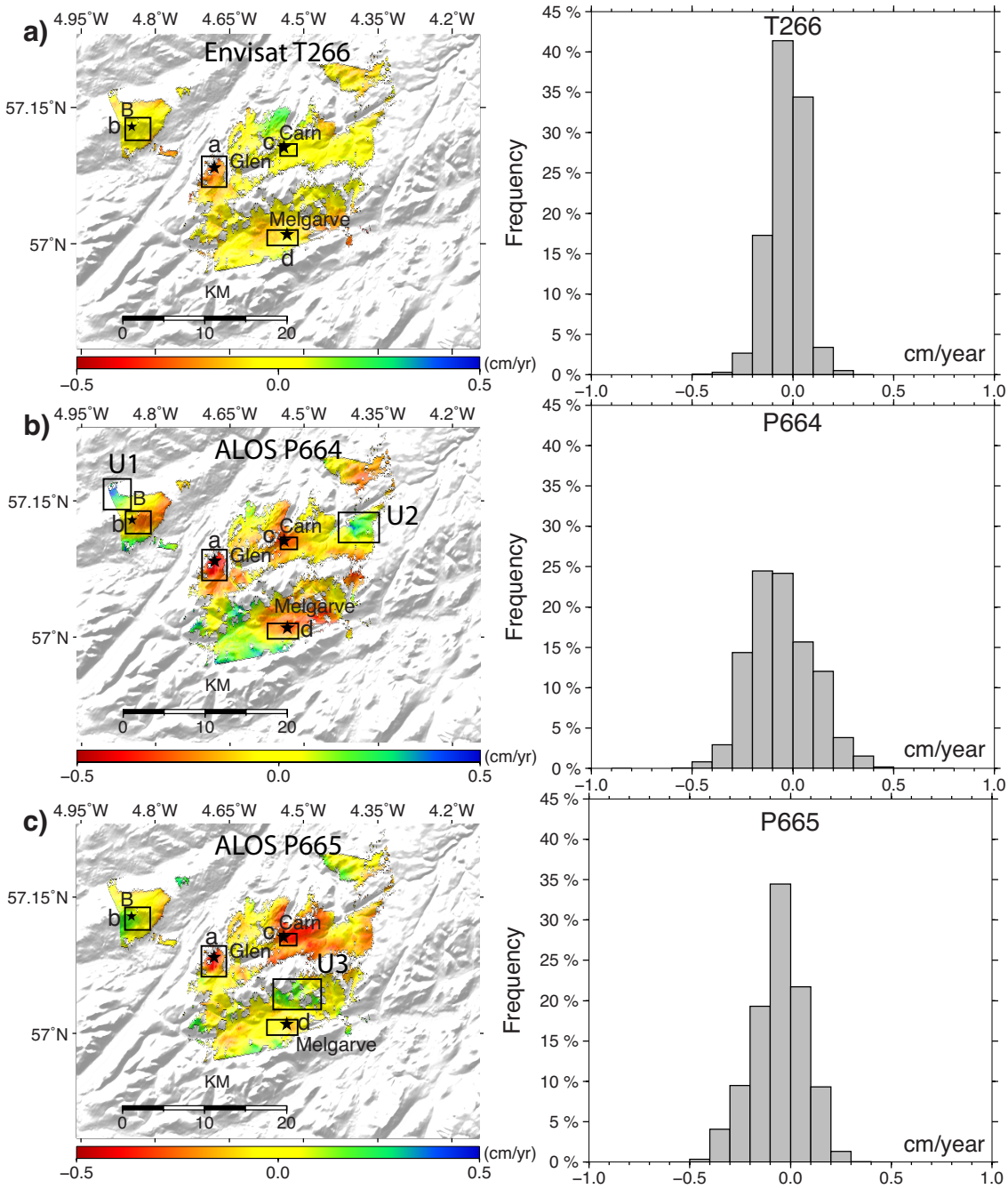

Figure 4.21 Three tracks of mean height change rate maps (in the LOS direction) and their associated histograms. Negative values mean surface height change, while positive values denote uplift. Areas Glen, B, Carn, and Melgarve are selected for correlation analysis, points a, b, c, and d are selected for time series analysis. Relatively stable signals range from -0.1 cm/yr to 0.1 cm/yr, dominating the study area. Surface height change signals are shown in Glen in all three tracks. In terms of area, uplift signals are relative less. Signals in areas labeled as U1, U2 and U3 are highly correlated with 'topographical' features on the ground.

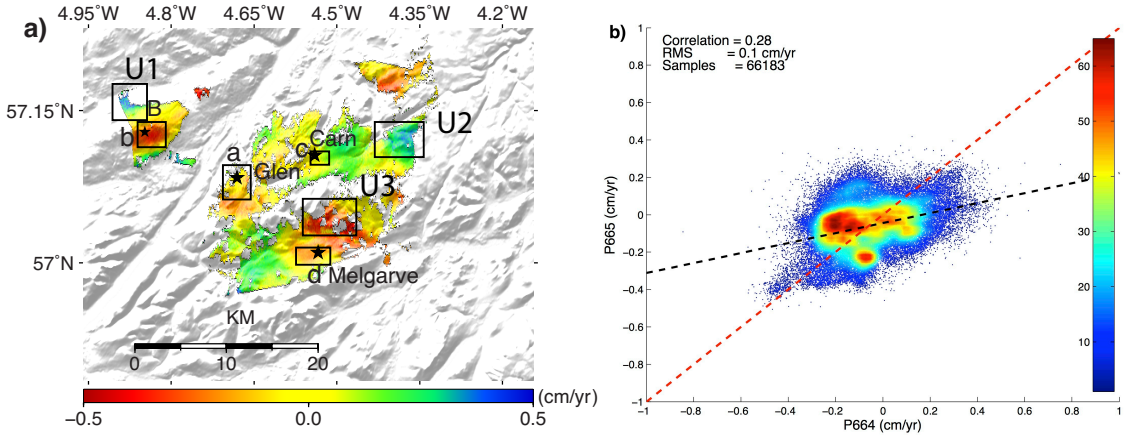

Figure 4.22 Difference map and the correlation between ALOS tracks 664 and 665. (a) The difference map of mean height change rate. (b) The correlation of the mean height change rate from the two tracks. The red line in the correlation map is the 1:1 line, and the black line the best-fit line; the color bar means the frequency of the value. LOS velocity uncertainty from near range and far range can be ignored (See Section 3.2.1). Areas labeled as U1, U2 and U3 show the largest variation, and they are highly correlated with the topography, which is likely caused by the residual topographic correlated APS effect, and the magnitude of this noise level is similar to the surface height change level.

Figure 4.22 shows the mean height change rate difference map and the correlation between ALOS tracks 664 and 665. The difference maps show large variation across the map: (1) the Glen area shows small variation; (2) in Area B the difference of mean surface height change is up to 0.5 cm/year; (3) Areas Carn and Melgarve show difference of 0.2 cm/yr in the mean height change rate. Areas labeled as U1, U2 and U3 show large variation as well, and they are clearly correlated with topography. The differences in the mean height change rates from two different tracks with a RMS of 0.1 cm/year (Figure 4.22b) are mainly due to the residual APS effects. It is clear in Figure 4.21b that the magnitude of measurement uncertainties is almost in the same level as surface movements, which explain why the overall correlation is as low as 0.28.

Figure 4.23 shows the correlation of the four areas between ALOS tracks 664 and 665. The rates of change detected from both tracks are well correlated for Area Glen (Figure 4.23a: correlation coefficient of 0.83, RMS of 0.1 cm/year), the average of the change rate is 0.3 and 0.2 cm/year for tracks 664 and 665 respectively. However there is more scatter in the data in the other three sites

(Figure 4.23b, c, d), with correlation coefficient of 0.41, 0.45 and 0.55 in Areas Carn, B and Melgarve. The Carn area has the maximum RMS of 0.2 cm/yr. The high correlation for Area Glen suggests that the results in this area are reliable and promising. The uncertainties from APS discussed above are able to explain why the correlation in Area Carn, B and Melgarve is low.

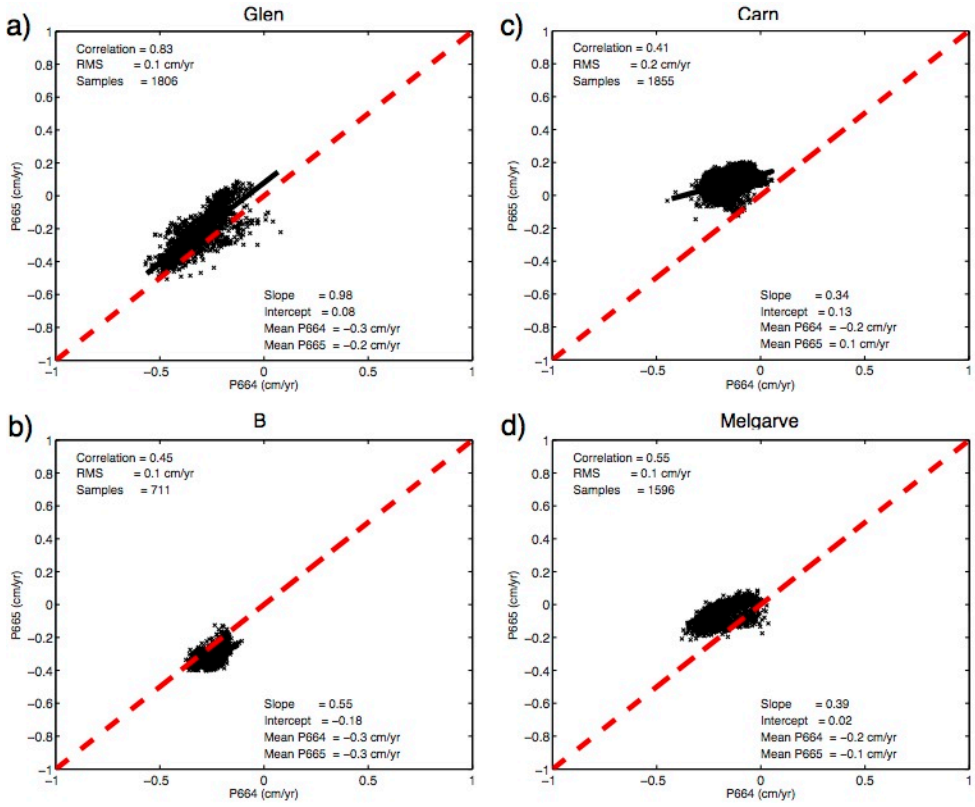

Figure 4.23 Correlation of Areas Glen, B, Carn and Melgarve between ALOS tracks 664 and 665. Black solid lines denote the linear regression, and red lines denote the 1:1 line.

Figure 4.24 shows the time series analysis of the four locations (a, b, c, d), and their associated RMS. In Area Glen (Figure 4.24a), for 9 pixels around point a, the three data tracks combined show a decrease in surface height, of about 0.9 cm from December 2002 to November 2007 for Envisat (~ 0.2 cm/year). The time series generated from ALOS tracks 664 and 665 shows about 1.2 cm decrease over the period from February 2007 to July 2010 (~ 0.4 cm/year). The same trend from Envisat and ALOS provides confidence that the trend of

decreasing surface height and the magnitude of change for Glen is likely to be representative.

For pixels around points b, c, d (Figure 4.24b, c, d), the three tracks data give different results and are not internally consistent; this is because of the limited capacity of L-band long wavelength in detecting slow deformation over a short period of time; measurement uncertainties due to residual noise may in the same level as the height change history in these three locations.

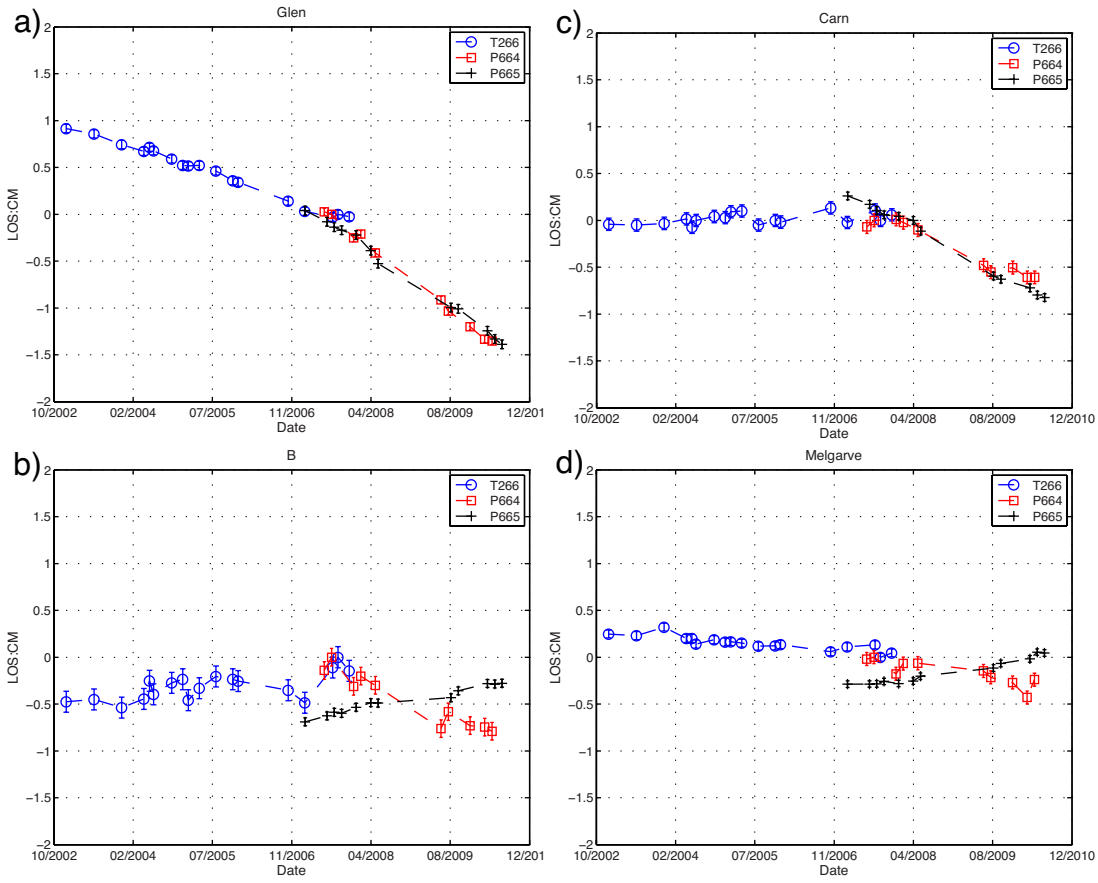

Figure 4.24 Time series of points a, b, c and d in Areas Glen, B, Carn and Melgarve respectively. Each point presents one SAR image acquisition date, the value corresponds to the average of a 3 pixels by 3 pixels window and the error bar is its associated RMS. Location a shows clear surface height change signals in three tracks, while the other three locations show variation due to residual noises. The blue color is the Envisat track 266, the red color is ALOS track 664, and the black color is ALOS track 665.

4.5 Discussion

In this chapter, Envisat C-band SAR images are used to produce the mean height change rate of peat between December 2002 and November 2007, and ALOS L-band for the period between February 2007 and July 2010; the movement history of specified locations are generated between December 2002 and July 2010. Relatively, L-band data provides larger spatial extent than C-band in vegetated peatland area, because L-band has longer wavelengths, which contribute better coherence in areas covered by vegetation than shorter wavelength due to its penetration capacity. The 66183 coherent pixels (measurements) in Figure 4.23b suggest that InSAR provides a much greater spatial extent than traditional monitoring techniques such as GPS.

4.5.1 Coherence

Generally, compared to longer wavelengths (e.g. L-band), the coherence of shorter wavelengths such as C-band, is sensitive to changes in the environment (such as wind and rain) and the growth or death of the vegetation in vegetated areas due to their penetration capacity (Smith et al., 1996; Meng and Sandwell, 2010). The study area covers different vegetation types (Figure 4.2, Figure 4.3, Figure 4.5), including forest and blanket bogs. For C-band, both Figure 4.7 and Figure 4.9 show that the woodland areas always present low coherence (< 0.2), even with short time interval (70 days) and spatial baselines (0.8 m) (coherence map: Figure 4.7a, Figure 4.9a, and Table 4.1). For L-band, the coherence in woodland areas presents higher coherence (> 0.2). This is because the short wavelength C-band radar is unable to penetrate the trees, the return signals are dominated from the top canopy of the tress and fewer signals return from the stems and the ground.

In blanket bogs areas, for C-band, with increasing time interval or spatial baseline, significant decorrelation is observed (Figure 4.7 and Figure 4.9). For L-band, the decorrelation effect is not obvious as C-band (Figure 4.8 and Figure 4.10), although the time interval is up to 30 months (Figure 4.8c) and the spatial baseline is up to 2388 m (Figure 4.10c). This is, in comparison with

C-band, radar signals from the ground soil dominate the backscatters. Note, for L-band, the changes in soil moisture, especially between the summer and winter seasons, have effects on decorrelation (Smith et al., 1996) (Figure 4.8b and Figure 4.10c).

The average coherence and percentages of low coherence (<0.2) of all the interferograms used in this analysis (Figure 4.6) are listed in Appendix 1 and Appendix 2. The decorrelation patterns in Figure 4.11 and Figure 4.12 with time and spatial baseline of C-band and L-band suggest:

(1) compared to spatial decorrelation, temporal decorrelation is the main source of losing coherence for C-band in the blanket bogs areas, most likely because of the environmental parameters change (rain, wind, etc.) and the growth or die of the vegetation;

(2) for C-band, interferograms generated by SAR images acquired within 6 months interval provides good coherence, while the time interval between 6 months and 18 month provides reasonable coherence, and the coherence is poor when the temporal baseline is larger than 18 months;

(3) for L-band, no significant decorrelation is observed with increasing temporal (up to 36 months) and spatial baselines (up to 2388 m). Therefore, in blanket bogs areas, to generate interferograms for InSAR analysis, shorter temporal and spatial baselines are required for C-band, compared to L-band.

4.5.2 Accuracy and uncertainty

As ground data to quantify accuracy is not available, I am using the RMS of two independent adjacent tracks 664 and 665 to assess the accuracy of the InSAR results in this study. Figure 4.22b shows the RMS of the measurements for ALOS L-band is 0.1 cm/yr, and I suggest the value approximate represents the margins of accuracy for Envisat C-band measurements in this study. Due to the low rate change and the large uncertainty from other noise, such as the influence of atmospheric interference, the residual noise level is of the same level

as real surface change signals. This residual noise level can explain correlation of overall mean height change rate between the two ALOS tracks of 0.28.

The uncertainty or residual noise in ALOS results mainly arises from the residual APS, and C-band shows relatively less residual noise. I use the TLV model (Li et al., 2009a) to remove the APS effect, which can remove most of APS effects, as evidenced by Figure 4.20. More recently, there have been several new advanced methods developed to remove such topography correlated APS effects (Samsonov, 2010; Shirzaei and Bürgmann, 2012), and this is worth trying in the future.

4.5.3 Validation

No ground truth data is available to quantitatively evaluate InSAR results in this study. Fortunately, two adjacent tracks of ALOS images with an overlapping area over the same observation period can be compared with each other so as to assess the accuracy of InSAR results.

For InSAR results, in Glen Area, the mean change rate maps from the three tracks data show that stable signals (within a sigma of +/- 0.1 cm/yr) dominate this study area. In the main subsiding area Glen, the mean height change rate results appear promising (Figure 4.23a, with a correlation coefficient of 0.83 and an RMS of 0.1 cm). In the Glen area, the height change time series (Figure 4.24a) of all the three tracks are internally consistent and indicate a loss in surface height. Combing the mean change rate map and time series of Glen suggests that InSAR results in the Glen area are reliable.

In Carn, B and Melgarve Area, the low correlations (Figure 4.23b, c, and d) and internally inconsistent time series (Figure 4.24b, c and d) of these areas show the InSAR results are noisy. The likely reason is the uncertainty from residual APS, which is in the same level of real peat height change signals. For InSAR, this causes difficulty in separating the real peat height change rate and history from noise. Long-term SAR observations have potential to separate this ambiguity, because the longer time observations, the greater magnitude of accumulated peat height change for such low rate change. Peat height change

signals in Glen Area are detected because they are higher than noise and successfully separated.

4.5.4 Limitations

Compared to surface height mapping with GPS, InSAR provides greater spatial extent in monitoring surface height changes, whilst keeping good precision. Further it is more economical than LiDAR. However, InSAR has its disadvantages: long-term SAR observation is required to separate displacement signals from noises.

The soon-to-be-launched Sentinel-1 (C-band) (Ramon et al., 2012) and ALOS-2 (L-band) (Suzuki et al., 2011), have the potential to provide continuous observations over the upland peatland. Because Sentinel-1 has shorter temporal resolution (6-12 days for Sentinel-1 vs 35 days for Envisat/ERS) and higher spatial resolution (5m for Sentinel-1 vs 20m for Envisat/ERS), which offers better coherence over the uplands.

4.5.5 Erosion extent and severity

By assessing the peat height change, peatland erosion extent and severity can be mapped (Evans and Lindsay, 2010b; Evans and Lindsay, 2010a) and that is what has been done here. In section 4.5.3 Validation, the Glen area shows a significant subsidence rate, while low change rates (+/- 0.1 cm/yr) dominate in the other areas (e.g. Carn, Melgarve). Therefore, it is likely that the Glen area has the most severe erosion and the other areas are very probably stable. As a result any estimates of carbon loss are based on the Glen area. As discussed in section 2.2.2 Carbon loss from upland eroding, peatland erosion causes direct loss of POC and the POC loss can be estimated using the InSAR-derived peat height change rate data. Carbon loss estimation is calculated using equation 2.6. A typical carbon content of 50%, and bulk density of 0.1 g/cm^3 is applied in this study (Billett et al., 2010).

Table 4.5 POC Carbon loss from the Glen area

Study area	Glen
Number of pixels	1806
Area (ha)	1462.86
Mean Velocity (cm/yr)	0.25
Peat volume (Mt/yr)	3692.7
C loss (t/yr)	1846.35
CO_2 loss (t/yr)	6769.95
Annual C loss (t/ha/yr)	1.26
Annual CO_2 loss (t/ha/yr, 100% oxidation)	4.62

The results in **Table 4.5** suggest that the average annual C loss rate from 2007 to 2010 is 1.26 t/ha/yr (126 $gC/m^2/yr$) in the Glen area, and the CO_2 emission rate can be up to 4.62 t/ha/yr if all the peat carbon is oxidized. The POC flux rateis higher than the POC flux rate of 79 $gC/m^2/yr$ from heavily eroding systems (Pawson et al., 2008). If a typical carbon sequestration value of 50 $gC/m^2/yr$ is considered (Worrall et al., 2003), a net carbon sink of 76 $gC/m^2/yr$ can be estimated for the Glen area suggesting that the Glen area is relatively heavily eroded.

4.6 Conclusions

In this chapter, 18 SAR image from Envisat track 266, and 21 SAR images from ALOS tracks 664 and 665 have been used to produce the mean height change rate map and time series over Monadliath Montains, Scotland. InSAR results show that both Envisat C-band and ALOS L-band have the capability to monitoring changes in peat height over a long time, accommodating the low rate change over peatland height change. Over vegetated areas, ALOS L-band data provides better coherence and is more feasible to map wider spatial extent than C-band. In the case of low rate change signals, it is difficult to separate out reliable peat height change signals because the magnitude of the displacement signals is almost the same level as noise in the system. It is believed that an increased number of SAR images may make this possible, but over a longer timescale than more frequently as the latter is confounded by environmental conditions such as snow cover. Based on the mean peat height change rate in the Glen area, a POC flux rate of 1.26 t/ha/yr is estimated.

This result suggests that the Glen area is a heavily eroding area, while the other areas are relatively stable.

Chapter 5 Subsidence and carbon loss in drainage tropical peatland using InSAR time series - A case study of Sumatra, Indonesia

Abstract: In this chapter, InSAR time series of two adjacent tracks of L-band ALOS PALSAR data are used to map the spatiotemporal land surface height change of Jambi, Sumatra, Indonesia. Two independent ALOS L-band tracks SAR images acquired from July 2007 to January 2011 are used in this study, which provides confidence of the results without the ground data for validation. The results show that: 1) the subsidence rate is up to 5 cm/year in drainage plantation area; 2) the different drainage areas show different subsidence rate due to drainage ages; 3) The largest subsidence area shows about 15 cm total amount of decrease in peat height within the observed time; 4) Based on the subsidence rate data, CO_2 emission rate of 21.41~26.26 t/ha/yr in this region is estimated. Combining these suggest that InSAR time series can monitor long-term peatland height change trends, which is useful for C loss estimation in this region.

5.1 Introduction

In this study, InSAR time series are used to assess the if there is subsidence in areas of tropical peatland converted to other crops (mainly palm oil), and if so to quantify the amount and contextualize this as a loss of C. Our main objectives are to: 1) provide the mean change rate map of peat subsidence within the study area and peat height changes over time; 2) estimate the carbon loss from peat oxidation based on drainage peat features in observation time.

5.2 Study area

The study area is located in the eastern part of Jambi Province, central Sumatran peninsula, Indonesia (Figure 5.1).

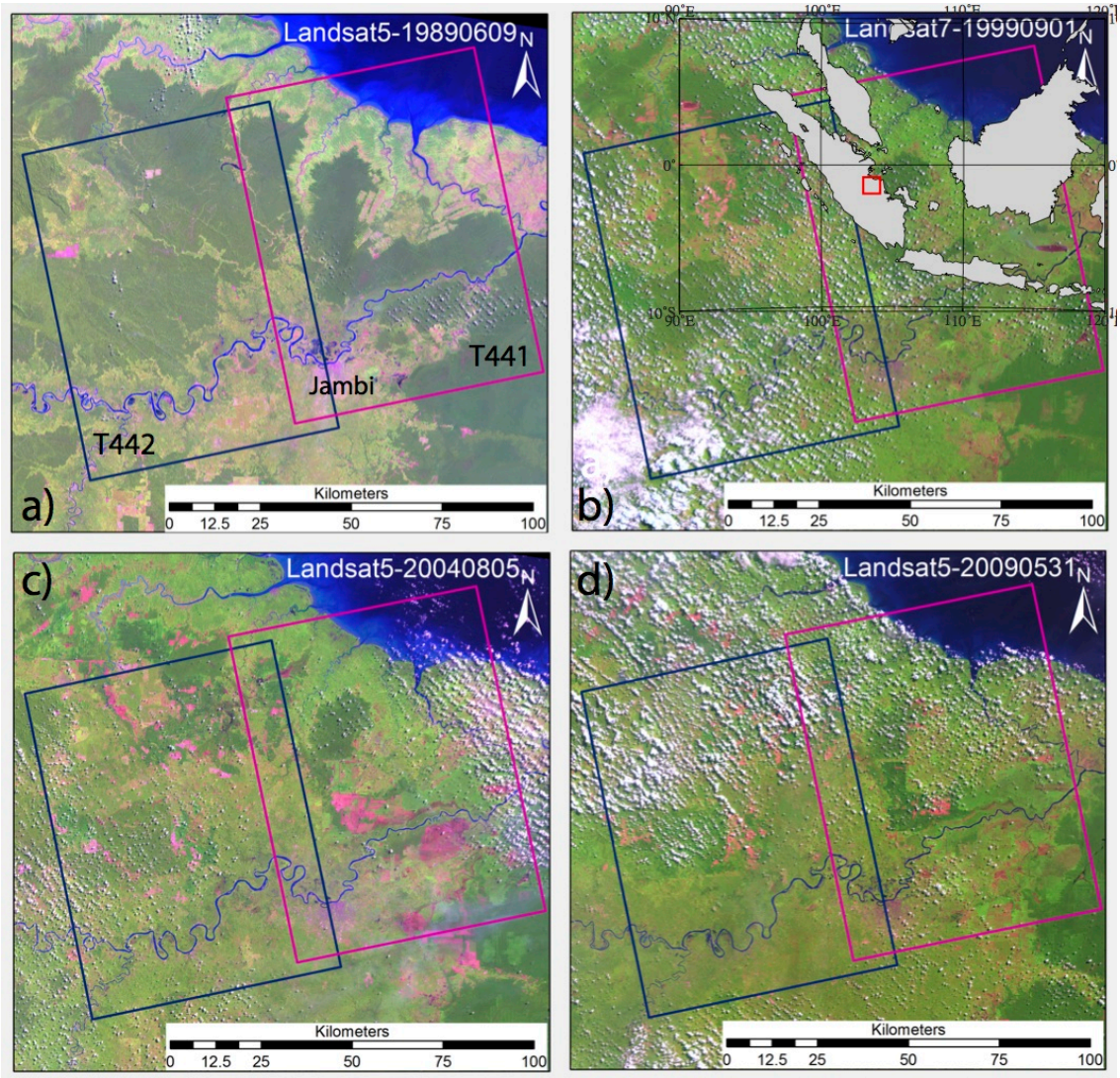

Figure 5.1 Longing and plantation concession development between 1989 and 2009 in study area (red square area of the top left figure). The background image is Landsat 5 and 7 (USGS, 2013). The RGB Landsat images are stacked with Bands 5, 4 and 3; peat swamp forest is shown in green. a, c and d) Landsat 5 image collected on 19890609, 20040805 and 20090531 respectively); b) Landsat 7 images acquired on 19990901. Note: the blue and red squares are SAR data coverage. The northeast and south part of the study area was deforested before 1989 (a), and since then till 20090503 almost the whole study area were logged. Purple color areas represent new developed areas.

Topographic height ranges from 0 to 200 m above sea level. The entire region is typically hot and humid; the monthly average of daily maximum and minimum temperature is ~ 32 ºC and ~ 23 ºC respectively (source data 1989-1997) (Miettinen et al., 2011b). It has yearly wet and dry seasons, which last from October to April and from May to September respectively; the average monthly precipitation in the rainy season (270 mm) is about 2.5 times of that in the dry season (114 mm) (Shigehiro et al., 2005) and the average annual rainfall is approximately 2,500 mm (source data 1951-1997) (Siderius, 2004). According to the latest peatland distribution and carbon content map for Sumatra (released in 2002), the study area is largely covered with peat soils ranging from 0.5 m to over 4 m in depth (Wahyunto and Suryadiputra, 2008; UK, 2013). In the study area, large areas were designated to logging and plantation concessions by the Ministry of Forestry and Estate Crops (MOFEC), and a smaller extent has been logged by smallholders since the mid-1980s (Figure 5.1) (Stolle et al., 2003; Beukema and Noordwijk, 2004).

The rapid changes over this region result in diverse land covers and land uses (industrial forest plantation, national parks, and oil palms plantation, etc.). A land cover map (Figure 5.2) has been created using data released by the Ministry of Forestry of Indonesia in 2009 (Kementerian Kehutanan Republik Indonesia, 2012). The original land cover map has 18 types of land use, but only 11 of them are used and re-produced in this study; those excluded do not exist in this study area. This study focuses on areas of plantation (oil palm plantation), industrial forest plantation (such as pulp, timber), shrub, swamp shrub, and cleared (deforested). Intensive and long-term drainage has been conducted in the above land use areas, which cause decreasing peatland surface height due to the peat soil oxidation.

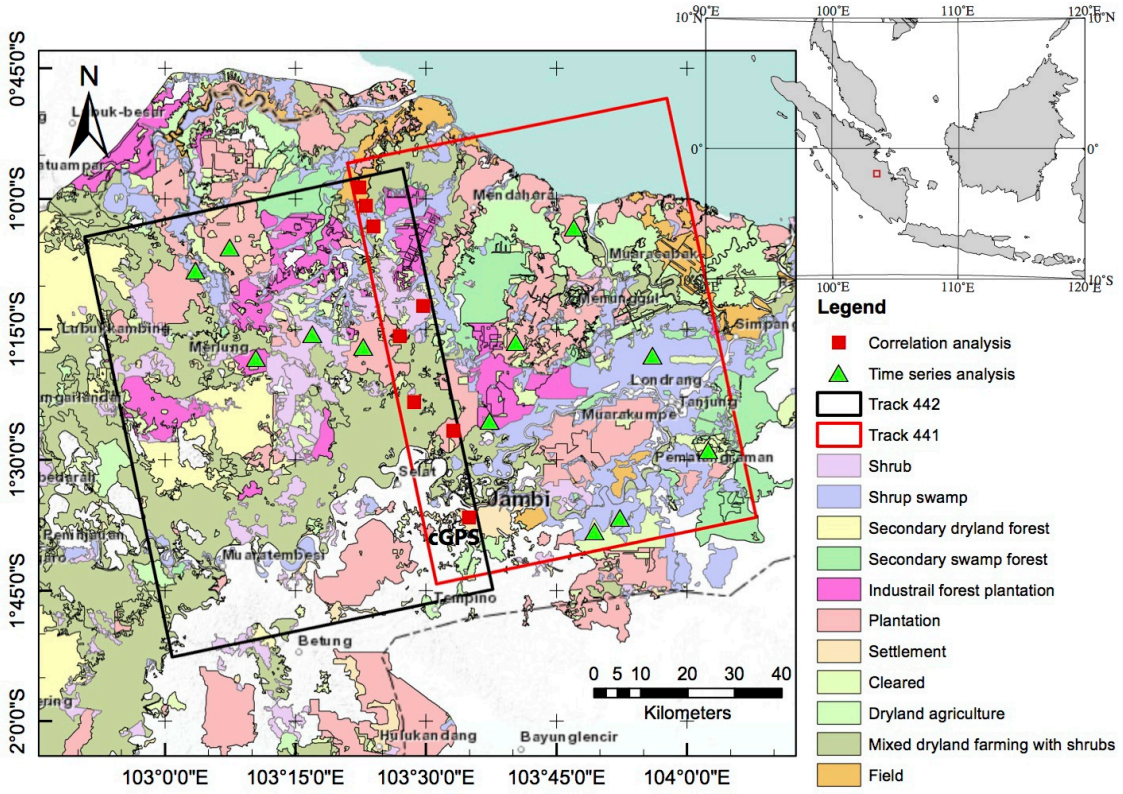

Figure 5.2 The landscape of the study area (red square area of the top right figure). There are eleven land covers on a shaded terrain in this area (Kementerian Kehutanan Republik Indonesia, 2012). Two adjacent PALSAR tracks 441 and 442 cover this study area, and overlap. Eight points in the overlap area (red squares) are randomly selected for correlation and time series analysis. Another 12 points (denoted by green triangles) in specifically interested area are randomly chosen for time series analysis only. The cGPS site is the reference site discussed in the next section.

5.3 ALOS data processing

Two adjacent tracks (T441 and T442) of ALOS PALSAR images are ultilized to produce interferograms - if both tracks present consistent height change patterns over the same observation period then there is greater confidence the observations are representative of the local site. A continous GPS station (cGPS) (E103.52033°, S-1.61564°) (Caltech Tectonics Observatory, 2013), is located in the overlap area of the two adjacent SAR tracks, and 4-year GPS data suggests that the surface of GPS station is stable during the period

between 2005 and 2009; therefore this cGPS station is chosen as a reference site for the InSAR deformation and time series outputs (Figure 5.2).

The temporal and spatial baseline of available images for each track are shown in Table 5.1 and Figure 5.2. Track 441 includes 15 images acquired from 25th November 2007 to 18th January 2011. Track 442 includes 16 images collected from 27th July 2007 to 19th September 2010.

Table 5.1 ALOS images from Tracks 441 and 442 used in this study. Image date is given as Year-Month-Day (YYYYMMDD) format, and as the number of days since the first image of each track. Perpendicular baselines for Tracks 441 and 442 are relative to 20110118 and 20070727 respectively. These reference dates were chosen because of limited atmospheric effects on these corresponding SAR images assessed by checking all interferograms involved SAR images acquired on these dates.

T441				T442			
Image Number	Date(YYYYMMDD)	Number of days	Baseline (m)	Image Number	Date(YYYYMMDD)	Number of days	Baseline (m)
1	20071125	0	331.1	1	20070727	0	0.0
2	20080110	46	287.4	2	20070911	46	18.9
3	20080712	230	189.8	3	20071027	92	204.0
4	20080827	276	-120.9	4	20080127	184	-128.5
5	20081012	322	621.7	5	20080729	368	-240.2
6	20081127	368	648.7	6	20080913	414	282.4
7	20090715	598	741.8	7	20081214	506	217.1
8	20090830	644	862.0	8	20090129	552	89.4
9	20091015	690	658.3	9	20090616	690	12.3
10	20100115	782	357.7	10	20090801	736	-470.5
11	20100718	966	262.6	11	20090916	782	-279.3
12	20100902	1012	378.1	12	20091217	874	-65.8
13	20101018	1058	199.7	13	20100201	920	27.4
14	20101203	1104	-46.6	14	20100619	1058	-174.4
15	20110118	1150	0.0	15	20100804	1104	-61.6
				16	20100919	1150	-375.6

From these 15 and 16 PALSAR images within tracks 441 and 442, 34 and 35 interconnected interferograms are generated respectively (Figure 5.3). These interferograms show high coherence and they are free of obvious ionospheric artifacts (Gray et al., 2000). Finally all the deformation rate maps and time series were geocoded into a 60-m spacing geographic grid.

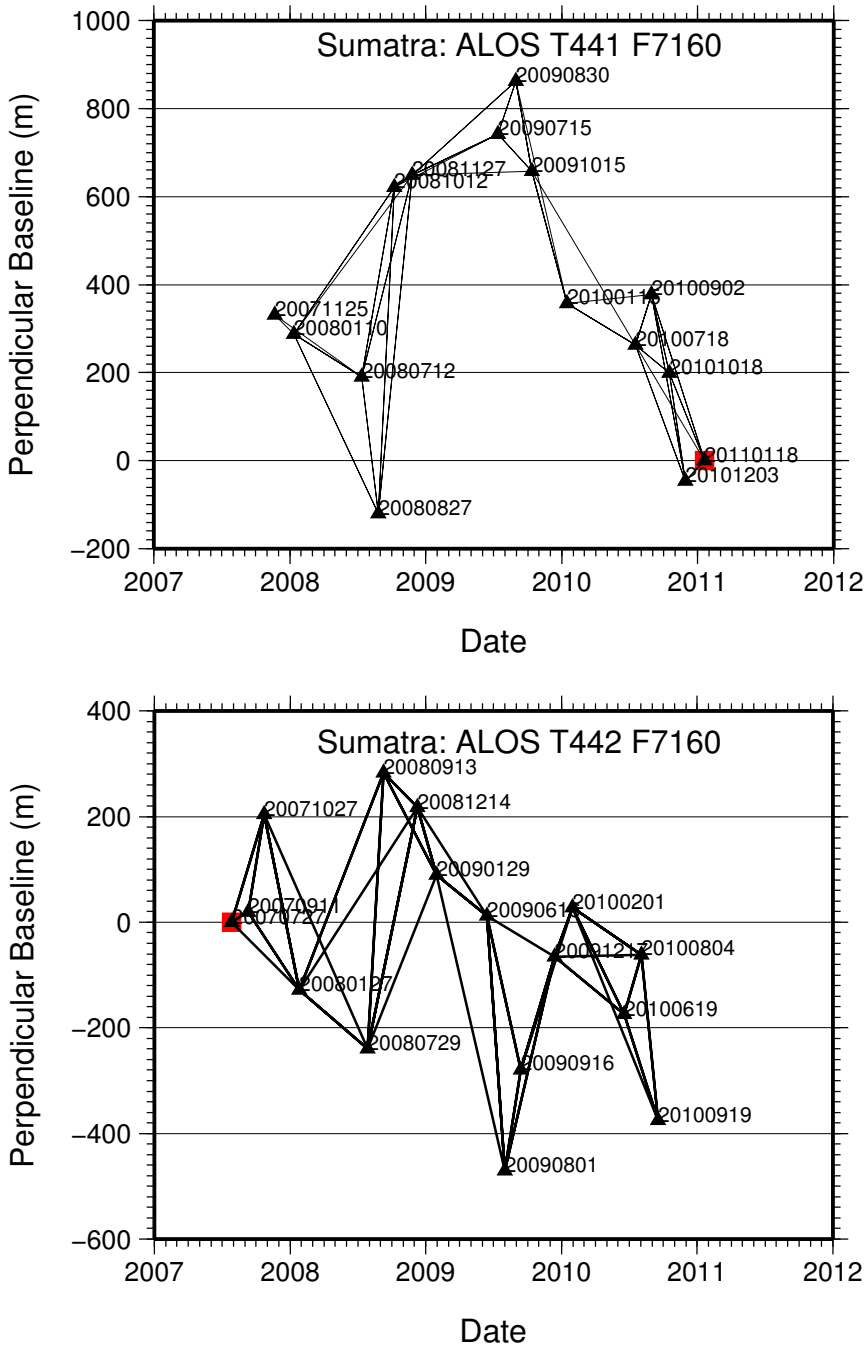

Figure 5.3 SBAS network for ALOS PALSAR Tracks 441 and 442. Each black triangle denotes one SAR image, and the black solid line between two black triangles represents one interferogram. The black square marks the reference date for the TS.

Table 5.2 Location and landscape type of points selected in this study

Points	Longitude (degrees)	Latitude (degrees)	Landscape type
O1	103.373	-0.978	Field
O2	103.386	-1.013	Mixed dryland farming with shrubs
O3	103.400	-1.052	Swamp shrub
O4	103.450	-1.263	Oil palm plantation
O5	103.495	-1.204	Shrub
O6	103.478	-1.389	Mixed dryland framing with shrubs
O7	103.554	-1.443	Oil palm plantation
O8	103.583	-1.609	Settlement (Jambi city)
C1	103.824	-1.637	Cleared
C2	104.042	-1.481	Cleared
SS1	103.873	-1.611	Swamp shrub
SS2	103.936	-1.300	Swamp shrub
SS3	103.059	-1.137	Swamp shrub
S1	103.284	-1.259	Shrub
HTI1	103.622	-1.424	Industrial forest plantation
HTI2	103.176	-1.304	Industrial forest plantation
P1	103.785	-1.055	Oil palm plantation
P2	103.674	-1.274	Oil palm plantation
P3	103.381	-1.284	Oil palm plantation
P4	103.124	-1.092	Oil palm plantation

After the mean height change rate maps are generated independently from the two adjacent tracks, the overlap area between them is used to validate InSAR results with correlation analysis. To moderate the orbit error between the two deformation rate maps, a best-fitted plane of the difference of them is removed before the correlation analysis. Eight points within the overlap area (from O1 to O8) were chosen for further time series analysis. Twelve points distributed in various landscapes are selected for investigating their movement histories and change rates. The time series of these twenty points are constructed using an

area of 3x3 pixels (corresponding to 180x180 m on the ground) with corresponding RMS values. The details of the twenty points are listed in Table 5.2.

5.3.1 Interferograms

Due to the high density of vegetation, forest, argicultural activities and flooding events, surface variations from time to time in SAR images are expected in this area, which can easily cause loss of coherence (Zebker and Villasenor, 1992). To address such temporal decorrelation problems, a shorter temporal baseline is sought during the interferogram generation. The longest temporal baseline for the interferogram generation is limited to one year in this study. Figure 5.4 shows an example of unwrapped phase. By checking Figure 5.1 and Figure 5.2 visually, decorrelation patterns over the dense forest or low land are apparent.

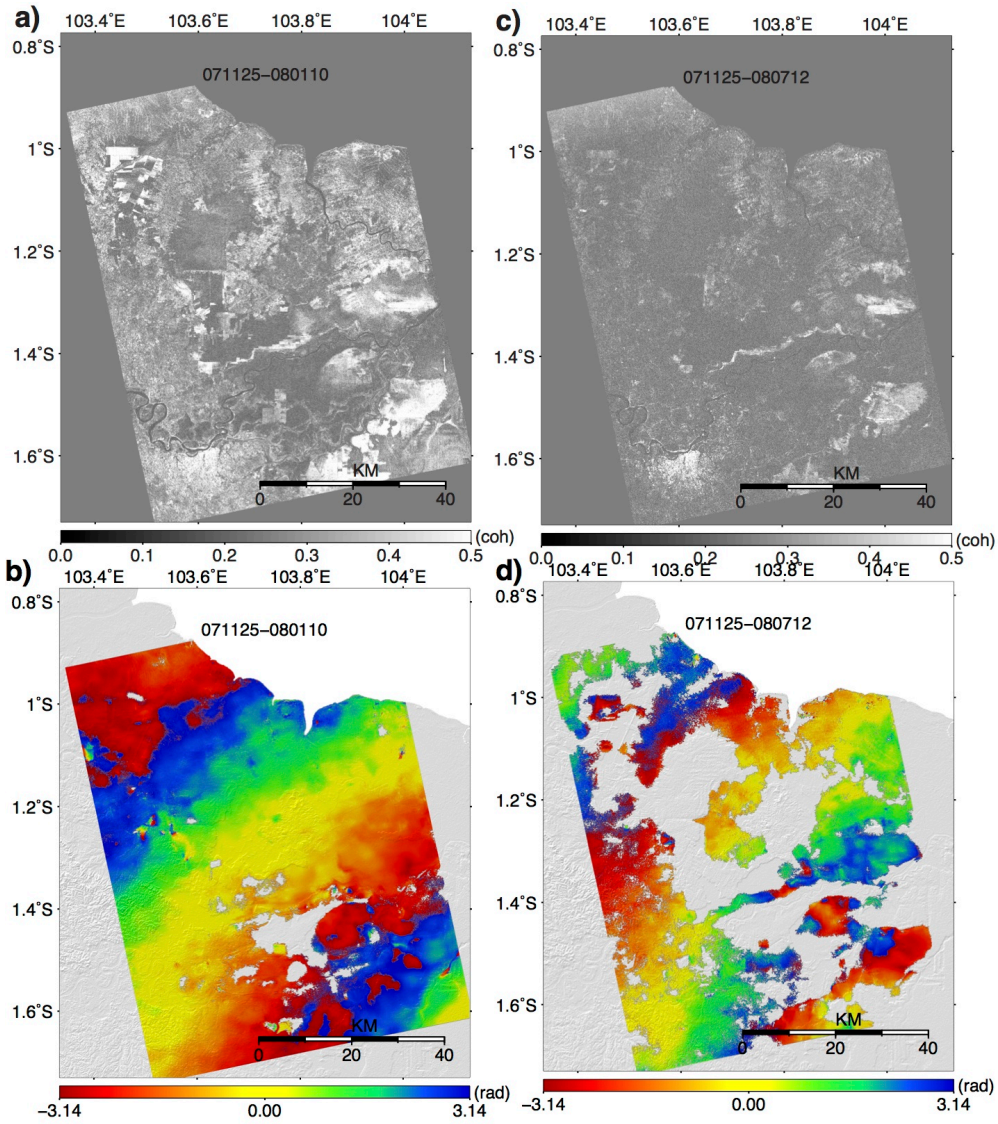

Figure 5.4 Rewrapped phase superimposed on an SRTM DEM shown as shaded relief. (a) coherence map 20071125-20080110 (46 days apart); (b) unwrapped interferogram 20071125-20080110; (c) coherence map 20071125-20080712 230 days apart); (d) unwrapped interferogram 20071125-20080712. Coherence value with lower 0.2 is not unwrapped. With a longer temporal baseline, there is less coherence in the 071125-080712 interferogram. The phases are rewrapped so that each 2π color cycle from blue to red represents an increase of 11.8 cm in the radar line of sight.

5.3.2 Phase unwrapping error

Phase unwrapping error is checked using the phase closure technique, see Section 3.2.4 Phase unwrapping. Figure 5.5 and Figure 5.6 shows phase closure results form two tracks. In Figure 5.5, it shows a closure loop example from

track 441 (a, b, c), and 4π phase jumps can be identified in the residual (d). To find out which is the wrong unwrapped interferogram, each one should be investigated. By checking the phase of each interferogram visually, 4π phase jumps can be identified in interferogram a, since the phase value of W area jumps 4π comparing the other phase of the area. In this case, we subtract 4π from W (e), the closure residual (f) shows a relatively successful phase unwrapping map. Because there is still unwrapping error labeled as R. As area R is a small area and from one or more unwrapped phase, it is uncorrected in this study.

Figure 5.6 shows a closure loop from track 442 (a, b, c); the phase unwrapping error can be identified in the residual (d), and labeled as R. Because it is a small area and comes from one or more unwrapped phase, it is uncorrected.

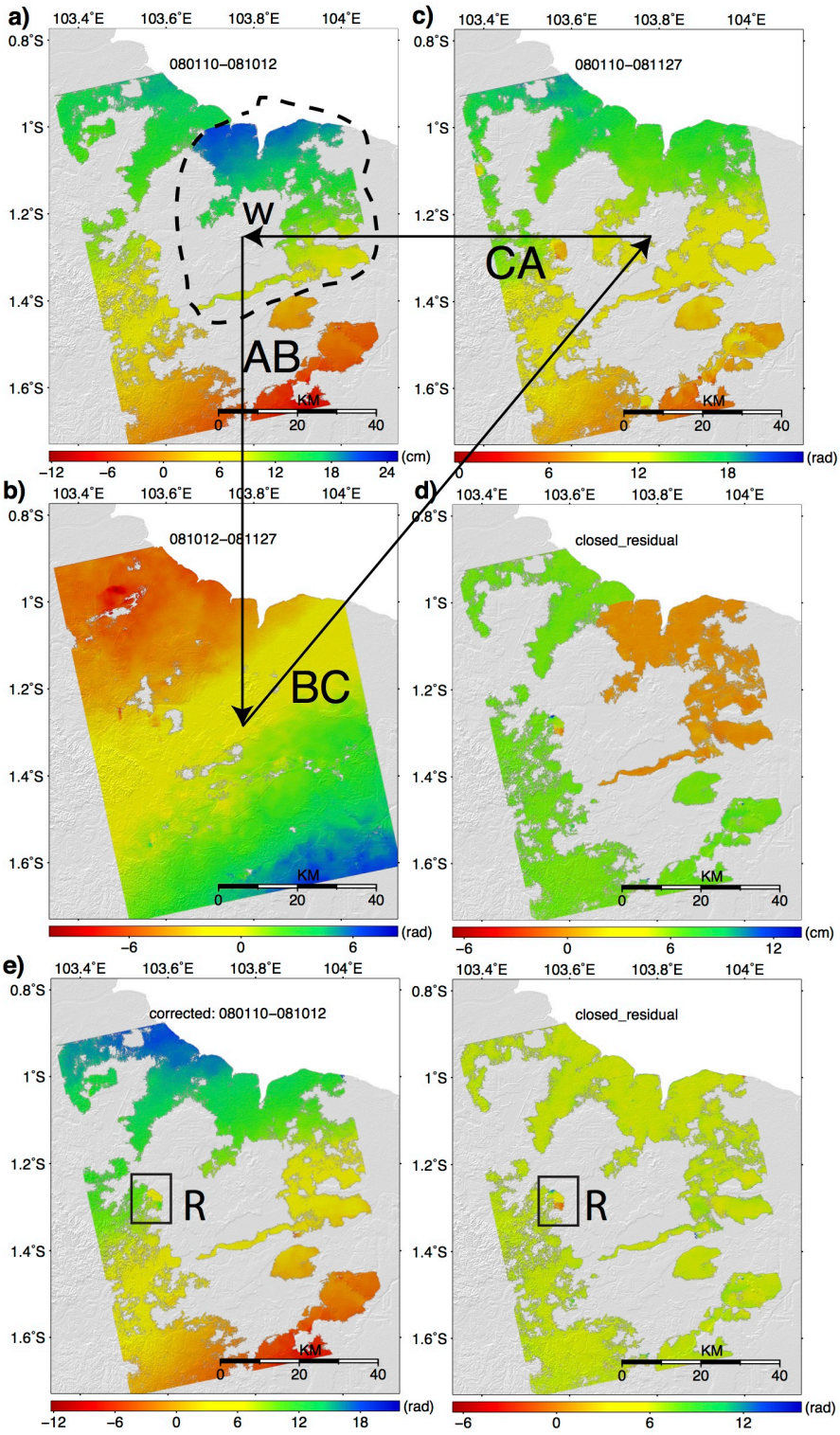

Figure 5.5 Phase closure and unwrapping error from track 441. Unwrapped phases are from interferograms of a (AB: 090110-081012), b (BC: 081012-081127) and c (AC: 080110-081127). Unwrapping errors can be identified by checking the closed residual (d). Phase jumps are shown in d, which could be contributed from one or more interferograms. In this case, the phase jump area labeled as W is from interferogram a, since the phase value of W area jumped 4π in W area comparing the phase values in its surrounding area. After correction (e), there is still phase jump in the residual (f) label as R, and uncorrected.

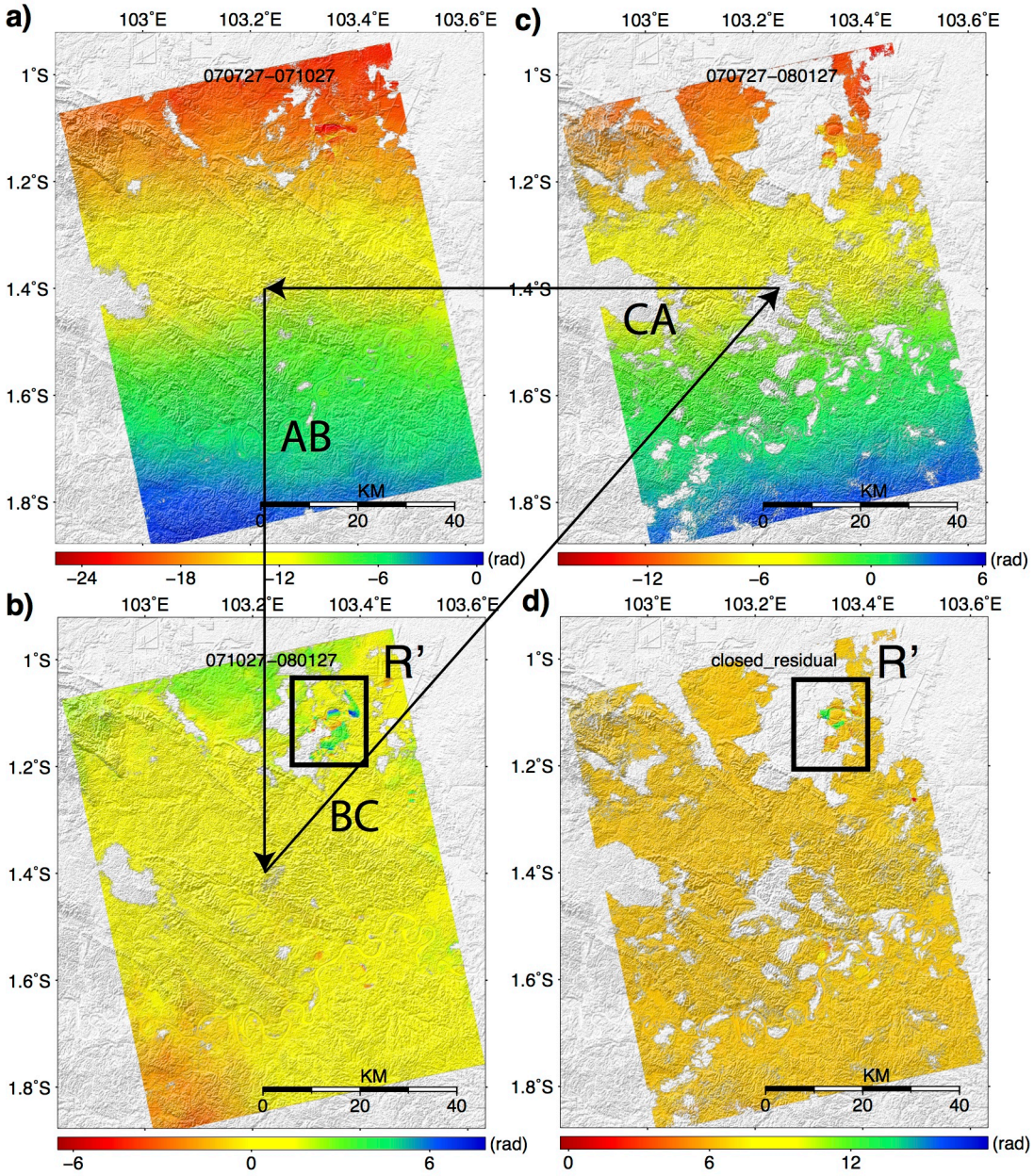

Figure 5.6 Phase closure and unwrapping error from track 442. Unwrapped phases are from interferograms of a (AB: 070727-071027), b (BC: 071027-080127) and c (AC: 070727-080127). Unwrapping errors can be identified by checking the closed residual (d) visually. Phase jumps are shown in d, which are contributed from one or more interferograms. In this case, the phase jump area is from interferogram b labeled as R' by checking visually, which is uncorrected.

5.4 Results

5.4.1 Peat subsidence

The LOS average velocity maps and their RMS maps are shown in Figure 5.7. The mean velocity has been draped on SRTM DEM.

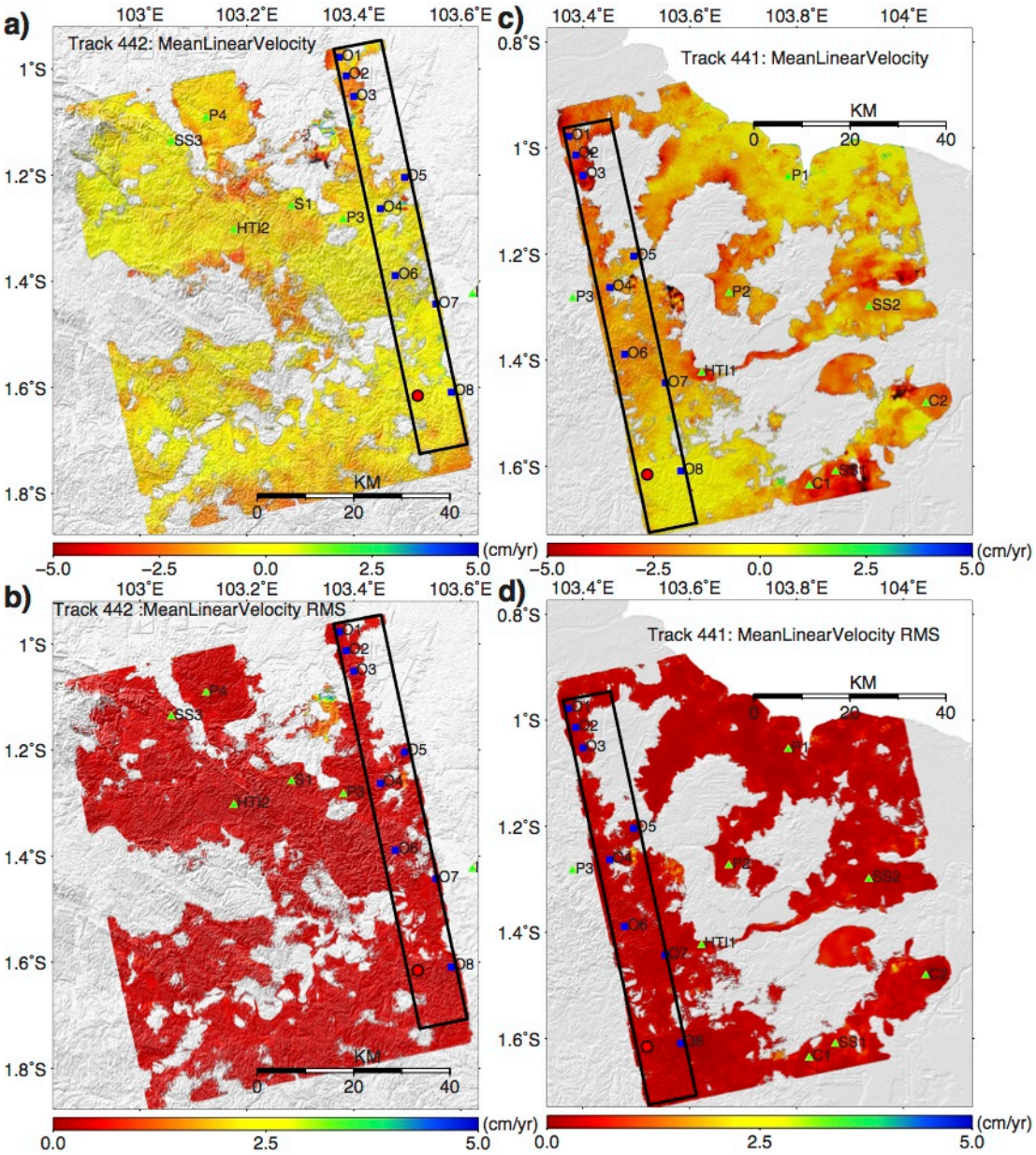

Figure 5.7 SBAS-derived LOS means peat height change rate maps for the study area and its RMS maps, superimposed on an SRTM DEM shown as shaded relief. (a) Mean velocity map from track 442; (b) Mean velocity RMS from track 442; (c) Mean velocity map from track 441; (d) Mean velocity RMS from track 441. Negative values means the surface moves away the satellite (i.e. decrease in topographic height). The black rectangle area is the overlap between the two tracks, and all points of this area are selected for correlation analysis. High subsidence rate areas (red) can be identified in new-developed area by cross-reference to the optical images (Table 5.1).

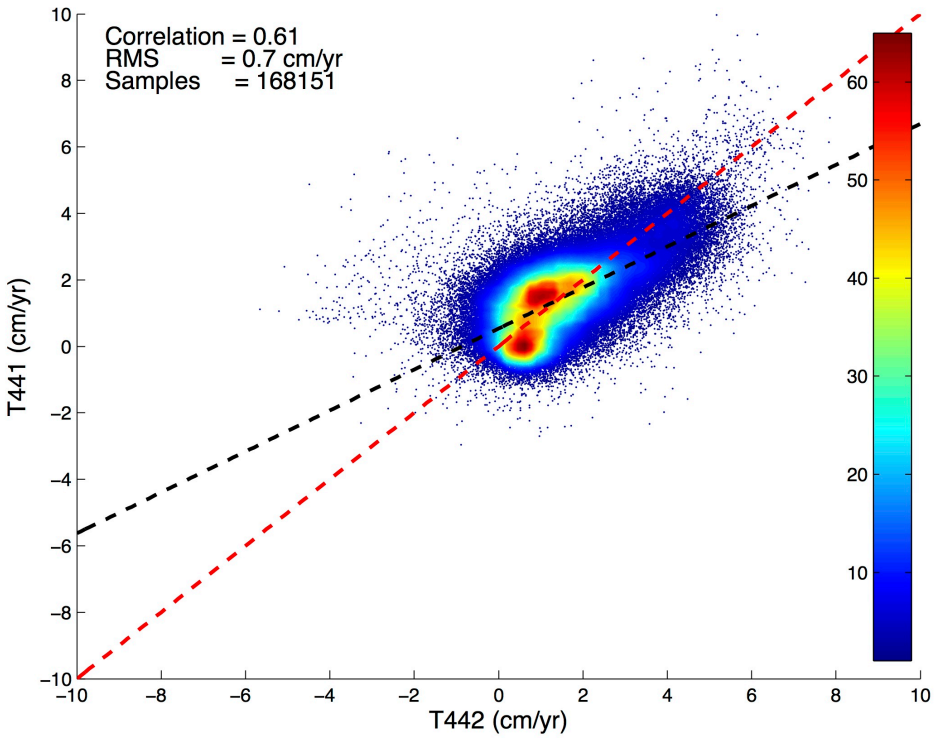

Figure 5.8 Correlation of mean velocities between tracks 441 and 442 within the overlap area. Red line is the 1:1 line, and the black the best-fit line. The colourbar from blue to red indicates the density of the points. LOS velocity uncertainty from near range and far range can be ignored (See Section 3.2.1).

There is a good correlation of the overlap area between tracks 441 and 442 (Figure 5.8) and, the estimated root mean square (RMS) error is 0.7 cm/yr. This provides confidence that InSAR can be utilized to map the change in land surface height. The estimated LOS displacement time series (Figure 5.9) have been constructed for eight randomly selected points (whose locations are shown in Figure 5.7) for each track. The mean velocities and their associated RMS are given in Table 5.3.

There is good agreement between both tracks for each location, except for O3, O4 (Figure 5.9b) and O6 (Figure 5.9c) where the individual track time series have similar trends but different gradients. This can probably be attributed to the limited valid observations (i.e. coherent measurements) used in estimation of displacement time series and their rates over these sites, such that slight variations occur to the velocities and displacement histories from different tracks.

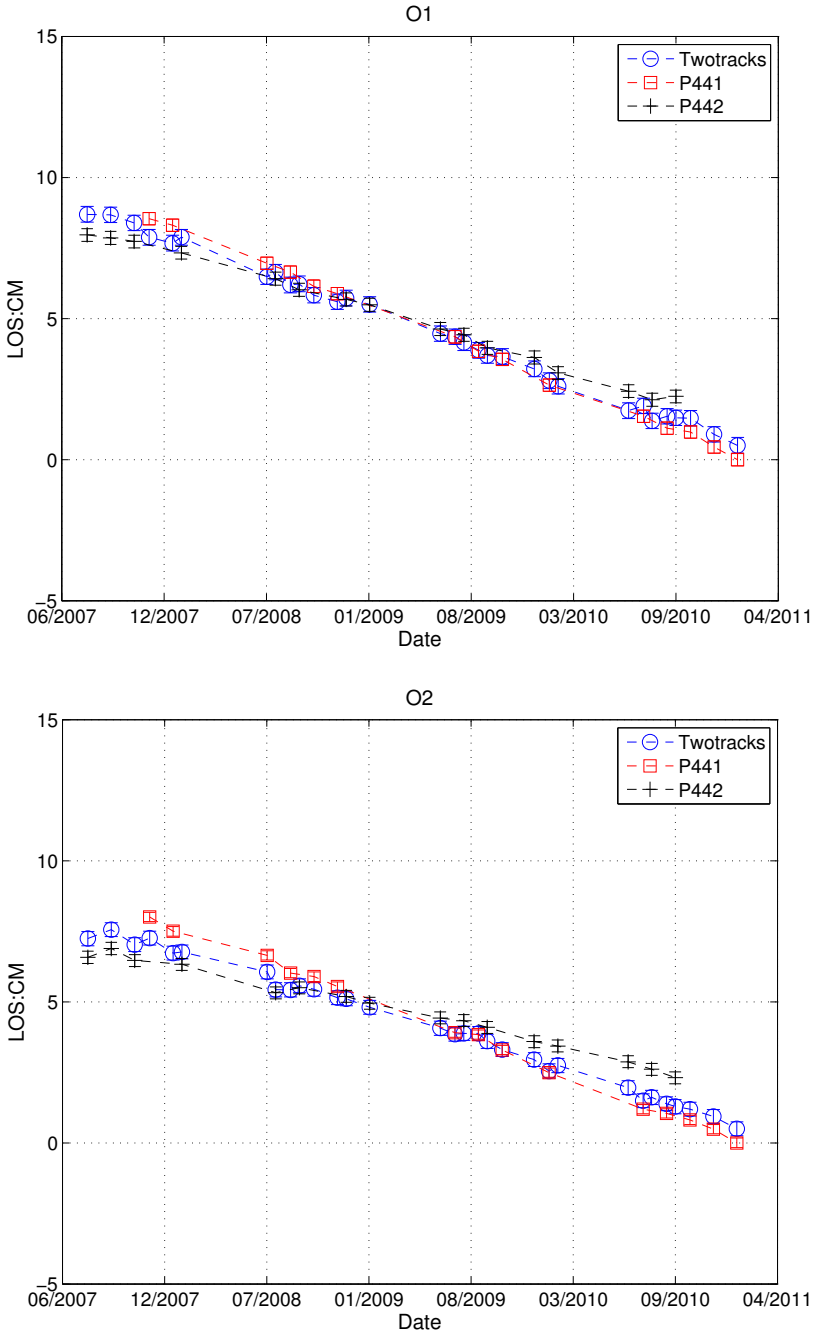

Figure 5.9a Time series of the O1 (up) to O2 (bottom) selected within the overlap area. The red squares represent time series from track 441, the black crosses represent those from track 442 and the blue circles represent those from both tracks. Each point represents one SAR image acquisition date, the reference date is 18 January 2011, the value corresponds to the average of a 3 pixels by 3 pixels window and the error-bar is the associated RMS.

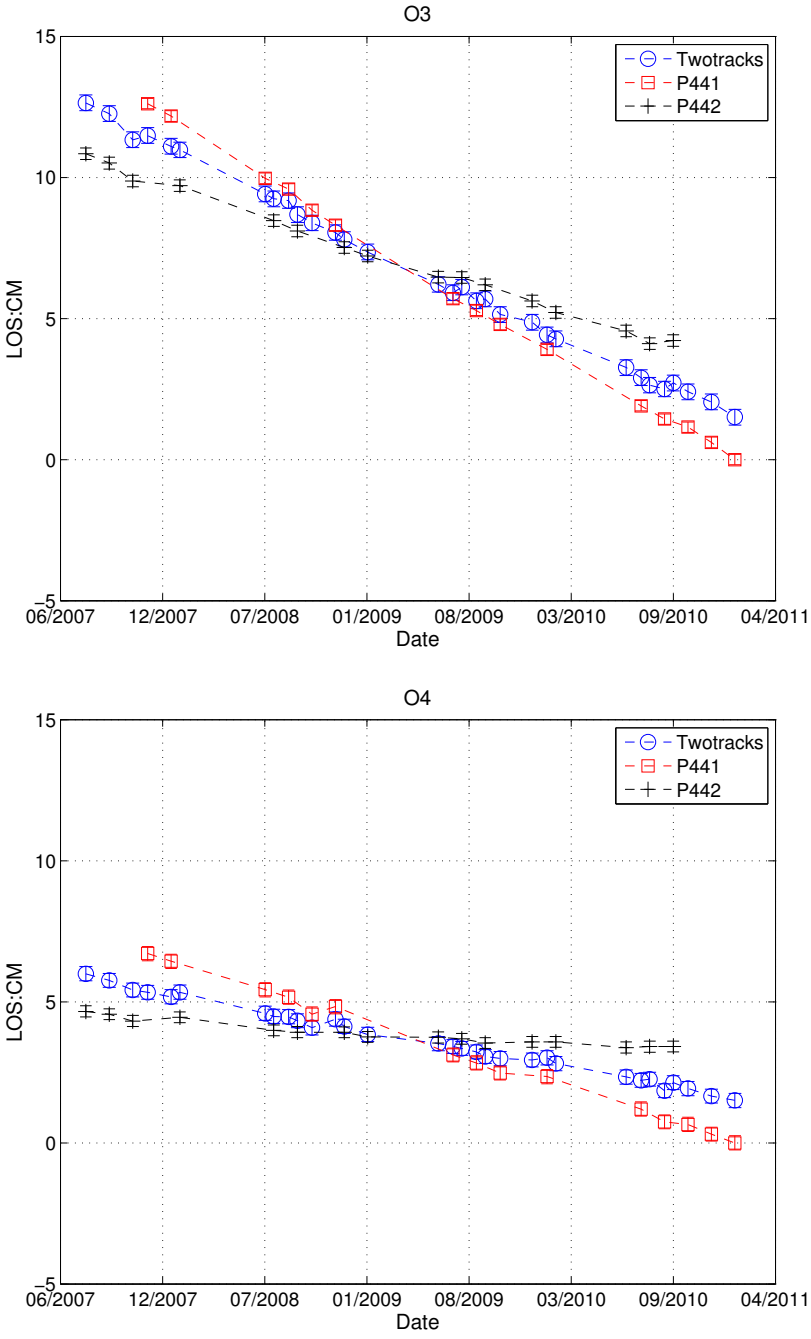

Figure 5.9b Time series of the O3 (up) to O4 (bottom) selected within the overlap area. The red squares represent time series from track 441, the black crosses represent those from track 442 and the blue circles represent those from both tracks. Each point represents one SAR image acquisition date, the reference date is 18 January 2011, the value corresponds to the average of a 3 pixels by 3 pixels window and the error-bar is the associated RMS.

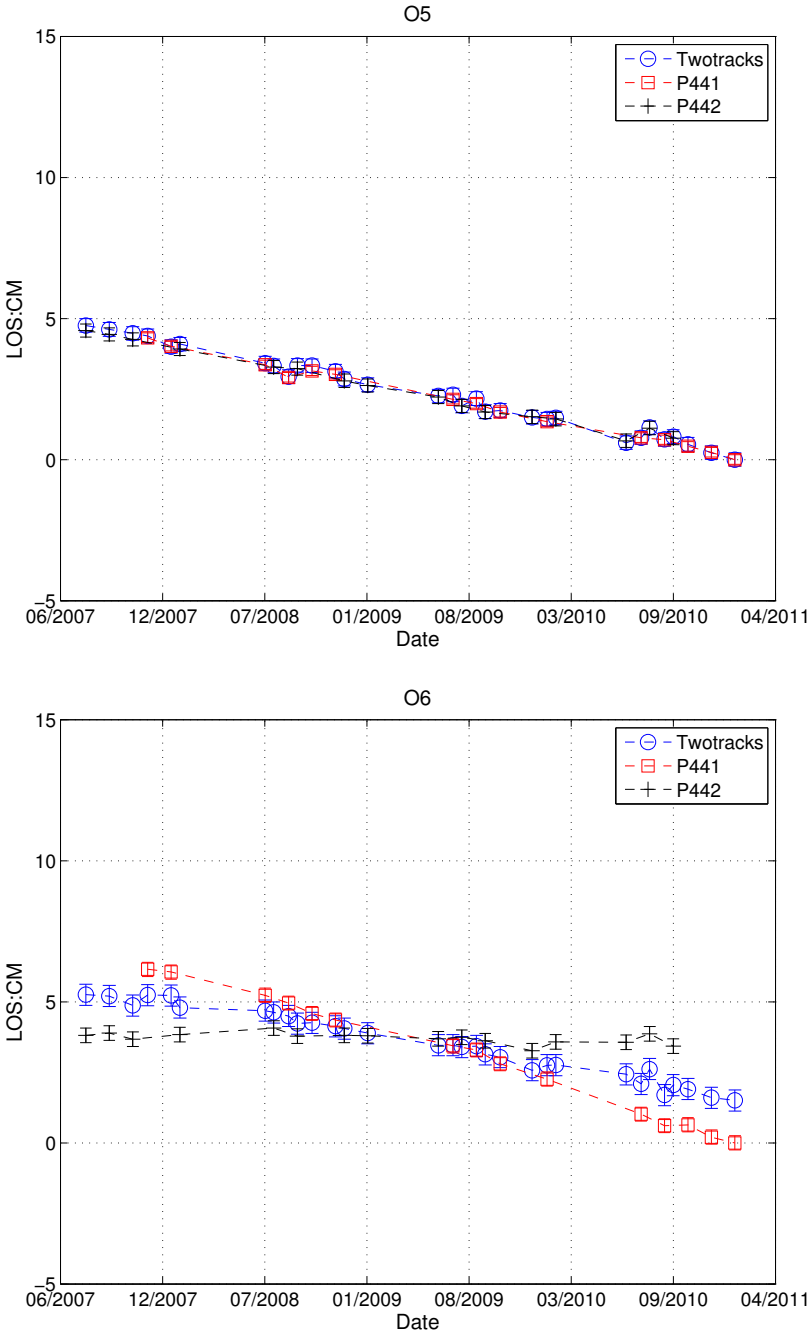

Figure 5.9c Time series of the O5 (up) to O6 (bottom) selected within the overlap area. The red squares represent time series from track 441, the black crosses represent those from track 442 and the blue circles represent those from both tracks. Each point represents one SAR image acquisition date, the reference date is 18 January 2011, the value corresponds to the average of a 3 pixels by 3 pixels window and the error-bar is the associated RMS.

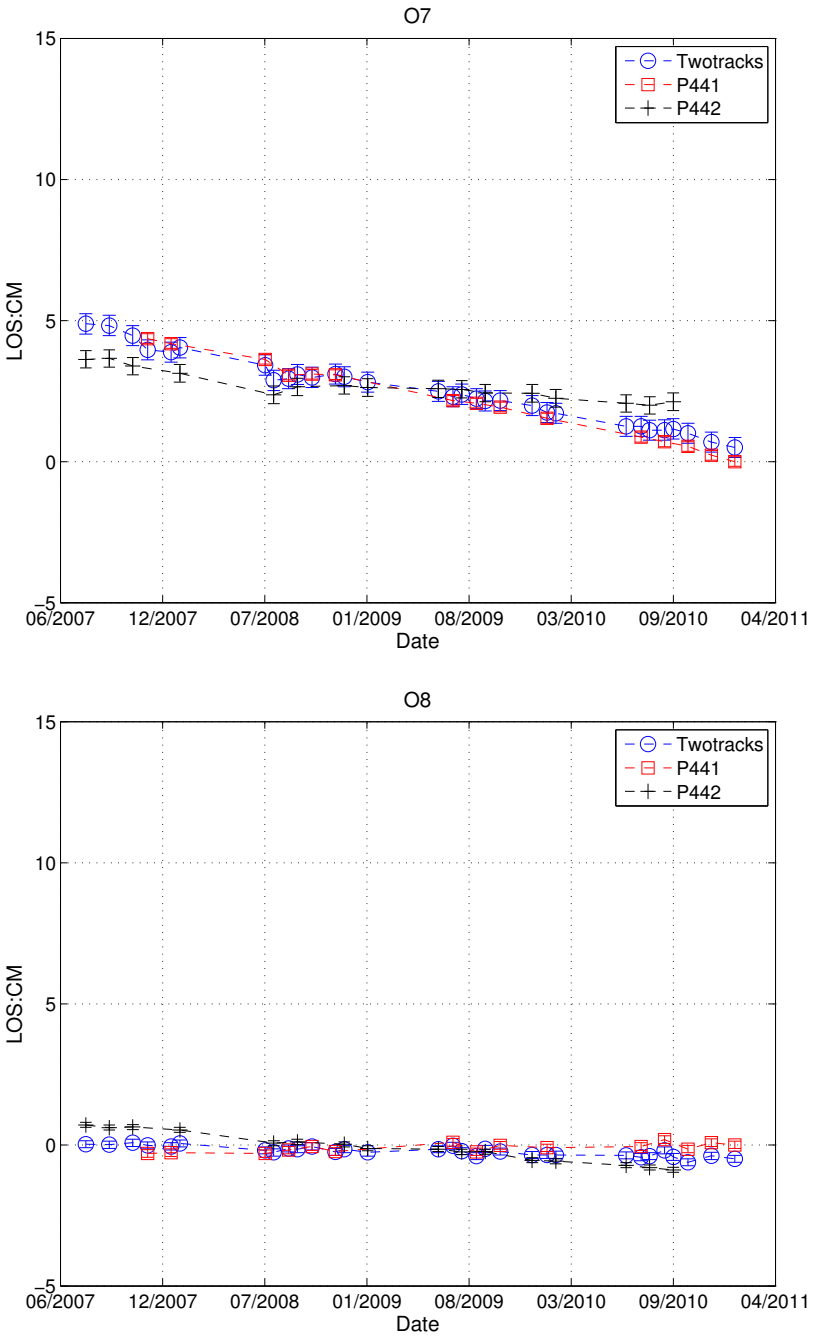

Figure 5.9d Time series of points O7 (up) and O8 (bottom) selected within the overlap area. The red squares represent time series from track 441, the black crosses represent those from track 442 and the blue circles represent those from both tracks. Each point represents one SAR image acquisition date, the reference date is 18 January 2011, the value corresponds to the average of a 3 pixels by 3 pixels window and the error-bar is the associated RMS.

Table 5.3 Mean velocity and RMS (both in cm/yr) results from the eight selected points. A good agreement can be found between both tracks for each location, except for O3, O4 and O6. The combined tracks provide better estimation within overlapping area.

Point	Track 441 mean	Track 442 mean	Combined mean	T441 RMS	T442 RMS	Combination RMS
O1	-2.70	-1.95	-2.39	0.22	0.23	0.28
O2	-2.52	-1.39	-2.02	0.16	0.21	0.25
O3	-3.98	-2.12	-3.18	0.19	0.21	0.28
O4	-2.12	-0.39	-1.21	0.25	0.19	0.25
O5	-1.30	-1.25	-1.32	0.17	0.23	0.24
O6	-2.01	-0.10	-1.11	0.25	0.26	0.37
O7	-1.33	-0.46	-1.13	0.17	0.31	0.36
O8	0.10	-0.50	-0.14	0.13	0.09	0.12

We can also combine the two tracks to produce the final mean height change rate map and displacement history (Figure 5.10). This was done with 31 SAR images acquired from 27th July 2007 to 18th January 2011. Within the overlap area, SAR images are from the two tracks, which provide more observations and contribute better estimation on the mean rate and displacement history. Beyond this overlap area, SAR images only from one track are used. The generally good internal consistency between time series tracks in the overlapping images (Figure 5.9) gives confidence that this area is correctly modeled.

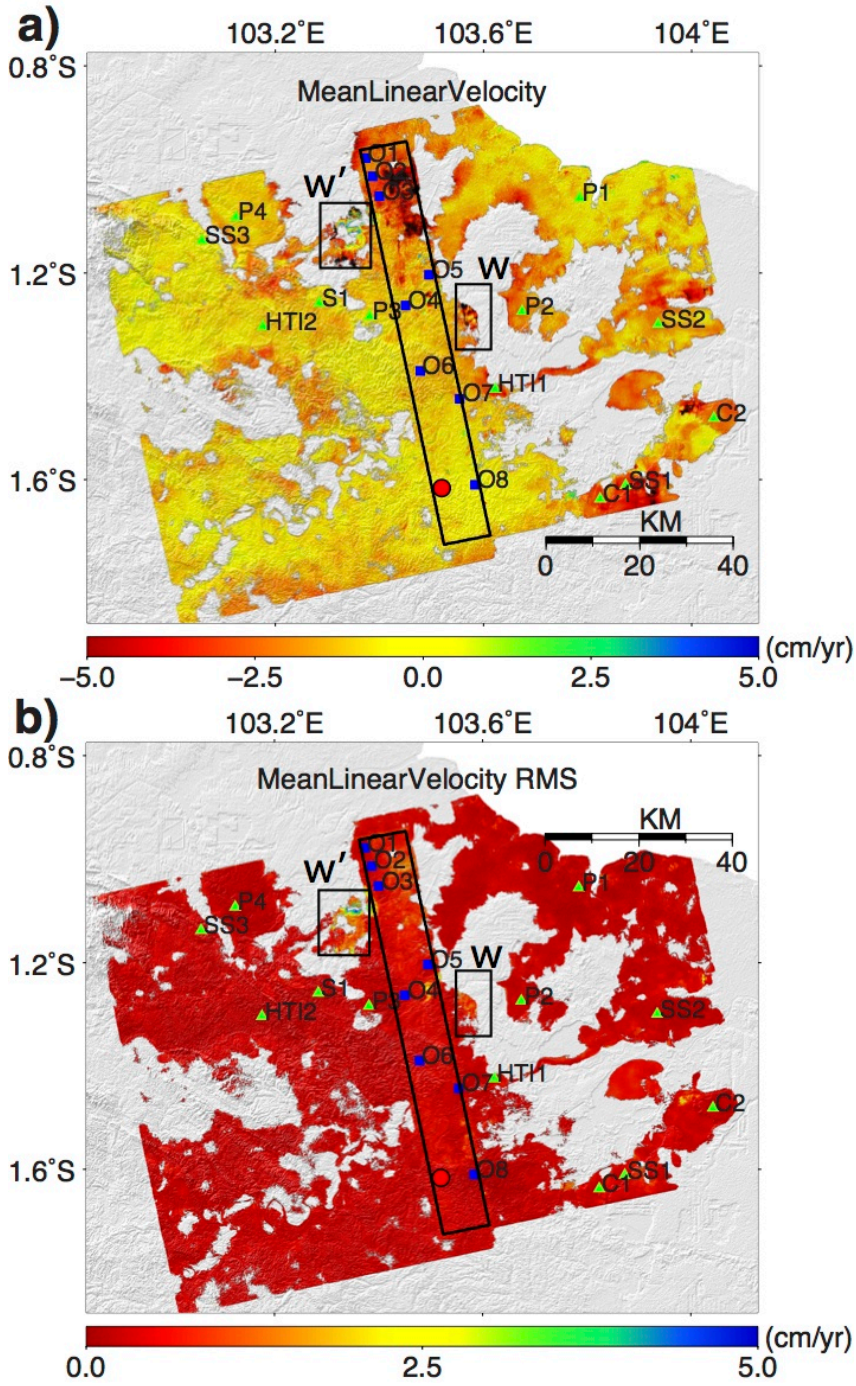

Figure 5.10 (a) SBAS-derived LOS mean peat height change rate map over the study area by combining two tracks of ALOS images, and (b) its corresponding RMS map. Negative values mean loss of topographic height in the LOS, whilst positive values mean gain in the LOS. The red circle is the deformation reference point. Blue square points (O1 to O8) were selected in the overlapping area for validation purposes, and green triangle points (e.g. C1, C2, P1, HT12,) were selected in different landscape areas for time series analysis. The black rectangle area is the overlapping area between the two tracks, and all points of this area are selected for correlation analysis. Areas labeled as W and W' are phase unwrapping errors. High subsidence rate areas (red) can be identified in new-developed areas by cross-reference to the optical images (Figure 5.1).

The resultant mean velocity map and its RMS map are shown in Figure 5.10. The correlation between combined and previous independent results is presented in Figure 5.11. For tracks 441 and 442, the correlation coefficients are 0.87 and 0.9, with RMS of 0.5 cm/yr and 0.4 cm/yr respectively, providing the confidence of the final mean velocity result. The time series comparisons are also shown in Figure 5.9 and a quantitative analysis is provided for the eight points within the overlap area in Table 5.3. Combing the mean velocity correlation analysis and the comparison of time series, suggests that InSAR derived mean velocity and time series are reliable. Therefore, the following analysis and discussion is based on the combination mean velocity map (Figure 5.10 and Figure 5.12) and time series (Figure 5.9 and Figure 5.13).

Figure 5.10 shows a good spatial coverage across the study area with various land use types (Figure 5.12), except for the secondary swamp forest. There is no coherent pixel in such areas; this is because the secondary swamp forest is more likely to lose radar coherence due to flooding under the forest from dry to wet seasons. There is also coherence loss in oil palm and industrial plantation areas because of temporal decorrelation.

The mean velocity (Figure 5.10a) mainly ranges from -5 cm/yr to 5 cm/yr, varying spatially within one type of land cover and differing from one type to another (Figure 5.12). The Jambi city keeps relatively stable during the observation period. the cleared, swap shrub, and industrial forest areas have the largest subsidence rate with up to 5 cm/yr. The shrub area has a maximum subsidence rate of approximately 2 cm/yr. The mean velocity in oil palm area shows relatively slow subsidence rates ranging from 0 to 3 cm/yr.

The RMS map (Figure 5.10b) of the average velocity shows small variations with less than 1 cm/yr in most of areas. In areas labeled as W and W', the RMS values was up to -5 cm/yr. This is most likely due to phase unwrapping errors. Note that the areas labeled as R and R' with uncorrected unwrapping errors in Figure 5.6 correspond to Areas W and W'.

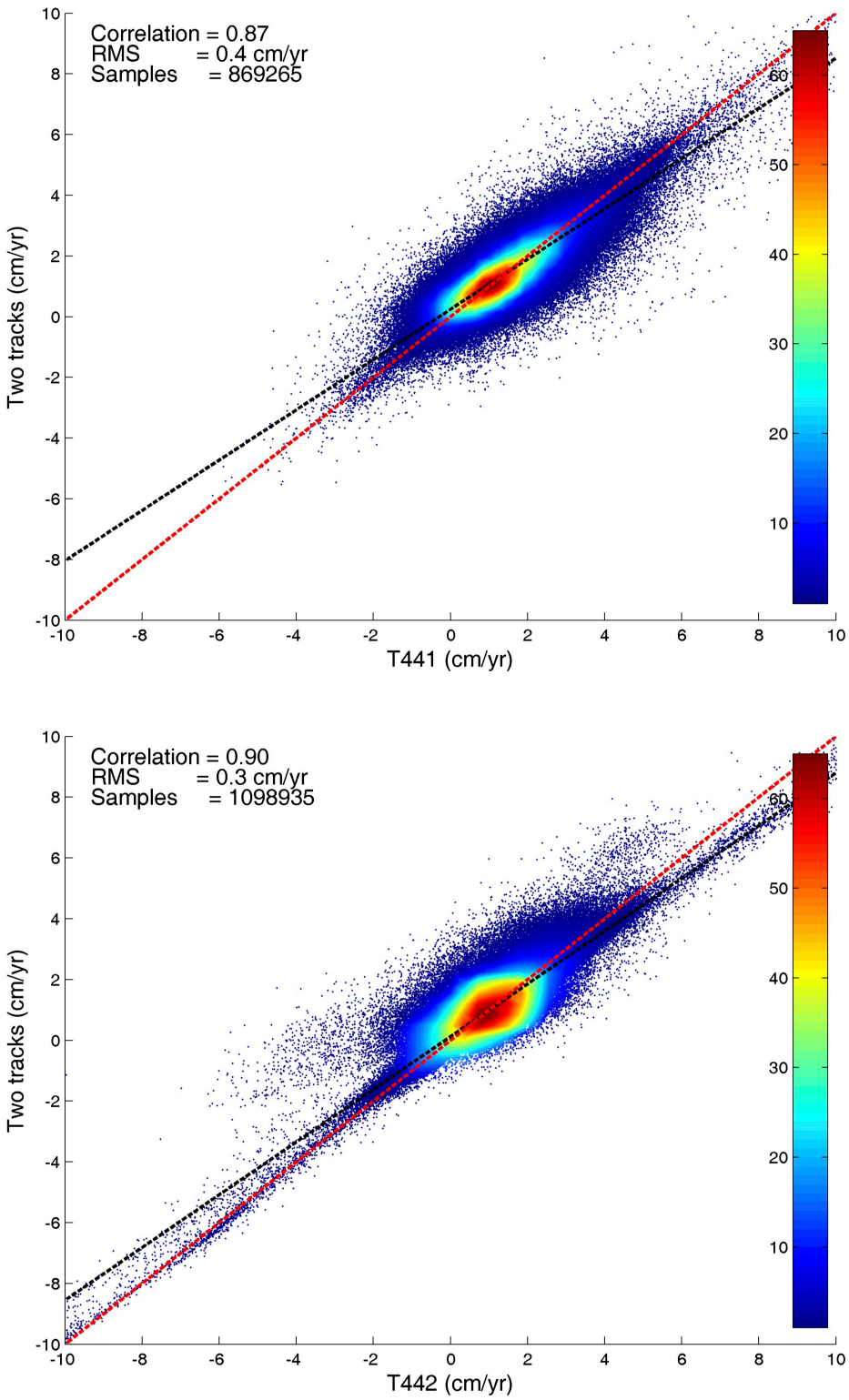

Figure 5.11 Correlation of the mean velocities: (a) Track 441 vs the combination of the two tracks, and (b) Track 442 vs the combination of the two tracks. Red line is the 1:1 line and back line is the best-fit line. The color from blue to red means the increasing density of points in a pixel. Note: negative values represent the surface moves away the satellite (i.e. subsidence).

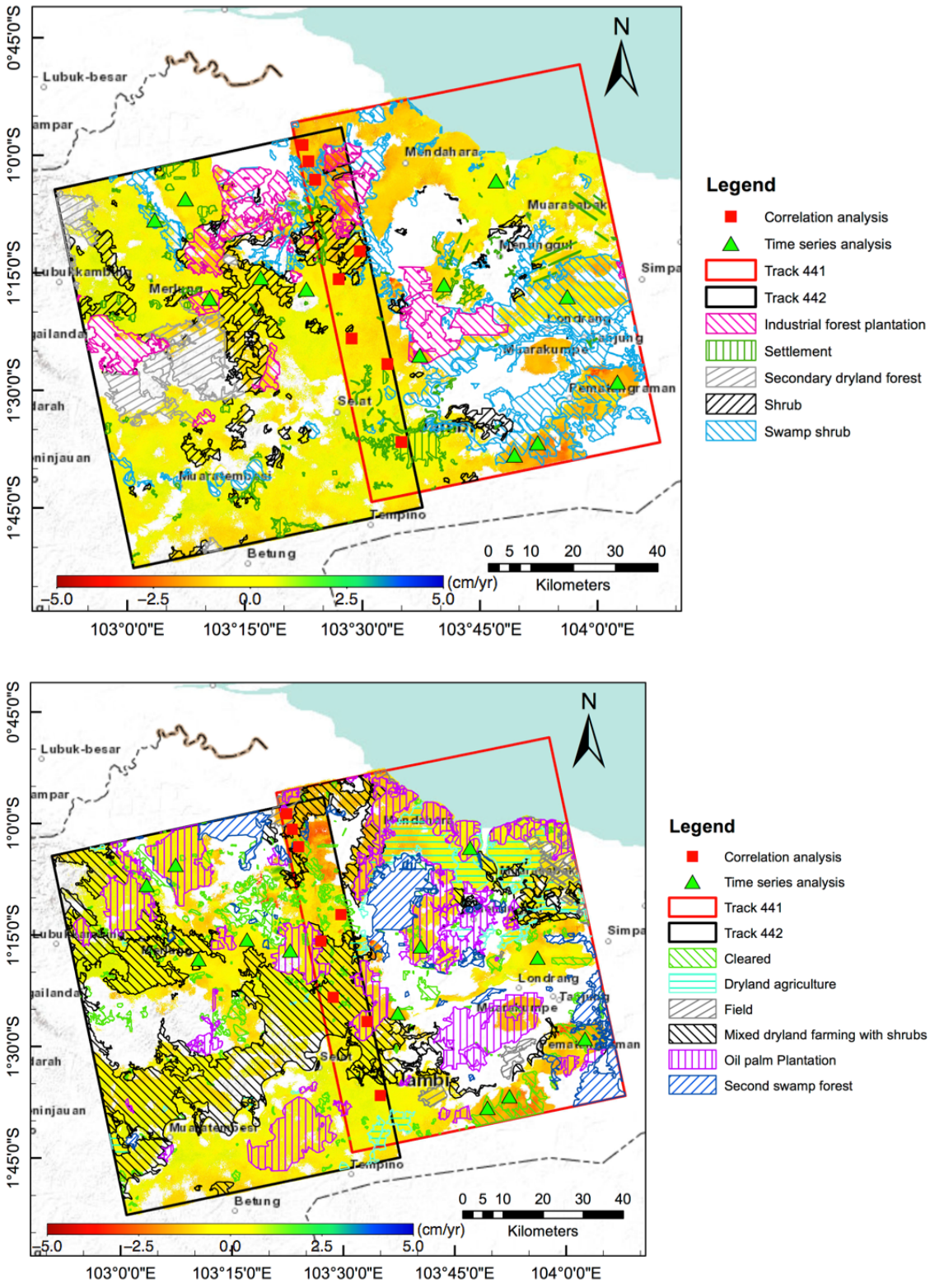

Figure 5.12 Land cover map (Kementerian Kehutanan Republik Indonesia, 2012) Superimposed on the LOS mean peat height change rate map (red-yellow-blue color), the colour scale is identical to that in Figure 5.8. (a) Five land uses superimposed on a mean velocity map; (b) the other six land uses superimposed on a mean velocity map.

Figure 5.9 and Figure 5.13 show the time series of selected points distributed in areas of cleared forest, shrub, swamp shrub, oil palm and industrial forest plantation. The quantitative analysis of these points is provided in Table 5.3 and Table 5.4. Located in the Jambi city, O8 is relatively stable with a mean velocity of -0.14 cm/yr (Figure 5.9d). Except for the relatively stable points of O8 and SS3 (Figure 5.13c), all the other points show a steady decrease in surface heights ranging from -0.74 cm/yr (P1, Figure 5.13e) to -3.45 cm/yr (HTI1, Figure 5.13d). The maximum decrease is HTI1 point with about 12 cm between 27th July 2007 and 18th January 2011. No obvious seasonal change is observed, which might be due to the relatively limited number of observations.

Table 5.4 Mean velocities and RMS (both cm/yr) for the twelve selected points from the combination two data tracks.

Points	C1	C2	SS1	SS2	SS3	S1
Mean	-3.35	-2.31	-3.06	-2.03	0.03	-1.36
RMS	0.29	0.24	0.28	0.24	0.34	0.21
Points	HTI1	HTI2	P1	P2	P3	P4
Mean	-3.45	-1.05	-0.74	-2.37	-0.83	-0.87
RMS	0.43	0.16	0.21	0.39	0.21	0.2

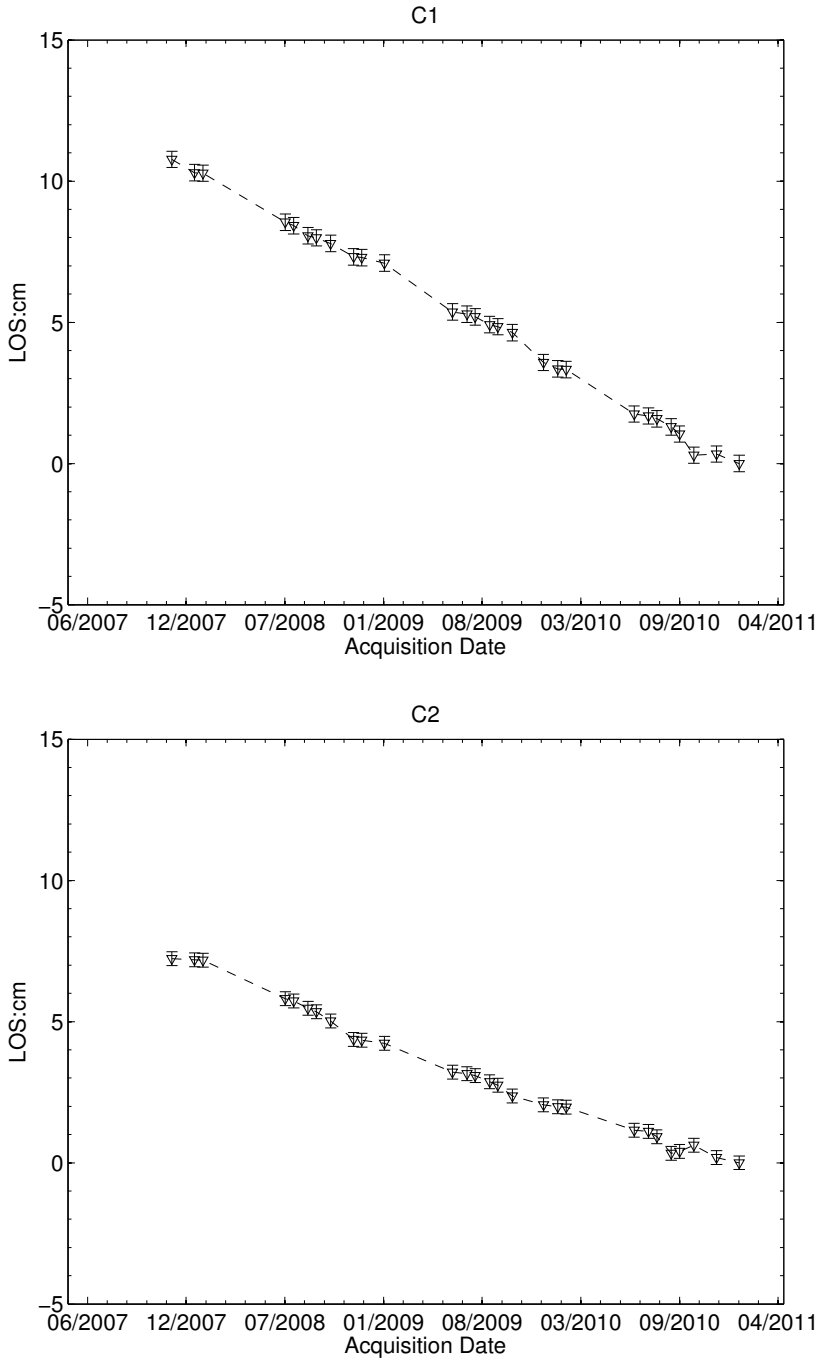

Figure 5.13a Time series of cleared area C1 and C2 selected within the study area. Each point presents one SAR image acquisition date, the LOS displacement values correspond to the average in a 3 pixels by 3 pixels window and the error bar on each point is its associated RMS.

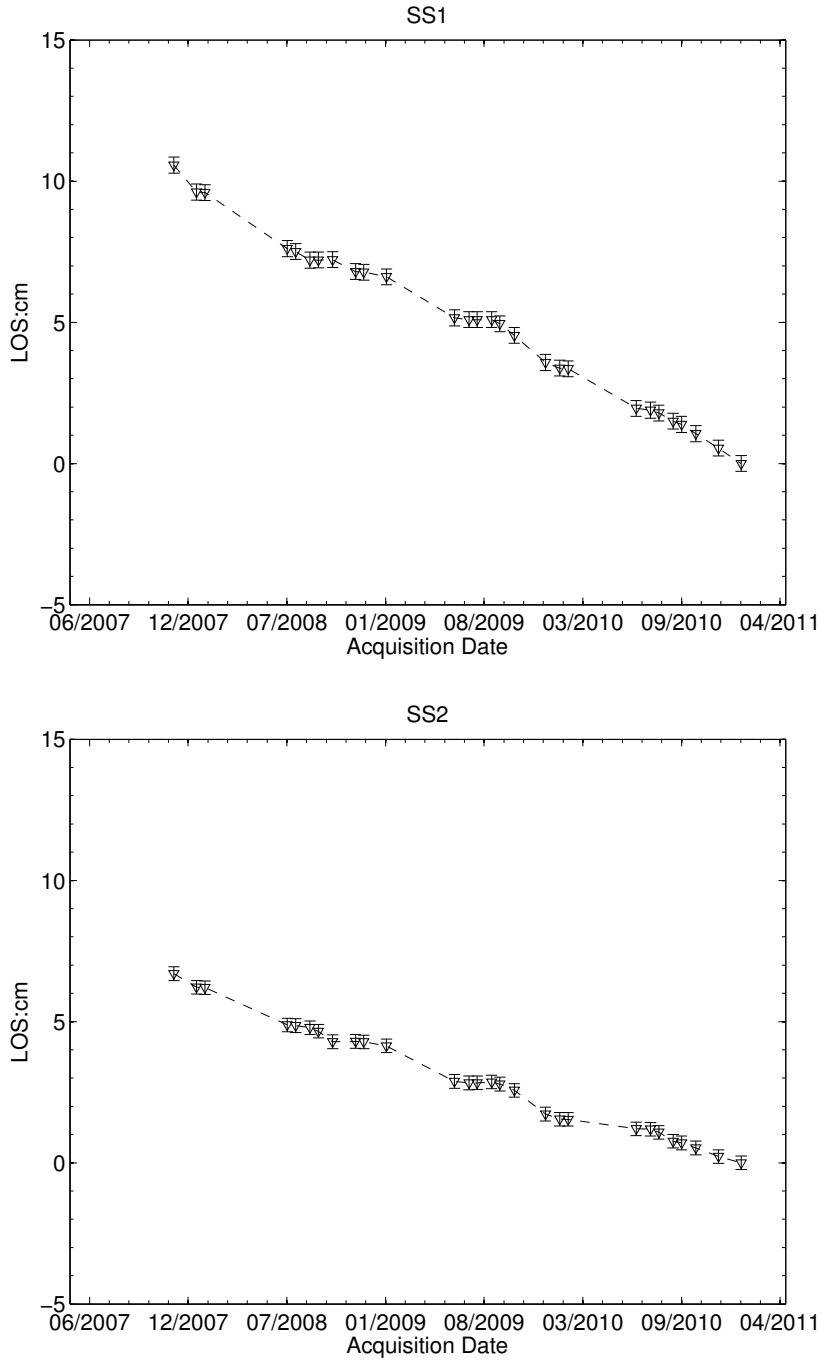

Figure 5.13b Time series of swamp shrub area SS1 and SS2 selected within the study area. Each point presents one SAR image acquisition date, the LOS displacement values correspond to the average in a 3 pixels by 3 pixels window and the error bar on each point is its associated RMS.

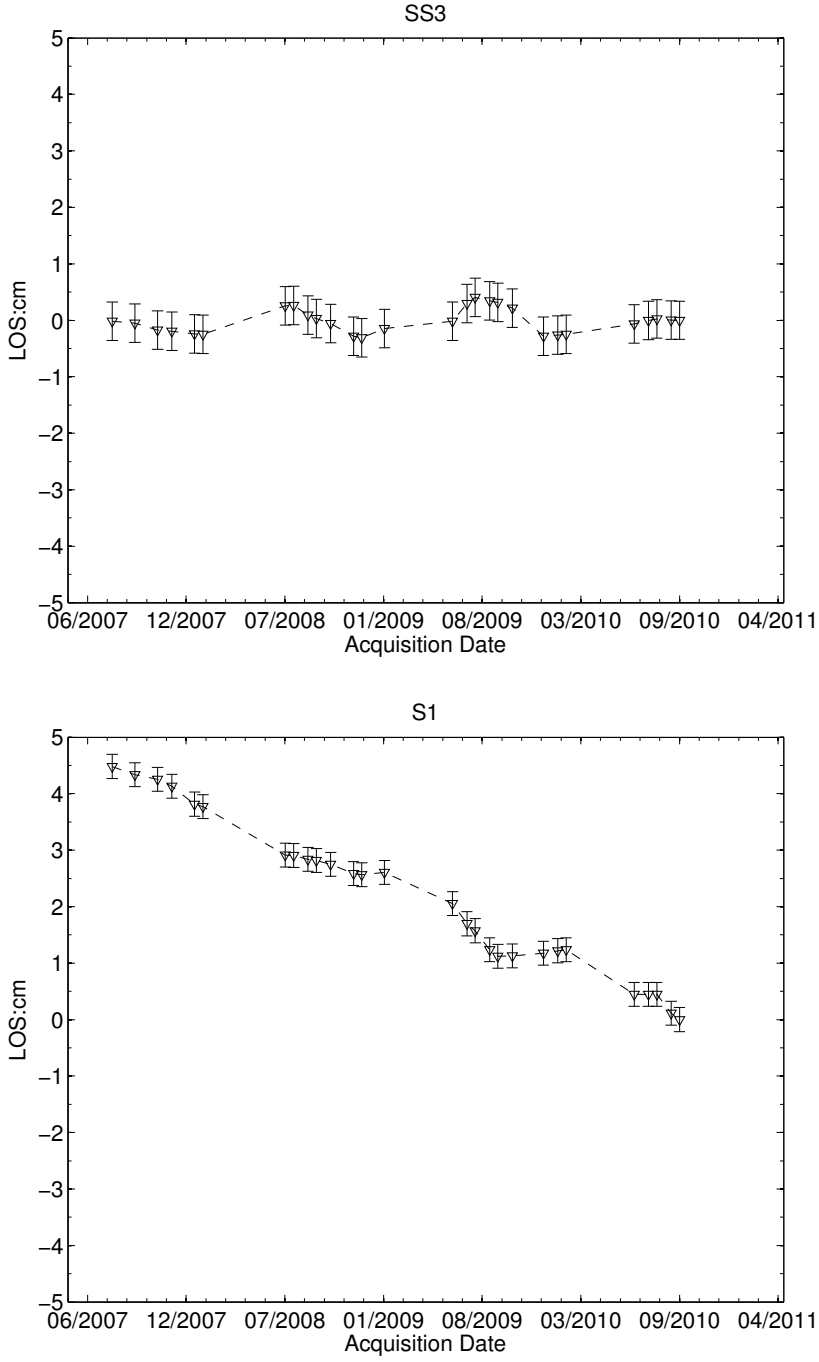

Figure 5.13c Time series of swamp shrub area SS3 and shrub area S1 selected within the study area. Each point presents one SAR image acquisition date, the LOS displacement values correspond to the average in a 3 pixels by 3 pixels window and the error bar on each point is its associated RMS.

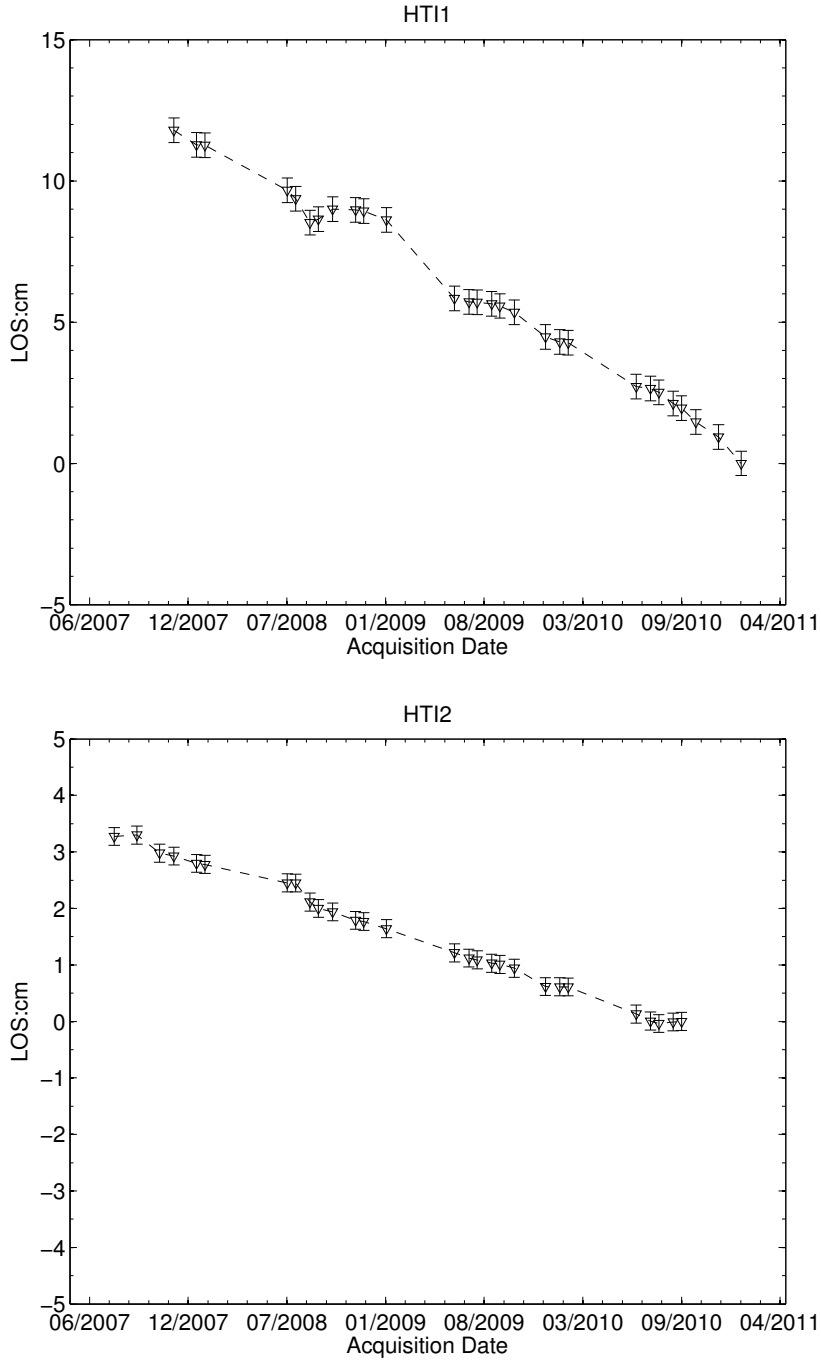

Figure 5.13d Time series of industrial forest plantation area HTI1 and HTI2 selected within the study area. Each point presents one SAR image acquisition date, the LOS displacement values correspond to the average in a 3 pixels by 3 pixels window and the error bar on each point is its associated RMS.

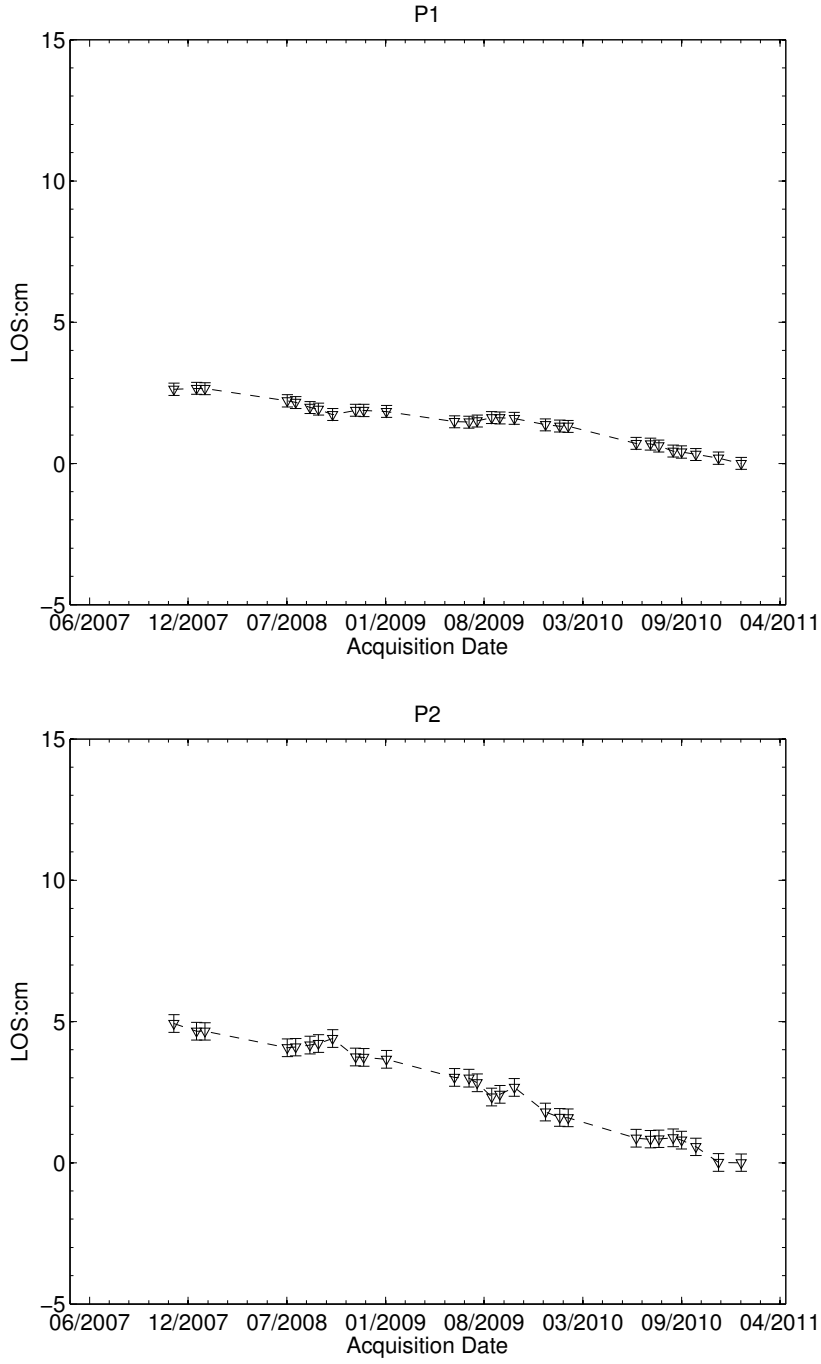

Figure 5.13e Time series of oil palm plantation area P1 and P2 selected within the study area. Each point presents one SAR image acquisition date, the LOS displacement values correspond to the average in a 3 pixels by 3 pixels window and the error bar on each point is its associated RMS.

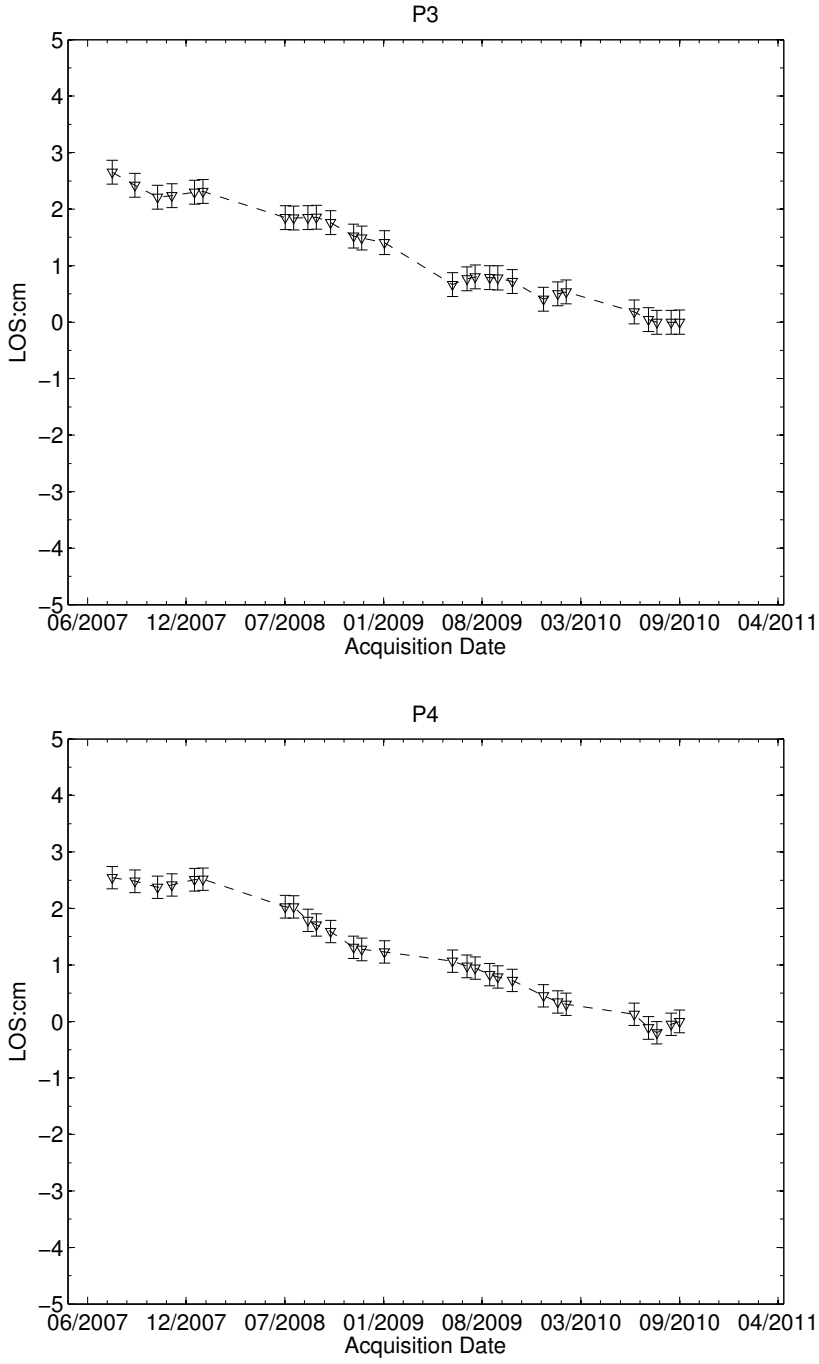

Figure 5.13f Time series of oil palm plantation area P3 and P4 selected within the study area. Each point presents one SAR image acquisition date, the LOS displacement values correspond to the average in a 3 pixels by 3 pixels window and the error bar on each point is its associated RMS.

5.4.2 Estimation of carbon loss

In Section 2.4.3 Estimation based on peat subsidence, carbon loss based on peat height change was discussed. In this chapter, peat volumes and carbon loss can be estimated by calculating the peat loss in each pixel (60 m x 60 m) based on a subsidence map. The peat volume loss rate is estimated by multiplying subsidence rates by the cell size (60 m x 60 m) and appropriate value of peat bulk density. Then the carbon loss estimation is achieved by multiplying the peat volume loss by appropriate value of carbon content (Ballhorn et al., 2009; Dahdal, 2011):

$$Carbon\ loss\ rate\ (t/ha/yr) = V \times S \times \rho \times C \quad \textbf{(4.1)}$$

where V is the peat height change rate; S is the drained area in ha; ρ is the peat bulk density in g/cm^{-3}; C is the carbon content in fraction.

Peat bulk density and carbon content values of 0.087 g/cm^3 and 55% are employed respectively (Hooijer et al., 2012). Based on the subsidence rata shown in Figure 5.10, the peat volume loss rate and C loss rate can be calculated and are shown in Table 5.5. The estimated peat volumes losses range from 0.59 Mt/yr (industrial plantation area) to 1.32 Mt/yr (Oil palm area), corresponding to C loss rates from 0.33 Mt/yr to 0.73 Mt/yr, and annual C loss rate between 11.95 t/ha/yr and 6.05 t/ha/yr. The average peat volume loss rate is 1.01 Mt/yr, which contributes C loss rate with 0.56 Mt/yr and annual C loss rate of 7.78t/ha/yr in this study area. CO_2 emission can be estimated by multiplying C loss by oxidation percentage (Wösten et al., 1997):

$$CO_2\ emission\ rate\ (t/ha/yr) = Carbon\ loss\ rate \times V_{oxi} \times 3.67 \quad \textbf{(4.2)}$$

where V_{oxi} is the oxidation part over the whole subsidence volume in fraction;

In this study, without drainage age data, we use the drainage age based on a study of Hooijer et al. (2012) in the same area, which is over 5 years and 18 years. This study suggests 75% and 92% oxidation of the total subsidence for drainage age of 5 and 18 years for estimating the CO_2 emission rate.

The results in Table 5.5 show that industrial plantation area has the maximum annual CO_2 emission rate, which ranges from 32.87 t/ha/yr and 40.32 t/ha/yr, and oil palm plantation area has the minimum CO_2 emission rate ranging from 16.64 t/ha/yr and 20.41 t/ha/yr. Regarding 75% and 92% oxidation percentage, the whole study area has an annual CO_2 emission rate of 21.41 t/ha/yr and 26.26 t/ha/yr.

Table 5.5 C loss and CO_2 emission from drained peatland

Study area	Cleared	HTI	Oil palm	Swamp shrub	Shrub	Total
Pixels	113911	76002	333613	191787	146642	861955
Mean velocity (cm/yr)	2.03	2.5	1.26	1.89	1.35	1.63
Area (ha)	41007.96	27360.72	120100.68	69043.32	52791.12	310303.8
Peat volume (Mt/yr)	0.72	0.59	1.32	1.13	0.62	1.01
C loss (Mt/yr)	0.4	0.33	0.73	0.62	0.34	0.56
CO_2 loss (Mt/yr; 75% Oxidation)	1.1	0.9	2	1.71	0.94	1.54
CO_2 loss (Mt/yr; 92% Oxidation)	1.34	1.1	2.45	2.1	1.15	1.89
Annual C loss (t/ha/yr)	9.72	11.95	6.05	9.02	6.45	7.78
Annual CO_2 loss (t/ha/yr, 75% Oxidation)	26.73	32.87	16.64	24.81	17.74	21.41
Annual CO_2 loss (t/ha/yr, 92% Oxidation)	32.78	40.32	20.41	30.44	21.76	26.26

5.5 Discussion

In this Chapter, L-band PALSAR SAR images have been used to map the spatiotemporal land surface height change in Jambi, Sumatra (Indonesia). The result shown in Figure 5.10 and Figure 5.12 has a high accuracy, good coverage, and has a great advantage in covering various land uses, such as areas covered by oil palms, shrubs, and industrial forest plantations. Meanwhile, carbon loss rate of this study area and its annual CO_2 emission rate are estimated.

Shorter wavelength SAR data can be used to generate useful interferograms if the two SAR images separation period is short enough. For example, using

ERS1/2 (C-band) tandem SAR images, one day apart between two SAR acquisitions, peatland subsidence was be able to be detected (Dahdal, 2011). However, there are two obvious disadvantages in this specific approach: (1) ERS tandem data is limited, and (2) no information of long-term peatland height changes is available. In this study, long wavelength images (i.e. L-band) were employed as L-band has a better penetration capability than shorter wavelength signal (such as C/X-band), and the ground and the trunks contribute to the signal and to avoid decorrelation caused by changes on the ground. Nonetheless, parts of the study area lost coherence in some interferograms, probably due to the flooding, fire or agriculture activities.

Mean velocity maps shown in Figure 5.7 and Figure 5.10 contain errors, including as unwrapping errors and atmospheric effects. Using the phase closure technique, residual unwrapping errors can be identified (e.g. W and W' in Figure 5.10). For unwrapping errors in a relative large area such as R and R' in Figure 5.6, these errors can be corrected by adding or subtracting 2π back to the original unwrapped phase.

The decrease in surface height of drained peatland in this study ranges mainly from - 5 to 0 cm/yr, which is in the same level of the subsidence rate estimated using perforated PVC tubes in the drained peatlands in SE Asian (Hooijer et al., 2012). Our measurement covers a much greater spatial extension comparing point measurements, although it is limited by data availability, e.g. the ALOS images are only available during the period from January 2006 to April 2011. The individual monitoring may provide longer history measurement data, such as over 28 years monitoring data were used to estimate the peat subsidence rate in Malaysia (Wösten et al., 1997).

From an analysis of 42 locations in oil palm area (Lon: 103.601; Lat: -1.566) from July 2009 to June 2010, drained 18 years, it is reported that the average subsidence rate was stabilized at around 5.4 ± 1.1 cm/yr (Hooijer et al., 2012). Our SAR images cover this site; unfortunately there is no valid InSAR measurement in the final results because of loss of coherence. In our measurements, the subsidence rate of oil palm area ranges from - 3 to 0 cm/yr between 2007 and 2010, which is less than the above measurements (Hooijer et

al., 2012), and is more comparable the long term subsidence rate of about 2 cm/yr reported by Wösten et al., (1997). A set of over 28 years monitoring records in a drained peatland in Johor, Malaysia, show that the average subsidence rate was 4.6 cm/yr after 14 to 28 years drainage, and was 2 cm/yr after 28 to 36 years drainage (Wösten et al., 1997), suggesting the subsidence decreased with the drainage time. This means subsidence rates less than 2 cm/yr may be expected in the long term (Wösten et al., 1997; Rieley and Page, 2008). It should be noted that individual measurements were measured from a single monitoring location, whilst the subsidence rates represent a mean value of an area of 60×60m in this study.

A recent study shows cities in Indonesia (including Medan, Padang, Bengkulu, Bandung, but not Jambi) are sinking that due to underground water and gas extraction; the subsidence rate was up to 22 cm/yr from 2007 t 2010 (Chaussard et al., 2013). The nearest study city to Jambi is Bengkulu, which is about 300 km from Jambi. This subsidence signal is not observed in Jambi city in our study, the mean velocity map and the time series of O8 point both show that the city of Jambi is relatively stable, and this could be because there are limited industrial activities such as low rates of groundwater or gas extraction.

The results of this study suggest that the average carbon loss rate between 2007 and 2011 is 0.56 Mt/yr for the 310304 ha area, and the CO_2 emission rate is up to 1.89 Mt/yr, corresponding annual carbon loss rate of 7.78 t/ha/yr and 26.26 t/ha/yr. This result is similar to the long term results reported by Wösten *et al.*, (1997) for Johor, Malaysia, where the C loss rate and CO_2 emission rate were estimated to be 7.2 t/ha/yr and 26.5 t/ha/yr respectively. However, due to the large variations in bulk density, carbon content, and oxidation percentage, there are uncertainties associated with the estimation of carbon loss and CO_2 emission. In this study, an average bulk density of 0.087 g/cm^3 and 55% carbon content are applied (Hooijer et al., 2012). Bulk density changes with the peat thickness and drainage age: near surface bulk density is approximately 0.15 g/cm^3. However at depths below 0.5 m in palm study areas this decreases to approximately 0.075 g/cm^3, and after two years drainage, the bulk density is approximately 0.085 g/cm^3 at the top of 1 m in acacia plantation area, while it

is approximately 0.087 g/cm^3 after six years drainage (Hooijer et al., 2012). In other studies, a typical bulk density of 0.1 g/cm^3 is used in tropical peatland (Wösten et al., 1997; Page et al., 2002; Hooijer et al., 2010). 55% peat content is used in this study, and it is close to the representative value of 56% for hemic and fibric tropical peat in SE Asia suggested by *Page et al.* (2011b). A range of 50% to 60% carbon content is applied in estimation of carbon loss (Page et al., 2002; Bambang Hero and Canesio, 2005; Ballhorn et al., 2009).

By applying the groundwater depth, there is another approach to estimate the CO_2 (discussed in Section 2.4.2 Estimation based on water table depth). A linear relationship is a archived by modeling previous studies, that is every 10 cm reduction in groundwater table resulting an increase in CO_2 emission of 9.1 t/ha/yr (Hooijer et al., 2010). Since the groundwater table data is not available, the CO_2 emission rate based on this method is not calculated. Section 2.4.2 Estimation based on water table depth also discussed the relationship between subsidence rate and water table.

5.6 Conclusion

This study has demonstrated that InSAR shows significant potential in identifying the relative magnitude and spatial pattern of subsidence of peatland caused by drainage. InSAR has its great advantage in offering regional coverage than individual monitoring measurements. InSAR also has high reliability with an accuracy of 0.7 cm/yr for its derived mean velocity. However, there are limitations that constrain the application of InSAR in peatland, such as temporal decorrelation, and phase unwrapping.

Despite the limitations discussed about, the InSAR time series presented here demonstrate the potential for this approach to detect changes in surface height of peat now under different land uses, such that the data can be extrapolated to estimate carbon loss or CO_2 emission and the estimation of the subsidence rate.

Chapter 6 Monitoring the effect of restoration in Indonesian peatlands using InSAR time series

Abstract: In this chapter, InSAR time series of two adjacent tracks of L-band ALOS PALSAR data are used to map the spatiotemporal land surface height change of Central Kalimantan (Indonesia) peatland with and without restoration. Through the analysis of 26 images acquired between December 2006 and September 2010, this study shows that the restoration is affected by the construction time and density of dams - the earlier the dam is constructed, the more significant the restoration is. In addition high-density dams have positive effects on restoration in a short time. Without dam construction and restoration work, the peatland is losing height especially in burned area; the subsidence rate is up to -7.65 cm/yr. This study has demonstrated that InSAR is a powerful tool in investigating the restoration effects, and can also be used to indirectly assess the relative magnitude and spatial pattern of damages of peatland caused by drainage and fires; the latter provides key information for guiding future restoration activities.

6.1 Introduction

Over the period of 1985~2005, about 12 million ha of peatland has been deforested and drained in Southeast Asia, of which 1.5 million are tropical peat swamp forests in Central Kalimantan, Indonesia. The deforestation occurs through both legal (concession) and illegal logging, and conversion to agricultural use (Hooijer et al., 2006). Drainage causes peat oxidation and releases carbon to the atmosphere as CO_2, which results in peat subsidence (Wösten et al., 1997). It is estimated that an additional drainage depth of 10 cm results in 0.9 cm peat subsidence and about 9 t CO_2 $ha^{-1}a^{-1}$ emissions (Couwenberg et al., 2010). Another severe consequence of drainage is that the peat surface becomes dry and the peat is susceptible to fires during the dry season. Fire can result in a significant loss of carbon due to combustion of both

above ground vegetation (such as primary and secondary forest, agricultural land) and underlying peat. The droughts fires are most severe in very long dry seasons, such as in the 1997/98 El Niño Southern Oscillation (ENSO) event. It is reported that about 0.12-0.15 Gt of carbon was emitted from the Ex-Mega Rice Project (Ex-MRP) area alone (Figure 6.1), and the total carbon loss in Indonesia is between 0.81 and 2.57 Gt, which is equivalent to 13-40% of the mean annual global carbon emissions from fossil fuels (Page et al., 2002). Therefore, restoration of the peat hydrology and conservation of tropical peatlands is critical to prevent peat oxidation and mitigate CO_2 emission (Wösten et al., 2008; Jaenicke et al., 2011; Sasha et al., 2011).

Restoration can be aided by replanting with native peat swamp tree species on impaired peatlands - fires cause loss of propagule for vegetation re-establishment (loss of seed bank and tree bases) (CKPP, 2008; Page et al., 2009b). However, blocking the drainage channels by building dams is one of the most practical and economical peatland restoration actions - peat (primarily deeper) swells when rewetted, and thus the groundwater level of the surrounding peatland can rise after blocking the drainage canals (CKPP, 2008; Page et al., 2009b; Jaenicke et al., 2010). Due to the high permeability and low load bearing capacity of tropical peat, water can not be stored for long periods as it will seep away through the surrounding peat, hence a practical and effective way of dam construction is cascade of closely spaced dams for water control, and with consideration of the distance between the dams, which is dependent on the gradient of the peat dome (CKPP, 2008; Page et al., 2009b; Jaenicke et al., 2010). A blocking dam can be regarded as successful if it raises the groundwater, so decreasing depth and duration of the lowest water level conditions in the dry seasons (Wösten et al., 2008; Jaenicke et al., 2010).

There is intensive experience and knowledge of peatland restoration in the boreal and temperate zones (e.g. Line *et al* (2003), but currently very little is known about the restoration of large areas of degraded tropical peatland (Wösten et al., 2006; Page et al., 2009b). A recent report released by the Central Kalimantan Peatlands Project (CKPP) (2008) indicates that the dams successfully raised the ground water level between 50 cm to over 1 m in the Ex-

MRP area.

Based on the backscatter changes between one JERS-1 (acquired on 21st January 1998, dry period) and one ALOS PALSAR (acquired on 9th November 2006, dry period) L-band SAR images, peat swamp restoration and continuously degrading areas were identified for the period from 1998 to 2006 in the Ex-MRP area (Hoekman, 2009). Jaenicke *et al* (2011) confirmed that the backscatter information of SAR images can be used to detect an increase in ground water level after dam construction, especially in deforested areas with high density of dams. After blocking a drainage canal in degraded site Block C of the Ex-MRP in 2005, water level monitoring showed the mean water level in the dry season rose from -52 cm (2004-2005) to -40 cm (2005-2006), the annual minimum water level from -144 cm to -76 cm; the precipitation distribution in dry and wet seasons was comparable in these two years (Jauhiainen et al., 2008; Page et al., 2009b).

Since each centimeter of groundwater level rise mitigates approximately 0.8-0.9t CO_2 emission (Couwenberg et al., 2010), rewetting of the 590 km^2 area of drained peat swamp forest could mitigate 1.4-1.6 Mt CO_2 emission yearly (Jaenicke et al., 2010), which is equivalent to 6% of the CO_2 emissions by civil aviation in the European Union in 2006 (UNFCCC, 2009). Since the ground water level plays a key role in controlling CO_2 emissions, quantifying the rise of ground water level will provide important information for making GHG emission mitigation tradable under the voluntary carbon market or REDD (Reducing Emissions from Deforestation and Degradation) mechanism (Jaenicke et al., 2011; Sasha et al., 2011; Purnomo et al., 2012).

Manual field groundwater level measurements are challenging because it is difficult to access the wet and densely-vegetated tropical peatlands. In this study, InSAR time series characterization is applied to assess if there has been a change in peat surface height from restoration of tropical peatland through canal blocking in the Ex-MRP area (Blocks A, B, C, and D). The main objective of this chapter is to map and assess the spatial and temporal effects of hydrological restoration by dams, such that this larger scale understanding may inform future restoration work.

6.2 Study area

In 1996, the One Million Hectare Mega Rice Project (MRP) was initiated by the Indonesian Government. Its principal objective was food (rice) production in the area between the Sabangau river in the West, river of Kahayan, Kapuas and Barito in the East, and the Java Sea in the South, and the area was divided into 5 blocks (A, B, C, D and E), where city of Palangkaraya is located in the north of Block C (Figure 6.1) (CKPP, 2008). Large scale deforestation was initiated in January 1996 for preparing land for rice paddies, which involved clear-felling of most of the peat swamp forest and excavation of a massive network of more than 4400 km of drainage channels across the deep peat domes; some drainage channels were up to 30 m wide and 10 m deep (CKPP, 2008; Jaenicke et al., 2010; Jaenicke et al., 2011). The channels were planned to drain excess water from the new agricultural areas during the wet season and provide water for irrigation of rice fields during the dry season.

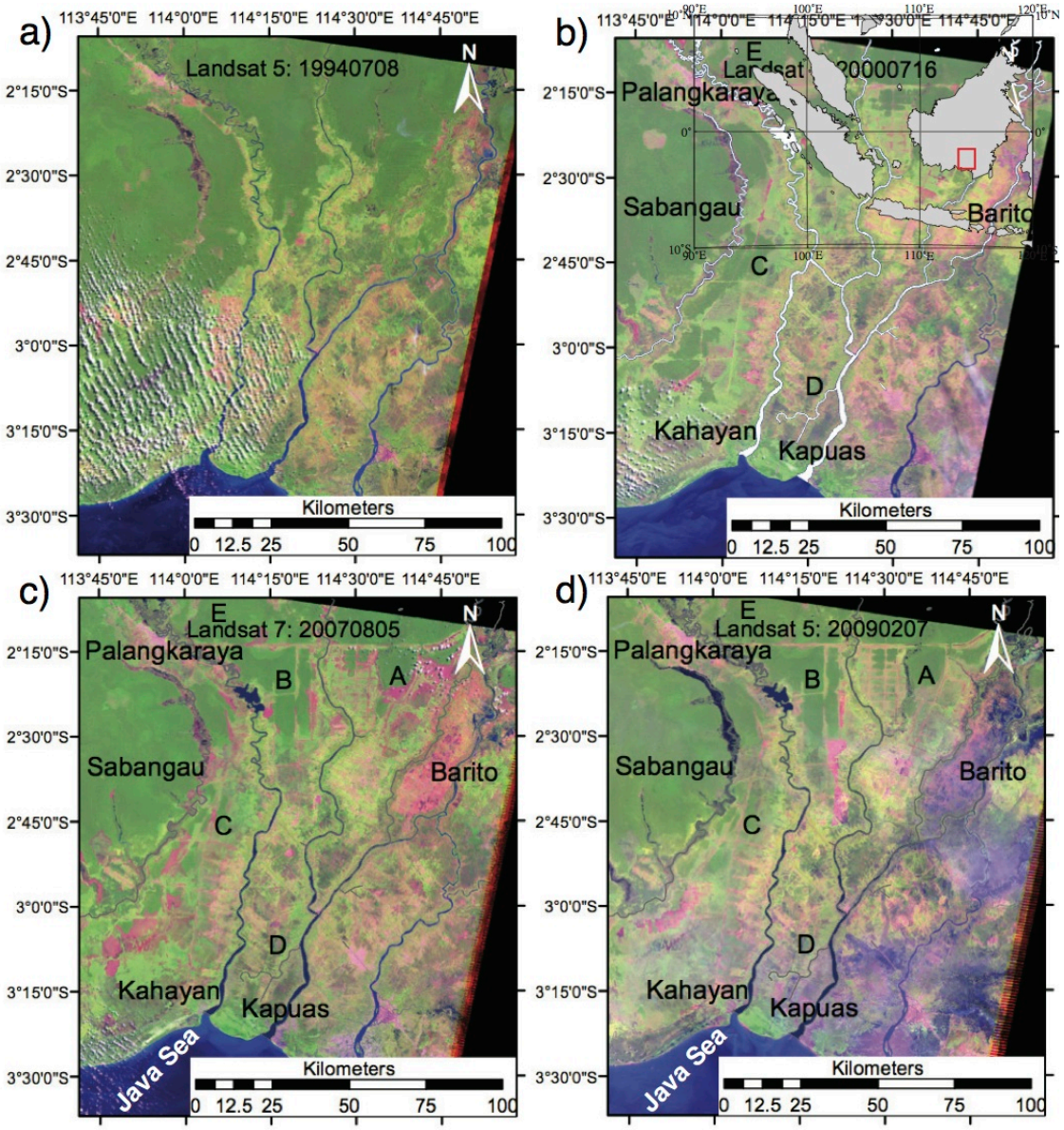

Figure 6.1 Degrading development of Ex-MRP area during the period between 1994 and 2009. The background image is Landsat 5 and 7 (USGS, 2013). The RGB Landsat images are stacked with Bands 5, 4 and 3; peat swamp forest is shown in green, fire scars in purple (Page et al., 2002; Jaenicke et al., 2011). The area is divided into 5 Blocks by rivers (indicated by white lines in b). a) Landsat 5 image (19940708, dry season) before MRP development; b, c) Landsat 7 images acquired on 20000716 and 20070805 respectively, both in dry seasons, after MRP development, the degree of deforestation and fire scars in Blocks A, B, C, D and E are clear in the map; (d) Landsat 5 image acquired on 20090207 in a wet season, along the Barito river, the flooding area is shown in blue.

In July 1999, the MRP failed and was closed down because the area was over-drained by the channels and unable to store the water needed for agriculture

irrigation, primarily due to the difficulties in controlling peat hydrology and demanding physicochemical peat properties for agriculture (Hoekman, 2007). Consequently, the area was largely abandoned and is now an 'unproductive' and susceptible to flooding landscape, and the drainage of the peatland caused by the network of massive channels results in peat oxidation, subsidence, and a land of regular outbreaks of large-scale fires (Figure 6.1) (Hoekman, 2009; Page et al., 2009b; Sasha et al., 2011).

The climate of the MRP area is characterized by a relatively uniform temperature, high humidity and high rainfall intensity. The average monthly temperature ranges between 24-27 °C. Annual rainfall varied from 1848 mm (1997) to 3788 mm (1999) with an overall average of around 2800 mm (such as 2003) (data from 1994-2004, Figure 6.2a) (Wösten et al., 2008). Usually the wet season starts from November to May, and the dry season is from June to October (Figure 6.2b). The average evaporation is fairly constant (3.5~4.8 mm/d) with a total of around 1500 mm per year. The evaporation in the wettest months (Dec-Feb) exceeds the average monthly rainfall of the driest months (Aug-Sep) (Figure 6.2b) (Hoekman and Vissers, 2007; Wösten et al., 2008).

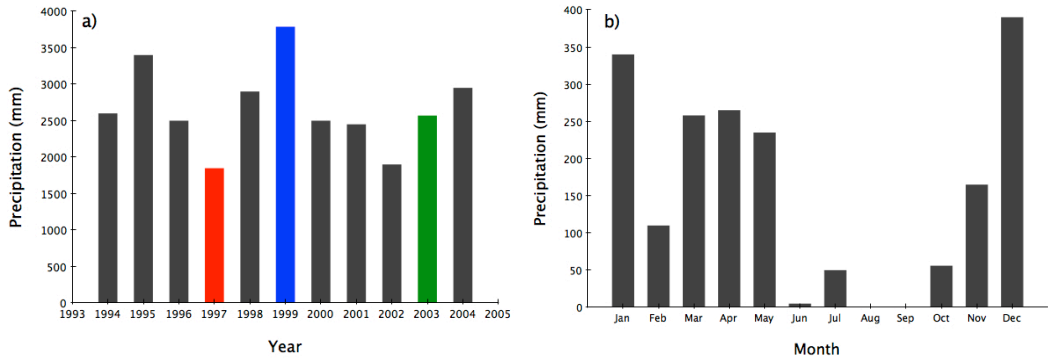

Figure 6.2 (a) Annual precipitations during the period from1994 to 2004, and (b) monthly precipitation in the driest year 1997, reproduced from (Wösten et al., 2008). Usually the wet season starts from November to May, and the dry season is from June to October.

The Ex-MRP area is relatively flat, with an elevation that increases from sea level at the coast, to only 30 m above sea level at the distance of 200 km from the coast (Wösten et al., 2008). Almost half of the peat area is over 3 m deep, and the maximum depth is up to 12 m (CKPP, 2008), with decreasing depths towards the major rivers (Page et al., 1999). The maximum and average peat thicknesses in Block C are 9.3 m and 4.4 m respectively (Page et al., 2002).

Currently, seven land uses dominate this area (Figure 6.3). Most of the shrub swamp area and rice field area can be characterized as destroyed, abandoned and fire-damaged, and only a small part of the rice field area is in use (Wösten et al., 2008).

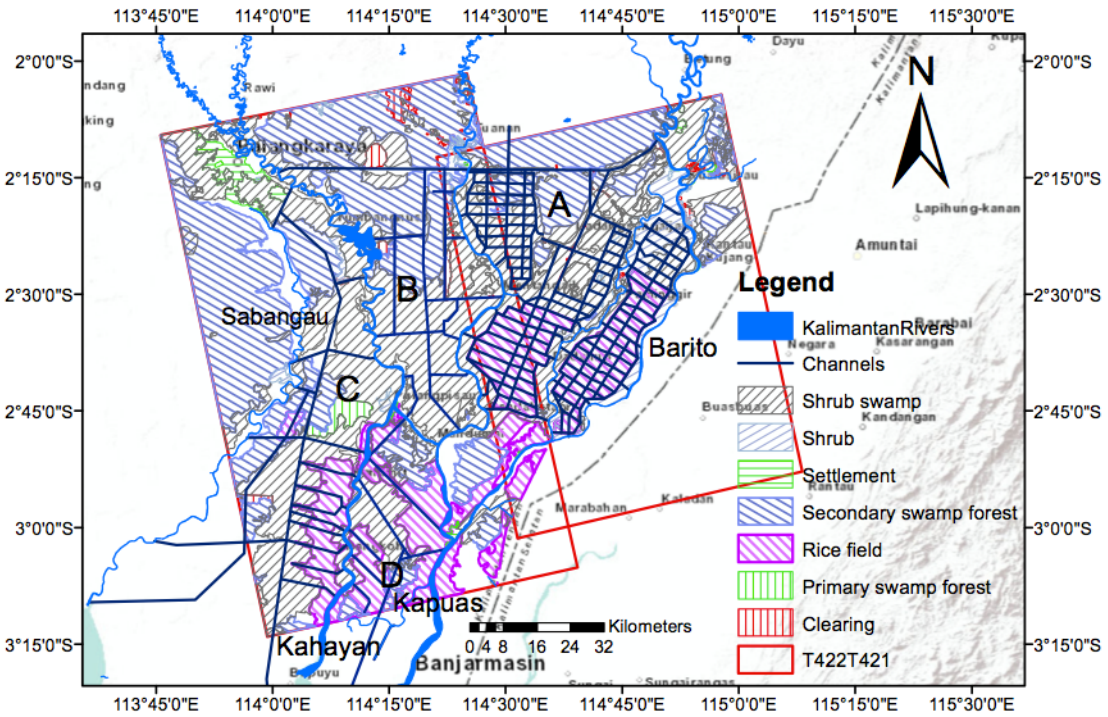

Figure 6.3 The Ex-MRP area and the study area. There are seven land uses in this area in 2009 (Kementerian Kehutanan Republik Indonesia, 2012). Two ALOS tracks (T421 & T421) cover this area. Drainage channels cross the main MRP area (Page et al., 2002; CKPP, 2008).

This study focuses on Blocks A, B, C, and D. Peatland restoration has been conducted only in Blocks A and C. In July 2004, hydrological restoration

commenced in Block A under the CCFPI (Climate Change Forests and Peatlands in Indonesia) project by building five large dams; 19 more dams were built in this area between 2007 and 2008, funded by the Central Kalimantan Peatland Project (CKPP) (Figure 6.4). In June-September 2005, seven dams were constructed in Block C within the framework of the Academy of Finland funded project "Keys for Securing Tropical Peat Carbon" (KEYTROP) and the EU funded RESTORPEAT (Restoration of Tropical Peatland for Sustainable Management of Renewable Natural Resources) (Figure 6.4) (CKPP, 2008; Jaenicke et al., 2011). The dam framework and wooden covering were constructed from dead wood collected from the forest site. Vertical supports were piled deep into peat in the canal floor and horizontal rests were attached to the framework. The construction was filled with compressed peat. The dimensions of the largest dams were 25 m in length, 4.4 m in width at the bottom, and 1.2 m at the top. The structures had narrowing shapes with 1 m steps upward. The height of the structure above canal bottom surface was about 3 m, and it reached the peat surface next to the canal. Trees were planted on top and behind the dams to increase resistance (Figure 6.5). The dams in Block A are very similar to those in Block C in terms of size and design (Hoekman, 2007; CKPP, 2008; Jaenicke et al., 2011).

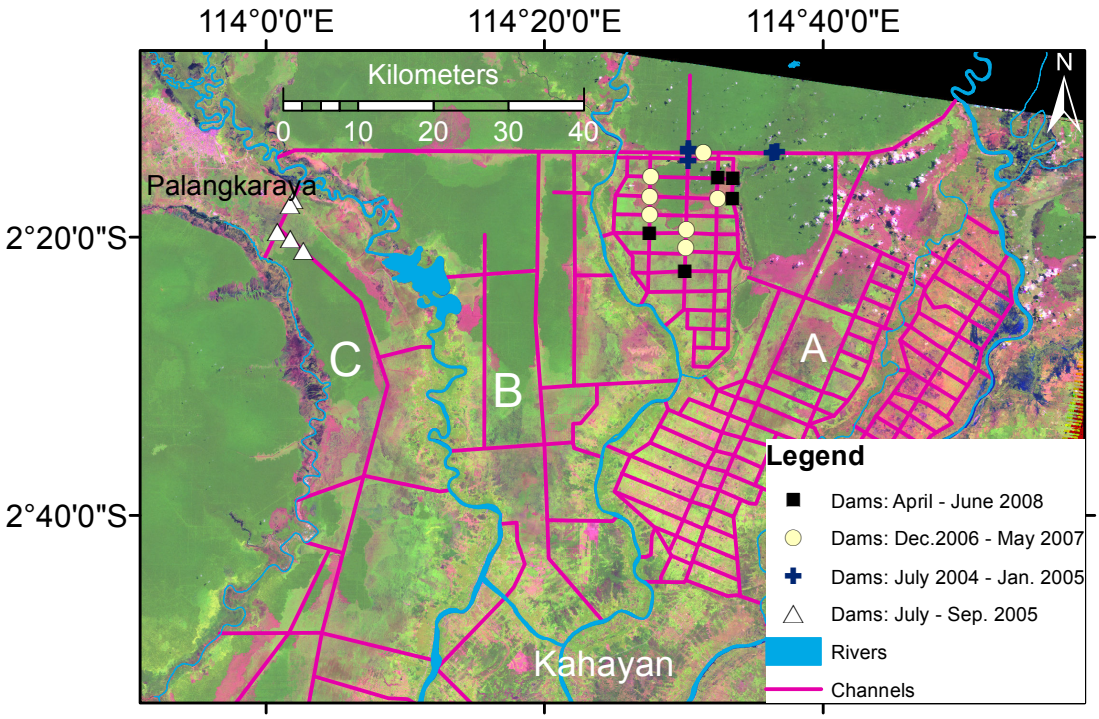

Figure 6.4 Dam locations and construction dates. The background image is Landsat 7 acquired on 5th Aug 2007 (USGS, 2013). The RGB Landsat images are stacked with Bands 5-4-3; peat swamp forest is shown in green, burn scars in purple (Page et al., 2002; Jaenicke et al., 2011). Note: Not all of the dams are shown due to short distances between some of them.

Figure 6.5 Large dam constructed across a drainage canal in degraded peatland in Block C, Mega Rice Project area. A timber frame was sealed with plastic sheeting and then filled with peat, adapted from *Jaenicke et al.* (Jaenicke et al., 2011).

6.3 ALOS data processing

Two adjacent Tracks (T421 Frame 7130 and T422 Frame 7130) of ALOS PALSAR images are ultilized to produce interferograms; if both tracks show agreement in change patterns during the same observation period then there is greater confidence that the observations are representative of the local site.

Whether a dam has effectively blocked a drainage system may be easiest detected from data from the dry season where there is less surface water. Thus SAR images acquired in dry seaons are primary used in this study. The temporal and spatial baselines of the ALOS images of each track are shown in Table 6.1 and Figure 6.6. Track 421 includes 12 images acquired from 20th December 2006 to 12th Feburary 2010 and Track 442 includes 16 images collected from 27th July 2007 to 19th September 2010.

Table 6.1 ALOS images from Tracks 421 and 422 used in this study. For reference, dates are given in Year-Month-Day (YYYYMMDD) format, and as number of days since the first image for each track. Perpendicular baselines for Tracks 421 and 422 are relative to 20080809 and 20080711 respectively. These reference dates were chosen because of limited atmospheric effects on these two SAR images assessed by checking all interferograms involved SAR images acquired on these dates.

T421				T422			
Image Number	Date(YYYYMMDD)	Number of days	Baseline (m)	Image Number	Date(YYYYMMDD)	Number of days	Baseline (m)
1	20061220	0	139.6	1	20070709	0	228.3
2	20070622	184	101.1	2	20070824	46	307.4
3	20070807	230	208.5	3	20071009	92	129.4
4	20070922	276	-245.5	4	20080526	322	-331.6
5	20080207	414	-16.1	5	20080711	368	0.0
6	20080809	598	0.0	6	20080826	414	-255.8
7	20080924	644	494.1	7	20081011	460	471.2
8	20081109	690	444.7	8	20090714	736	638.1
9	20090627	920	332.8	9	20090829	782	741.1
10	20090812	966	-27.9	10	20091014	828	396.0
11	20091112	1058	87.5	11	20091129	874	266.3
12	20100212	1150	234.9	12	20100301	966	136.9
				13	20100717	1104	-45.7
				14	20100901	1150	59.8

From the 12 and 14 PALSAR images, 27 and 30 interconnected interferograms are generated for Tracks 421 and 422 respectively (Figure 6.6). These interferograms show high coherence and they are free of obvious ionosphere artifacts (Gray et al., 2000). Firstly a small area (6x6 pixels, ~540 m x 540 m) located in Palangkaraya city (Lon: 113.916712, Lat: -2.020728) is assumed stable during the observation period and chosen as the reference site for InSAR time series analysis for Track 422 (Figure 6.11). To check the mean peat height change rate map from track 422, a relatively stable area (the same size as that for track 422) in the overlapping area (Lon: 114.447486, Lat: -2.316743) of these two adjacent tracks is chosen as the reference area for InSAR time series analysis for Track 421 (Figure 6.11). This small area is checked by mean height change rate results from Track 421, since it is not easy select a relative stable reference site from Track 422, because the land use of area covered by Track 422 is rice fields or peat swamp.The SBAS method introduced in section 3.3.2 Small baseline subset InSAR was used to generate the mean height change rate map and time series. Finally all the deformation rate maps and time series were geocoded into a 90-m spacing geographic grid.

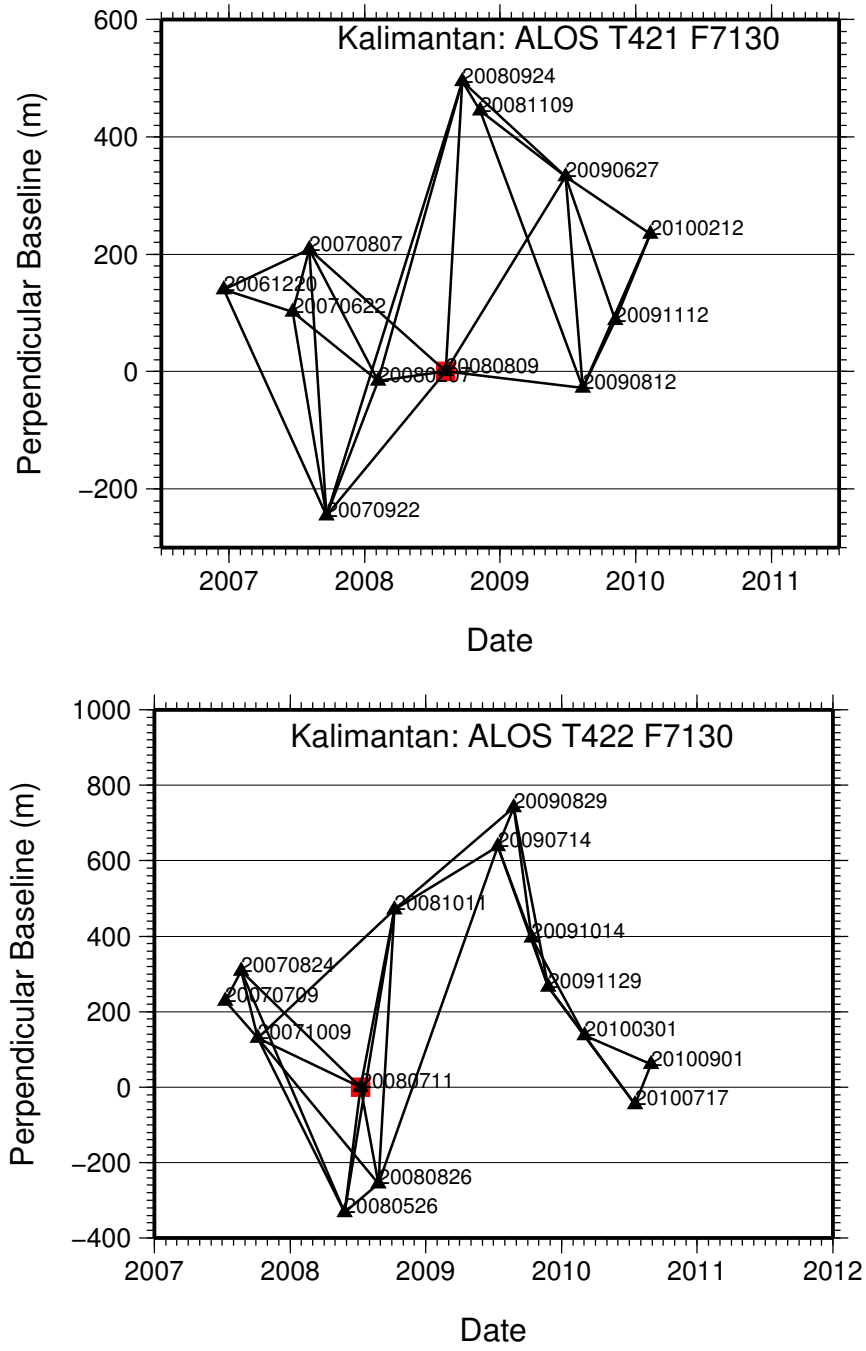

Figure 6.6 SBAS network for ALOS PALSAR Tracks 421 (up) and 422 (bottom). Each black triangle denotes one SAR image, and black solid lines between two black triangles represent interferograms. The black square marks the reference date for time series analysis.

After the mean height change rate maps are generated independently from the two adjacent tracks, the overlapping area between them is used to validate InSAR results with correlation analysis. To moderate the orbit error between

the two deformation rate maps, a best-fit plane of the difference of them is removed before the correlation analysis. Six points within the overlapping area (O1 to O6) in different land use type are chosen randomly for the purpose of validating InSAR-derived displacement time series. Another thirteen points distributed in various land uses are selected for investigating the movement history and change rates. Land use types were classified in 2009 (Figure 6.3). The time series of these nineteen points are constructed using an area of 3x3 pixels (corresponding to 270x270 m on the ground). The details of the twenty points are listed in the Table 6.2.

Table 6.2 Location and land use type of points selected in this study

Points	Longitude Degrees	Latitude Degrees	Land use type
O1	114.4475	-2.3167	Shrub swamp
O2	114.4742	-2.3413	Shrub swamp
O3	114.4772	-2.3873	Shrub swamp
O4	114.5118	-2.5647	Rice field
O5	114.5052	-2.6371	Rice field
O6	114.5581	-2.9547	Unknown (not covered in the land use map)
C1	114.2395	-2.2077	Cleared
FS1	114.6195	-2.3630	Fire scar (in shrub swamp)
FS2	114.7020	-2.3135	Fire scar (in shrub swamp)
FS3	114.3765	-2.3915	Fire scar (in shrub swamp)
FS4	114.4431	-2.4576	Fire scar (in shrub swamp)
FS5	114.3467	-2.5248	Fire scar (in shrub swamp)
FS6	113.9837	-2.9556	Fire scar (in shrub swamp)
RF1	114.5186	-2.6655	Rice field
RF2	114.6808	-2.6127	Rice field
RF3	114.1330	-2.9520	Rice field
RF4	114.1220	-3.0370	Rice field
SF1	114.4182	-2.8581	Secondary swamp forest
SF2	114.0741	-2.8173	Secondary swamp forest

To monitor the restoration effects of dams in Blocks A and C, eight profiles of mean height change rate are selected for Block A, and two for Block C (Figure 6.7). In Block A, five of the eight profiles are along the channels (AA', BB', DD', FF' and HH'), while the other three profiles are through the middle of the mini block (CC', EE' and GG'). The width of all profiles is about 100 m. In Block C, both profiles (MM' and NN') are along the channels, and with a width of about 100 m.

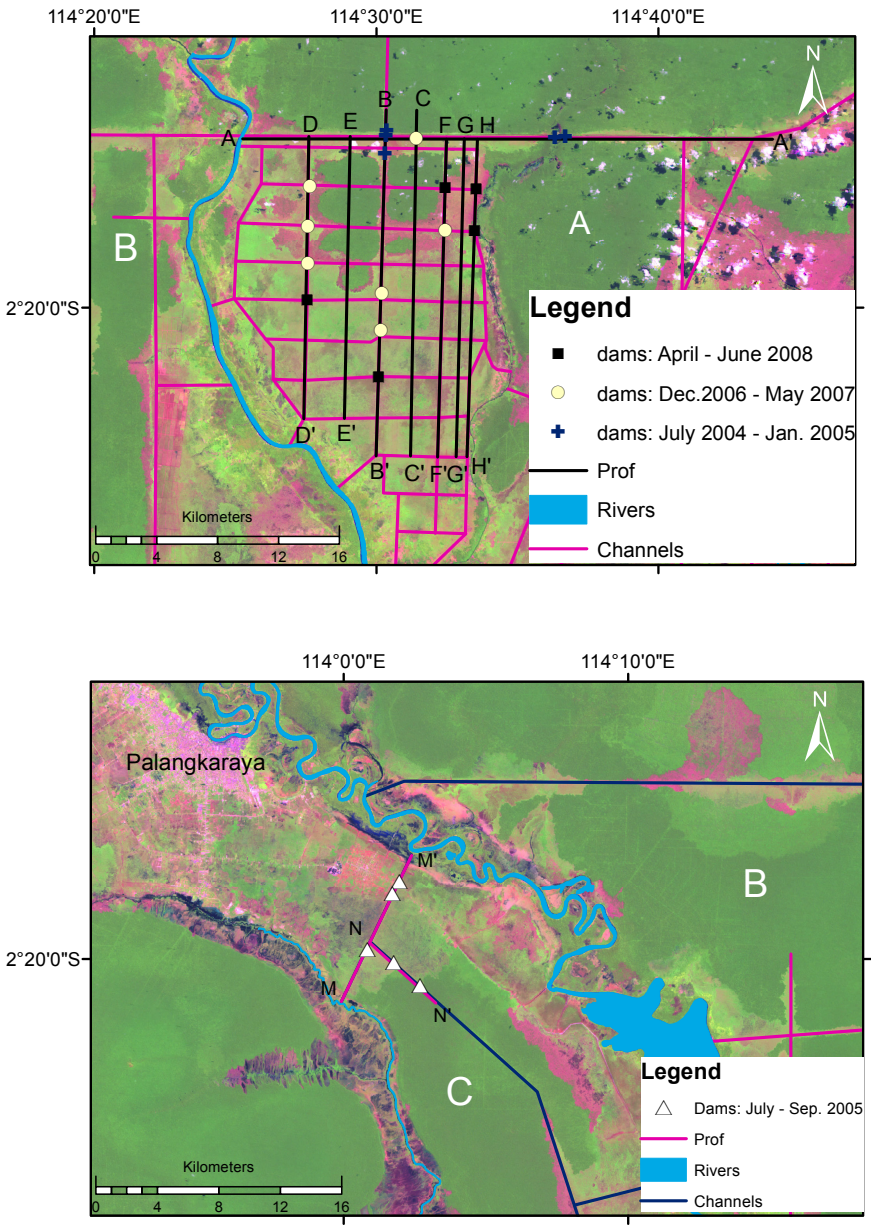

Figure 6.7 Details of each profile and dam. The background image is a Landsat 7 image acquired on 20070805 (USGS, 2013). The RGB Landsat images are stacked by Bands 5-4-3, peat swamp forest is shown in green, burn scars in purple (Page et al., 2002; Jaenicke et al., 2011).

6.3.1 Interferograms

Figure 6.8 shows unwrapped phased SAR-generated images acquired in wet and dry seasons. It is clear that there are surface change signals (couples of fringe) along the river in the interferograms with SAR images acquired in wet seasons (Figure 6.8a, b, and c), which is likely caused by the significant changes of water level. For areas with forest or high vegetation, when there is water under the canopy, such as being flooded, the radar can receive double-bounce backscattering signals reflected mainly by tree trunks (Jin-Woo et al., 2009); if there is a large fluctuation in water level, interfergrams produced with SAR images collected in wet seasons could show apparent changes (fringes). In wet seasons, the study area is susceptible to flooding, which can lead to low or no coherence; terrain (such as rice fields) with low vegetation is flooded in wet seasons (Hoekman, 2009), and radar signals are directly reflected away due to water acting as a mirror. In dry seasons, the water lever of the river is relatively stable; therefore there is no clear surface change signal along the river in the interferograms with SAR images acquired in dry seasons (Figure 6.8d) and there is unlikely to be flooding under the forests confounding the application.

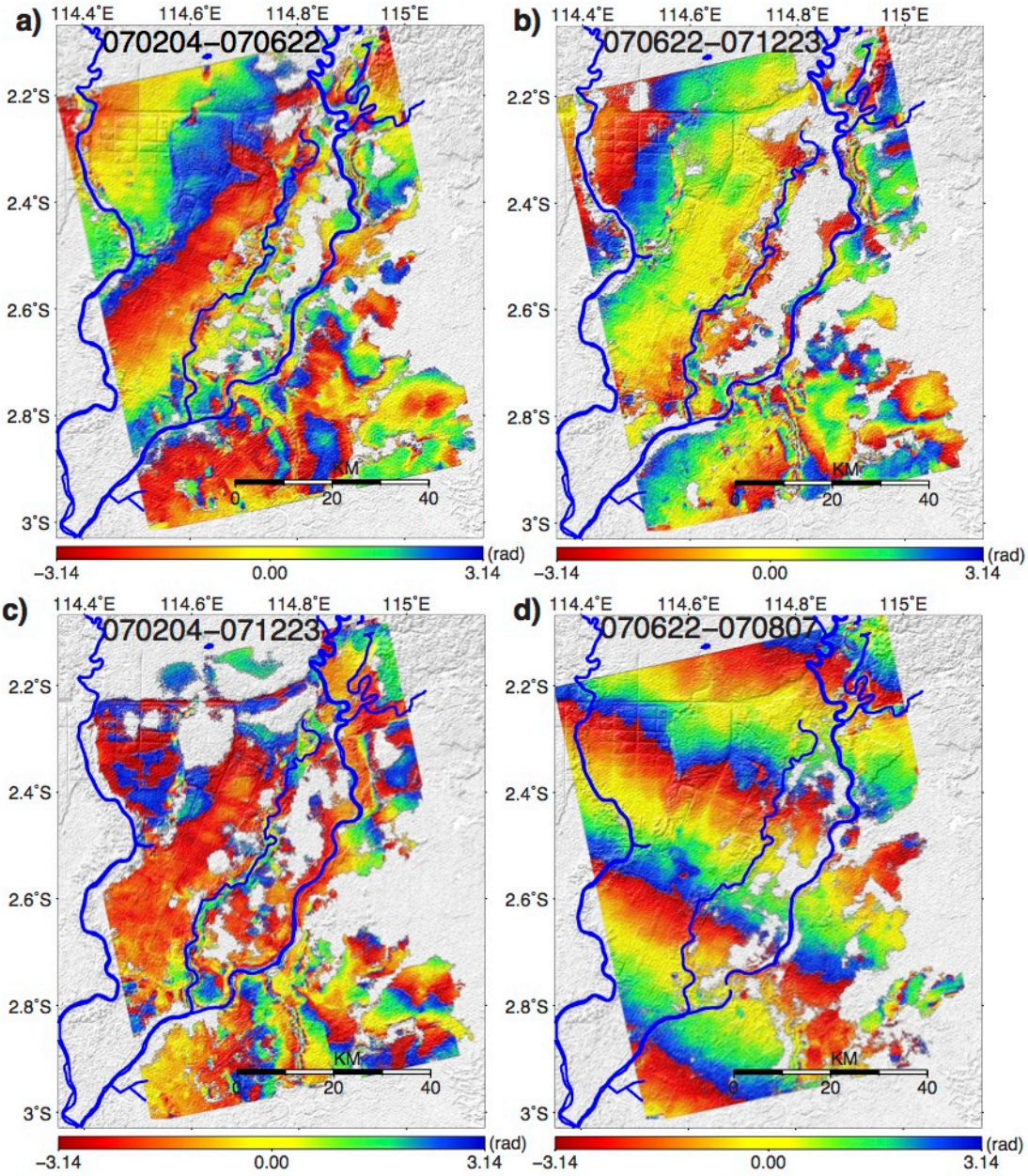

Figure 6.8 Unwrapped phase generated with images acquired in dry and wet seasons superimposed on an SRTM DEM of Block A in Ex-MRP area. Blue lines represent rivers. The phases are rewrapped so that each 2π colour cycle from red to blue represents an increase of 11.8 cm in the range from ground to satellite. In wet season (a, b, c), the water change (particularly along the river) produces apparent fringes, while it is not clear in dry season (d). a) Re-wrapped unwrapped phase from images acquired between 20070204 (wet season) and 20070622 (dry season); b) Re-wrapped unwrapped phase from images acquired between 20070622 and 20071223 (wet season); c) Re-wrapped unwrapped phase from images acquired between 20070204 and 20071223; d) Re-wrapped unwrapped phase from images acquired between 20070622 and 20070807 (dry season).

6.3.2 Phase unwrapping error

Phase unwrapping error is checked by the phase closure technique described in section 3.2.4 Phase unwrapping. Figure 6.9 and Figure 6.10 show interferograms from wet and dry seasons respectively. Clear phase jumps along the river can be observed in Figure 6.9, but none in Figure 6.10. This is because of the large fluctuations of water level between wet and dry seasons or wet and wet seasons within a year. The terrain along the rivers produces relatively narrow and complex fringe patterns due to water level changes; such complex and steep fringes are prone to cause phase jumps (Jin-Woo et al., 2009). In the dry season, due to the relatively stable water level, smoothly wrapped fringes are expected and observed in Figure 6.10, which are not vulnerable to phase jumps.

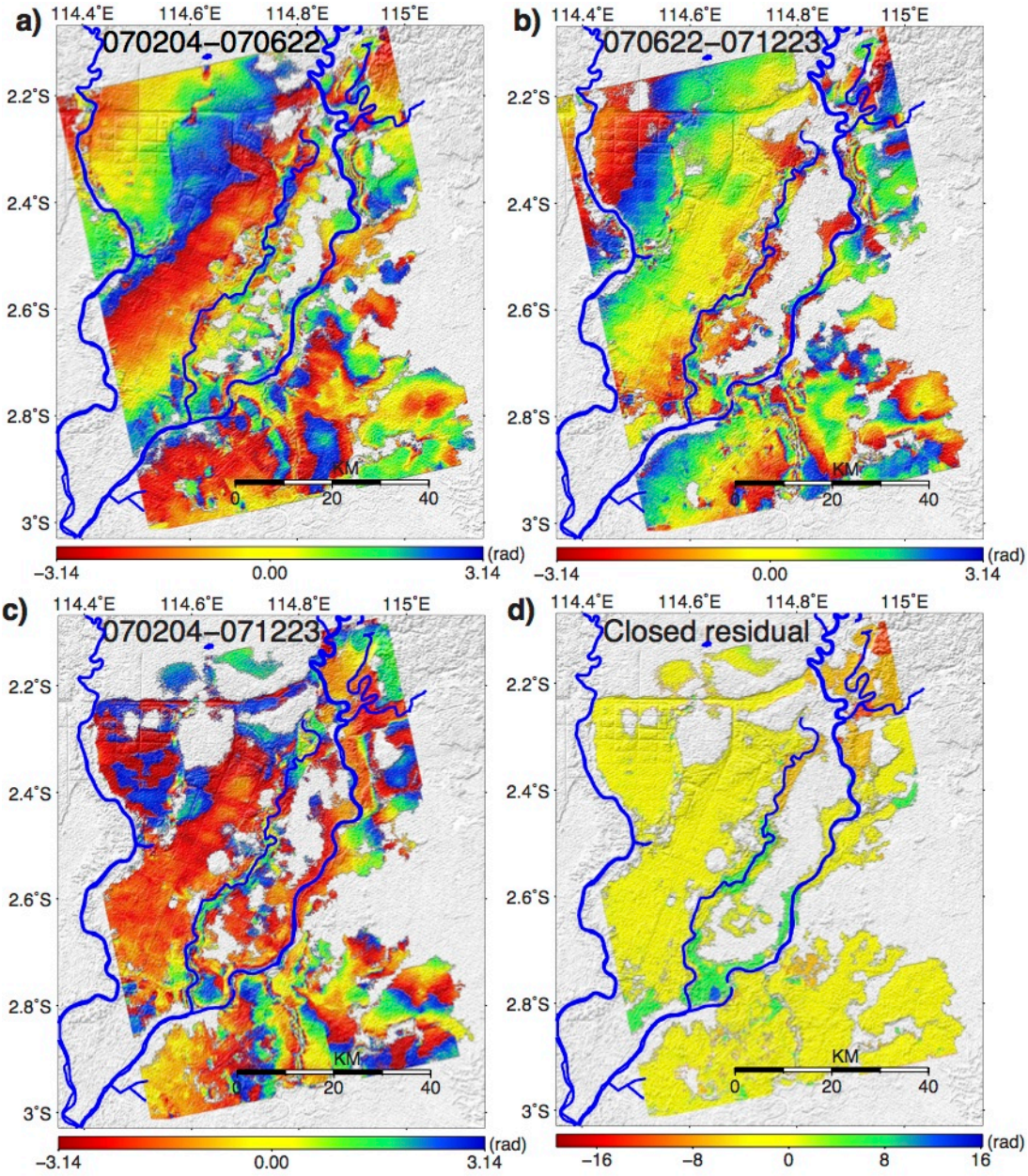

Figure 6.9 Phase unwrapping errors of unwrapped phase from wet seasons. Unwrapped phase is superimposed on an SRTM DEM of Block A in Ex-MRP area. Blue lines represent rives. The phases (a, b and c) are rewrapped so that each 2π color cycle from red to blue represents an increase of 11.8 cm in the range from ground to satellite. Phase jumps shown in d) is caused by the large fluctuations of water level between wet and dry seasons or wet and wet seasons. a) Re-wrapped unwrapped phase from image acquired between 20070204 (wet season) and 20070622 (dry season); b) Re-wrapped unwrapped phase from image acquired between 20070622 and 20071223 (wet season); c) Re-wrapped unwrapped phase from image acquired between 20070204 and 20071223; d) phase closure.

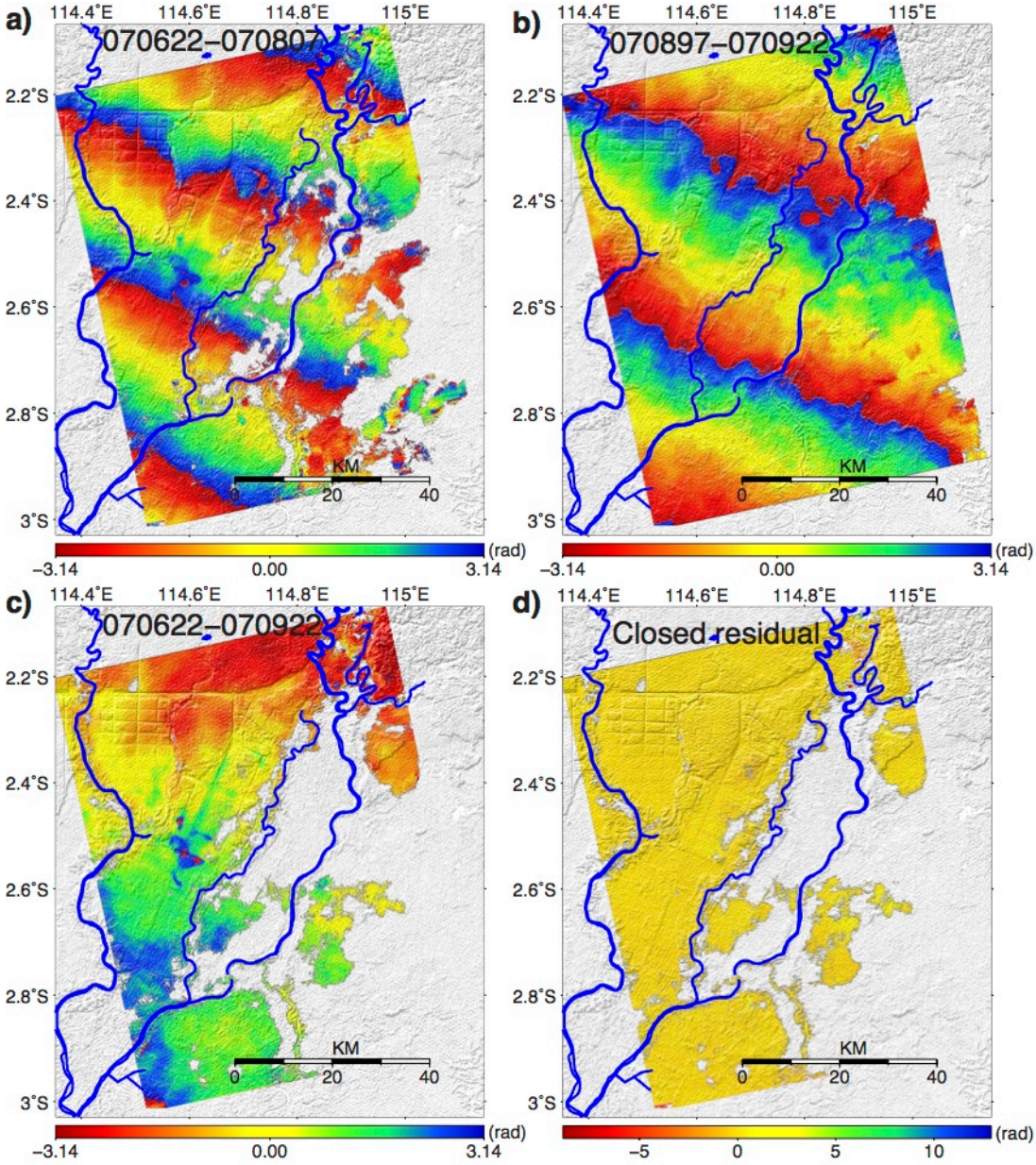

Figure 6.10 Unwrapped phase from dry seasons without any noticeable unwrapping error. Blue lines represent rivers. In the dry season, phase jumps are not easy to occur. The phases (a, b and c) are rewrapped to 2π, so that each 2π color cycle from red to blue represents an increase of 11.8 cm in the range from ground to satellite. a) Re-wrapped unwrapped phase from images acquired between 20070622 and 20070807; b) Re-wrapped unwrapped phase from images acquired between 20070807 and 20070922; c) Re-wrapped unwrapped phase from images acquired between 20070622 and 20070922; d) phase closure.

6.4. Results

6.4.1 InSAR result validation

The LOS average velocity maps and their corresponding root mean square error (RMS) maps are shown in Figure 6.11. The mean velocity has been draped on SRTM DEM shown as shaded relief.

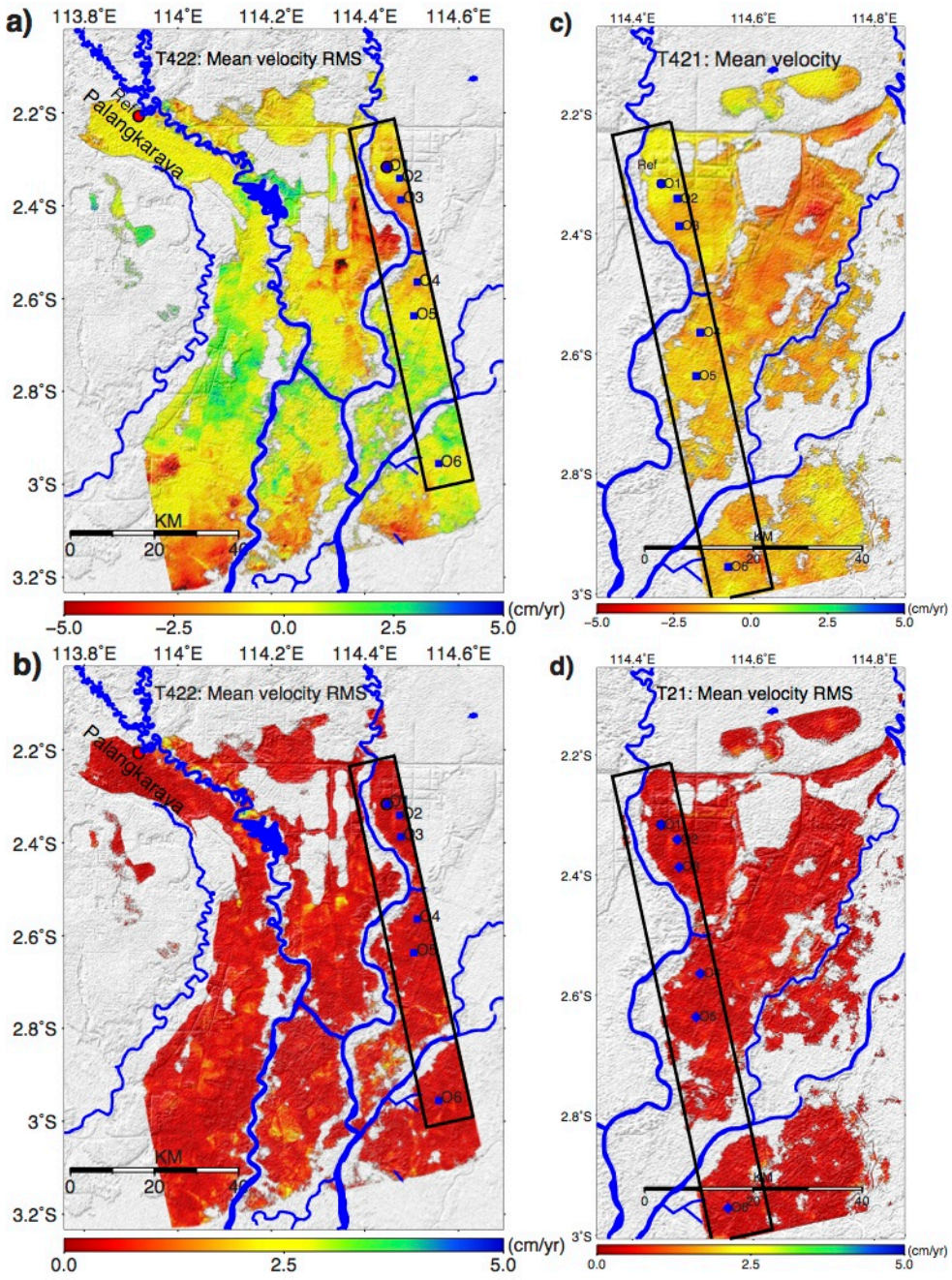

Figure 6.11 SBAS-derived LOS mean velocity map of the study area and associated RMS for Tracks 421 and 422, superimposed on an SRTM DEM shown as shade relief. Negative value means the surface moves away the satellite (i.e. subsidence). a): Mean velocity map from Track 422; b) Mean velocity RMS from Track 422; c) Mean velocity map from Track 421; d) Mean velocity RMS from Track 421. The red circle in the city of Palangkarava (Figure. a) is the deformation reference point, O1 is selected for calibration purpose and as the reference point for Track 421 as well. Blue square points (form O1 to O6) were selected in the overlapping area for validation use. The black rectangle area is the overlapping area between the two tracks, and all common points of this area are selected for correlation analysis.

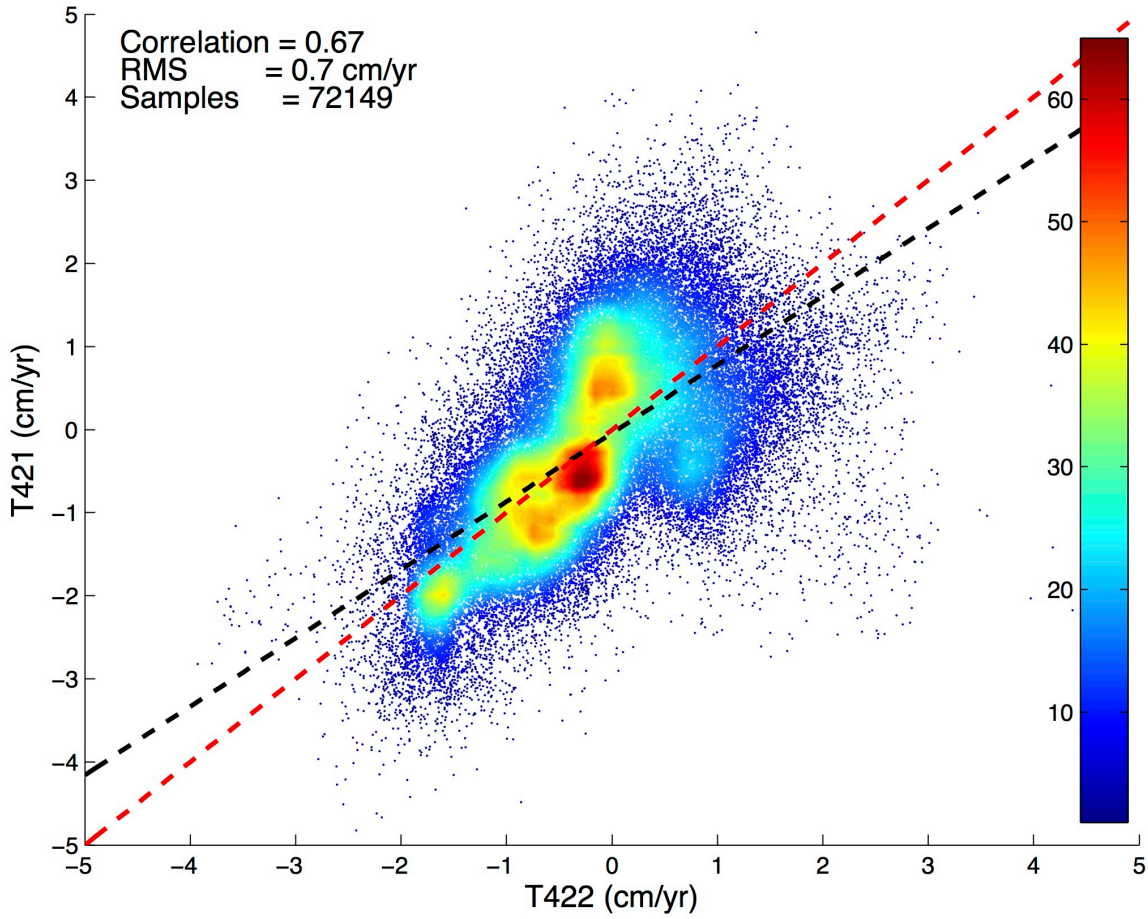

Figure 6.12 Correlation of the mean velocities between Tracks 421 and 422 within the overlapping area. This is produced by points within overlapping area of both tracks. Red line is the 1:1 line and black line is the best-fit line. The colourbar from blue to red means the density of the points. Note: Negative values represent subsidence signals. LOS velocity uncertainty from near range and far range can be ignored (See Section 3.2.1).

A good correlation and RMS error of the overlapping area between Tracks 441 and 442 are shown in Figure 6.12. Using all points within overlapping area of both tracks, the estimated RMS error is 0.7 cm/yr. The agreement between two tracks provides confidence that InSAR can be utilized to map the change in peat height and monitor the effects of restoration. The estimated LOS displacement time series (Figure 6.13) have been constructed for six randomly selected points (whose locations are shown Figure 6.11) from each track. The mean annual velocity and associated computed RMS between the linear model used in the InSAR TS package and the data are given in

Table 6.3.

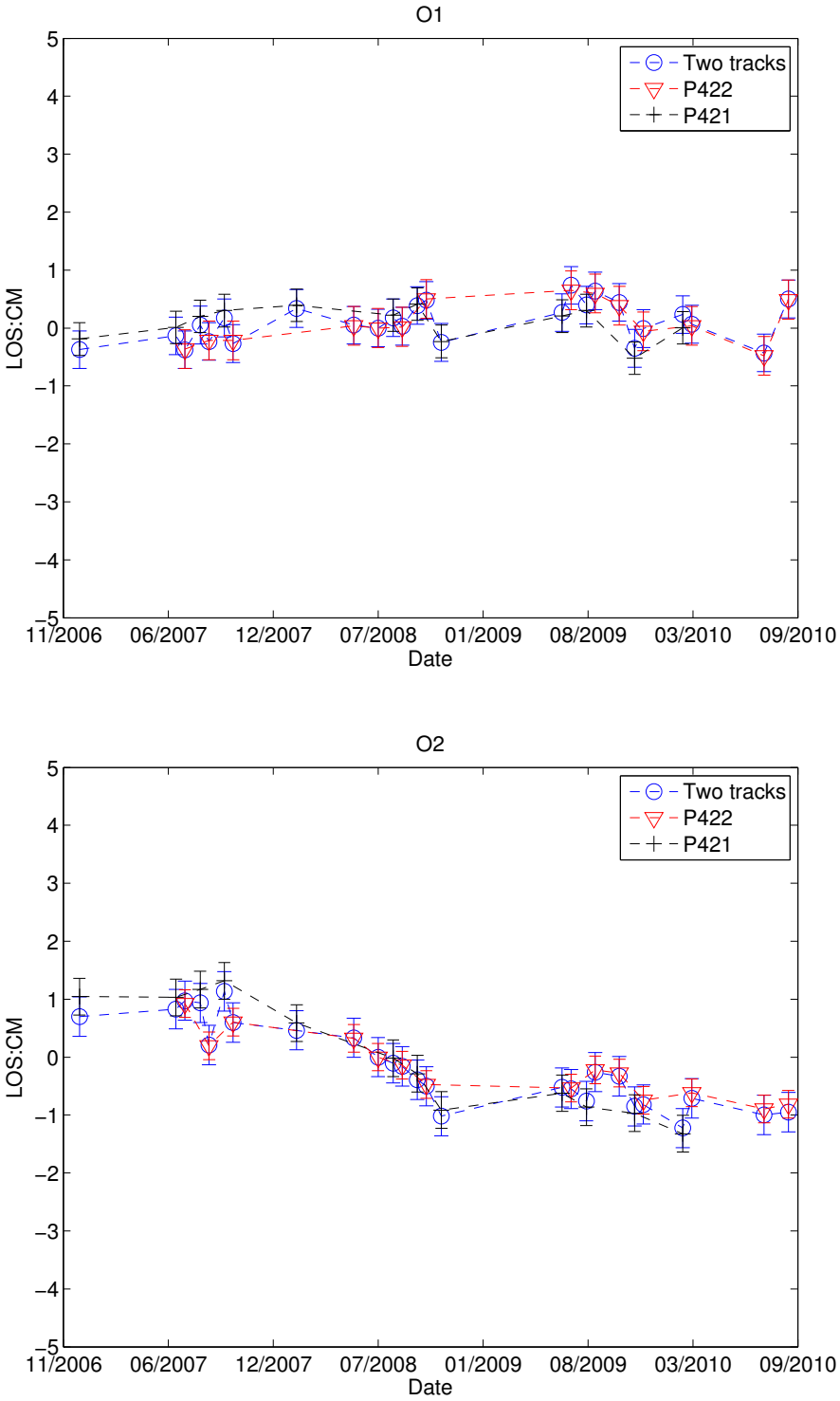

Figure 6.13a Displacement time series O1 and O2 selected within the overlapping area, shown in Figure 6.11. Red triangles represent for track 421, black crosses for track 442 and blue circles for the combination of two tracks. Each point represents one SAR image acquisition date, the reference date is 2080809 for track 421, 20070711 for track 422 and the combined tracks, and all displacement values correspond to the average of a 3 pixels by 3 pixels window and error-bars are their associated RMS values.

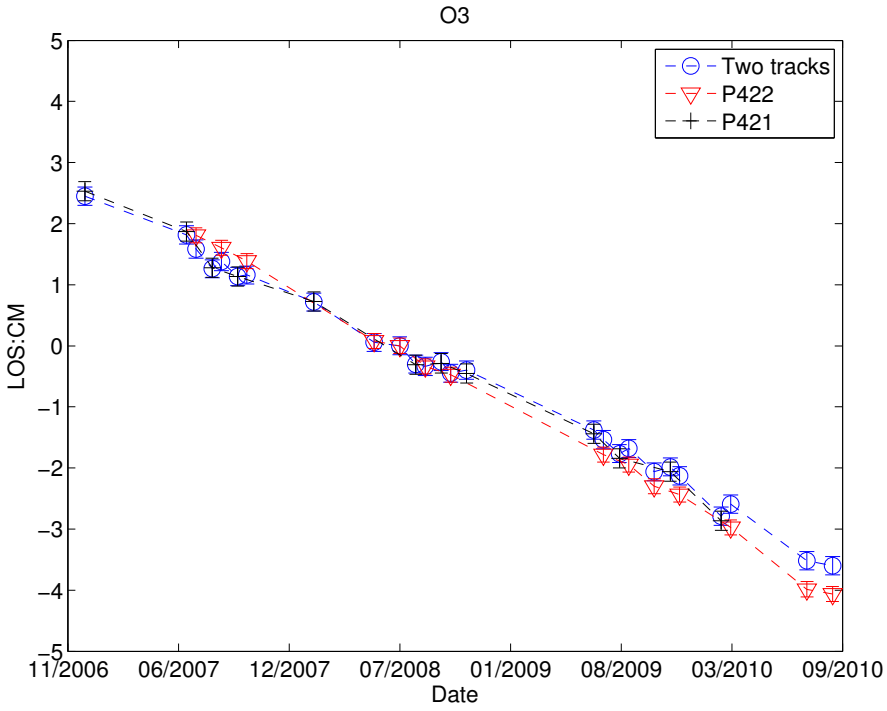

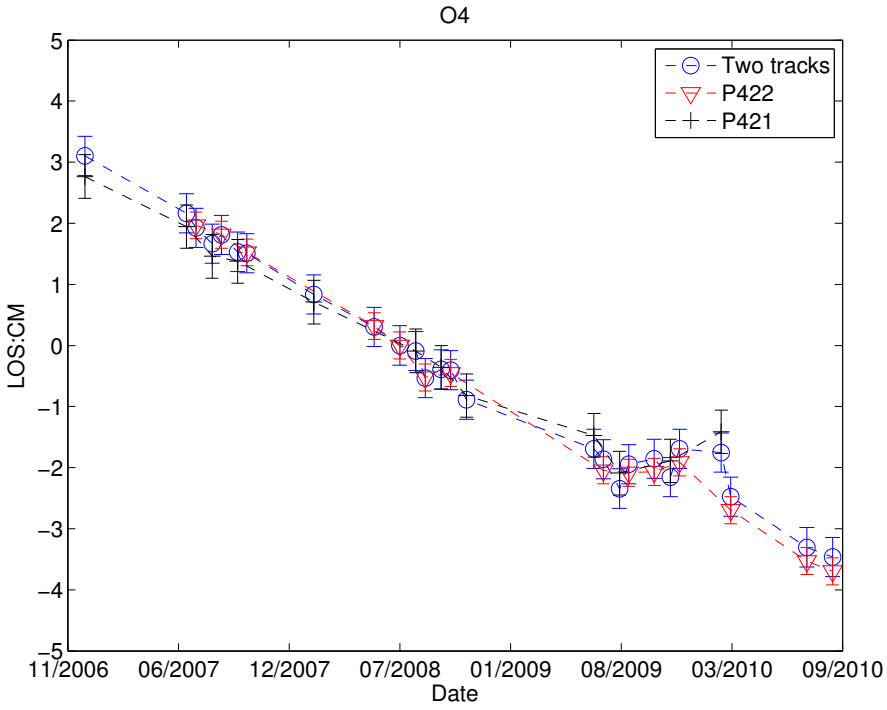

Figure 6.13a Displacement time series O3 and O4 selected within the overlapping area, shown in Figure 6.11. Red triangles represent for track 421, black crosses for track 442 and blue circles for the combination of two tracks.Each point represents one SAR image acquisition date, the reference date is 2080809 for track 421, 20070711 for track 422 and the combined tracks, and all displacement values correspond to the average of a 3 pixels by 3 pixels window and error-bars are their associated RMS values.

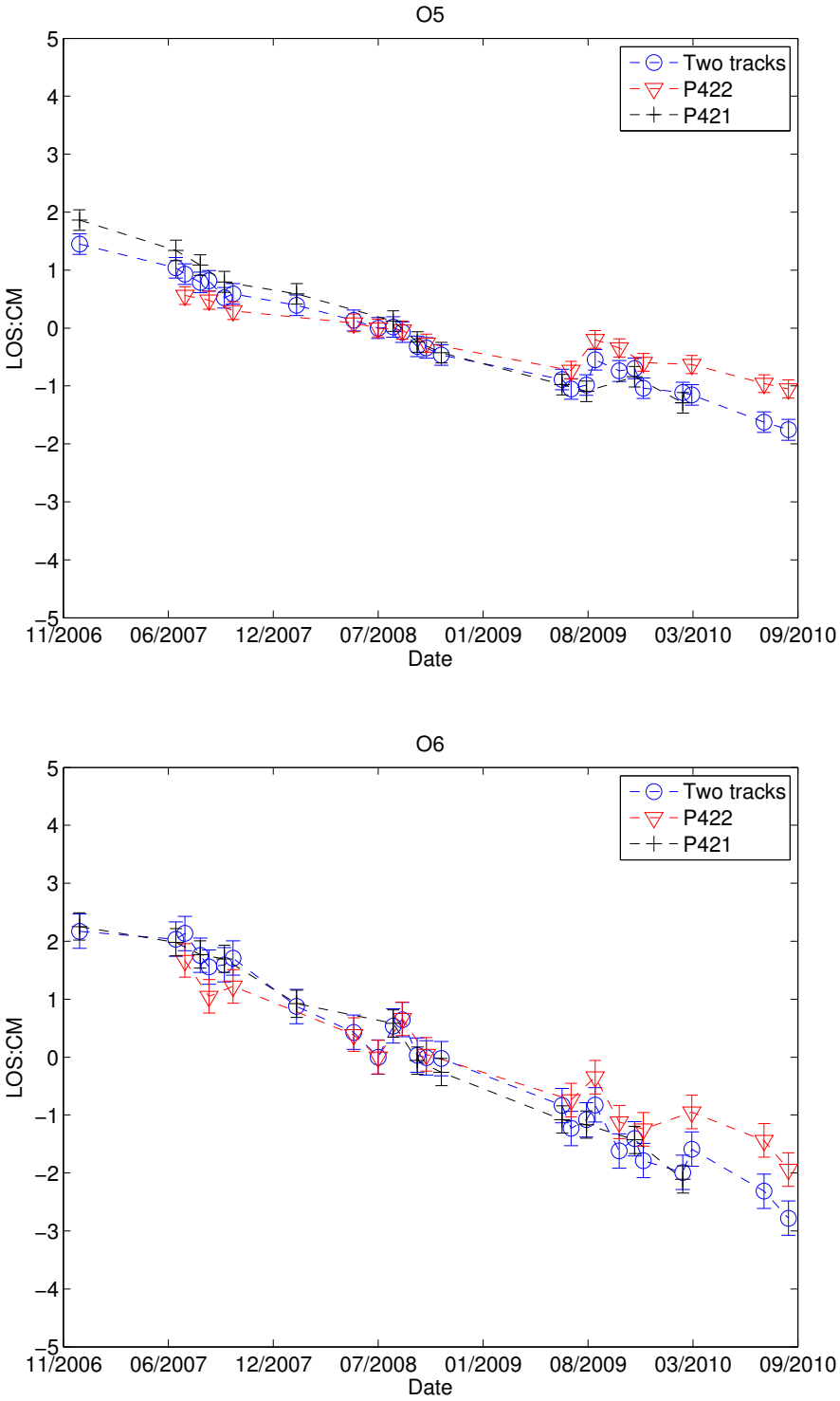

Figure 6.13c Displacement time series of six points O6 selected within the overlapping area, shown in Figure 6.11. Red triangles represent for track 421, black crosses for track 442 and blue circles for the combination of two tracks. Each point represents one SAR image acquisition date, the reference date is 2080809 for track 421, 20070711 for track 422 and the combined tracks, and all displacement values correspond to the average of a 3 pixels by 3 pixels window and error-bars are their associated RMS values.

Table 6.3 Mean velocities and RMS (both in cm/yr) over selected points.

Points	T421 Mean Vel	T422 Mean Vel	Combined Mean Vel	T421 RMS	T422 RMS	Combined RMS
O1	-0.05	0.13	0.12	-0.28	-0.33	-0.33
O2	-0.89	-0.46	-0.59	-0.32	-0.24	-0.34
O3	-1.63	-1.85	-1.60	-0.16	-0.12	-0.15
O4	-1.53	-1.77	-1.70	-0.36	-0.22	-0.32
O5	-1.00	-0.46	-0.80	-0.18	-0.15	-0.18
O6	-1.43	-1.00	-1.41	-0.23	-0.29	-0.30

We can also combine the two tracks to produce the final mean height change rate map and recover displacement history. This was done with 26 SAR images acquired from 20th December 2006 to 1st September 2010. Within the overlapping area, SAR images from both tracks are used in time series analysis; thus nearly double the observations are used in time series analysis with an increased temporal resolution, which in turn makes it a better estimate of the mean rate and displacement history. Outside the overlapping area, SAR images only from one track are used. The generally good internal consistency between time series tracks in the overlapping images gives confidence that this area is correctly modelled.

The resultant mean velocity map and its RMS map are shown in Figure 6.14. The correlation between the combined and individual tracks is presented in Figure 6.15. Each correlation map is generated between individual and combined track. The combined track differs from individual track in estimating the mean height change rate within the overlapping area of both tracks. For Tracks 441 and 442, the correlation is up to 0.82 and 0.91, with an RMS of 0.3 cm/yr and 0.4 cm/yr respectively, suggesting the confidence of the final mean velocity result. The time series comparison is shown in Figure 6.13 and a quantitative analysis is provided for six points within the overlapping area in

Table 6.3. Combing the mean velocity correlation analysis and the comparison of time series, suggest that InSAR derived mean velocities and time series are reliable. The following restoration effect analysis and discussion will be based on the combined mean velocity map and time series.

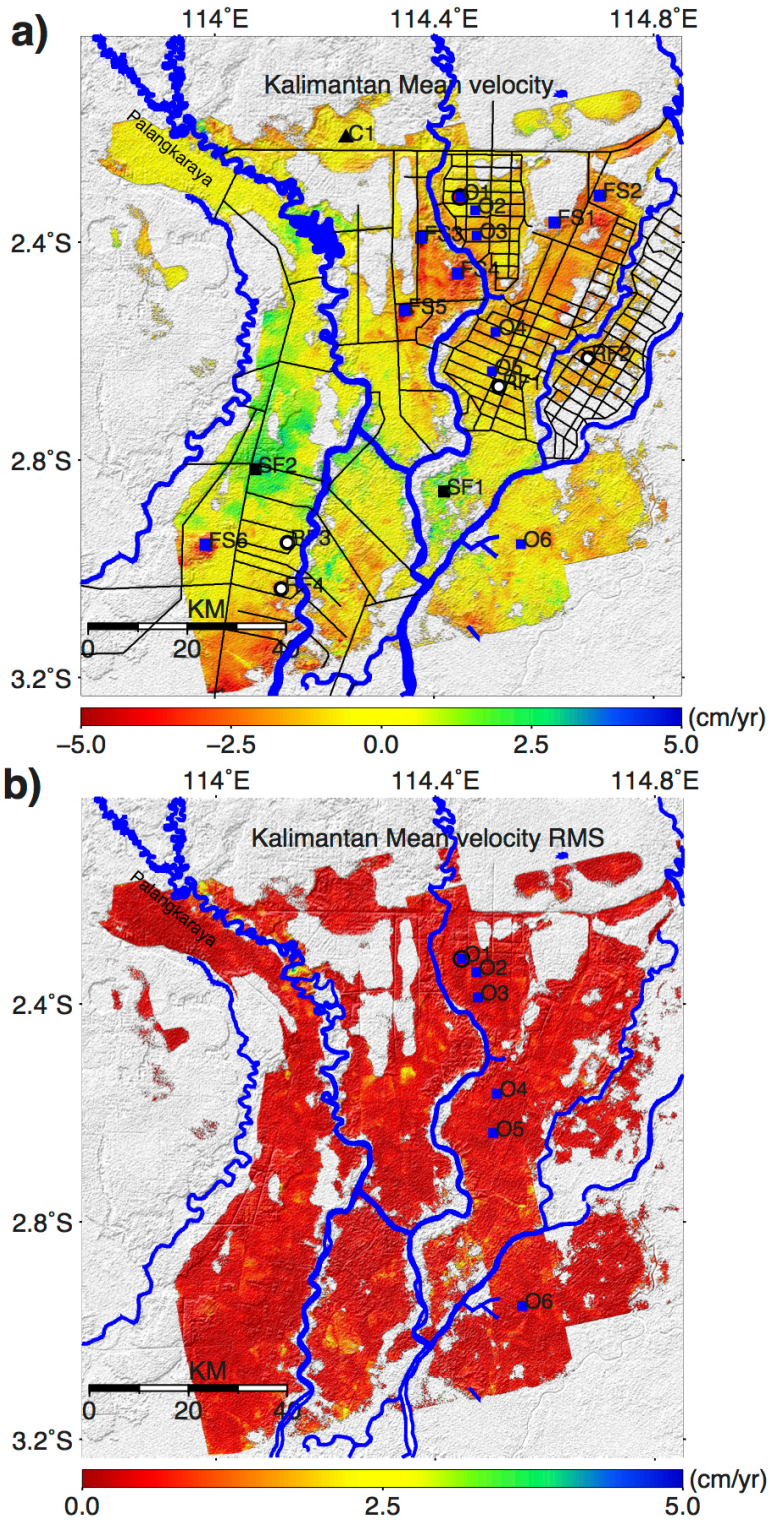

Figure 6.14 Two tracks combined SBAS-derived LOS mean peat height change rate map and associated RMS for the study area. Negative value means loss of topographic height in the LOS, positive value means gain in the LOS. The red circle (labeled as O1) is the deformation reference point. Blue square points (from O1 to O6) were selected in the overlapping area for validation use, and other labeled points (such as C1, FS1, RF1, etc.,) were selected in different landscape area for time series analysis.

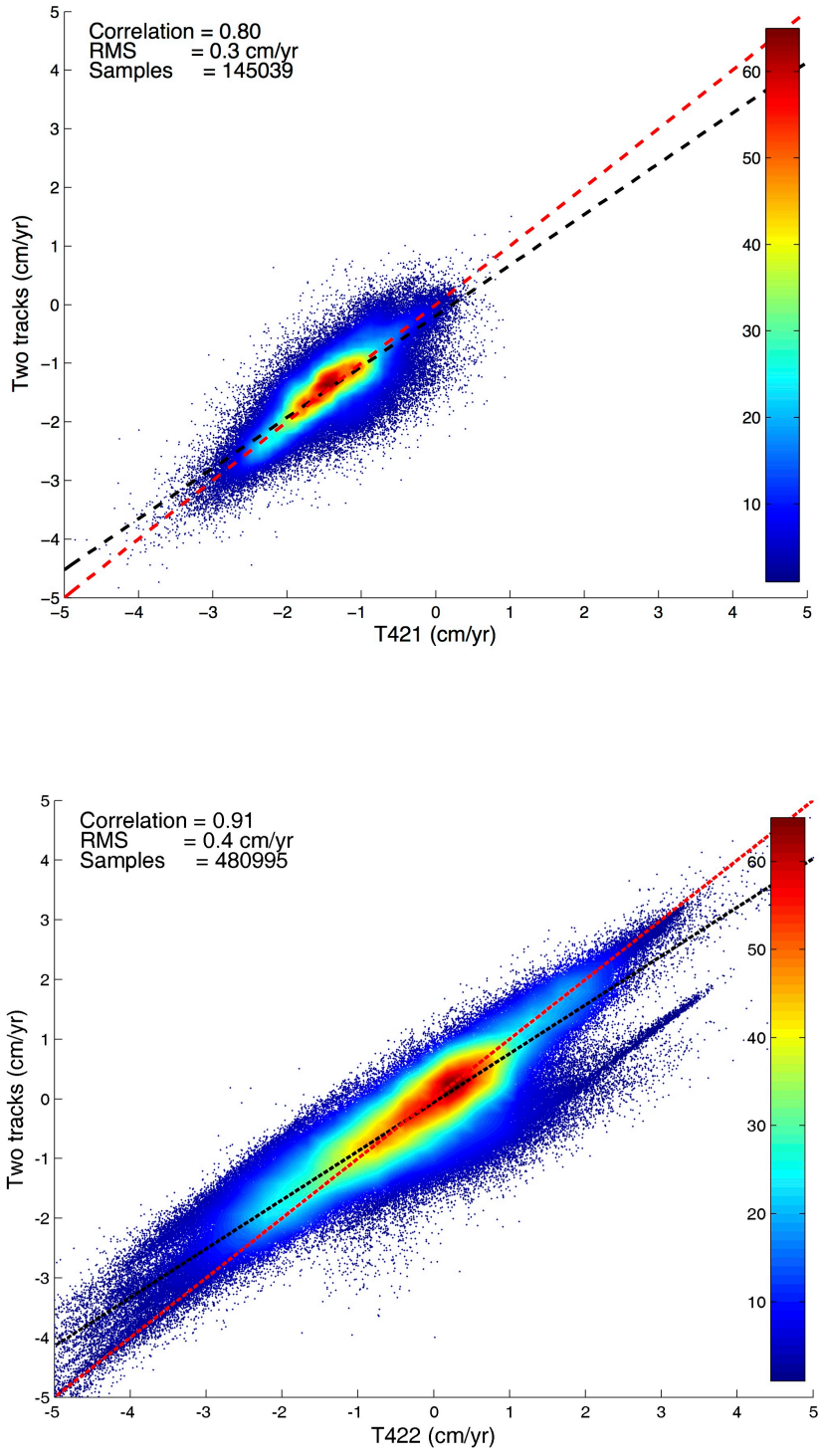

Figure 6.15 Correlation of the mean velocities. Each correlation map is generated between individual and combined track. The combined track differs from individual track in estimating the mean height change rate within the overlapping area of both tracks. Each correlation map suggests the confidence of the final mean velocity result. The red line is the 1:1 line. The colourbar from blue to red means the density of the points. Note: negative values represent the surface move away the satellite (i.e. subsidence).

Figure 6.16 shows land cover for Year 2009 overlying the InSAR-derived mean velocity, and from this composite thirteen points were selected for further time series analysis of different types of areas, e.g. cleared area, rice field, fire scars and secondary swamp forest.

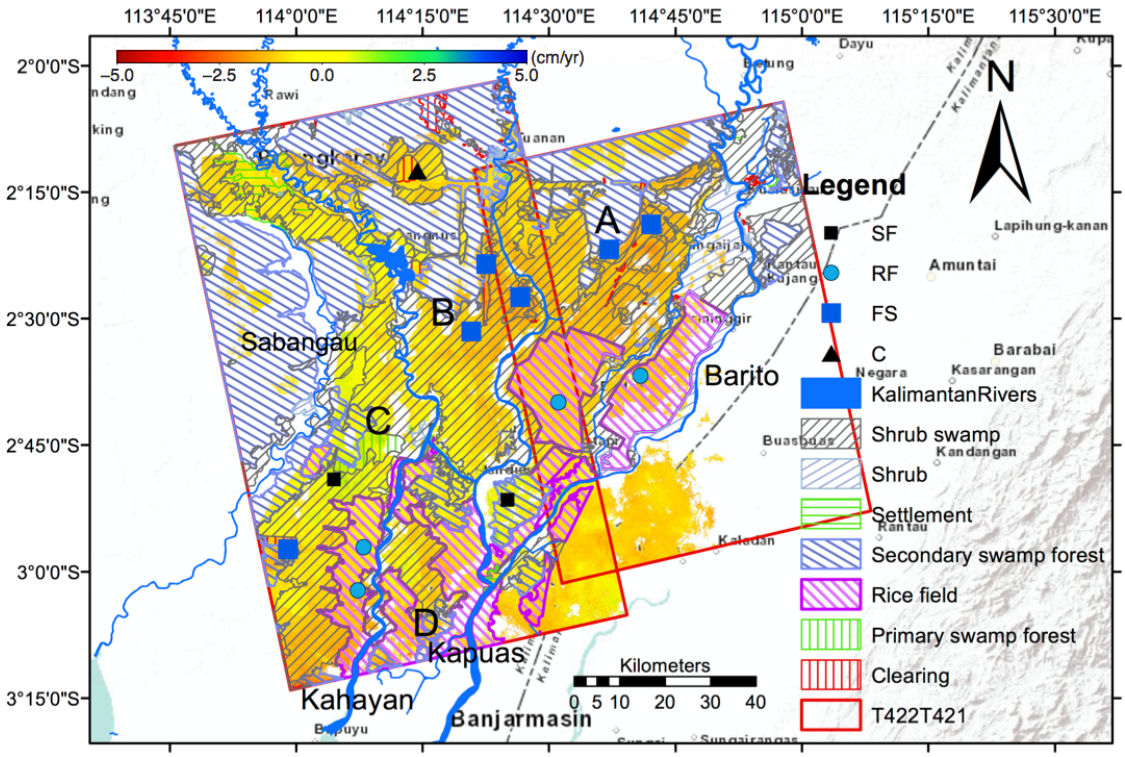

Figure 6.16 Land cover map for Year 2009 (adapted from (Kementerian Kehutanan Republik Indonesia, 2012)) superimposed on the LOS mean peat height change rate map, the colour of the velocity map is identical to that in Figure 6.14.

Figure 6.14 shows the InSAR results have a good spatial coverage across the study area, covering various landscapes (Figure 6.16). Note that coherent pixels are almost lost in secondary swamp forest, such as the western part of Block C, the northern part of Block B, and a small area of in the northern part of Block A. This is because of high density of forest means that the return radar signals are primary from the canopy of the forest. Therefore temporal decorrelation occurs easily.

The mean velocity (Figure 6.13a) mainly ranges from -5 cm/yr to 2.5 cm/yr. The mean velocity varies spatially within one type of land cover and differs from one type to another. In the corner of northwest of this study area, the

Palangkaraya city remains relatively stable during the observation period; the drained shrub swamp area has the largest subsidence rate in Block B. The rice field areas in Block A and C have a different pattern of subsidence, and the subsidence rate is up to ~ 5 cm/yr in Block D. The cleared area has relatively smaller subsidence rates ranging from 0 to 2 cm/yr. Signals in secondary swamp forest area show uplift in the observation time, with rates of up to ~ 3 cm/yr. The RMS (Figure 6.14b) of the average velocity shows small variations (most smaller than 1 cm/yr), and no obvious error is observed.

6.4.2 Monitoring the restoration effects

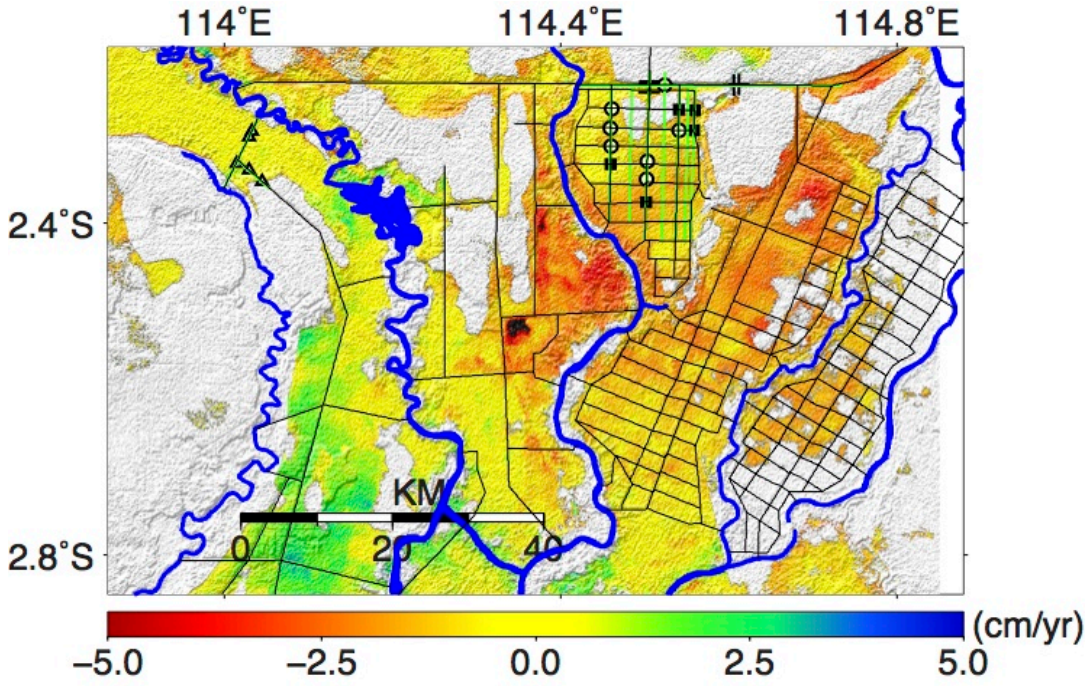

Figure 6.17 Profiles and dams overlays on mean peat height change map. Details of profiles and dams are shown in Figure 6.7

Ten profiles of InSAR-derived mean velocities are shown in Figure 6.18. Details of profiles and dams are shown in Figure 6.7. In Figure 6.18a, between the two dams constructed before January 2005 (denoted by red rectangles), Profile AA' shows that peatland along the channel is subsiding with a rate ranging from ~ -0.5 to - ~ -1.0 cm/yr; the closer to the two dams (indicated by red rectangles),

the smaller the subsidence rates. It is clear that the subsidence rates in unblocked areas are much higher than those in blocked areas, especially near the crossing of the Eastern channel at the distance of 30km (denoted by a dashed blue line), which is up to -3 cm/yr.

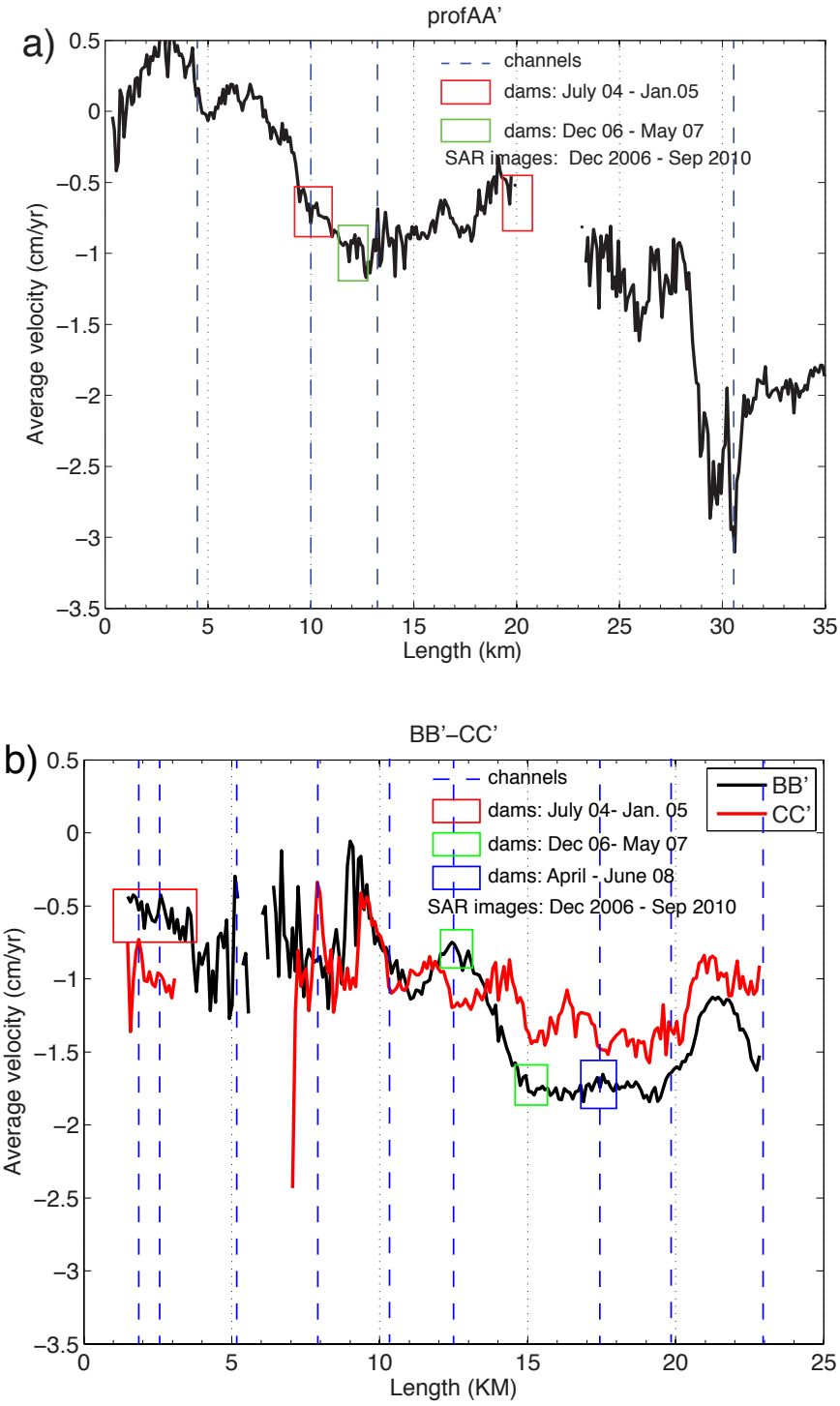

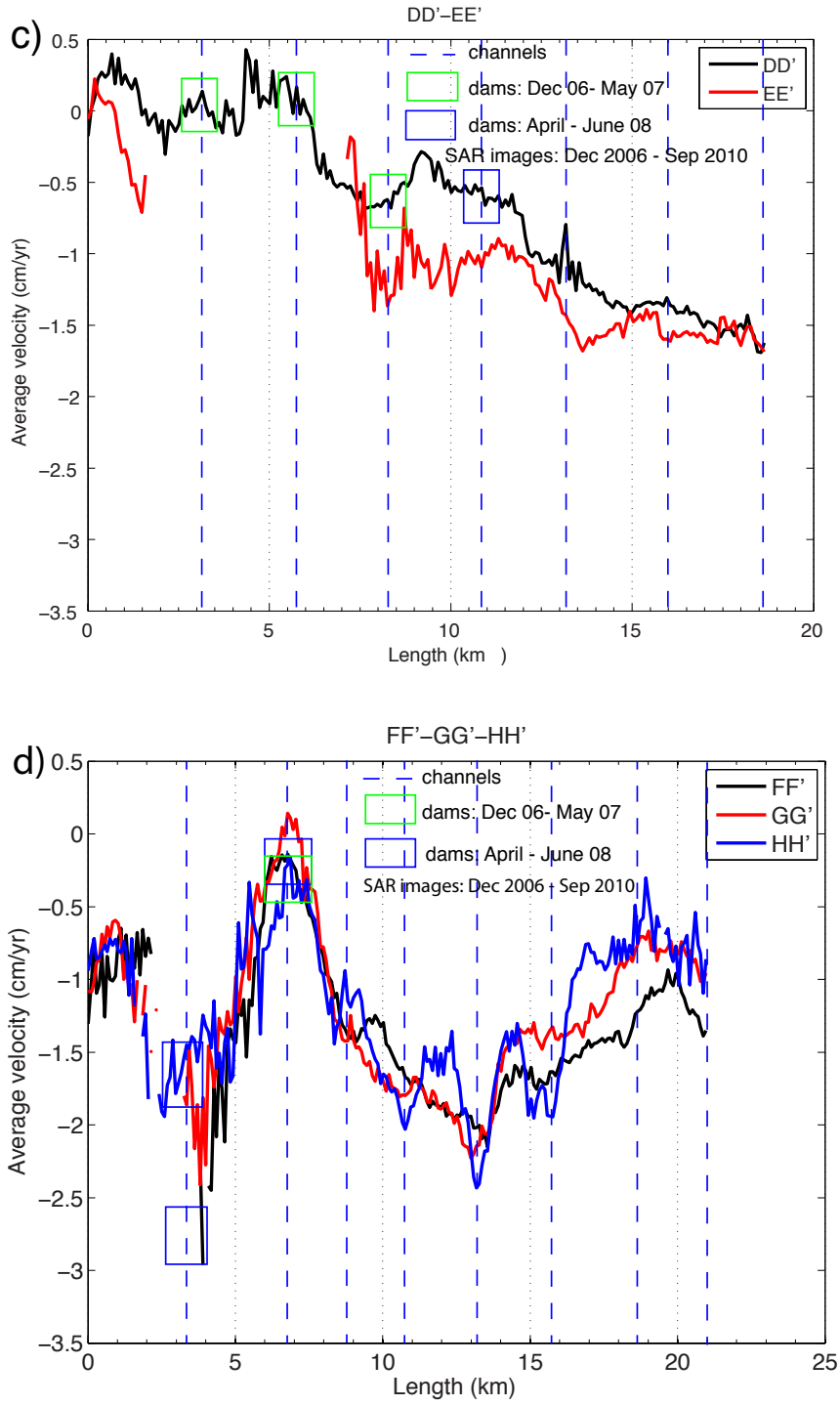

Figure 6.18 Mean velocity profiles in Block A. Note: (1) A gap of signals means there is no coherent pixel of the profile; (2) Rectangles represent dams whose construction periods are also labeled; (3) Dashed blue lines indicate channels; and (4) Dams show great potential on reducing the subsidence rate of peatland, and a successful dam could stop the subsidence rate and raise the ground water level. a) Profile from A to A'; b) Profile from B to B', and C to C'; c) Profile from D to D', and E to E'; d) Profile from F to F', G to G', and H to H'.

Figure 6.18b shows Profiles BB' and CC'. Although there are a total of six dams (three types) along Profile BB', the peatland in the channel was still losing height during the observation period. Near the dams constructed between July 2004 and January 2005 (denoted by blue crosses in Figure 6.7a and a red rectangle in Figure 6.18b), the subsidence rates of BB' (~ -0.5 cm/yr) are less than CC' (~ - 1.0 cm/yr). Both profiles show similar fluctuation signals at the distance between 7km and 12km, just north to the first dam constructed in the period between December 2006 and May 2007 (denoted by a yellow circle in Figure 6.7a and a green rectangle in Figure 6.18b). At the distance between 13 km and 23 km, the subsidence rate of Profile CC' is smaller than that of Profile BB'; the rate of BB' dropped from ~ - 1 cm/yr to ~ -2.0 cm/yr and the rate of CC' decreased to ~ -1.0 cm/yr from to ~ -1.5 cm/yr.

Figure 6.18c shows Profiles DD' and EE' with a continuously decreasing trend from ~ 0.5 cm/yr to ~ -1.8 cm/yr; the decreasing rate of Profile EE' is relatively higher than that of Profile DD'. Within the first 6 km, Between the first two dams constructed in the period from December 2006 to May 2007 (denoted by black squares in Figure 6.7a and green rectangles in Figure 6.18c), the rate of profile DD' remains in the same level of 0 cm/yr. At the distance greater than 6 km, the subsiding rate of the peatland increased, especially to the south of the dam built in April – June 2008 (indicated by blue rectangles).

Figure 6.18d shows similar profiles FF', GG' and HH'. Within the first 2 km, the subsiding rates are between -0.5 and -1.0 cm/yr. Close to the first two dams constructed in April - June 2008 (denoted by blue rectangles), the subsidence rate dropped to -2 cm/yr for Profiles GG' and HH', and to -3 cm/yr for Profile FF'. When reaching to the two dams in the south (denoted by a green rectangle and a blue rectangle respectively), all the three profiles show a subsidence rate close to zero, suggesting that peatland was no longer losing height in this local area. All the profiles exhibited an increasing subsidence rate with a peak of up to -2.5 cm/yr at the distance of 13 km, and then the subsidence rate started to decrease when moving towards the southern end of the profiles.

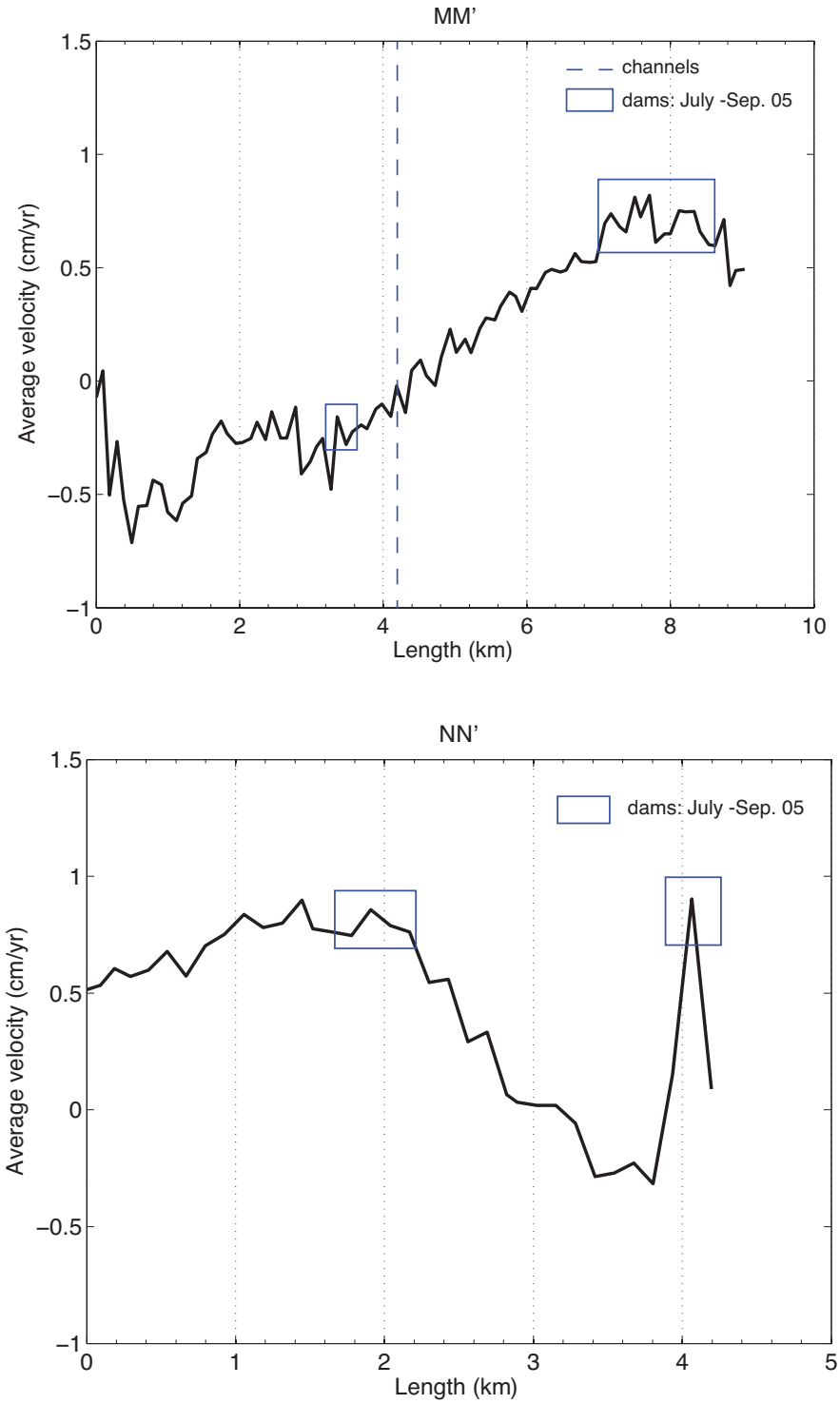

Figure 6.19 Mean velocity profiles in Block C. The dams have shown great potential in stopping peatland subsidence and helped restore the water table. a) Profile from M to M'; b) Profile from N to N'. Note: SAR images are from December 2006 to September 2010.

Figure 6.19 shows two profiles in Block C with clear uplift signals along the channels. Profile MM' shows a subsidence rate of up to ~ -0.7 cm/yr at the distance 0.5 km, in the southwest of the first dam (denoted by the smaller blue rectangle). The surface exhibited uplift signals with an increasing rate from SW to NE along Profile MM' until it reached to the two dams constructed in 2005 (indicated by the bigger blue rectangle) with an uplifting rate of ~ 0.8 cm/yr. Since this channel is blocked by two adjacent dams with a short distance, uplift signals with similar rates can be observed between these two dams. Profile NN' exhibited a different pattern (Figure 6.19b). The uplift rates increased from NW to SE with a maximum of ~ 0.9 cm/yr in the neighboring area of the first dam (indicated by the bigger blue rectangle), followed by a decrease to ~ -0.3 cm/yr at the distance of 3.8 km, and then reached to the highest value of 0.9 cm/yr in which the second dam is located.

6.4.3 Peatland without restoration

Figure 6.20 shows land cover changes from 2006 to 2009. Thirteen points distributed in various land uses are selected for investigating the movement history and change rates.

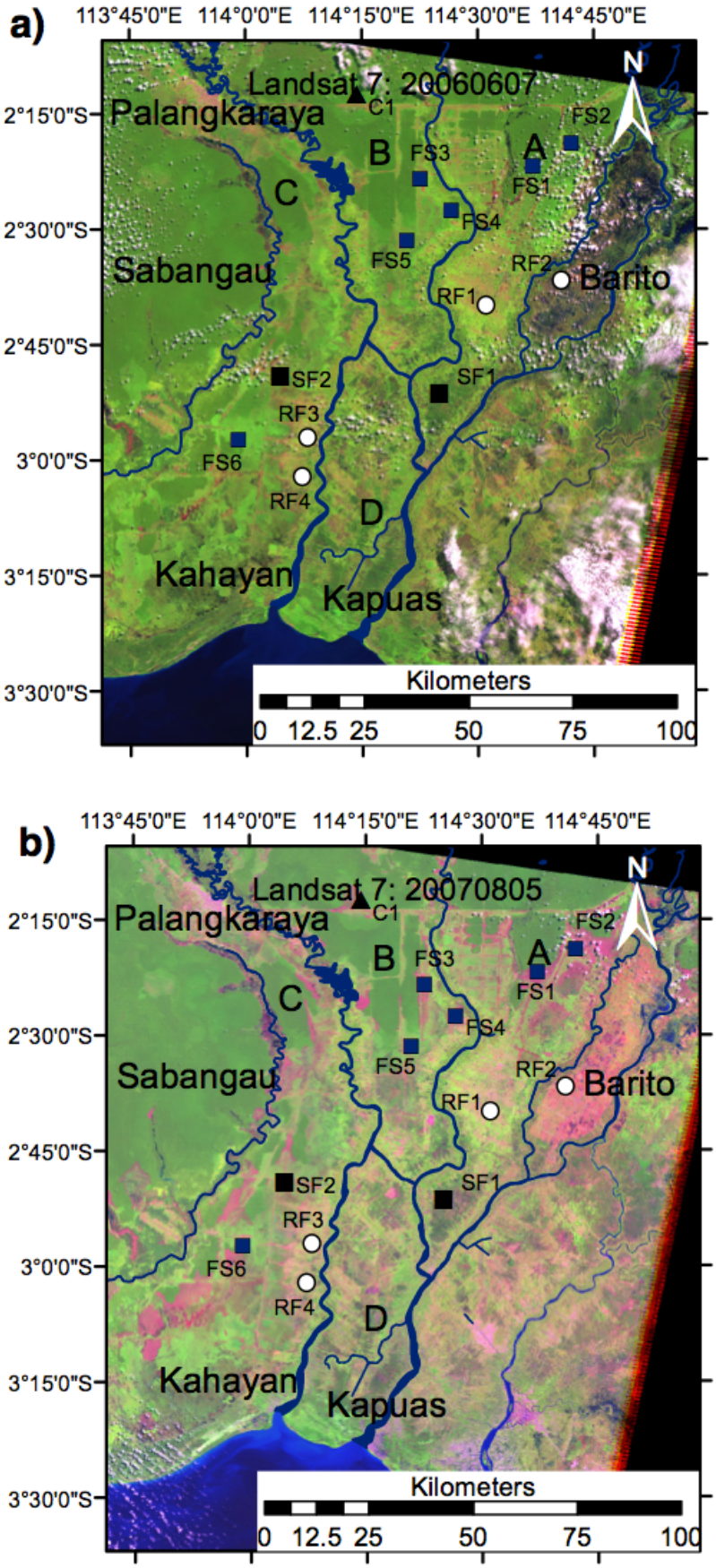
a)
113°45'0"E
114°0'0"E
114°15'0"E
114°30'0"E
114°45'0"E
2°15'0"S
2°30'0"S
2°45'0"S
3°0'0"S
3°15'0"S
3°30'0"S
N
Landsat 7: 20060607
Palangkaraya
C1
FS2
B
FS3
A
FS1
C
FS4
FS5
RF2
Barito
Sabangau
RF1
SF2
SF1
RF3
FS6
RF4
D
Kahayan
Kapuas
Kilometers
0 12.5 25 50 75 100
b)
113°45'0"E
114°0'0"E
114°15'0"E
114°30'0"E
114°45'0"E
2°15'0"S
2°30'0"S
2°45'0"S
3°0'0"S
3°15'0"S
3°30'0"S
N
Landsat 7: 20070805
Palangkaraya
C1
FS2
B
FS3
A
FS1
C
FS4
FS5
RF2
Barito
Sabangau
RF1
SF2
SF1
RF3
FS6
RF4
D
Kahayan
Kapuas
Kilometers
0 12.5 25 50 75 100

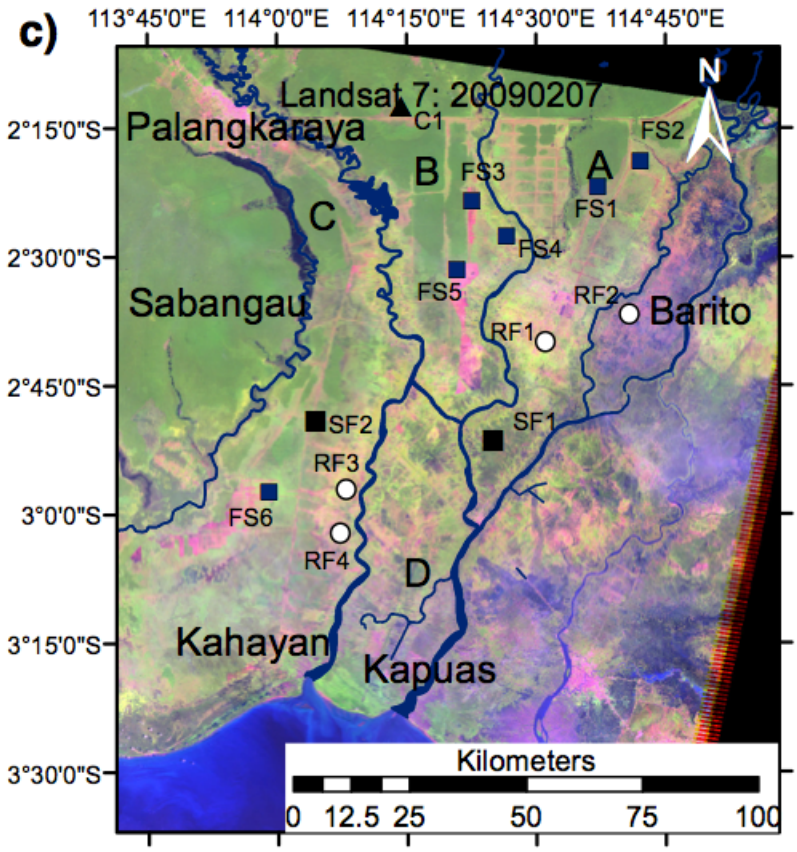

Figure 6.20 Land cover change over the study area during the period from 20060607 to 20090206. The background RGB Landsat images acquired on different dates are stacked with Bands 5-4-3 (USGS, 2013). Peat swamp forest is shown in green, and burn scars in purple (Page et al., 2002; Jaenicke et al., 2011). Thirteen points distributed in various land uses are selected for investigating the movement history and change rates.

Point C1 (Figure 6.21a) in the cleared area shows peat height decreasing at an average rate of -0.8 cm/yr with an increasing trend. All six points in fire scars (FS, Figure 6.21b, c, d) present high subsidence rates, with a range of -2.5 cm/yr (FS2, Figure 6.21b) to -7.7 cm/yr (FS5, Figure 6.21d). FS1, FS2, FS3 and FS4 exhibited a constant subsidence rate of -2.6, -2.5, -4.0 and -4.2 cm/yr respectively (Figure 6.21 b and c). FS5 had the largest subsidence rate, and it subsided 17 cm from the dry season of 2007 to 2008, and 8 cm from 2008 to 2010, totally 25 cm from 20070709 to 20100901. FS6 is relatively stable from 2007 to 2008, but it subsided 10 cm in the following two years after the dry season of 2008 (Figure 6.21d).

Points in the rice field (RF, Figure 6.21e and f) area exhibited relative stable rates ranging from -1.0 to -2.9 cm/yr. RF1 and RF2 had constant subsidence rates of -1.0 and -2.2 cm/yr respectively (Figure 6.21e). RF4 shows a decrease of 6 cm during the period between dry season of 2007 and 2009, and additional 6 cm is observed between dry seasons of 2009 to 2010 (Figure 6.21f). The two points (SF1 and SF2) in swamp forest both show uplifting signals, with a rate of 1.4 and 2.7 cm/yr respectively (Figure 6.21g).

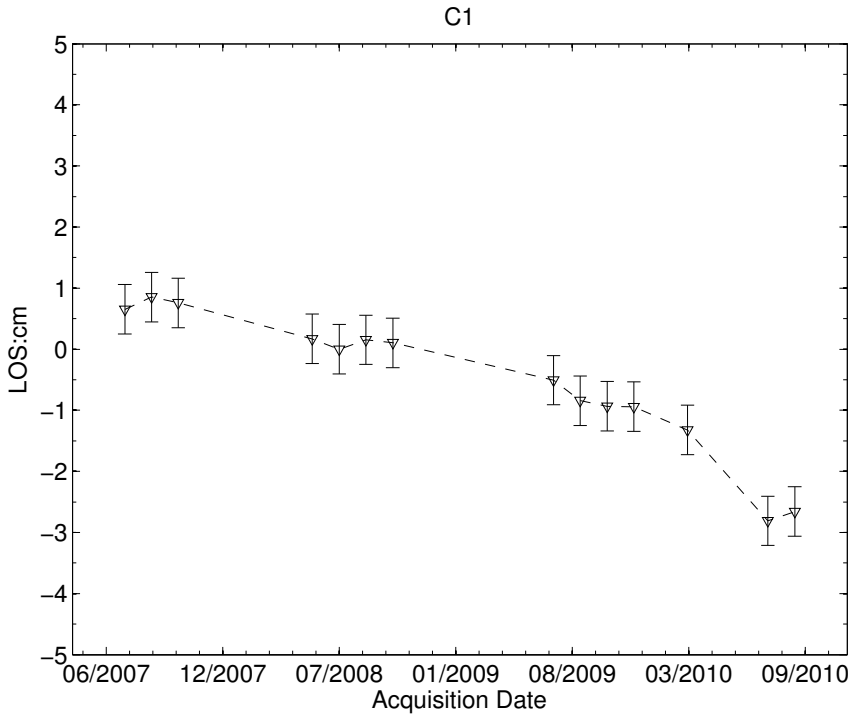

Figure 6.21a Time series of the point C1 selected within cleared area in the study area, as shown in 6.20. Each point presents one SAR image acquisition date. Each value corresponds to the average of a 3 pixels by 3 pixels window and the errorbar on each point is its associated RMS.

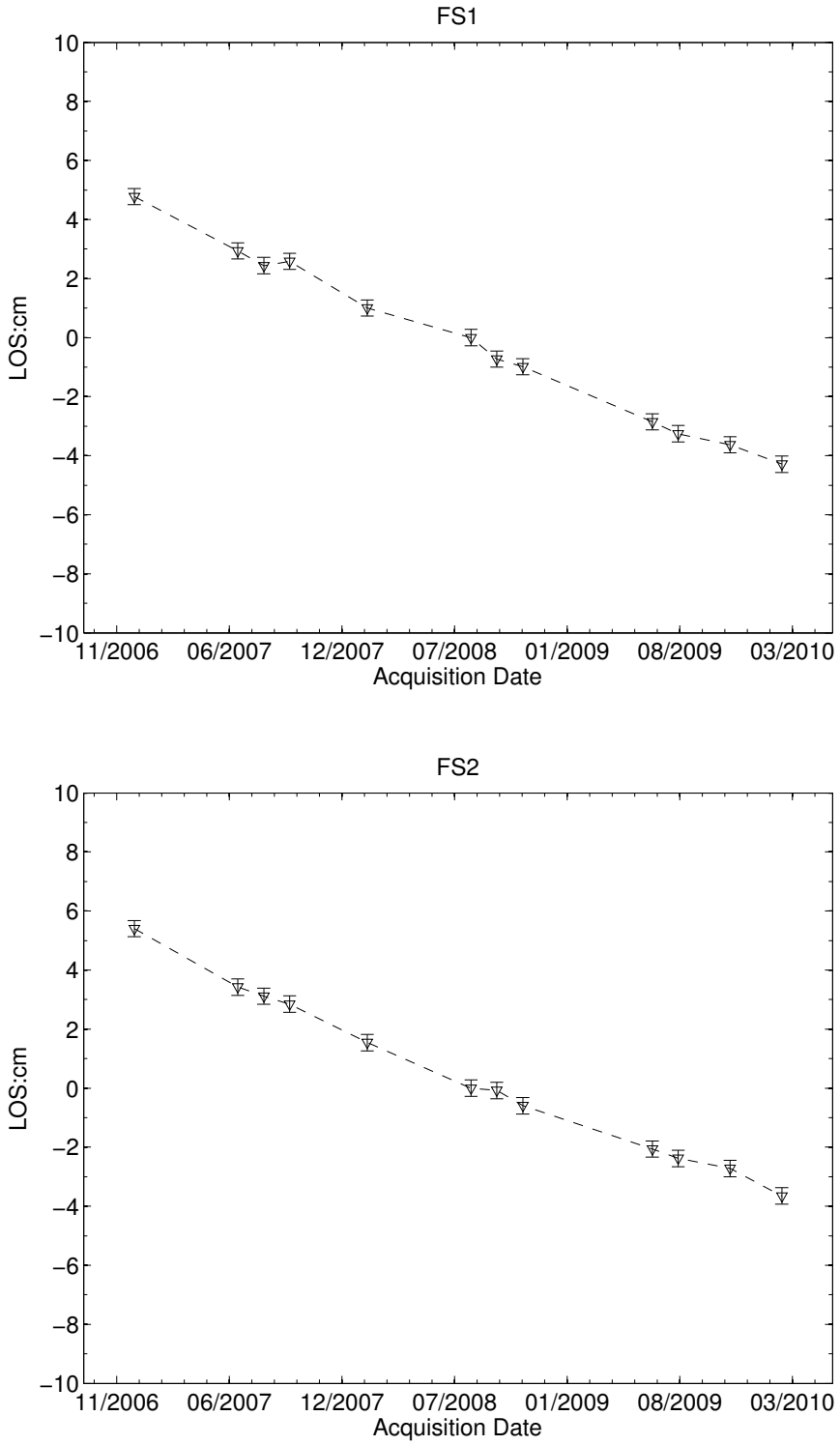

Figure 6.21b Time series of the points FS1 (up) and FS2 (bottom) selected within fire scar area in the study area, as shown in 6.20. Each point presents one SAR image acquisition date. Each value corresponds to the average of a 3 pixels by 3 pixels window and the error bar on each point is its associated RMS.

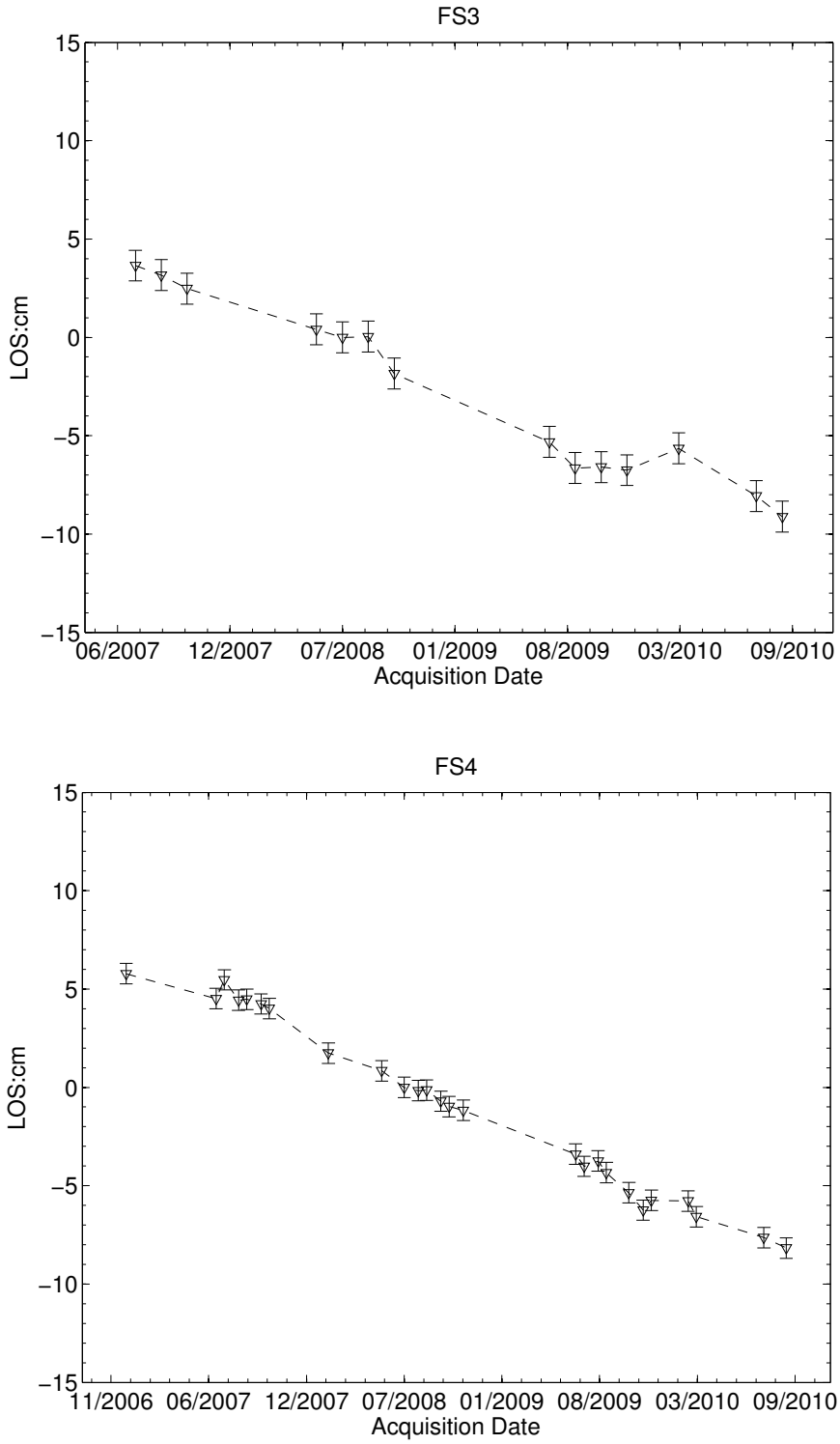

Figure 6.21c Time series of the points FS3 (up) and FS4 (bottom) selected within fire scar area in the study area, as shown in 6.20. Each point presents one SAR image acquisition date. Each value corresponds to the average of a 3 pixels by 3 pixels window and the errorbar on each point is its associated RMS.

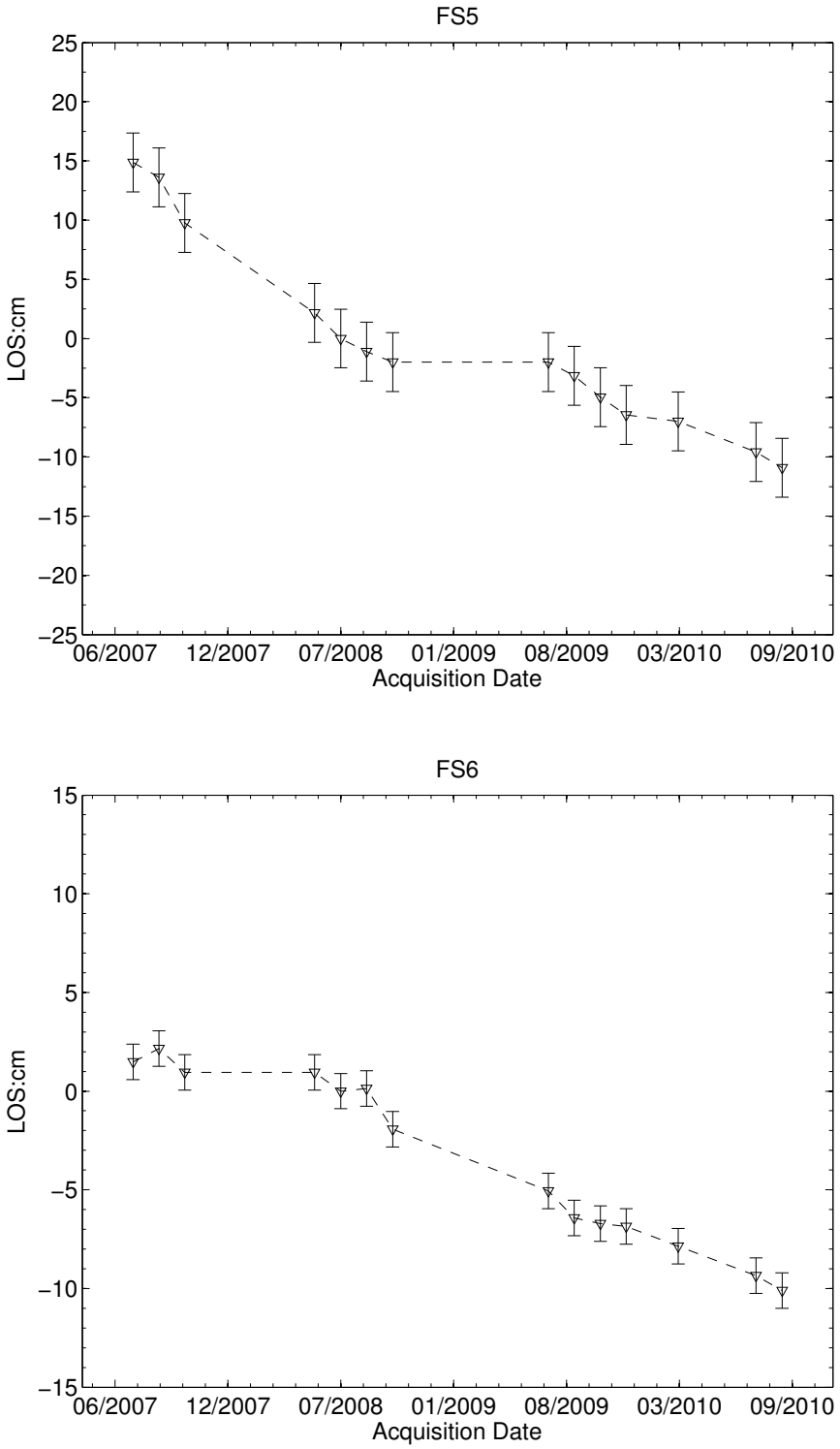

Figure 6.21d Time series of the points FS5 (up) and FS6 (bottom) selected within fire scar area in the study area, as shown in 6.20. Each point presents one SAR image acquisition date. Each value corresponds to the average of a 3 pixels by 3 pixels window and the errorbar on each point is its associated RMS.

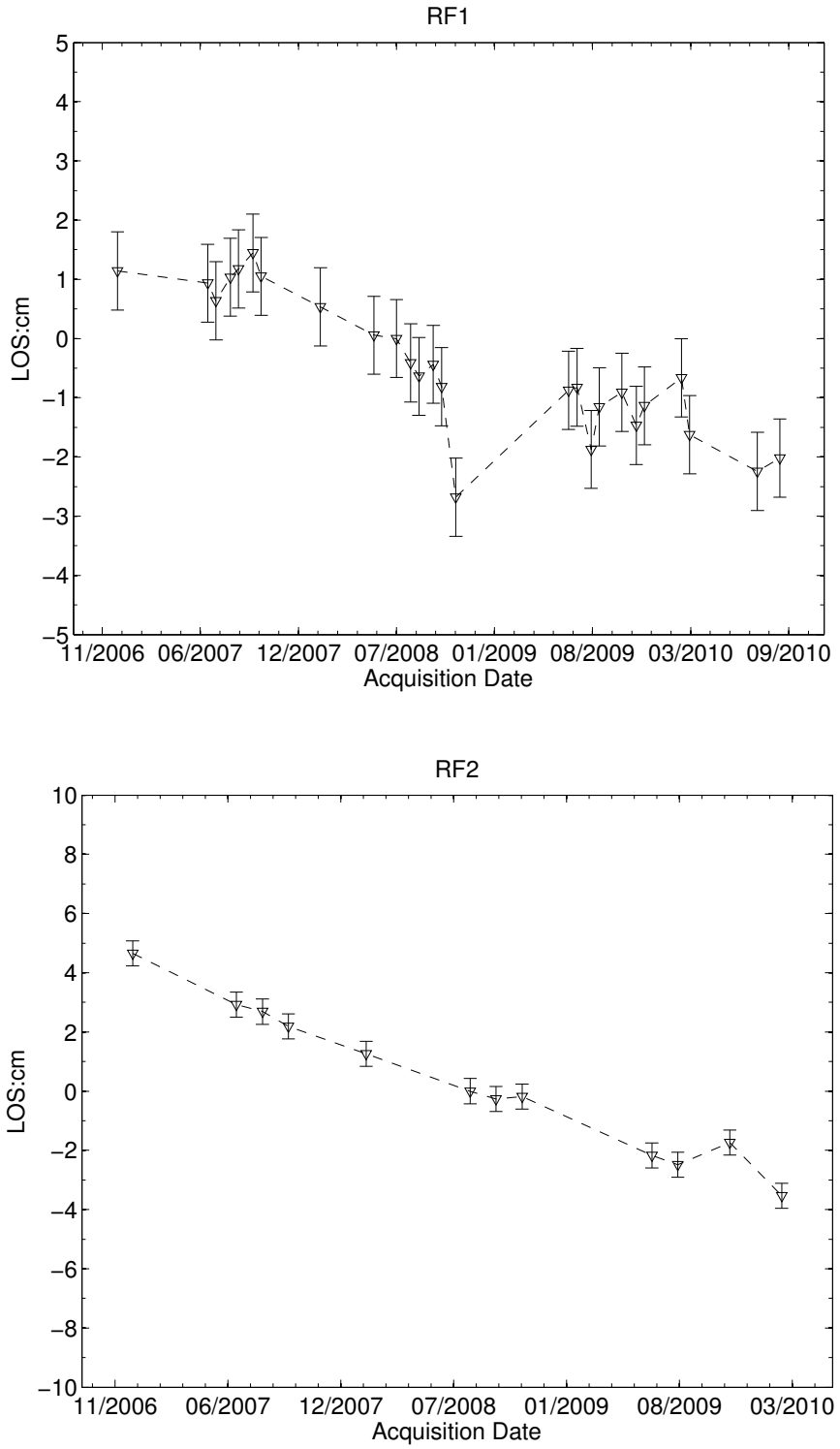

Figure 6.21e Time series of the points RF1 (up) and RF2 (bottom) selected within rice field area in the study area, as shown in 6.20. Each point presents one SAR image acquisition date. Each value corresponds to the average of a 3 pixels by 3 pixels window and the errorbar on each point is its associated RMS.

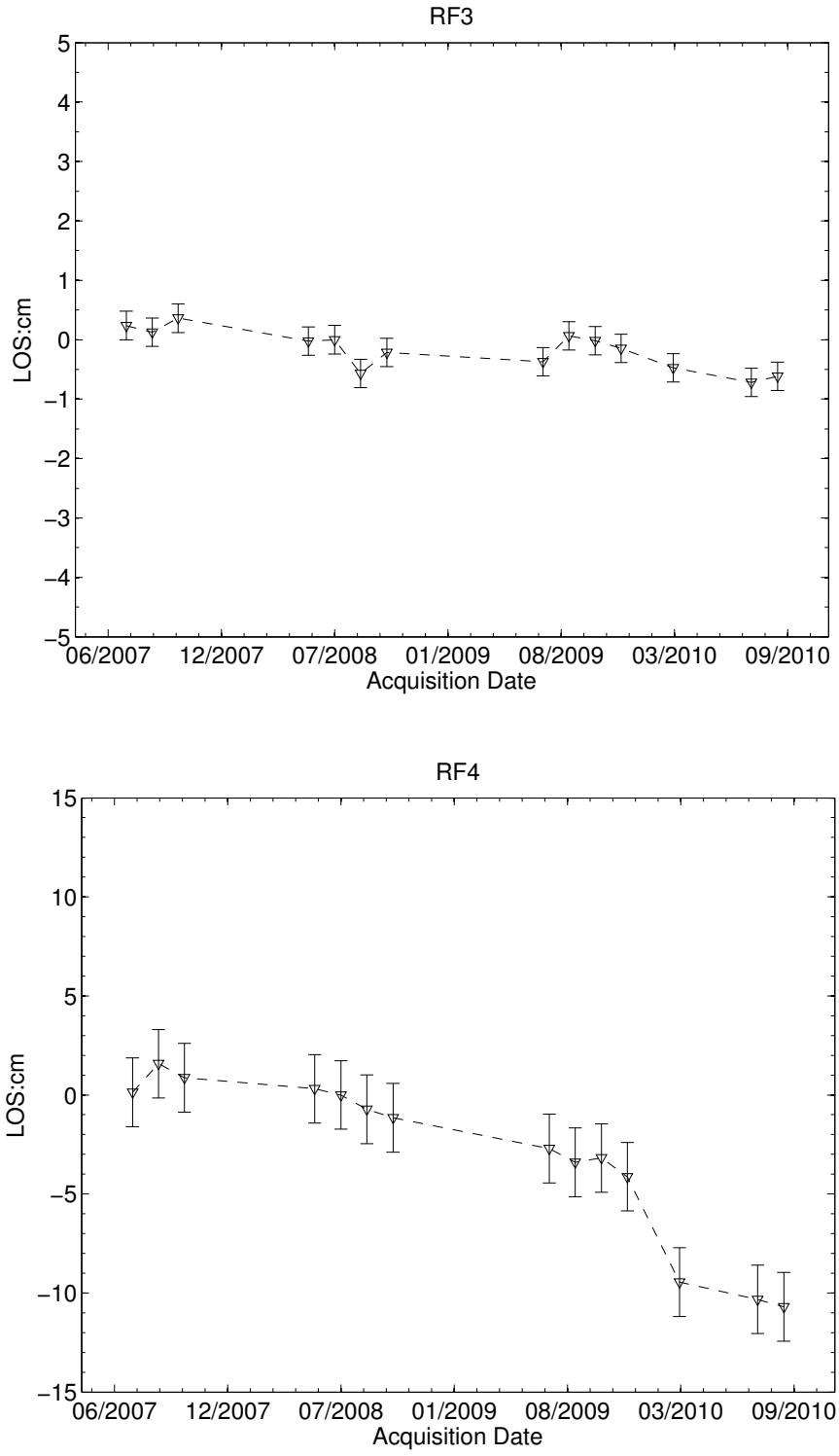

Figure 6.21f Time series of the points RF3 (up) and RF4 (bottom) selected within rice field area in the study area, as shown in 6.20. Each point presents one SAR image acquisition date. Each value corresponds to the average of a 3 pixels by 3 pixels window and the errorbar on each point is its associated RMS.

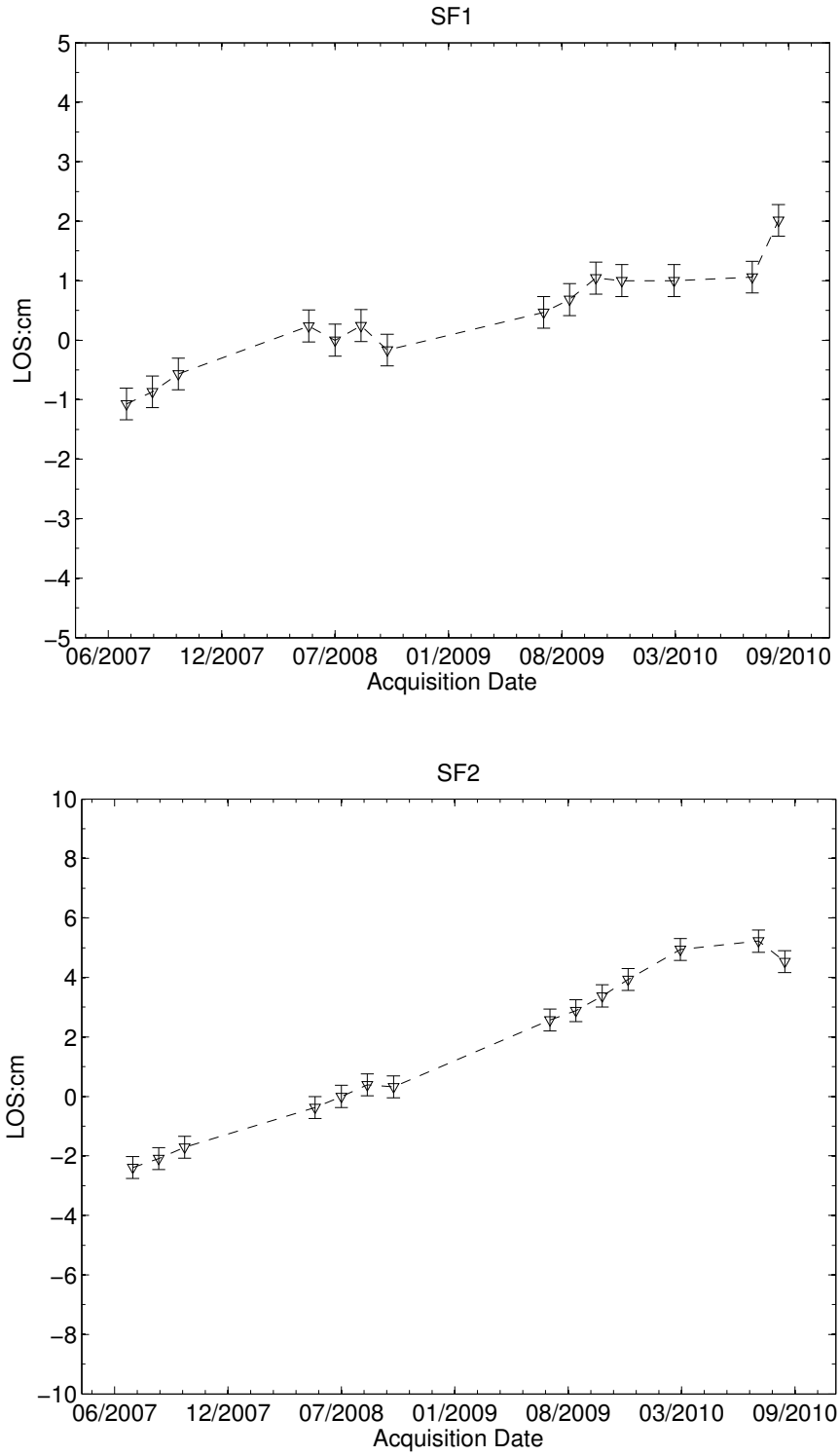

Figure 6.21g Time series of the points SF1 (up) and SF2 (bottom) selected within swamp forest area in the study area, as shown in 6.20. Each point presents one SAR image acquisition date. Each value corresponds to the average of a 3 pixels by 3 pixels window and the errorbar on each point is its associated RMS.

Table 6.4 Mean velocities of thirteen selected points from the combined two tracks. Note: the units of mean velocities and RMS are cm/yr.

Points	**C1**	**FS1**	**FS2**	**FS3**	**FS4**	**FS5**	**FS6**
Mean	-0.8	-2.6	-2.5	-4.0	-4.2	-7.7	-3.4
RMS	-0.4	-0.4	-0.4	-0.9	-0.5	-2.5	-1.0
Points	**RF1**	**RF2**	**RF3**	**RF4**	**SF1**	**SF2**	
Mean	-1.0	-2.2	0.0	-2.9	1.4	2.7	
RMS	-0.7	-0.5	-0.2	-1.7	-0.3	-0.5	

6.4.4 Estimation of carbon loss

In this chapter, carbon loss and CO_2 emission estimation is carried out using the same procedure as section 5.4.2 Estimation of carbon loss. A carbon content value of 57% and bulk density of 0.1 g/cm^3 is used in this study and CO_2 estimation is calculated by assuming that all carbon loss is converted into CO_2 (Page et al., 2002; Dahdal, 2011). Based on the subsidence rate shown in Figure 6.14, the peat volume loss rate and C loss rate can be calculated and are shown in Table 6.5. The estimated peat volume losses range from 0.07 Mt/yr (shrub area) to 3.0 Mt/yr (swamp shrub area), corresponding to C loss rates from 0.04 Mt/yr to 1.71 Mt/yr, and annual C loss rate between 7.58 t/ha/yr and 6.71 t/ha/yr. The average peat height loss rate is 1.27 cm/yr, and peat volume loss rate is 2.36 Mt/yr, which contributes C loss rate with 1.35 Mt/yr and annual C loss rate of 7.22 t/ha/yr in this study area.

Table 6.5 C loss and CO_2 emission from drained peatland.

Study area	Cleared	Rice Field	Swamp shrub	Shrub	Total
Pixels	8896	114402	284216	6885	414399
Area (ha)	7205.76	92665.62	230214.96	5576.85	335663.19
Mean Velocity (cm/yr)	1.33	1.18	1.3	1.18	1.27
Peat volume (Mt/yr)	0.10	1.09	3.00	0.07	2.36
C loss (Mt/yr)	0.05	0.62	1.71	0.04	1.35
CO_2 loss (Mt/yr; 92% Oxidation)	0.17	2.09	5.77	0.13	4.56
Annual C loss (t/ha/yr)	7.58	6.72	7.43	6.71	7.22
Annual CO_2 loss (Mt/yr; 92% Oxidation)	25.57	22.67	25.06	22.63	24.36

Since the Ex-MRP area has been drained from the 1990s on wards and the SAR images date from December 2006 to September 2010, a 92% oxidation of the total subsidence for peatlands drained over 18 years is used for estimating the CO_2 emission rate in this chapter (Hooijer et al., 2012). The Table 6.5 shows that the cleared area has the maximum annual CO_2 emission rate of 25.57 t/ha/yr. The shrub area has the minimum CO_2 emission rate ranging of 22.63 t/ha/yr. The whole study area has an annual CO_2 emission rate of 24.36 t/ha/yr.

6.5 Discussion

In this Chapter, L-band PALSAR images have been used to map the spatiotemporal land surface height change with InSAR time series, and the restoration effects after the dam construction have been investigated. Comparisons between adjacent tracks in the overlapping area suggest InSAR derived mean velocities have a high accuracy of 0.7 cm/yr with a great advantage in coverage, almost covering the whole area of Blocks A, B, C and D, especially along the channels.

However, there are two main limitations in applying InSAR in this study. Interferograms generated by SAR images acquired in wet seasons are more likely to cause phase unwrapping errors than interferograms produced by SAR images collected in dry seasons. Between wet and dry seasons, or wet and wet seasons, a large fluctuations of water level between is expected along the rivers. This produces relatively narrow and complex fringe patterns due to water level changes, while complex and steep fringes are prone to cause phase jumps (Figure 6.9) (Jin-Woo et al., 2009). But in the dry season, the rivers keep a relatively stable and low water level, and smoothly wrapped fringes are more likely expected. This contributes stable unwrapped phases (Figure 6.10). Temporal decorrelation is the other limitation. In dense forest, such as secondary swamp forest in this study, L-band is unable to penetrate the canopy if the above ground biomass is above the saturation limit (greater than 100 t/ha) (Morel et al., 2011; Basuki et al., 2013). Return radar signals are primary from the canopy of the forest, which means these signals are more likely

changed from time to time and cause loss of coherence. Therefore, the western part of Block C, the northern part of Block B, and a small area of in the northern part of Block A lost coherence (Figure 6.14). Shorter temporal ($<$ 1 year) is able to produce more coherent pixels over this density forest.

Since the availability of ALOS PALSAR images are limited between December 2006 and May 2011 the surface height change trend before dam construction is not possible via ALOS PALSAR. However, JERS data (L-band) can be used to produce a surface height change map for before dam construction, as JERS SAR images are available between 1992 and 1998. In Block A, there are three types of dams built in July 2004, May 2007 and June 2008 respectively. Our SAR images are acquired from December 2006 to September 2010. All the profiles in Block A show that the dam construction has a positive effect on reducing the subsidence rate of peatland along the channels; the restoration effects decrease with the distance away from the dams. In the neighboring areas of the dams, the subsidence rate remains relatively stable, ranging from -0.5 to -1.0 cm/yr; in contrast, the subsidence rate is up to -3 cm/yr at the junction of channels that are about 10 km away from the dams. The large subsidence rate at Profile AA' was probably due to fire as burn scars can be observed by checking the Landsat 7 images acquired on 20070805, and the burn scars were still observed till 20090207 (Figure 6.20 b and c). Profile DD' show that within the area blocked by dams, the subsidence rate ranged from 0 to -0.5 cm/yr, but beyond that area, the subsidence rate increased continuously to reach -1.8 cm/yr. Profiles FF', GG' and HH' also confirm that dams had impacts on subsidence rates; their subsidence rates increased from 0 cm/yr in the area close to the dams to -2.5 cm/yr at the distance of 6.5 km away from the dams.

Restoration requires time to take effect (Wösten et al., 2008; Jaenicke et al., 2011), which means the earlier the dam is constructed, the more significant effect of the dam is. This is confirmed by the dams in Block D. Our SAR images are acquired from 20070709, nearly two years after the dam construction, and the uplift signals show that the channels are blocked well, and the ground water level is raised in dry seasons. By analyzing the backscatter of PALSAR image acquired from 2007 and 2009, Jaenicke *et al*

(2011) believed that after dam construction in Block C, the peatland was successfully continuously rewetted, even in the very prolonged dry season of 2006. In Block A, rewet effects were observed in Profiles BB' and CC'. Here there are dams constructed in different periods with the earliest dams were constructed in January 2005. The area close to the dams constructed in January 2005 shows stable and low subsidence rates of -0.5 cm/yr, and the subsidence rate is about -2.0 to -1.0 cm/yr around the dam constructed on May 2007, which means these later dams are not yet as effective as the earlier ones. The subsidence rate did not increase significantly around the dam constructed in June 2008, although the distance is only about 2.5 km between the dam constructed on May 2007 and that constructed in June 2008.

High-density dams appear effective in reducing the subsidence rate in a short period. In Block A, there is a small fully blocked area with three dams constructed in April-June 2008 and one dam constructed in December 2006-May 2007. Profiles FF', GG' and HH' show the subsidence rate near the second dam decreased to zero, whilst the subsidence rate near the first dam was as high as -2.5 cm/yr, which is likely caused by fire. Fresh fire scars can be observed in the Landsat image acquired on 20070805, and vegetation regeneration were not observed in the Landsat image acquired on 2009027, while the original is covered by forest in the Landsat image acquired on 20060607 (Figure 6.20), our data sets ended in 20100901.

The time series of points in the drained peatland shows that, without dam construction and restoration work, the peatland is still losing height and therefore peat. For the cleared area (C1), the clearing activity can be identified by comparing Figure 6.20a and Figure 6.20b. In Figure 6.20a, the area around C1 is green, which means covered by swamp forest, while in Figure 6.20b, the area is changed into purple, indicating fire scars. This area was affected by a fire occurring during the 2006 El Niño period (Hoekman, 2009). Among the six fire scar points, the first four points (FS1 to FS4) show constantly subsiding signals. The subsidence rates of FS1 and FS2 are lower than those of FS3 and FS4. This is probably due to the trees regeneration since areas around FS1 and FS2 are green shown in Figure 6.20c, which keeps the peatland un-exposed to

the sun. The areas around FS3 and FS4 still show purple in Figure 6.20c, and regeneration of trees is not observed. For FS5 site, fire scar is not observed in Figure 6.20a and b, but it is clearly shown in Figure 6.20c, which can explain why Point FS5 shows a 17 cm decrease between the dry seasons of 2007 and 2008, and only 8 cm in the following 2 years. Point FS6 is relatively stable in the first year, while it decreased 10 cm in the following two years, attributed to fire occurrence in the dry season of 2008 - the fire scar is clear in Figure 6.20c while it is not in Figure 6.20b.

From Figure 6.20, we can identify that rice field in Block A was affected by the 2006 El Niño. Figure 6.20b shows fire scars across the rice field area, and the area around RF2 is much worse than that around RF1, because there is more green vegetation in the area around RF1. This can also explain why the subsidence rate of RF2 is greater than RF1, and RF3 is great than RF4.

Since there are no dams constructed around points of SF1 and SF2 in swamp forest area, one possible reason for uplifting signals for these two points could be the rising of water level under the canopy.

The results of this study suggest that the annual carbon loss rate and CO_2 emission rate was 7.22 t/ha/yr and 24.36 t/ha/yr between December 2006 and September 2010. This result is similar to the long term results reported by Wösten *et al.*, (1997) for Johor, Malaysia, where the C loss rate and CO_2 emission rate were estimated to be 7.2 t/ha/yr and 26.5 t/ha/yr respectively. However, bulk density, carbon content, and oxidation percentage does cause uncertainty in the estimation of carbon loss and CO_2 emission as discussed in section 5.5 Discussion.

6.6 Conclusion

This study has demonstrated that InSAR is a powerful tool in investigating the restoration effects, and can also be used to indirectly assess the relative magnitude and spatial pattern of damages of peatland caused by drainage and fires; the latter provides key information for guiding future restoration activities. InSAR offers great advantage through regional coverage comparing to field-

based observation of individual monitoring points. However, there are limitations that constrain the application of InSAR in peatland, such as temporal decorrelation caused by flooding and phase unwrapping errors along the rivers, especially in wet seasons. In addition, InSAR measurement is only sensitive to the LOS direction.

The study shows that the restoration is affected by the construction time and density of dams, the earlier the dam is constructed, the more significant the restoration is. High-density dams have positive effects on peatlands restoration in a short time. In addition, an annual carbon loss rate of 7.22 t/ha/yr and annual CO_2 mission rate of and 24.36 t/ha/yris estimated as well.

Chapter 7 Conclusions and future work

Abstract: In this chapter, I discuss how the measurement of peat height change observed in my research contributes to our knowledge regarding to carbon loss or gain from peatlands in uplands, tropical areas. This is achieved by answering the three specified questions listed in Chapter 1. I also discuss future work that could be executed measuring peat height change using InSAR and estimating carbon loss from peatlands based on InSAR-derived peat height change information.

In the past two decades, with the advantages of accuracy of a few millimeters and metres of resolution over a wide region (e.g. $100\,km \times 100\,km$), InSAR has been developing rapidly and is being widely applied to measure the Earth's surface movements, e.g. earthquakes and subsidence. In this thesis, I have used InSAR for a less common activity: to examine the peat height change and estimate carbon loss or gain from two globally important categories of peatland, upland blanket bog (UK), and tropical fens (Indonesia). These two sites are degrading due to different mechanisms – natural and anthropogenic land use.

To contextualize the application of InSAR and understand field limitations I have reviewed peatland function, and processes of carbon losses in upland and tropical peatlands, and outlined common approaches currently used to estimate carbon loss, including the method based on peat height change (Chapter 2).

In order to understand how InSAR may be used to assess the carbon loss from peatlands by detecting peat height changes, the principles of SAR, InSAR, and InSAR time series are reviewed in Chapter 3.

I have applied Envisat C-band and ALOS L-band data to investigate the eroding extent and severity of upland UK peatlands. Deorrelation of both C-

and L-band over upland peatlands were examined first. InSAR time series results showed that both C- and L-band have capability in monitoring changes in peat height over a long time. However, when the uncertainty from noise and the actual signals are of the same magnitude, InSAR measurements have difficulty in differentiating this ambiguity (Chapter 4).

I also have applied two adjacent tracks of ALOS L-band images to assess the subsidence of drained peatland in Sumatra, Indonesia, and from the InSAR-derived subsidence rate data, I estimated carbon loss (i.e. CO_2 emissions) in the study area (Chapter 5).

The effectiveness of restoration work in tropical peatlands was assessed from two adjacent tracks of ALOS L-band images to document peatland land surface change in Central Kalimantan, Indonesia. This study has demonstrated that InSAR is a powerful tool in investigating the restoration effects and providing key information for guiding future restoration activities (Chapter 6).

In summary, it appears there is significant potential to use InSAR to map the spatial and temporal peat height change of peatlands, and from this, carbon loss and gain can be estimated. The principal contributions of this research are:

1. For the first time, repeat-pass InSAR has been successfully applied to map the spatial and temporal changes in peat heights in two globally important categories of peatland: upland blanket bog (UK) and tropical fens (Indonesia);

2. For the first time, peat height change information derived by repeat-pass InSAR has been employed to estimate carbon loss, and monitor the restoration effects in peatlands of Indonesia.

The conclusions of this research are elaborated in relation to the three specific research questions listed in Chapter 1, followed by a summary of the major contributions of this research as well as recommendations for future work.

7.1 Conclusions of this research

7.1.1 InSAR application in peatlands

Specific Research Question 1: Is it feasible to use InSAR to monitor peatland height change? What are the limitations in applying InSAR to peatlands? How accurate can InSAR results be in the case of peatlands?

In this thesis, the feasibility of InSAR on mapping the surface change in peatlands has been examined by three case studies:

(1) In the case study of upland erosion, C- and L-band datasets spanning the period from December 2002 to July 2010 are used to investigate peat height change. The correlation analysis between the two adjacent ALOS tracks 664 and 665 suggests that InSAR provides high correlation (0.83) in the main subsidence areas, with a total decrease of ~ 2 cm of in peat height during the observed period (Figure 4.22 and Figure 4.23). This means InSAR time series generated by C- and L-band SAR images have capability in mapping the long-term eroding extent and severity of the upland peatland surface. However, in areas with a low height change rate, particularly when the uncertainty and the actual signals are of the same magnitude, InSAR measurements have difficulty in differentiating this ambiguity.

(2) In the case study of subsidence of drained peatland in Sumatra, Indonesia, two adjacent tracks of L-band ALOS images collected between 20070727 and 20110118 are applied to assess the subsidence. With a high correlation of 0.61, the relatively small RMS difference (0.7 cm/yr) of mean velocities (Figure 5.6)

between the two adjacent tracks provides strong support that InSAR can be used to identify the magnitude and spatial pattern of subsidence of peatland caused by drainage.

(3) In the case study of peatland restoration work in Central Kalimantan, Indonesia, two adjacent tracks of L-band ALOS data collected between 20061220 and 20100901 are used to monitor the restoration effects. The two adjacent tracks of InSAR results show a high correlation of 0.67 and a relatively small RMS difference (0.7 cm/yr) of mean velocities (Figure 6.11) within the overlapping area, suggesting that InSAR is a useful tool in investigating restoration effects, and can also be used to indirectly assess the relative magnitude and spatial pattern of damages of peatland caused by drainage and fires; the latter provides key information for guiding future restoration activities.

Combining these three case studies suggest that it is feasible to use InSAR to monitor peatland height change of peatlands.

Through the three case studies over two different types of peatlands, three primary limitations of applying repeat-pass InSAR on peatlands can be summarized as follows:

1) **Decorrelation in space and time**: In Section 3.2.3 InSAR decorrelation, decorrelation factors are discussed, and spatial and temporal decorrelations are regarded as the two main factors leading to the loss of coherence. In Chapter 4, both short wavelength C-band (5.6 cm) and long wavelength L-band (23.6 cm) SAR images are used to generate interferograms for coherence analysis over upland peatlands. The decorrelation patterns with time and spatial baseline of C-band and L-band shown in Figure 4.11 and Figure 4.12 suggest:

(i) For C-band, temporal decorrelation is a more critical source of losing coherence in the blanket bogs areas compared to spatial decorrelation. Within the spatial baseline of 500 m, a temporal baseline of 6 months is still able to offer good coherence, and a temporal baseline of 6 ~ 18 months provides relatively fair coherence; but coherence is almost lost when the temporal baseline is greater than 18 months.

(ii) For L-band, significant decorrelation is not observed with a temporal baseline of up to 36 months and a spatial baseline of up to 2 km. In Chapters 5 and 6, only L-band SAR images are used to generate interferograms for InSAR time series analysis in tropical peatlands, because severe decorrelation occurs with C-band in this high-density forest covered region. *Takeuchi and Oguro* (2003) investigated InSAR coherence patterns of C-band ERS and L-band JERS in tropical forest areas in southern part of Sumatra, Indonesia. Their study showed that the coherence of JERS L-band repeat-pass InSAR pairs was compatible to that of ERS C-band tandem (1 day interval) pairs, while the coherence of ERS C-band repeat-pass pairs was very poor. This was also confirmed by other studies, such as (Eriksson, 2004; Chul Jung and Alsdorf, 2010).

However, decorrelation is also found in some L-band interferograms, probably due to flooding, fires, agriculture activities and high density of forest (above ground biomass $>$ 100 t/ha) (Dobson et al., 1992; Adrian et al., 1998; Luckman et al., 1998).

2) **Phase unwrapping errors**: phase unwrapping error is discussed in Section 3.2.4. Low coherence, incoherence and discontinuities in phase can easily lead to phase unwrapping error, as shown in Figure 4.16 and Figure 5.4. Complex

fringe patterns and steep phase gradients are also prone to cause phase jumps, as shown in Figure 6.8.

3) **Atmosphere effects or atmosphere phase screen** (APS): APS is the major limitation in applying repeat-pass InSAR; the concept of APS and its related correction approaches are reviewed in Sections 3.2.5 Atmospheric phase screen and 3.2.6 Atmospheric corrections respectively. In this thesis, APS is reduced by the temporal linear velocity (TLV) model (Li et al., 2009a). Most of APS effects can be estimated and removed, and the residual contributes to the total measurement uncertainty, as evidenced by Figure 4.19. However, the total measurement uncertainty causes difficulty in separating reliable and actual surface movement signals when the uncertainty and the actual signals are of the same magnitude. This is the case of mapping the peat eroding in the UK upland. Only the main subsidence area shows clear surface movement signals (Figure 4.20), and a total decrease of about 2 cm in peat height is observed (Figure 4.23). In the study of peat height change in Sumatra and Central Kalimantan, Indonesia, the residual APS is less significant and the magnitude of surface change is larger than the uncertainty. This helps to extract the real peat height change signals.

The accuracy of InSAR measurements in this thesis is given by root mean square (RMS) differences between two independent observations from two adjacent tracks of SAR images. These SAR images were collected almost in the same period with an overlapping area. In the case study of UK upland erosion, a RMS difference of 0.1 cm/yr is observed in the main subsidence areas (Figure 4.22). In the two case studies in tropical peatlands in Sumatra and Central Kalimantan of Indonesia, the correlation of the mean velocities between two adjacent tracks is 0.61 and 0.67 respectively (Figure 5.6 and Figure 6.11), and both case studies had a RMS difference of 0.7 cm/yr. Therefore, it is clear that

a few mm/yr accuracy of InSAR derived mean velocities of peat height changes is achievable.

7.1.2 Carbon loss estimation from peatlands

Specific Research Question 2: Is it applicable to estimate carbon loss from peatland height change derived from InSAR? What are the limitations for estimating carbon loss based on peatland subsidence data?

As suggested by *Page et al.* (2011a), subsidence monitoring is generally considered to be more reliable for estimating carbon losses from drained peat because it is capable of providing a time-integrated measure of the net carbon balance of the peat. This method has been applied over the past few decades; *Wösten et al.* (1997) quantified the total subsidence in Malaysia, and the emission of CO_2 was estimated to be 27 tones per hectare per year due to oxidation component of the total subsidence. There have been multiple similar studies (Couwenberg et al., 2010; Hooijer et al., 2010; Hooijer et al., 2012). In comparison to the above, InSAR provides advantages in subsidence monitoring, such as competitive accuracy (a few mm/yr), better spatial resolution (10s m), wider coverage (100 km x 100 km, even global coverage), and long-term dataset (since 1991). In Chapter 4, using the peat height change rate data derived from InSAR, an annual carbon loss rate of 1.26 t/ha/yr and the associated CO_2 emission rate of 4.62 t/ha/yr is estimated. Based on these results, the heavily eroding area is identified as a source of carbon loss (Section 4.5.5 Erosion extent and severity). Chapter 5 shows that InSAR is able to detect peat subsidence (Figure 5.8), and based on this result, an annual carbon loss rate of 7.78 t/ha/yr and the associated CO_2 emission rate of 26.26 t/ha/yr can be estimated (Section 5.4.2 Estimation of carbon loss). Similar results are also estimated in Chapter 6 (Section 6.4.4 Estimation of carbon loss). Therefore, InSAR can be

applied to support estimates of carbon loss as a result of peatland height change.

It should be noted that InSAR measurements have inherited uncertainties. One major uncertainty is atmospheric effects, which is discussed in Sections 4.5.2 Accuracy and uncertainty, 5.5 Discussion and 6.5 Discussion. In addition, large variations in bulk density, carbon content, and oxidation percentage also introduce uncertainties in estimating carbon loss and CO_2 emission based on peatland subsidence data. This is discussed in Section 5.5 Discussion.

7.1.3 Restoration work monitoring in peatlands

Specific Research Question 3: If peatlands are being restored, is InSAR a useful tool to monitor or guide the restoration activities?

Restoration of the peat hydrology and conservation of tropical peatlands is regarded as a critical way to prevent peat oxidation and mitigate CO_2 emission, but currently very little is known about the restoration of large areas of degraded tropical peatland (Wösten et al., 2006; Page et al., 2009b). In Chapter 6, using InSAR, restoration effects after the dam construction have been investigated in Centre Kalimantan, Indonesia. In the restoration area, the study shows that the restoration is affected by the construction time and density of dams, the earlier the dam was constructed, the more significant the restoration was. In addition high-density dams have positive effects on restoration in a short time. In areas without dam construction and restoration work, my research identified the relative magnitude and spatial pattern of damages of peatland caused by drainage and fires. InSAR time series results show the peatland is still losing peat, especially in burned area; the subsidence rate is up to -7.65 cm/yr. Combining these suggest that InSAR is a powerful tool in

investigating the restoration effects and providing key information for guiding future restoration activities in tropical peatlands.

7.2 Contributions of this research

The contributions to knowledge of the research conducted for this thesis can be summarized as follows:

1. The investigation of C-band and L-band decorrelation over upland peatlands shows that in this environment the overall coherence of L-band is better than C-band. The spatial and temporal decorrelation patterns suggest that for C-band, the temporal decorrelation is the main source of losing coherence in the blanket bogs areas. For L-band, significant decorrelation is not observed in the study.

2. In areas without ground truth data, two adjacent tracks data are successfully used to validate each other. The advantage of this approach is all common points within the overlay area between two adjacent tracks can be subject to correlation analysis. For example, in the Sumatra case study, using 168151 points within the overlay area, a correlation of 0.61 is generated (Figure 5.8).

3. For the first time, repeat-pass InSAR has been applied to map the spatial and temporal peat height change in two globally important categories of peatland over a large area at 90-meter resolution. InSAR offers great potential in mapping the eroding extent and severity of upland blanket bog (UK), and successfully detected the peat height change in tropical fens (Indonesia).

4. For the first time, with the peat height change information derived by repeat-pass InSAR, and peat property data (such as bulk density, carbon content), carbon loss or CO_2 emissions are successfully estimated in Sumatra, Indonesia.

5. For the first time, repeat-pass InSAR is successfully applied in monitoring restoration effects in peatlands of Indonesia. This tool provides an insight into the factors that affect the restoration effects, and key information for guiding future restoration activities.

7.3 Recommendations for future research and applications

This work is the first study to apply InSAR time series for monitoring long-term surface change in peatlands. It is also the first to map the erosion in uplands, quantify carbon loss and monitor restoration effects in tropical peatlands using InSAR. It is believed that this work sets a good example for future studies of peatland height changes and its associated carbon loss/gain using InSAR in the world.

Coherence should be always borne in mind when using C-band SAR datasets (e.g. ERS1/2 and Envisat) to investigate peatland height changes. As demonstrated in Chapter 4, short spatial and temporal baselines are required to ensure good coherence for C-band interferograms in uplands. Our previous experience in Sumatra suggests that archived C-band SAR datasets are not applicable because of temporal decorrelation, but soon-to-be-launched Sentinel-1 might be usable due to its shorter temporal resolution (6-12 days for Sentinel-1 vs 35 days for Envisat/ERS) and higher spatial resolution (5m for Sentinel-1 vs 20m for Envisat/ERS). One alternative to address the coherence issue is to further develop existing InSAR time series techniques to detect more coherent or stable pixels (especially those temporally coherent ones (e.g. (Zhang et al., 2011; Sowter et al., 2013)) in rural and vegetated areas.

It is of great interest to combine archived JERS L-band dataset (1992-1998) with the ALOS dataset (2006-2011) to investigate peatland height changes in two different time periods. More interestingly, with the launch of Sentinel-1 (C-band; repeat time: 12 days) and ALOS-2 (L-band; repeat time: 14 days), it may be practical not only to monitor peatland height changes continuously and globally, but also to investigate seasonal variations of peatland height changes in the future (rather than long-term trends only).

By further reducing measurement uncertainties including atmospheric effects, InSAR can provide more accurate peat height change information. A more specific bulk density, carbon content, oxidation component information in study area will help to better calculate the amount of carbon loss and CO_2 emission. Meanwhile, combing CO_2 uptaking by surface biomass (Ulander et al., 2011) and estimated CO_2 emission, it is possible to estimate net CO_2 exchange in a regional scale (Moore et al., 2002; Gielen et al., 2013).

References:

Abdul-Rahman, H. S., Gdeisat, M. A., Burton, D. R., Lalor, M. J., Lilley, F. & Moore, C. J. 2007. Fast and robust three-dimensional best path phase unwrapping algorithm. *Applied optics,* 46**,** 6623-6635.

Adrian, L., John, B., Miroslav, H. & Richard, L. 1998. Tropical Forest Biomass Density Estimation Using JERS-1 SAR: Seasonal Variation, Confidence Limits, and Application to Image Mosaics. *Remote Sensing of Environment,* 63**,** 126-139.

Ali, M., Taylor, D. & Inubushi, K. 2006. Effects of environmental variations on CO2 efflux from a tropical peatland in eastern Sumatra. *Wetlands,* 26**,** 612-618.

Askne, J. & Smith, G. 1997. Forest INSAR decorrelation and classification properties. *ERS SAR Interferometry,* 406**,** 95-103.

Attema, E. P. W. 1991. The active microwave instrument on-board the ERS-1 satellite. *Proceedings of the IEEE,* 79**,** 791-799.

Baldocchi, D. D. 2003. Assessing the eddy covariance technique for evaluating carbon dioxide exchange rates of ecosystems: past, present and future. *Global Change Biology,* 9**,** 479-492.

Ballhorn, U., Siegert, F., Mason, M. & Limin, S. 2009. Derivation of burn scar depths and estimation of carbon emissions with LIDAR in Indonesian peatlands. *Proceedings of the National Academy of Sciences,* 106**,** 21213-21218.

Balzter, H. 2001. Forest mapping and monitoring with interferometric synthetic aperture radar (InSAR). *Progress in Physical Geography,* 25**,** 159-177.

Bambang Hero, S. & Canesio, P. M. 2005. Controlled burning in peat lands owned by small farmers: a case study in land preparation. *Wetlands Ecology and Management,* 13**,** 105-111.

Bamler, R. & Hartl, P. 1998. Synthetic aperture radar interferometry. *Inverse Problems,* 14**,** 1-54.

Bamler, R. & Just, D. Phase statistics and decorrelation in SAR interferograms. Geoscience and Remote Sensing Symposium, 1993. IGARSS '93. Better Understanding of Earth Environment., International, 18-21 Aug 1993 1993. 980-984 vol.3.

Basuki, T. M., Skidmore, A. K., Hussin, Y. A. & Van Duren, I. 2013. Estimating tropical forest biomass more accurately by integrating ALOS PALSAR and Landsat-7 ETM+ data. *International Journal of Remote Sensing,* 34**,** 4871-4888.

Becker, T., Kutzbach, L., Forbrich, I., Schneider, J., Jager, D., Thees, B. & Wilmking, M. 2008. Do we miss the hot spots?? The use of very high resolution aerial photographs to quantify carbon fluxes in peatlands. *Biogeosciences Discussions,* 5**,** 1097-1117.

Berardino, P., Fornaro, G., Lanari, R. & Sansosti, E. 2002. A new algorithm for surface deformation monitoring based on small baseline differential SAR interferograms. *Geoscience and Remote Sensing, IEEE Transactions on,* 40**,** 2375-2383.

Beukema, H. & Noordwijk, M. V. 2004. Terrestrial pteridophytes as indicators of a forest-like environment in rubber production systems in the lowlands of Jambi, Sumatra. *Agriculture, Ecosystems & Environment,* 104**,** 63-73.

Biggs, J., Wright, T., Lu, Z. & Parsons, B. 2007. Multi-interferogram method for measuring interseismic deformation: Denali Fault, Alaska. *Geophysical Journal International,* 170**,** 1165-1179.

Billett, M. F., Charman, D. J., Clark, J. M., Evans, C. D., Evans, M. G., Ostle, N. J., Worrall, F., Burden, A., Dinsmore, K. J. & Jones, T. 2010. Carbon balance of UK peatlands: current state of knowledge and future research challenges. *Climate Research,* 45**,** 13-29.

Bovenga, F., Wasowski, J., Nitti, D. O., Nutricato, R. & Chiaradia, M. T. 2012. Using COSMO/SkyMed X-band and ENVISAT C-band SAR interferometry for landslides analysis. *Remote Sensing of Environment,* 119**,** 272-285.

Brautigam, B., Martone, M., Rizzoli, P., Bachmann, M. & Krieger, G. Interferometric performance of TanDEM-X Global DEM acquisitions. Synthetic Aperture Radar, 2012. EUSAR. 9th European Conference on, 23-26 April 2012. 89-92.

Buckley, S. M., Rosen, P. A., Hensley, S. & Tapley, B. D. 2003. Land subsidence in Houston, Texas, measured by radar interferometry and constrained by extensometers. *Journal of Geophysical Research: Solid Earth,* 108**,** 2542.

Buckreuss, S., Balzer, W., Muhlbauer, P., Werninghaus, R. & Pitz, W. 2003. The TerraSAR-X satellite project. *IEEE,* 5**,** 3096-3098.

Byrne, K. A., Chojnicki, B., Christensen, T. R., Drösler, M., Freibauer, A., Friborg, T., Frolking, S., Lindroth, A., Mailhammer, J. & Malmer, N. 2004. EU peatlands: Current carbon stocks and trace gas fluxes. *CarboEurope-GHG Concerted Action–Synthesis of the European Greenhouse Gas Budget, Report,* 4**,** 2004.

Caltech Tectonics Observatory, I. M. S. 2013. *JMBI overview* [Online]. Available: http://tectonics-ims.caltech.edu/ims/net/1/sis/station/8/.

Carolina, P., Freysteinn, S., Rikke, P., Páll, E., Thóra, Á. & Kurt, L. F. 2007. Crustal deformation associated with the 1996 Gjálp subglacial eruption, Iceland: InSAR studies in affected areas adjacent to the Vatnajökull ice cap. *Earth and Planetary Science Letters,* 259**,** 24-33.

Chan, Y. K. & Koo, V. C. 2008. An introduction to synthetic aperture radar (SAR). *Progress In Electromagnetics Research B,* 2**,** 27-60.

Charman, D. J., Joosten, H., Laine, J., Lee, D., Minayeva, T., Opdam, S., Parish, F., Silvius, M. & Sirin, A. 2008. *Assessment on Peatlands, Biodiversity and Climate Change: Main Report,* Wageningen, Global Enviroment Centre, Kuala Lumpur & Wetlands International.

Chaussard, E., Amelung, F., Abidin, H. & Hong, S.-H. 2013. Sinking cities in Indonesia: ALOS PALSAR detects rapid subsidence due to groundwater and gas extraction. *Remote Sensing of Environment,* 128**,** 150-161.

Chen, C. W. & Zebker, H. A. 2000. Network approaches to two-dimensional phase unwrapping: intractability and two new algorithms. *J. Opt. Soc. Am. A,* 17**,** 401-414.

Chen, C. W. & Zebker, H. A. 2002. Phase unwrapping for large SAR interferograms: statistical segmentation and generalized network models. *Geoscience and Remote Sensing, IEEE Transactions on,* 40**,** 1709-1719.

Chul Jung, H. & Alsdorf, D. 2010. Repeat-pass multi-temporal interferometric SAR coherence variations with Amazon floodplain and lake habitats. *International Journal of Remote Sensing,* 31**,** 881-901.

Ckpp 2008. Provisional Report of the Central Kalimantan Peatland Project. Novermber 2008. CKPP Consortium, Palangka Raya, Indonesia.

Connolly, J. & Holden, N. M. Mapping peatland disturbance in Ireland: an object oriented approach. Proc. SPIE 8174, Remote Sensing for Agriculture, Ecosystems, and Hydrology XIII, 2011. 81740G.

Couwenberg, J. 2011. Greenhouse gas emissions from managed peat soils: is the IPCC reporting guidance realistic? *Mires and Peat,* 8**,** 1-10.

Couwenberg, J., Dommain, R. & Joosten, H. 2010. Greenhouse gas fluxes from tropical peatlands in south-east Asia. *Global Change Biology,* 16**,** 1715-1732.

Curlander, J. C. & Mcdonough, R. N. 1991. *Synthetic aperture radar: systems and signal processing*, Wiley New York.

Dahdal, B. 2011. *The use of interferometric spaceborne radar and GIS to measure peat subsidence in Indonesia.* Ph.D, University of Leicester.

Delouis, B., Giardini, D., Lundgren, P. & Salichon, J. 2002. Joint inversion of InSAR, GPS, teleseismic, and strong-motion data for the spatial and temporal distribution of earthquake slip: Application to the 1999 Izmit mainshock. *Bulletin of the Seismological Society of America,* 92**,** 278-299.

Denmead, O. T. 2008. Approaches to measuring fluxes of methane and nitrous oxide between landscapes and the atmosphere. *Plant and Soil,* 309**,** 5-24.

Deos. 2008. *Delft Object-oriented Radar Interferometric Software- User's manual and technical documentation* [Online]. Available: http://doris.tudelft.nl/usermanual/ [Accessed 10th January 2013].

Deutscher, J., Perko, R., Gutjahr, K., Hirschmugl, M. & Schardt, M. 2013. Mapping Tropical Rainforest Canopy Disturbances in 3D by COSMO-SkyMed Spotlight InSAR-Stereo Data to Detect Areas of Forest Degradation. *Remote Sensing,* 5**,** 648-663.

Dise, N. B. 2009. Peatland response to global change. *Science,* 326**,** 810-811.

Dobson, M. C., Ulaby, F. T., Letoan, T., Beaudoin, A., Kasischke, E. S. & Christensen, N. 1992. Dependence of radar backscatter on coniferous forest biomass. *Geoscience and Remote Sensing, IEEE Transactions on,* 30**,** 412-415.

Doin, M.-P., Guillaso, S., Jolivet, R., Lasserre, C., Lodge, F., Ducret, G. & Grandin, R. Presentation of the small-baseline NSBAS processing chain on a case example: The Etna deformation monitoring from 2003 to 2010 using ENVISAT data. 2011. 303-304.

Doin, M. P., Lasserre, C., Peltzer, G., Cavalié, O. & Doubre, C. 2009. Corrections of stratified tropospheric delays in SAR interferometry: Validation with global atmospheric models. *Journal of Applied Geophysics,* 69**,** 35-50.

Edwards, R., Mulligan, D. & Marelli, L. 2010. Indirect land use change from increased biofuels demand. *JRC Scientific and Technical Reports. JRC,* 59771.

Elliott, J. R. 2009. *Strain accumulation & release on the Tibetan Plateau measured using InSAR.* PhD, University of Oxford.

Elliott, J. R., Walters, R. J., England, P. C., Jackson, J. A., Li, Z. & Parsons, B. 2010. Extension on the Tibetan plateau: recent normal faulting measured by InSAR and body wave seismology. *Geophysical Journal International,* 183**,** 503-535.

Eriksson, L. E. B. 2004. *Satellite-borne L-band interferometric coherence for forestry applications in the boreal zone.* PhD, Friedrich-Schiller-Univ.

Esa. 2011a. *Parameters affecting radar backscatter* [Online]. Available: http://earth.esa.int/applications/data_util/SARDOCS/spaceborne/Radar_Courses/Radar_Course_III/parameters_affecting.htm [Accessed 14th Feburary 2011].

Esa. 2011b. *Scientific Background* [Online]. Available: http://envisat.esa.int/handbooks/asar/CNTR1-1-2.htm - eph.asar.ug.choos.sci [Accessed 14th Feburary 2011].

Esa. 2013. *MERIS - Earthnet Online* [Online]. Available: https://earth.esa.int/web/guest/missions/esa-operational-eo-missions/envisat/instruments/meris [Accessed 7th June 2013].

Evans, M. & Lindsay, J. 2010a. High resolution quantification of gully erosion in upland peatlands at the landscape scale. *Earth Surface Processes and Landforms,* 35**,** 876-886.

Evans, M. & Lindsay, J. 2010b. Impact of gully erosion on carbon sequestration in blanket peatlands. *Climate Research,* 45**,** 31-41.

Evans, M. & Warburton, J. 2007. The Geomorphology of Upland Peat: Process, Form and Landscape Change. Blackwell, Oxford.

Evans, M., Warburton, J. & Yang, J. 2006. Eroding blanket peat catchments: global and local implications of upland organic sediment budgets. *Geomorphology,* 79**,** 45-57.

Evans, M. G. & Warburton, J. 2010. Peatland Geomorphology and Carbon Cycling. *Geography Compass,* 4**,** 1513-1531.

F.Covello, Battazza, F., Coletta, A., Lopinto, E., Fiorentino, C., Pietranera, L., Valentini, G. & Zoffoli, S. 2010. COSMO-SkyMed an existing opportunity for observing the Earth. *Journal of Geodynamics,* 49.

Farr, T. G., Rosen, P. A., Caro, E., Crippen, R., Duren, R., Hensley, S., Kobrick, M., Paller, M., Rodriguez, E., Roth, L., Seal, D., Shaffer, S., Shimada, J., Umland, J., Werner, M., Oskin, M., Burbank, D. & Alsdorf, D. 2007. The Shuttle Radar Topography Mission. *Rev. Geophys.,* 45**,** RG2004.

Ferretti, A., Fumagalli, A., Novali, F., Prati, C., Rocca, F. & Rucci, A. 2011. A New Algorithm for Processing Interferometric Data-Stacks: SqueeSAR. *Geoscience and Remote Sensing, IEEE Transactions on,* 49**,** 1-11.

Ferretti, A., Monti-Guarnieri, A. & Claudio Prati, F. R. 2007. *InSAR Principles: Guidelines for SAR Interferometry Processing and Interpretation(TM-19)*, ESA Publications.

Ferretti, A., Prati, C. & Rocca, F. 2000. Nonlinear subsidence rate estimation using permanent scatterers in differential SAR interferometry. *Geoscience and Remote Sensing, IEEE Transactions on,* 38**,** 2202-2212.

Ferretti, A., Prati, C. & Rocca, F. 2001. Permanent scatterers in SAR interferometry. *Geoscience and Remote Sensing, IEEE Transactions on,* 39**,** 8-20.

Fialko, Y. 2006. Interseismic strain accumulation and the earthquake potential on the southern San Andreas fault system. *Nature,* 441**,** 968-971.

Fialko, Y., Sandwell, D., Simons, M. & Rosen, P. 2005. Three-dimensional deformation caused by the Bam, Iran, earthquake and the origin of shallow slip deficit. *Nature,* 435**,** 295-299.

Fialko, Y., Simons, M. & Agnew, D. 2001. The Complete (3-D) Surface Displacement Field in the Epicentral Area of the 1999 MW 7.1 Hector Mine Earthquake, California, from Space Geodetic Observations. *Geophys. Res. Lett.,* 28**,** 3063-3066.

Fie. 2013. *peatlandtypes* [Online]. Available: http://www.friendsoftheirishenvironment.net/cmsfiles/images/peatlandtypes.jpg [Accessed 19 June 2013].

Fielding, E. J., Blom, R. G. & Goldstein, R. M. 1998. Rapid subsidence over oil fields measured by SAR interferometry. *Geophys. Res. Lett.,* 25**,** 3215-3218.

Fluxnet. 2013. *Methodology & Tools | FLUXNET* [Online]. Available: http://fluxnet.ornl.gov/methodology [Accessed 23 June 2013].

Foster, J., Brooks, B., Cherubini, T., Shacat, C., Businger, S. & Werner, C. L. 2006. Mitigating atmospheric noise for InSAR using a high resolution weather model. *Geophysical Research Letters,* 33**,** L16304.

Foster, J., Kealy, J., Cherubini, T., Businger, S., Lu, Z. & Murphy, M. 2013. The utility of atmospheric analyses for the mitigation of artifacts in InSAR. *Journal of Geophysical Research: Solid Earth,* 118**,** 748-758.

Francis, I. S. 1990. Blanket peat erosion in a mid-wales catchment during two drought years. *Earth Surface Processes and Landforms,* 15**,** 445-456.

Fujiwara, S., Nishimura, T., Murakami, M., Nakagawa, H., Tobita, M. & Rosen, P. A. 2000. 2.5 D surface deformation of M6. 1 earthquake near Mt Iwate detected by SAR interferometry. *Geophysical Research Letters,* 27**,** 2049-2052.

Gabriel, A. K., Goldstein, R. M. & Zebker, H. A. 1989. Mapping small elevation changes over large areas: Differential radar interferometry. *Journal of Geophysical Research: Solid Earth (1978–2012),* 94**,** 9183-9191.

Galloway, D. L., Hudnut, K. W., Ingebritsen, S. E., Phillips, S. P., Peltzer, G., Rogez, F. & Rosen, P. A. 1998. Detection of aquifer system compaction and land subsidence using interferometric synthetic aperture radar, Antelope Valley, Mojave Desert, California. *Water Resources Research,* 34**,** 2573-2585.

Ghiglia, D. C. & Pritt, M. D. 1998. *Two-dimensional phase unwrapping: theory, algorithms, and software*, Wiley New York.

Gielen, D. J., Bos, A. J. M., Feber, M. D. & Gerlagh, T. 2013. Biomass for greenhouse gas emission reduction task 8: optimal emission reduction strategies for Western Europe. *Policy Studies,* 2012**,** 2011.

Goldstein, R. 1995. Atmospheric limitations to repeat-track radar interferometry. *Geophys. Res. Lett.,* 22**,** 2517-2520.

Goldstein, R. M., Engelhardt, H., Kamb, B. & Frolich, R. M. 1993. Satellite radar interferometry for monitoring ice-sheet motion: Application to an Antarctic ice stream. *Science,* 262**,** 1525-1530.

Goldstein, R. M., Zebker, H. A. & Werner, C. L. 1988. Satellite radar interferometry: Two-dimensional phase unwrapping. *Radio Science,* 23**,** 713-720.

Gorham, E. 1991. Northern Peatlands: Role in the Carbon Cycle and Probable Responses to Climatic Warming. *Ecological Applications,* 1**,** 182-195.

Grace, J. 2004. Understanding and managing the global carbon cycle. *Journal of Ecology,* 92**,** 189-202.

Graham, L. C. 1974. Synthetic interferometer radar for topographic mapping. *Proceedings of the IEEE,* 62**,** 763-768.

Gray, A. L., Mattar, K. E. & Sofko, G. 2000. Influence of ionospheric electron density fluctuations on satellite radar interferometry. *Geophysical Research Letters,* 27**,** 1451-1454.

Great Britain, F. C. 2012. *Forestry Commission - Scotland datasets* [Online]. Available: http://www.forestry.gov.uk/forestry/infd-8g5bzf - 5 [Accessed 20th October 2012.

Grieve, I. C., Davidson, D. A. & Gordon, J. E. 1995. Nature, extent and severity of soil erosion in upland Scotland. *Land Degradation & Development,* 6**,** 41-55.

Group, S. R. I. R. 2013. *SNAPHU* [Online]. Available: http://www.stanford.edu/group/radar/softwareandlinks/sw/snaphu/ [Accessed 10 May 2010].

Hagberg, J. O., Ulander, L. M. H. & Askne, J. 1995. Repeat-pass SAR interferometry over forested terrain. *Geoscience and Remote Sensing, IEEE Transactions on,* 33**,** 331-340.

Hall, D. K., Riggs, G. A., Salomonson, V. V., Digirolamo, N. E. & Bayr, K. J. 2002. MODIS snow-cover products. *Remote Sensing of Environment,* 83**,** 181-194.

Hanssen, R. F. (ed.) 2001. *Radar interferometry:data interpretation and error analysis,* Dordrecht: Kluwer Academic Plublishers.

Harris, A. & Bryant, R. G. 2009a. A multi-scale remote sensing approach for monitoring northern peatland hydrology: Present possibilities and future challenges. *Journal of Environmental Management,* 90**,** 2178-2188.

Harris, A. & Bryant, R. G. 2009b. Northern peatland vegetation and the carbon cycle: a remote sensing approach. American Geophysical Union.

Herráez, M. A., Burton, D. R., Lalor, M. J. & Gdeisat, M. A. 2002. Fast two-dimensional phase-unwrapping algorithm based on sorting by reliability following a noncontinuous path. *Applied Optics,* 41**,** 7437-7444.

Hirano, T., Jauhiainen, J., Inoue, T. & Takahashi, H. 2009. Controls on the Carbon Balance of Tropical Peatlands. *Ecosystems,* 12**,** 873-887.

Hirano, T., Segah, H., Harada, T., Limin, S., June, T., Hirata, R. & Osaki, M. 2007. Carbon dioxide balance of a tropical peat swamp forest in Kalimantan, Indonesia. *Global Change Biology,* 13**,** 412-425.

Hirano, T., Segah, H., Kusin, K., Limin, S., Takahashi, H. & Osaki, M. 2012. Effects of disturbances on the carbon balance of tropical peat swamp forests. *Global Change Biology,* 18**,** 3410-3422.

Hoekman, D. & Vissers, M. ALOS PALSAR radar observation of tropical peat swamp forest as a monitoring tool for environmental protection and restoration. Geoscience and Remote Sensing Symposium, 2007. IGARSS 2007. IEEE International, 23-28 July 2007. 3710-3714.

Hoekman, D. H. 2007. Satellite radar observation of tropical peat swamp forest as a tool for hydrological modelling and environmental protection. *Aquatic Conservation: Marine and Freshwater Ecosystems,* 17**,** 265-275.

Hoekman, D. H. 2009. Monitoring tropical peat swamp deforestation and hydrological dynamics by ASAR and PALSAR. *Geoscience and Remote Sensing, In-Tech, Vienna***,** 257-275.

Holden, J. 2005. Peatland hydrology and carbon release: why small-scale process matters. *Philosophical Transactions of the Royal Society A: Mathematical, Physical and Engineering Sciences,* 363**,** 2891-2913.

Holden, J., Chapman, P. J. & Labadz, J. C. 2004. Artificial drainage of peatlands: hydrological and hydrochemical process and wetland restoration. *Progress in Physical Geography,* 28**,** 95-123.

Hong, S.-H., Wdowinski, S., Kim, S.-W. & Won, J.-S. 2010. Multi-temporal monitoring of wetland water levels in the Florida Everglades using interferometric synthetic aperture radar (InSAR). *Remote Sensing of Environment,* 114**,** 2436-2447.

Hooijer, A., Page, S., Canadell, J. G., Silvius, M., Kwadijk, J., W¨Osten, H. & Jauhiainen, J. 2010. Current and future CO2 emissions from drained peatlands in Southeast Asia. *Biogeosciences,* 7**,** 1505-1514.

Hooijer, A., Page, S., Jauhiainen, J., Lee, W. A., Lu, X. X., Idris, A. & Anshari, G. 2012. Subsidence and carbon loss in drained tropical peatlands. *Biogeosciences,* 9**,** 1053-1071.

Hooijer, A., Silvius, M., Wösten, H. & Page, S. 2006. *PEAT-CO2,Assessment of CO2 emissions from drained peatlands in SE Asia. Delft Hydraulics report Q3943.*

Hooper, A. 2008. A multi-temporal InSAR method incorporating both persistent scatterer and small baseline approaches. *Geophys. Res. Lett.,* 35**,** L16302.

Hooper, A., Segall, P. & Zebker, H. 2007. Persistent scatterer interferometric synthetic aperture radar for crustal deformation analysis, with application to Volcán Alcedo, Galápagos. *J. Geophys. Res.,* 112**,** B07407.

Hooper, A., Zebker, H., Segall, P. & Kampes, B. 2004. A new method for measuring deformation on volcanoes and other natural terrains using InSAR persistent scatterers. *Geophys. Res. Lett.,* 31**,** L23611.

Hope, D., Billett, M. F. & Cresser, M. S. 1997. Exports of organic carbon in two river systems in NE Scotland. *Journal of Hydrology,* 193**,** 61-82.

Hulme, M., Jenkins, G. J., Lu, X., Turnpenny, J. R., Mitchell, T. D., Jones, R. G., Lowe, J., Murphy, J. M., Hassell, D. & Boorman, P. 2002. *Climate change scenarios for the United Kingdom: the UKCIP02 scientific report*, Tyndall Centre for Climate Change Research, School of Environmental Sciences, University of East Anglia Norwich.

Imhoff, M. L. Radar backscatter/biomass saturation: Observations and implications for global biomass assessment. Geoscience and Remote Sensing Symposium, 1993. IGARSS '93. Better Understanding of Earth Environment., International, 18-21 Aug 1993. 43-45.

Ipcc 2006. IPCC guidelines for national greenhouse gas inventories. *IGES, Japan.*

Jaber, W. A., Floricioiu, D., Rott, H. & Eineder, M. Dynamics of fast glaciers in the Patagonia Icefields derived from TerraSAR-X and TanDEM-X data. Geoscience and Remote Sensing Symposium (IGARSS), 2012 IEEE International, 22-27 July 2012. 3226-3229.

Jaenicke, J., Englhart, S. & Siegert, F. 2011. Monitoring the effect of restoration measures in Indonesian peatlands by radar satellite imagery. *Journal of Environmental Management,* 92**,** 630-638.

Jaenicke, J., Rieley, J. O., Mott, C., Kimman, P. & Siegert, F. 2008. Determination of the amount of carbon stored in Indonesian peatlands. *Geoderma,* 147**,** 151-158.

Jaenicke, J., Wösten, H., Budiman, A. & Siegert, F. 2010. Planning hydrological restoration of peatlands in Indonesia to mitigate carbon dioxide emissions. *Mitigation and Adaptation Strategies for Global Change,* 15**,** 223-239.

Jauhiainen, J., H, V., A, J., I, T., J, H. & P, M. Carbon balance in managed tropical peat in Central Kalimantan, Indonesia. Wise Use of Peatlands-Proceedings of the 12th International Peat Congress, 06-11 June 2004 Tampere. 653-659.

Jauhiainen, J., Hooijer, A. & Page, S. E. 2012. Carbon dioxide emissions from an Acacia plantation on peatland in Sumatra, Indonesia. *Biogeosciences,* 9**,** 617-630.

Jauhiainen, J., Limin, S., Silvennoinen, H. & Vasander, H. 2008. Carbon dioxide and methane fluxes in drained tropical peat before and after hydrological restoration. *Ecology,* 89**,** 3503-3514.

Jin-Woo, K., Zhong, L., Hyongki, L., Shum, C. K., Christopher, M. S., Thomas, W. D. & Sang-Ho, B. 2009. Integrated analysis of PALSAR/Radarsat-1 InSAR and ENVISAT altimeter data for mapping of absolute water level changes in Louisiana wetlands. *Remote Sensing of Environment,* 113**,** 2356-2365.

Joosten, H. 2009. *The Global Peatland CO2 Picture-Peatland status and drainage related emissions in all countries of the world*, Wetlands International.

Kaat, A. & Joosten, H. 2009. *Fact book for UNFCCC policies on peat carbon emissions*, Wetlands International.

Kampes, B. M. 2006. *Radar Interferometry:Persistent Scatterer Technique*, Springer.

Kementerian Kehutanan Republik Indonesia, D. J. P. K. 2012. *WebGIS Kehutanan* [Online]. Available: http://appgis.dephut.go.id/appgis/kml.aspx [Accessed 3 February 2013].

Keyworth, S., Jarman, M. & Medcalf, K. 2009. Assessing the Extent and Severity of Erosion on the Upland Organic Soils of Scotland using Earth Observation: A GIFTSS Implementation Test: Final Report.

Kimberly, M. C., Lisa, M. C., Gregory, P. A., Alice Mcdonald, P., Simon, N. T. & Adeney, J. M. 2012. Carbon emissions from forest conversion by Kalimantan oil palm plantations. *Nature Climate Change.*

Klobuchar, J. 1996. Ionospheric effects on GPS. *Global Positioning System: Theory and applications.,* 1**,** 485-515.

Koh, L. P., Miettinen, J., Liew, S. C. & Ghazoul, J. 2011. Remotely sensed evidence of tropical peatland conversion to oil palm. *Proceedings of the National Academy of Sciences,* 108**,** 5127-5132.

Laine, A., Sottocornola, M., Kiely, G., Byrne, K. A., Wilson, D. & Tuittila, E.-S. 2006. Estimating net ecosystem exchange in a patterned ecosystem: Example from blanket bog. *Agricultural and Forest Meteorology,* 138**,** 231-243.

Lanari, R., Casu, F., Manzo, M., Zeni, G., Berardino, P., Manunta, M. & Pepe, A. 2007. An Overview of the Small BAseline Subset Algorithm: a DInSAR Technique for Surface Deformation Analysis. *Pure and Applied Geophysics,* 164**,** 637-661.

Lanari, R., Mora, O., Manunta, M., Mallorqui, J. J., Berardino, P. & Sansosti, E. 2004. A small-baseline approach for investigating deformations on full-resolution differential SAR interferograms. *Geoscience and Remote Sensing, IEEE Transactions on,* 42**,** 1377-1386.

Lauknes, I. & Malnes, E. Automatical geocoding of SAR products. 2004.

Lee, X., Massman, W. J. & Law, B. E. 2004. *Handbook of micrometeorology: a guide for surface flux measurement and analysis*, Springer.

Li, Z. 2005. *Correction of atmospheric water vapour effects on repeat-pass sar interferometry using GPS, MODIS and MERIS data.* Ph.D, University College London.

Li, Z., Fielding, E. J. & Cross, P. 2009a. Integration of InSAR Time-Series Analysis and Water-Vapor Correction for Mapping Postseismic Motion After the 2003 Bam (Iran) Earthquake. *Geoscience and Remote Sensing, IEEE Transactions on,* 47**,** 3220-3230.

Li, Z., Fielding, E. J., Cross, P. & Muller, J.-P. 2006a. Interferometric synthetic aperture radar atmospheric correction: GPS topography-dependent turbulence model. *Journal of Geophysical Research: Solid Earth,* 111**,** B02404.

Li, Z., Fielding, E. J., Cross, P. & Muller, J.-P. 2006b. Interferometric synthetic aperture radar atmospheric correction: Medium Resolution Imaging Spectrometer and Advanced Synthetic Aperture Radar integration. *Geophysical Research Letters,* 33**,** L06816.

Li, Z., Fielding, E. J., Cross, P. & Preusker, R. 2009b. Advanced InSAR atmospheric correction: MERIS/MODIS combination and stacked water vapour models. *International Journal of Remote Sensing,* 30**,** 3343-3363.

Li, Z., Muller, J.-P. & Cross, P. 2003. Comparison of precipitable water vapor derived from radiosonde, GPS, and Moderate-Resolution Imaging Spectroradiometer measurements. *Journal of Geophysical Research: Atmospheres,* 108**,** 4651.

Li, Z., Muller, J.-P., Cross, P. & Fielding, E. J. 2005. Interferometric synthetic aperture radar (InSAR) atmospheric correction: GPS, Moderate Resolution Imaging Spectroradiometer (MODIS), and InSAR integration. *J. Geophys. Res.,* 110**,** B03410.

Lillesand, T. M., Kiefer, R. W. & Chipman, J. W. 2004. *Remote sensing and image interpretation*, John Wiley & Sons Ltd.

Limpens, J., Berendse, F., Blodau, C., Canadell, J. G., Freeman, C., Holden, J., Roulet, N., Rydin, H. & Schaepman-Strub, G. 2008. Peatlands and the carbon cycle: from local processes to global implications – a synthesis. *Biogeosciences,* 5**,** 1475-1491.

Line, R., François, Q., Suzanne, C., Kurt, J. & Thomas, M. 2003. North American approach to the restoration of Sphagnum dominated peatlands. *Wetlands Ecology and Management,* 11**,** 3-20.

Liu, P., Li, Z., Hoey, T., Kincal, C., Zhang, J., Zeng, Q. & Muller, J.-P. 2013. Using advanced InSAR time series techniques to monitor landslide movements in Badong of the Three Gorges region, China. *International Journal of Applied Earth Observation and Geoinformation,* 21**,** 253-264.

Lu, Z., Fatland, R., Wyss, M., Li, S., Eichelberger, J., Dean, K. & Freymueller, J. 1997. Deformation of New Trident Volcano measured by ERS-1 SAR interferometry, Katmai National Park, Alaska. *Geophys. Res. Lett.,* 24**,** 695-698.

Luckman, A., Baker, J., Honzák, M. & Lucas, R. 1998. Tropical Forest Biomass Density Estimation Using JERS-1 SAR: Seasonal Variation, Confidence Limits, and Application to Image Mosaics. *Remote Sensing of Environment,* 63**,** 126-139.

Lunetta, R. S., Knight, J. F., Ediriwickrema, J., Lyon, J. G. & Worthy, L. D. 2006. Land-cover change detection using multi-temporal MODIS NDVI data. *Remote Sensing of Environment,* 105**,** 142-154.

Madsen, S. N., Mohr, J. J. & Reeh, N. Mapping Greenland by ERS-1/2 InSAR for ice mass balance and dynamics studies. Proceedings of ESA Fringe'99 Meeting, 10-12 Novemeber 1999 LieÁge, Belgium.

Massonnet, D., Briole, P. & Arnaud, A. 1995. Deflation of Mount Etna monitored by spaceborne radar interferometry. *Nature,* 375**,** 567-570.

Massonnet, D. & Feigl, K. L. 1995. Discrimination of geophysical phenomena in satellite radar interferograms. *Geophys. Res. Lett.,* 22**,** 1537-1540.

Massonnet, D. & Feigl, K. L. 1998. Radar Interferometry and Its Application to Changes in the Earth's Surface. *Rev. Geophys.,* 36**,** 441-500.

Massonnet, D., Rossi, M., Carmona, C., Adragna, F., Peltzer, G., Feigl, K. & Rabaute, T. 1993. The displacement field of the Landers earthquake mapped by radar interferometry. *Nature,* 364**,** 138-142.

Massonnet, D., Thatcher, W. & Vadon, H. 1996. Detection of postseismic fault-zone collapse following the Landers earthquake. *Nature,* 382**,** 612-616.

Melling, L., Hatano, R. & Goh, K. J. 2005. Soil CO2 flux from three ecosystems in tropical peatland of Sarawak, Malaysia. *Tellus B,* 57**,** 1-11.

Meng, W. & Sandwell, D. T. 2010. Decorrelation of L-Band and C-Band Interferometry Over Vegetated Areas in California. *Geoscience and Remote Sensing, IEEE Transactions on,* 48**,** 2942-2952.

Met, O. 2005. *Met Office: Regional climate: Northern Scotland* [Online]. Available: http://www.metoffice.gov.uk/climate/uk/ns/print.html [Accessed 10 November 2012].

Meyer, F. J., Mahoney, A. R., Eicken, H., Denny, C. L., Druckenmiller, H. C. & Hendricks, S. 2011. Mapping arctic landfast ice extent using L-band synthetic aperture radar interferometry. *Remote Sensing of Environment,* 115**,** 3029-3043.

Meyer, F. J. & Nicoll, J. The impact of the ionosphere on interferometric SAR processing. Geoscience and Remote Sensing Symposium, 2008. IGARSS 2008. IEEE International, 2008. IEEE, II-391.

Miettinen, J. & Liew, S. C. 2010. Degradation and development of peatlands in Peninsular Malaysia and in the islands of Sumatra and Borneo since 1990. *Land Degradation & Development,* 21**,** 285-296.

Miettinen, J., Shi, C. & Liew, S. C. 2011a. Deforestation rates in insular Southeast Asia between 2000 and 2010. *Global Change Biology,* 17**,** 2261-2270.

Miettinen, J., Wang, J., Hooijer, A. & Liew, S. 2011b. Peatland conversion and degradation processes in insular southeast asia: a case study in jambi, indonesia. *Land Degradation & Development,* 24**,** 334-341.

Milne, R. & Brown, T. A. 1997. Carbon in the vegetation and soils of Great Britain. *Journal of Environmental Management,* 49**,** 413-433.

Moore, T. R., Bubier, J. L., Frolking, S. E., Lafleur, P. M. & Roulet, N. T. 2002. Plant biomass and production and CO2 exchange in an ombrotrophic bog. *Journal of Ecology,* 90**,** 25-36.

Morel, A. C., Saatchi, S. S., Malhi, Y., Berry, N. J., Banin, L., Burslem, D., Nilus, R. & Ong, R. C. 2011. Estimating aboveground biomass in forest and oil palm plantation in Sabah, Malaysian Borneo using ALOS PALSAR data. *Forest Ecology and Management,* 262**,** 1786-1798.

Murayama, S. & Bakar, Z. A. 1996. Decomposition of tropical peat soils, 2: Estimation of in situ decomposition by measurement of CO2 flux. *JARQ,* 30**,** 153-158.

Murdiyarso, D., Hergoualc'h, K. & Verchot, L. V. 2010. Opportunities for reducing greenhouse gas emissions in tropical peatlands. *Proceedings of the National Academy of Sciences,* 107**,** 19655-19660.

Nasa. 2012. *Earth Observing System Data and Information System* [Online]. Available: http://earthdata.nasa.gov/about-eosdis [Accessed 4 March 2013].

Nasa. 2013a. *MODIS Website* [Online]. Available: http://modis.gsfc.nasa.gov/about/design.php [Accessed 7th June 2013].

Nasa. 2013b. *Reverb | ECHO* [Online]. Available: http://reverb.echo.nasa.gov/reverb/ -utf8=%E2%9C%93&spatial_map=satellite&spatial_type=rectangle [Accessed 31 August 2013].

Nolan, M. & Fatland, D. R. 2003. Penetration depth as a DInSAR observable and proxy for soil moisture. *Geoscience and Remote Sensing, IEEE Transactions on,* 41**,** 532-537.

O'donnell, J. A., Jorgenson, M. T., Harden, J. W., Mcguire, A. D., Kanevskiy, M. Z. & Wickland, K. P. 2012. The effects of permafrost thaw on soil hydrologic, thermal, and carbon dynamics in an Alaskan peatland. *Ecosystems,* 15**,** 213-229.

Page, S., Hoscilo, A., Langner, A., Tansey, K., Siegert, F., Limin, S. & Rieley, J. 2009a. Tropical peatland fires in Southeast Asia. *Tropical Fire Ecology.* Springer.

Page, S., Hosciło, A., Wösten, H., Jauhiainen, J., Silvius, M., Rieley, J., Ritzema, H., Tansey, K., Graham, L., Vasander, H. & Limin, S. 2009b. Restoration Ecology of Lowland Tropical Peatlands in Southeast Asia: Current Knowledge and Future Research Directions. *Ecosystems,* 12**,** 888-905.

Page, S., Morrison, R., Malins, C., Hooijer, A., Rieley, J. & Jauhiainen, J. 2011a. Review of peat surface greenhouse gas emissions from oil palm plantations in Southeast Asia. International Committee on Clean Transportation (ICCT).

Page, S., Rieley, J., Shotyk, W. & Weiss, D. 1999. Interdependence of peat and vegetation in a tropical peat swamp forest. *Philosophical transactions of the Royal Society of London. Series B, Biological sciences,* 354**,** 1885-1897.

Page, S. E., Rieley, J. O. & Banks, C. J. 2010. Global and regional importance of the tropical peatland carbon pool. *Global Change Biology,* 17**,** 798-818.

Page, S. E., Rieley, J. O. & Banks, C. J. 2011b. Global and regional importance of the tropical peatland carbon pool. *Global Change Biology,* 17**,** 798-818.

Page, S. E., Siegert, F., Rieley, J. O., Boehm, H.-D. V., Jaya, A. & Limin, S. 2002. The amount of carbon released from peat and forest fires in Indonesia during 1997. *Nature,* 420**,** 61-65.

Papoutsis, I., Papanikolaou, X., Floyd, M., Ji, K. H., Kontoes, C., Paradissis, D. & Zacharis, V. 2013. Mapping inflation at Santorini volcano, Greece, using GPS and InSAR. *Geophysical Research Letters,* 40**,** 267-272.

Pawson, R. R., Lord, D. R., Evans, M. G. & Allott, T. E. H. 2008. Fluvial organic carbon flux from an eroding peatland catchment, southern Pennines, UK. *Hydrology and Earth System Sciences Discussions,* 12**,** 625-634.

Perissin, D. & Ferretti, A. 2007. Urban-target recognition by means of repeated spaceborne SAR images. *Geoscience and Remote Sensing, IEEE Transactions on,* 45**,** 4043-4058.

Pettorelli, N., Vik, J. O., Mysterud, A., Gaillard, J.-M., Tucker, C. J. & Stenseth, N. C. 2005. Using the satellite-derived NDVI to assess ecological responses to environmental change. *Trends in Ecology & Evolution,* 20**,** 503-510.

Pritchard, M. E. & Simons, M. 2002. A satellite geodetic survey of large-scale deformation of volcanic centres in the central Andes. *Nature,* 418**,** 167-171.

Purnomo, H., Suyamto, D., Abdullah, L. & Irawati, R. 2012. REDD+ actor analysis and political mapping: an Indonesian case study. *International Forestry Review,* 14**,** 74-89.

Puysségur, B., Michel, R. & Avouac, J.-P. 2007. Tropospheric phase delay in interferometric synthetic aperture radar estimated from meteorological model and multispectral imagery. *Journal of Geophysical Research: Solid Earth,* 112**,** B05419.

Ramon, T., Paul, S., Dirk, G., David, B., Malcolm, D., Evert, A., Pierre, P., Björn, R., Nicolas, F., Mike, B., Ignacio Navas, T., Patrick, D., Berthyl, D., Betlem, R., Nuno, M., Claudio, B., Michelangelo, L. A., Renato, C., Andrea, P., Markus, H. & Friedhelm, R. 2012. GMES Sentinel-1 mission. *Remote Sensing of Environment,* 120**,** 9-24.

Ribbes, F., Le Toan, T., Bruniquel, J., Floury, N., Stussi, N., Liew, S. C. & Wasrin, U. R. 1997. Deforestation monitoring in tropical regions using multitemporal ERS/JERS SAR and INSAR data. *Geoscience and Remote Sensing, 1997. IGARSS'97. Remote Sensing-A Scientific Vision for Sustainable Development., 1997 IEEE International,* 4**,** 1560-1562.

Rieley, J. & Page, S. 2008. Master Plan for the Rehabilitation and Revitalisation of the Ex-Mega Rice Project Area in Central Kalimantan. Jakarta/Delft.

Rignot, E. 2008. Changes in West Antarctic ice stream dynamics observed with ALOS PALSAR data. *Geophysical Research Letters,* 35**,** L12505.

Rodriguez, E., Morris, C. S., Belz, J. E., Chapin, E. C., Martin, J. M., Daffer, W. & Hensley, S. 2005. *An assessment of the SRTM topographic products,* Pasadena, California, Jet Propulsion Laboratory.

Rogers, A. E. E. & Ingalls, R. P. 1969. Venus: Mapping the surface reflectivity by radar interferometry. *Science,* 165**,** 797-799.

Roi_Pac. 2013. *ROI_PAC - ROI_PAC Wiki* [Online]. Available: http://www.roipac.org/ [Accessed 04 June 2013].

Romshoo, S. 2004. Radar remote sensing for monitoring of dynamic ecosystem processes related to biogeochemical exchanges in tropical peatlands. *Visual Geosciences,* 9**,** 9-28.

Rosen, P. A., Hensley, S., Joughin, I. R., Li, F. K., Madsen, S. N., Rodriguez, E. & Goldstein, R. M. 2000. Synthetic aperture radar interferometry. *Proceedings of the IEEE,* 88**,** 333-382.

Rosen, P. A., Hensley, S., Peltzer, G. & Simons, M. 2004. Updated repeat orbit interferometry package released. *Eos Trans. AGU,* 85**,** 47-47.

Rosenqvist, A., Shimada, M., Ito, N. & Watanabe, M. 2007. ALOS PALSAR: A Pathfinder Mission for Global-Scale Monitoring of the Environment. *Geoscience and Remote Sensing, IEEE Transactions on,* 45**,** 3307-3316.

Rothwell, J. J., Evans, M. G., Daniels, S. M. & Allott, T. E. H. 2008. Peat soils as a source of lead contamination to upland fluvial systems. *Environmental Pollution,* 153**,** 582-589.

Samsonov, S. 2010. Topographic Correction for ALOS PALSAR Interferometry. *Geoscience and Remote Sensing, IEEE Transactions on,* 48**,** 3020-3027.

Sandwell, D. T., Myer, D., Mellors, R., Shimada, M., Brooks, B. & Foster, J. 2008. Accuracy and resolution of ALOS interferometry: Vector deformation maps of the Father's Day intrusion at Kilauea. *Geoscience and Remote Sensing, IEEE Transactions on,* 46**,** 3524-3534.

Santos, J. R., Neeff, T., Dutra, L. V., Araujo, L. S., Gama, F. F. & Elmiro, M. a. T. 2004. Tropical forest biomass mapping from dual frequency SAR interferometry (X-and P-bands). *International Archives of Photogrammetry and Remote Sensing,* 35**,** 1133-1136.

Sasha, A., Cara, R. N., James, A., David, L., An, C., Kevin, L. E., Finlayson, C. M., Rudolf, S. D. G., Jim, A. H., Eric, S. H., Richard, J. H., Roy, R. R. L., Dennis, M. & Carolina, M. 2011. Opportunities and Challenges for Ecological Restoration within REDD+. *Restoration Ecology,* 19**,** 683-689.

Schothorst, C. J. Drainage and behaviour of peat soils. Proceedings of the Symposium on Peat Lands Below Sea Level: peat lands lying below sea level in the western part of the Netherlands, their geology, reclamation, soils, management, and land use, 1982 1982. International Institute for Land Reclamation and Improvement, 130-168.

Shen, Z.-K., Sun, J., Zhang, P., Wan, Y., Wang, M., Burgmann, R., Zeng, Y., Gan, W., Liao, H. & Wang, Q. 2009. Slip maxima at fault junctions and rupturing of barriers during the 2008 Wenchuan earthquake. *Nature Geosci,* 2**,** 718-724.

Shigehiro, I., Anas, I., Yasuhiro, N., Seiichirou, Y., Shigeto, S., Haruo, T. & Daniel, M. 2005. The variation of greenhouse gas emissions from soils of various land-use/cover types in Jambi province, Indonesia. *Nutrient Cycling in Agroecosystems,* 71**,** 17-32.

Shimada, M. Correction of the satellite's state vector and the atmospheric excess path delay in SAR interferometry-application to surface deformation detection. Geoscience and Remote Sensing Symposium, 2000. Proceedings. IGARSS 2000. IEEE 2000 International, 2000 2000. 2236-2238 vol.5.

Shimada, M., Minamisawa, M. & Isoguchi, O. Correction of atmospheric excess path delay appeared in repeat-pass SAR interferometry using objective analysis data. Geoscience and Remote Sensing Symposium, 2001. IGARSS '01. IEEE 2001 International, 2001 2001. 2052-2054 vol.5.

Shirzaei, M. & Bürgmann, R. 2012. Topography correlated atmospheric delay correction in radar interferometry using wavelet transforms. *Geophysical Research Letters,* 39**,** L01305.1-L01305.6.

Siderius, C. 2004. A hydrological model of the Air Hitam Laut watershed and the impact of various land use scenarios. *Water for Food & Ecosystems Programme, International Agricultural Centre (IAC): Wageningen.*

Silvius, M., Kaat, A., Bund, H. V. D. & Hooijer, A. 2006. *Peatland degradation fuels climate change*, Wetlands International.

Simons, M., Fialko, Y. & Rivera, L. 2002. Coseismic deformation from the 1999 Mw 7.1 Hector Mine, California, earthquake as inferred from InSAR and GPS observations. *Bulletin of the Seismological Society of America,* 92**,** 1390-1402.

Simons, M., Minson, S., Sladen, A., Ortega, F., Jiang, J., Owen, S., Meng, L., Ampuero, J.-P., Wei, S., Chu, R., Helmberger, D., Kanamori, H., Hetland, E., Moore, A. & Webb, F. 2011. The 2011 magnitude 9.0 Tohoku-Oki earthquake: mosaicking the megathrust from seconds to centuries. *Science (New York, N.Y.),* 332**,** 1421-1425.

Smith, G., Dammert, P. B. & Askne, J. 1996. Decorrelation mechanisms in C-band SAR interferometry over boreal forest. *Satellite Remote Sensing III***,** 300-310.

Sousa, J. J., Ruiz, A. M., Hanssen, R. F., Bastos, L., Gil, A. J., Galindo-Zaldívar, J. & Sanz De Galdeano, C. 2010. PS-InSAR processing methodologies in the detection of field surface deformation--Study of the Granada basin (Central Betic Cordilleras, southern Spain). *Journal of Geodynamics,* 49**,** 181-189.

Sowter, A., Bateson, L., Strange, P., Ambrose, K. & Syafiudin, M. F. 2013. DInSAR estimation of land motion using intermittent coherence with application to the South Derbyshire and Leicestershire coalfields. *Remote Sensing Letters,* 4**,** 979-987.

Stolle, F., Chomitz, K. M., Lambin, E. F. & Tomich, T. P. 2003. Land use and vegetation fires in Jambi Province, Sumatra, Indonesia. *Forest Ecology and Management,* 179**,** 277-292.

Stramondo, S., Bozzano, F., Marra, F., Wegmuller, U., Cinti, F. R., Moro, M. & Saroli, M. 2008. Subsidence induced by urbanisation in the city of Rome detected by advanced InSAR technique and geotechnical investigations. *Remote Sensing of Environment,* 112**,** 3160-3172.

Stramondo, S., Chini, M., Bignami, C., Salvi, S. & Atzori, S. 2011. X-, C-, and L-band DInSAR investigation of the April 6, 2009, Abruzzi earthquake. *Geoscience and Remote Sensing Letters, IEEE,* 8**,** 49-53.

Suga, Y. & Takeuchi, S. Application of JERS-1 InSAR for monitoring deforestation of tropical rain forest. Geoscience and Remote Sensing Symposium, 2000. Proceedings. IGARSS 2000. IEEE 2000 International., 2000. 432-434.

Suzuki, S., Kankaku, Y. & Osawa, Y. Development Status of PALSAR-2 onboard ALOS-2. Proc. SPIE 8176, Sensors, Systems, and Next-Generation Satellites XV, 81760Q 3 October 2011. 1.

Takeuchi, S. & Oguro, Y. 2003. A comparative study of coherence patterns in C-band and L-band interferometric SAR from tropical rain forest areas. *Advances in Space Research,* 32**,** 2305-2310.

Tallis, J. 1997a. Peat erosion in the Pennines: the badlands of Britain. *Biologist,* 44**,** 277-279.

Tallis, J. H. 1997b. The southern Pennine experience: an overview of blanket mire degradation. *Blanket mire degradation: Causes, consequences and challenges***,** 7-15.

Tallis, J. H., Meade, R. & Hulme, P. D. 1997. *Blanket mire degradation: causes, consequences and challenges*, English Nature.

Tarayre, H. & Massonnet, D. 1996. Atmospheric Propagation heterogeneities revealed by ERS-1 interferometry. *Geophysical Research Letters,* 23**,** 989-992.

Teh, Y., Silver, W., Sonnentag, O., Detto, M., Kelly, M. & Baldocchi, D. 2011. Large Greenhouse Gas Emissions from a Temperate Peatland Pasture. *Ecosystems,* 14**,** 311-325.

Tralli, D. M., Blom, R. G., Zlotnicki, V., Donnellan, A. & Evans, D. L. 2005. Satellite remote sensing of earthquake, volcano, flood, landslide and coastal inundation hazards. *ISPRS Journal of Photogrammetry and Remote Sensing,* 59**,** 185-198.

Uk, G. 2013. *Indonesia map | Greenpeace UK* [Online]. Available: http://www.greenpeace.org.uk/files/maps/indonesia/index.html [Accessed 18 June 2011].

Ulaby, F. T., Moore, R. K. & Fung, A. K. 1981. Microwave remote sensing: Active and passive. Volume 1 - Microwave remote sensing fundamentals and radiometry. *Microwave Remote Sensing Active and Passive,* 1**,** 456-456.

Ulander, L. M. H., Gustavsson, A., Dubois-Fernandez, P., Dupuis, X., Fransson, J. E. S., Holmgren, J., Wallerman, J., Eriksson, L., Sandberg, G. & Soja, M. BIOSAR 2010 - A SAR campaign in support to the BIOMASS mission. Geoscience and Remote Sensing Symposium (IGARSS), 2011 IEEE International, 24-29 July 2011 2011. 1528-1531.

Unfccc. 2009. *GHG data* [Online]. Available: http://unfccc.int/ghg_data/ghg_data_unfccc/items/4146.php [Accessed 19/05/2013 2013].

Usgs. 2013. *EarthExplorer* [Online]. Available: http://earthexplorer.usgs.gov/ [Accessed 20 May 2013].

Van Der Werf, G. R., Dempewolf, J., Trigg, S. N., Randerson, J. T., Kasibhatla, P. S., Giglio, L., Murdiyarso, D., Peters, W., Morton, D. C., Collatz, G. J., Dolman, A. J. & Defries, R. S. 2008. Climate regulation of fire emissions and deforestation in equatorial Asia. *Proceedings of the National Academy of Sciences,* 105**,** 20350-20355.

Wahyunto & Suryadiputra, I. N. N. 2008. *Peatland Distribution in Sumatra and Kalimantan-explanation of its data sets including source of information, accuracy, data constraints and gaps*, Wetlands International and Indonesia Programme. Bogor.

Webley, P. W., Wadge, G. & James, I. N. 2004. Determining radio wave delay by non-hydrostatic atmospheric modelling of water vapour over mountains. *Physics and Chemistry of the Earth, Parts A/B/C,* 29**,** 139-148.

Wegmuller, U. & Werner, C. 1997. Retrieval of vegetation parameters with SAR interferometry. *Geoscience and Remote Sensing, IEEE Transactions on,* 35**,** 18-24.

Wegmuller, U., Werner, C., Strozzi, T. & Wiesmann, A. Ionospheric Electron Concentration Effects on SAR and INSAR. Geoscience and Remote Sensing Symposium, 2006. IGARSS 2006. IEEE International Conference on, July 31-Aug. 4 2006. 3731-3734.

Werninghaus, R. TerraSAR-X mission. Proc. SPIE 5236, SAR Image Analysis, Modeling, and Techniques VI, 9, 12 January 2004. 9-16.

Wicke, B., Dornburg, V., Junginger, M. & Faaij, A. 2008. Different palm oil production systems for energy purposes and their greenhouse gas implications. *Biomass and Bioenergy,* 32**,** 1322-1337.

Williams, S., Bock, Y. & Fang, P. 1998. Integrated satellite interferometry: Tropospheric noise, GPS estimates and implications for interferometric synthetic aperture radar products. *Journal of Geophysical Research: Solid Earth,* 103**,** 27051-27067.

Wooster, M. J., Perry, G. L. W. & Zoumas, A. 2012. Fire, drought and El Niño relationships on Borneo (Southeast Asia) in the pre-MODIS era (1980–2000). *Biogeosciences,* 9**,** 317-340.

Worrall, F., Burt, T. P., Rowson, J. G., Warburton, J. & Adamson, J. K. 2009. The multi-annual carbon budget of a peat-covered catchment. *Science of The Total Environment,* 407**,** 4084-4094.

Worrall, F., Reed, M., Warburton, J. & Burt, T. 2003. Carbon budget for a British upland peat catchment. *Science of The Total Environment,* 312**,** 133-146.

Wösten, J. & Ritzema, H. 2001. Land and water management options for peatland development in Sarawak, Malaysia. *International Peat Journal,* 11**,** 59-66.

Wösten, J. H. M., Clymans, E., Page, S. E., Rieley, J. O. & Limin, S. H. 2008. Peat–water interrelationships in a tropical peatland ecosystem in Southeast Asia. *CATENA,* 73.

Wösten, J. H. M., Ismail, A. B. & Van Wijk, A. L. M. 1997. Peat subsidence and its practical implications: a case study in Malaysia. *Geoderma,* 78**,** 25-36.

Wösten, J. H. M., Van Den Berg, J., Van Eijk, P., Gevers, G. J. M., Giesen, W., Hooijer, A., Idris, A., Leenman, P. H., Rais, D. S. & Siderius, C. 2006. Interrelationships between hydrology and ecology in fire degraded tropical peat swamp forests. *Water Resources Development,* 22**,** 157-174.

Wright, T., Parsons, B., England, P. & Fielding, E. 2004a. InSAR observations of low slip rates on the major faults of western Tibet. *Science (New York, N.Y.),* 305**,** 236-239.

Wright, T. J., Parsons, B., England, P. C. & Fielding, E. J. 2004b. InSAR Observations of Low Slip Rates on the Major Faults of Western Tibet. *Science,* 305**,** 236-239.

Wright, T. J., Parsons, B. E. & Lu, Z. 2004c. Toward mapping surface deformation in three dimensions using InSAR. *Geophys. Res. Lett.,* 31**,** L01607.

Xu, W. B., Li, Z. W., Ding, X. L. & Zhu, J. J. 2011. Interpolating atmospheric water vapor delay by incorporating terrain elevation information. *Journal of Geodesy,* 85**,** 555-564.

Yadvinder, M. 2010. The carbon balance of tropical forest regions, 1990–2005. *Current Opinion in Environmental Sustainability,* 2**,** 237-244.

Yuri, F., Mark, S. & Duncan, A. 2001. The complete (3-D) surface displacement field in the epicentral area of the 1999 M W 7.1 Hector Mine Earthquake, California, from space geodetic observations. *Geophysical Research Letters,* 28.

Zebker, H., Shankar, P. & Hooper, A. InSAR Remote Sensing Over Decorrelating Terrains: Persistent Scattering Methods. Radar Conference, 2007 IEEE, 17-20 April 2007. 717-722.

Zebker, H. A. & Goldstein, R. M. 1986. Topographic mapping from interferometric synthetic aperture radar observations. *Journal of Geophysical Research,* 91**,** 4993-4999.

Zebker, H. A., Rosen, P. A., Goldstein, R. M., Gabriel, A. & Werner, C. L. 1994a. On the derivation of coseismic displacement fields using differential radar interferometry: The Landers earthquake. *J. Geophys. Res.,* 99**,** 19617-19634.

Zebker, H. A., Rosen, P. A. & Hensley, S. 1997. Atmospheric effects in interferometric synthetic aperture radar surface deformation and topographic maps. *J. Geophys. Res.,* 102**,** 7547-7563.

Zebker, H. A. & Villasenor, J. 1992. Decorrelation in interferometric radar echoes. *Geoscience and Remote Sensing, IEEE Transactions on,* 30**,** 950-959.

Zebker, H. A., Werner, C. L., Rosen, P. A. & Hensley, S. 1994b. Accuracy of topographic maps derived from ERS-1 interferometric radar. *Geoscience and Remote Sensing, IEEE Transactions on,* 32**,** 823-836.

Zender, C. S., Krolewski, A. G., Tosca, M. G. & Randerson, J. T. 2012. Tropical biomass burning smoke plume size, shape, reflectance, and age based on 2001–2009 MISR imagery of Borneo. *Atmospheric Chemistry and Physics,* 12**,** 3437-3454.

Zhang, L., Ding, X. & Lu, Z. 2011. Ground settlement monitoring based on temporarily coherent points between two SAR acquisitions. *ISPRS Journal of Photogrammetry and Remote Sensing,* 66**,** 146-152.

Appendixes:

Appendix 1 Envisat interferograms used in Chapter 4

Master	Slave	Time interval (days)	Perpendicular baseline (m)	Average coherence	Coherence less than 0.2 (%)
20021228	20030621	175	-54.42	0.25	41.72
20021228	20031213	350	-265.24	0.18	71.07
20021228	20040501	490	-321.92	0.17	74.95
20021228	20040710	560	138.35	0.18	71.41
20030621	20031213	175	-211.95	0.19	67.58
20030621	20040501	315	-268.75	0.21	55.25
20030621	20040710	385	191.53	0.19	66.99
20030621	20050205	595	-51.69	0.16	84.63
20030621	20050416	665	373.73	0.16	87.84
20030621	20060610	1085	39.72	0.17	78.91
20030621	20061028	1225	-43.95	0.16	86.38
20030621	20070210	1330	51.44	0.16	87.16
20031213	20040501	140	-56.79	0.25	37.80
20031213	20050205	420	160.26	0.16	81.92
20031213	20061028	1050	168.00	0.16	87.16
20040501	20040710	70	460.27	0.21	56.72
20040501	20050205	280	217.07	0.16	81.98
20040501	20060610	770	308.45	0.16	86.69
20040501	20061028	910	224.82	0.15	88.21
20040501	20070210	1015	320.19	0.15	89.20
20040605	20040710	35	-421.24	0.22	54.51
20040605	20041023	140	-67.35	0.20	58.99
20040605	20050101	210	236.55	0.16	85.49
20040605	20050730	420	-1.44	0.19	66.05
20040605	20051112	525	69.09	0.16	81.82
20040605	20051217	560	116.87	0.17	75.53
20040710	20041023	105	352.37	0.22	53.14
20040710	20050205	210	-243.13	0.18	72.70
20040710	20050416	280	182.74	0.19	68.77

20040710	20060610	700	-151.72	0.16	86.00
20040710	20061028	840	-235.47	0.16	85.81
20041023	20050101	70	309.82	0.22	51.83
20041023	20050416	175	-169.39	0.22	55.54
20041023	20050730	280	70.16	0.20	60.02
20041023	20051112	385	138.92	0.19	66.97
20041023	20051217	420	190.24	0.18	74.78
20050101	20050730	210	-240.41	0.16	81.84
20050101	20051112	315	-171.22	0.18	73.82
20050101	20051217	350	-120.41	0.16	82.92
20050205	20060610	490	87.60	0.15	90.64
20050205	20061028	630	7.74	0.16	81.04
20050416	20050730	105	240.95	0.17	74.67
20050416	20051112	210	309.15	0.17	79.68
20050416	20051217	245	361.94	0.17	77.77
20050416	20070804	840	-27.63	0.16	84.19
20050730	20051112	105	68.33	0.21	55.71
20050730	20051217	140	120.49	0.20	58.58
20050730	20070908	770	77.40	0.17	77.36
20050730	20071117	840	77.94	0.16	84.89
20051112	20051217	35	52.16	0.24	44.20
20051112	20070908	665	9.08	0.17	76.69
20051112	20071117	735	9.61	0.17	76.64
20051217	20070908	630	-43.09	0.17	74.36
20051217	20071117	700	-42.56	0.16	84.28
20060610	20061028	140	-83.64	0.16	81.53
20060610	20070210	245	11.73	0.17	77.11
20061028	20070210	105	95.40	0.19	67.82
20070210	20070804	175	291.80	0.18	74.89
20070804	20070908	35	343.94	0.31	32.72
20070804	20071117	105	344.49	0.22	52.57
20070908	20071117	70	0.75	0.32	27.26

Appendix 2 ALOS PALSAR interferograms used in Chapter 4.

Master	Slave	Time interval (days)	Perpendicular baseline (m)	Average coherence	Coherence less than 0.2 (%)
20061211	20070126	46	-792.00	0.37	8.26
20061211	20070613	184	595.52	0.37	3.89
20061211	20070729	230	1029.41	0.38	3.43
20061211	20090618	920	-586.96	0.32	6.89
20070126	20070613	138	1387.57	0.34	10.22
20070126	20070729	184	1821.44	0.34	10.75
20070126	20090618	874	204.95	0.29	14.24
20070126	20090803	920	-35.46	0.30	14.17
20070613	20070729	46	433.87	0.60	0.59
20070613	20071214	184	1763.50	0.46	2.10
20070613	20090618	736	-1182.75	0.36	4.45
20070613	20090803	782	-1423.19	0.40	3.04
20070613	20091219	920	246.43	0.36	5.33
20070613	20100321	1012	1573.25	0.32	7.73
20070613	20100506	1058	1790.75	0.38	2.96
20070613	20100621	1104	1740.36	0.38	3.99
20070729	20071214	138	1329.55	0.54	1.31
20070729	20080129	184	1882.91	0.44	2.87
20070729	20080315	230	2377.92	0.34	8.62
20070729	20080430	276	3047.65	0.38	3.70
20070729	20090618	690	-1616.55	0.39	3.86
20070729	20090803	736	-1856.99	0.40	2.78
20070729	20091219	874	-187.43	0.34	7.06
20070729	20100203	920	532.19	0.28	13.68
20070729	20100321	966	1139.31	0.34	7.29
20070729	20100506	1012	1356.79	0.40	3.62
20070729	20100621	1058	1306.40	0.35	4.92
20071214	20080129	46	553.36	0.59	1.79
20071214	20080315	92	1048.35	0.46	8.50

20071214	20080430	138	1718.11	0.52	1.93
20071214	20090618	552	-2946.09	0.38	6.82
20071214	20090803	598	-3186.55	0.39	6.43
20071214	20091219	736	-1516.99	0.35	8.69
20071214	20100203	782	-797.37	0.29	17.22
20071214	20100321	828	-190.25	0.39	7.61
20071214	20100506	874	27.23	0.44	4.49
20071214	20100621	920	-23.16	0.37	7.49
20080129	20080315	46	495.18	0.48	8.45
20080129	20080430	92	1165.25	0.53	2.25
20080129	20100203	736	-1351.27	0.27	21.34
20080129	20100321	782	-743.89	0.37	8.71
20080129	20100506	828	-526.29	0.39	6.64
20080129	20100621	874	-576.65	0.34	10.20
20080315	20080430	46	670.01	0.49	7.06
20080315	20100203	690	-1846.32	0.27	18.92
20080315	20100321	736	-1238.98	0.34	15.31
20080315	20100506	782	-1021.41	0.33	12.47
20080315	20100621	828	-1071.77	0.29	15.24
20080430	20100203	644	-2516.94	0.27	15.92
20080430	20100321	690	-1909.45	0.36	6.30
20080430	20100506	736	-1691.81	0.40	3.72
20080430	20100621	782	-1742.16	0.33	6.25
20090618	20090803	46	-240.43	0.56	1.02
20090618	20091219	184	1428.87	0.32	7.21
20090618	20100203	230	2148.36	0.27	13.11
20090618	20100321	276	2755.34	0.36	5.72
20090618	20100506	322	2972.76	0.36	4.13
20090618	20100621	368	2922.35	0.31	7.43
20090803	20091219	138	1669.28	0.38	3.97
20090803	20100203	184	2388.77	0.30	10.45
20090803	20100321	230	2995.74	0.37	4.66
20090803	20100506	276	3213.16	0.39	3.40
20090803	20100621	322	3162.74	0.35	4.33
20091219	20100203	46	719.67	0.38	9.65
20091219	20100321	92	1326.84	0.38	7.88
20091219	20100506	138	1544.34	0.40	5.33

20091219	20100621	184	1493.95	0.40	5.27
20100203	20100321	46	607.24	0.34	12.39
20100203	20100506	92	824.77	0.34	11.57
20100203	20100621	138	774.39	0.33	10.20
20100321	20100506	46	217.44	0.53	3.16
20100321	20100621	92	167.03	0.37	7.07
20100506	20100621	46	-50.40	0.56	0.70

Appendix 3 MODIS daily/8-days snow coverage map, reproduced from (NASA, 2013b). The white rectangle in a and c presents the study area. (a) Daily snow coverage map collected on 20071214; (b) 8-days snow coverage map collected from 20071211 to 20071218; (c) Daily snow coverage map collected on 20100203; (d) 8-days snow coverage map collected from 20100202 to 20100209. Since the study area is covered by cloud in daily maps (a and c), 8-days snow coverage maps are used in this study (b and d). b and d suggest that the study was probably covered by snow.